UNIVERSITÀ DELLA CALABRIA

UNIVERSITA' DELLA CALABRIA

Dipartimento di Chimica e Tecnologie Chimiche

Dottorato di Ricerca in

Scienze e Tecnologie Fisiche, Chimiche e dei Materiali, in convenzione con il CNR

CICLO

XXX

TITOLO TESI

Water Soluble Ir(III) Complexes Towards Organised Phases and Nanostructured IrO$_2$ Thin Films

Settore Scientifico Disciplinare CHIM/03

Coordinatore: Ch.mo Prof. Vincenzo Carbone

Firma _Vincenzo Carbone_

Supervisore/Tutor: Dott. Nicolas Godbert

Firma _Godbert_

Dottorando: Dott.ssa Francesca Scarpelli

Firma _Francesca Scarpelli_

UNIVERSITÀ DELLA CALABRIA

Department of Chemistry and Chemical Technologies

Physical, Chemical and Materials Sciences and Technologies
XXX Cycle

Ph.D. Thesis

Water Soluble Ir(III) Complexes Towards Organised Phases and Nanostructured IrO$_2$ Thin Films

Supervisor   Ph.D. Candidate

Dr. Nicolas Godbert   Francesca Scarpelli

Table of Contents

ABSTRACT

Water soluble Ir(III) complexes towards organised phases and nanostructured IrO$_2$ thin films

This thesis comprises three main macro-topics: water-soluble Iridium (III) complexes, Iridium-based metallogels and nanostructured Iridium Oxide (IrO$_2$). More specifically, the synthesis of new water-soluble cationic Ir(III) complexes has been performed through a simple methodology which involves the incorporation of hydrophilic counterions into the final compounds. Some of the synthesized complexes have shown supramolecular organization in water. These self-assembling architectures have been thoroughly investigated through the combination of complementary characterization techniques, in particular Polarized Optical Microscopy (POM), Transmission Electron Microscopy (TEM), Powder X-Ray Diffraction (PXRD), etc. According to the nature of the featuring ligands, the water-soluble Ir(III) complexes display features of metallogels or lyotropic liquid crystals. The use of these highly organized metallo-hydrogels as Structural Directing Agent (SDA), and concomitantly as direct metal source, has been exploited for the preparation of nanostructured IrO$_2$ powders and thin films. All the presented materials display appealing features for specific applications: water-soluble Ir(III) complexes could represent interesting candidates for anticancer drugs or bioimaging probes, Ir(III) metallogels could find applications in thermosensing or as templating agents, and finally nanostructured IrO$_2$ could be employed in electrochromic devices and catalytic processes.

Chapter 1

General introduction

1.1 Iridium (III) complexes

In recent years, great consideration has been given to Iridium(III) complexes, by virtue of their interesting properties that make them suitable candidates for many applications, such as OLEDs, LEECs, anticancer agent, etc.

Ir (III) metal centre is characterized by a rich coordination chemistry, which allows to obtain a wide variety of compounds, including bis- and tris-cyclometalated complexes. The classical procedure adopted to synthesize bis-cyclometalated and tris-cyclometalated species, involves the formation of a chloro-bridged dimer incorporating the desired cyclometalated ligand (C^N), followed by the bridge splitting reaction of the chloro-bridge through the introduction of an ancillary ligand (N^N, L^X or X^X)[1,2] or of the cyclometalated ligand (C^N) already used for the formation of the dimer.[3] In the first case, a bis-cyclometalated complex will be obtained, whereas the second way leads to tris-cyclometalated compound.

In addition, through the appropriate choice of the chelating ligand, neutral, cationic or anionic Ir(III) complexes can be obtained (Fig.1.1). The use of a neutral ligand (N^N), such as 2,2'-bypyridine (**bpy**),[4] 1,10-phenanthroline (**phen**),[5] 2,2'-biquinoline (**biq**),[6] etc., results in a cationic complex. Conversely, neutral Ir (III) coordination compounds have been synthesized by using bidentate, anionic ancillary ligands (L^X), as acetylacetone (**acac**) or 2-picolinic acid (**pic**) and their derivatives.[7] Finally, anionic Ir(III) complexes were produced employing bidentate dianionic ligands, as tetrazolate (N^N),[8] catecholate (O^O)[9] and orotate acid (O^N).[10]
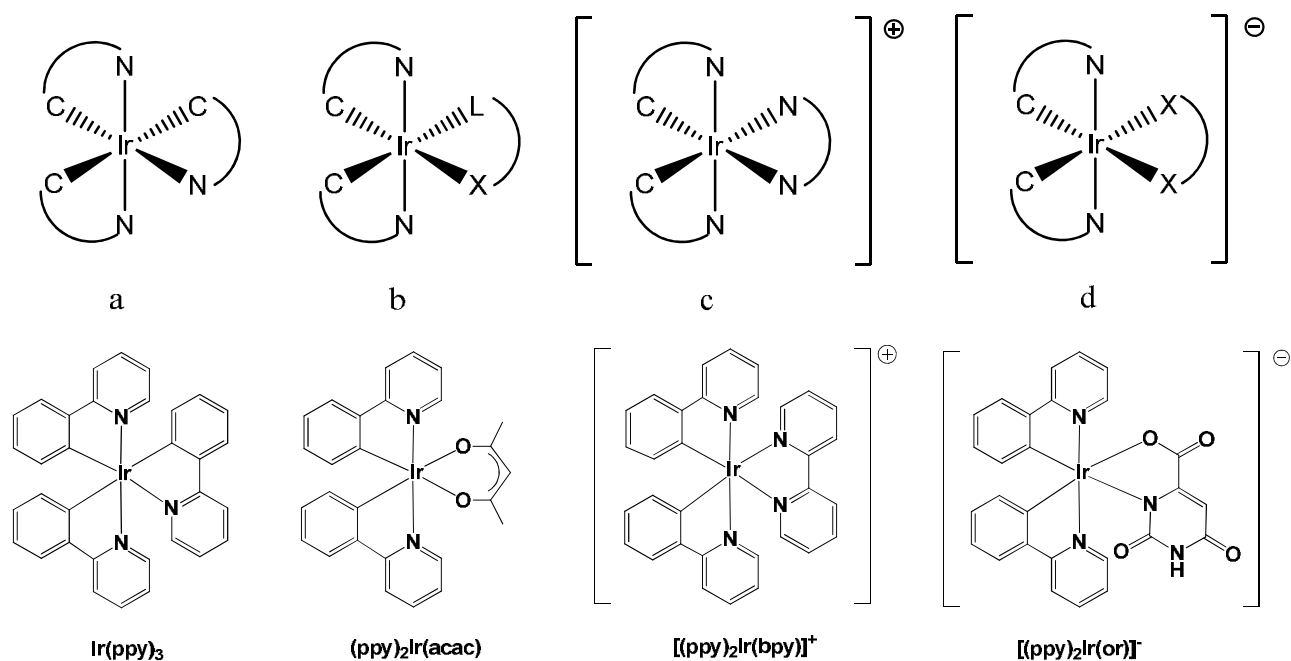
Fig.1.1. Schematic representation of a tris-cyclometalated Ir(III) complex (a), a neutral bis-cyclometalated Ir (III) complex (b), a cationic bis-cyclometalated Ir(III) complex (c) and an anionic bis-cyclometalated Ir(III) complex (d), with corresponding examples: **Ir(ppy)$_3$**[3], **(ppy)$_2$Ir(acac)**,[7] **[(ppy)$_2$Ir(bpy)]$^+$**,[4] **[(ppy)$_2$Ir(or)]$^-$**.[10]

1.2 Photophysical properties

The large attention received by Ir(III) compounds is due to the appealing features displayed by these materials, in particular to their interesting photophysical properties. Intense phosphorescence at room temperature, high photoluminescence quantum yields (ϕ), large Stokes shift and, in some cases, much longer (μs) lifetimes (τ) have been reported for many Ir(III) complexes.[11-13]

Iridium (III) complexes exhibit two basic transitions in their excited state: the metal-to-ligand charge transfer (MLCT) and the ligand-centered (LC) transitions. The MLCT involves the transition of an electron from a metal d orbital to a vacant π* antibonding orbital on one of the ligands, and it can be viewed as a metal oxidation with concomitant ligand reduction. This transition is typical of transition metal complexes with a d^6 configuration (W^0, Re^I, Os^{II} and Ir^{III}). Contrary, the LC transition is characterized by an electronic transition between a π and a π* orbitals, both localized on one of the ligands.[14] Generally, the transition identification is based on the measurement of the luminescence lifetimes and on the observation of the band shapes.[15]

The presence of the heavy metal centre affords strong spin-orbit coupling, which determines the inversion of the relative orientation of an electron pair, removing the spin-forbidden character of the phosphorescent transitions. This phenomenon promotes intersystem crossing, thus the transition from a singlet excited electron state to a triplet excited state, from which a phosphorescent emission can take place (Fig.1.2).
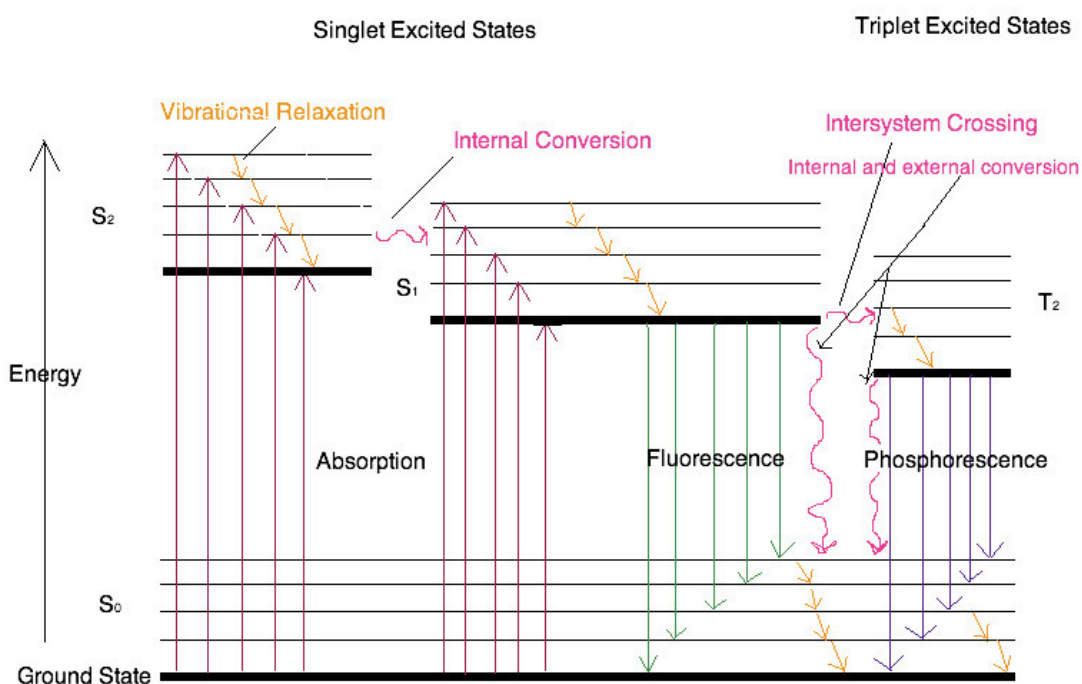
Fig.1.2. The Jablonski diagram.[16]

The triplet excited state in Iridium(III) complexes generally is a mixed excited state which derives from a good overlap between ^{3}LC and ^{3}MLCT (Fig.1.3).[15]

The photophysical properties of an Ir(III) coordination compound is based on absorption, emission and excited-state lifetime measurements in solution and/or in solid-state. These techniques allow the determination of two important parameters for a phosphor: **ϕ** and **τ**.

The emission quantum yield (**ϕ**) and the lifetime of the excited state (**τ**) depend on the combination of radiative (k_r) and non-radiative (k_{nr}) processes, as shown in the following equations:[17]

$$\emptyset = \frac{k_r}{k_r + k_{nr}}$$

$$\tau = \frac{1}{k_r + k_{nr}}$$

To further understand the luminescent properties of Ir (III) complexes, density functional theory (DFT) calculations can be performed in order to evaluate the highest occupied molecular orbital (HOMO) and the lowest unoccupied molecular orbital (LUMO). Generally, for Ir(III) complexes, DFT calculations are performed with the B3LYP[18] functional and the mixed "Double-ζ" quality basis sets 6-31G(d) for the ligands[19] and LANL2DZ for Ir. Theoretical calculations can be also be experimentally sustained by estimation of the energy level of the frontier orbitals through cyclic voltammetry. For example, Hay studied the primary energy levels responsible for the green emission of the prototypical cyclometalated complex Ir(ppy)$_3$.[20] According to his study, the HOMO level are consisting by a mix between the Iridium d orbitals and the π orbitals of the cyclometalated rings, whereas the LUMO level consists of the π* orbitals of the pyridine rings.
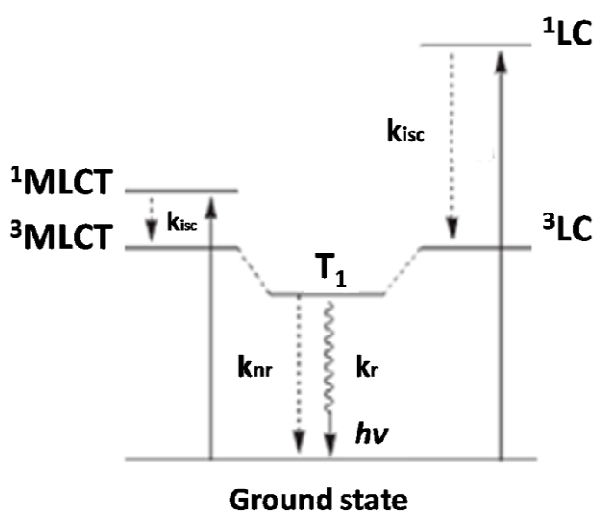
Fig.1.3. The overlap between ^{3}LC and ^{3}MLCT (adapted from ref. [1])

Since luminescence in Ir(III) complexes is by nature involving the ligand, tuning of the emission colour can be potentially performed over all the visible spectra, by simply varying the chemical nature of the ligand coordinated to the metal centre (Fig.1.4). For example, the above mentioned tris-cyclometalated Ir(III) complex **(ppy)$_3$Ir** and the complex **[(ppy)$_2$Ir(acac)]** are well-known green emitters (λ_{max} = 515 nm).[21] The expansion of the π system of both phenyl and pyridine rings, using benzoquinoline (**bzq**) or 2-phenylquinoline (**pq**) as cyclometalated ligands, leads to a bathochromic effect, thus the color emission shifts to red.[22] A hypsochromic effect, meaning a blue shift of the emission, can be achieved increasing the energy gap between HOMO and LUMO, e.g. lowering HOMO level. The presence of an electron-withdrawing group, such as fluoride atoms, on the phenyl rings represents an opportunity to induce this effect.[23]
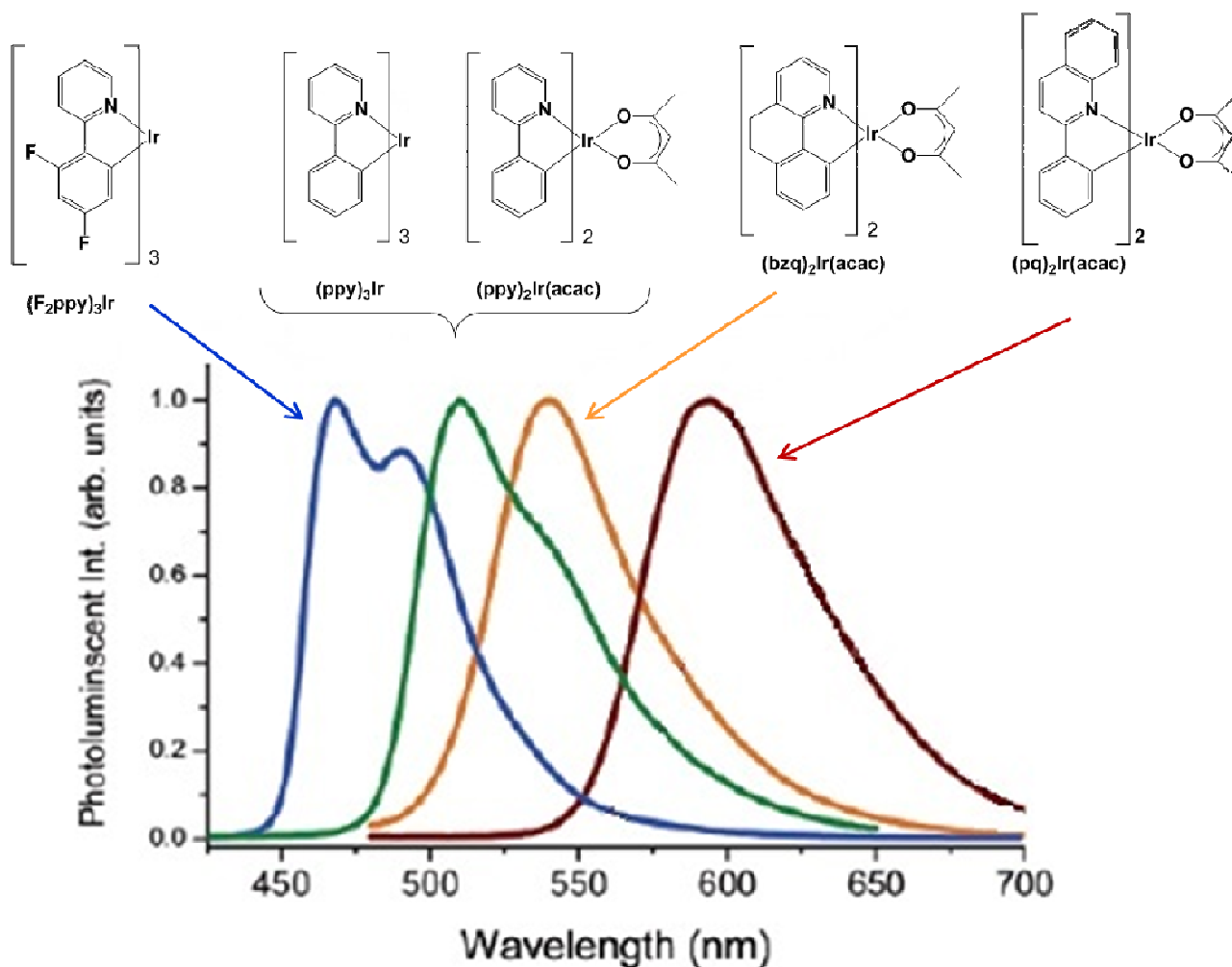
Fig.1.4. The shift of the emission spectra of some Iridium (III) complexes, obtained simply varying the cyclometalated ligand (adapted from ref. [24])

Therefore, the introduction of an electron-donating or of an electron-withdrawing substituent in the phenylpyridine ligand modifies the energy band gap between the HOMO and LUMO levels, resulting in a change in the emission colour of the resulting complex. Also the position of an eventual substituent plays an important role in the modulation of the energy levels involved in the transition, as reported for a **(ppy)₂Ir(pic)** complex (Fig.1.5).[25] In this case the cyclometalated ligands (**ppy**) are functionalised in two different positions with the electron-withdrawing dicyanovinyl group: the meta-modified complex (Fig.1.5_a) presents a blue-green emission, contrary to the para-modified complex (Fig.1.5_b) which displays a deep red emission.

a

b
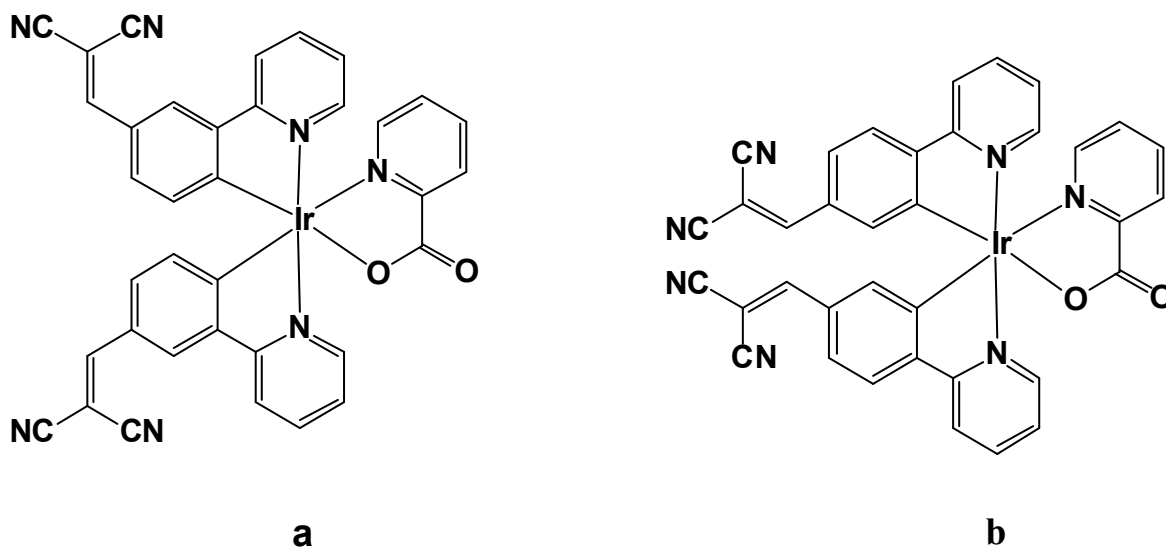
Fig.1.5. Chemical structures of **(ppy)₂Ir(pic)** derivative complexes: a)meta-substituted complex; b)para-substituted complex.[25]

Besides the maximum emission wavelength, the functionalisation of a ligand can affect also the emission quantum yield (ϕ) and the lifetime of the excited state (τ). An example was given by Dragonetti *et al.*, who compared the photophysical properties of some Ir (III) complexes bearing phenylpyridine as cyclometalated ligands and differently substituted 1,10-phenanthroline as ancillary ligand (Fig.1.6).[5] They observed a marked decrease of the quantum yields moving from the compounds incorporating the methyl group (ϕ = 34-38%) to the complexes including the electron-donor group NMe$_2$ (ϕ = 0.3-6%) and the electron-withdrawing moiety NO$_2$ (ϕ < 0.1%). Through DFT calculations, they explained these experimental observations as an effect of substituents on the energy level of the frontier orbitals. In particular, weak electron-donating substituents such as the methyl group do not significantly alter the geometry and the electronic structure of the **[(ppy)₂Ir(1,10-phen)]** cationic complex, whereas strong electron-withdrawing substituents, such as the NO$_2$ group, lead to extensive perturbation of the phenanthroline π^* levels, stabilizing the LUMO energy level. Finally, strong electron-donor substituents, as NMe$_2$, destabilize the π-bonding levels of the phenanthroline ligand.
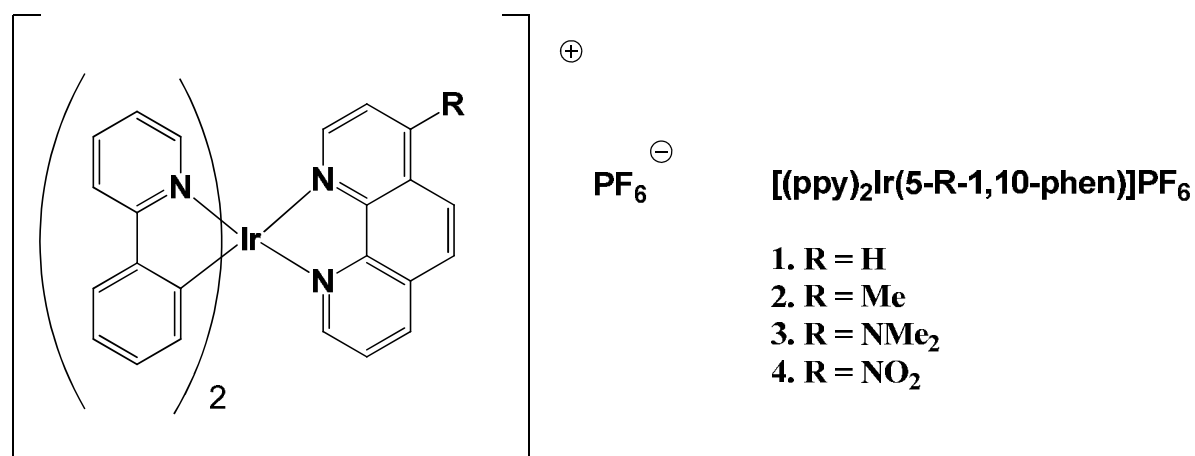
Fig.1.6. Chemical structures of **[(ppy)₂Ir(5-R-1,10-phen)]PF₆** derivative complexes.[5]

The interesting photophysical properties of Ir (III) complexes and the high tunability of their emission features prompt their use not only as phosphorescent dyes in highly efficient, color-switchable optoelectronic devices, such as organic light-emitting diodes (OLEDs) and light-emitting electrochemical cells (LEECs), but also as photosensitizer in photodynamic therapy and as probe for bioimaging.

Some of the main applications of Ir (III) coordination compounds are summarized below.

1.3 Application of Ir (III) complexes

1.3.1 Optoelectronic devices

1.3.1.1 OLEDs

An Organic-Light Emitting Diode (OLED) is a solid-state semiconductor device able to emit light as a response to an electric current. An OLED device consists of diverse layers, as schematically represented in Fig.1.7:

- a flat and transparent substrate, usually glass;
- a transparent anodic material, with low resistivity and large work function; generally indium tin oxide (ITO) meets these requirements; the anode is responsible for the holes injection into the device;

- a hole injection, or hole conducting, layer which acts as an interface layer between the anode and the hole transport layer and improves the injection process;
- a hole transport layer, which transports holes generated into the anode to the emissive material;
- an electron blocking layer, which prevents electron injected from the opposite electrode to be discharged on the cathode;
- an emissive layer;
- a hole blocking layer, which prevents holes injected from the opposite electrode to be discharged on the anode;
- an electron transport layer, which transports electrons generated into the cathode to the emissive layer;
- an electron injection layer, that, similar to the hole injection layer, acts as an interface layer between the electrode and the transport layer, minimizing the energy barrier for injection from the cathode;
- a cathode material, responsible for the generation of the negative charges, generally consisting of a reflective metallic layer.[26]
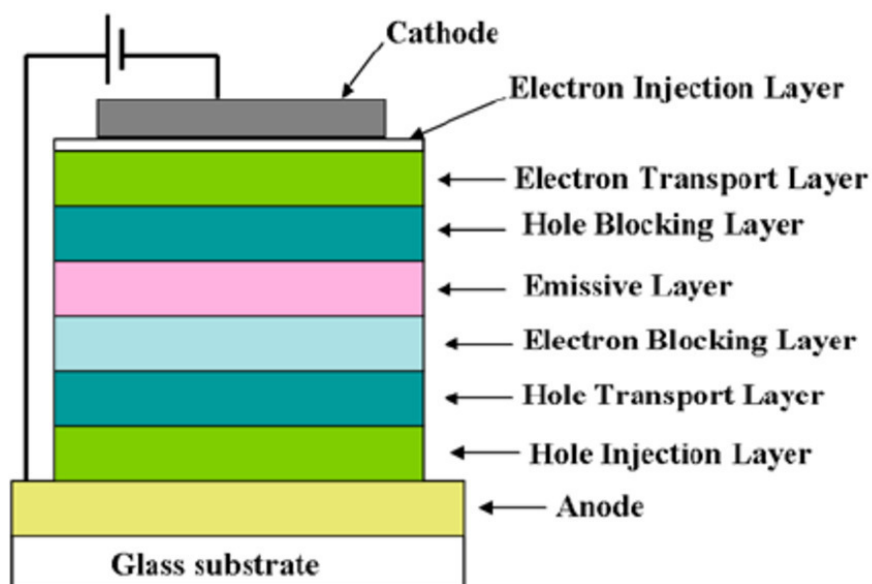
Fig.1.7. OLED schematic drawing[27]

Note that all the listed layers may not be needed in an OLED device because a single layer can often perform more than one function.

In an OLED device, light emission derives from a photoemissive relaxation mechanism of an exciton, arising from the recombination of an electron and a hole into the emissive material. The emissive layer is an electroluminescent material (EL) able to emit light under the influence of an applied electric field, and it can be made by small organic/organometallic compounds or by polymers. The main requirements for an EL material, suitable for use in OLEDs, are the monochromaticity of the wavelength emission, a high luminescence quantum yields and a medium excited-state lifetime, since lifetimes too short may avoid recombination of the exciton within the emissive layer, whereas lifetimes too long could induce non-radiative relaxation mechanisms, both phenomena decreasing the overall efficiency of the devices.[28] On this premise, triplet emitters based on Ir(III) complexes are ideal candidates as emissive materials for these optoelectronic devices. Potentially, phosphorescence emission of every wavelength in the visible spectra can be obtained with Ir(III) phosphors. For example, the homoleptic **Ir(ppy)₃** and the heteroleptic **(ppy)₂Ir(acac)** complexes, mentioned in the previous paragraph, have been widely used for the development of green-emitting OLEDs.[21]

Red-emitting OLEDs were recently fabricated using an active layer of 4,4'-Bis(N-carbazolyl)-1,1'-biphenyl (CBP) doped with Iridium(III) complexes of acetylacetone (acac) and 1-phenyl-isoquinoline (piq) derivatives.[29]

Furthermore, De Cola reported the fabrication of an OLED device with a bright blue emission, using an Ir(III) complex bearing two cyclometalating 2',6'-difluoro-2,3'-bipyridyl **H(dfpypy)** ligands and one pyridyl pyrazolate ligand **(fpbpz)**.[30]

The CIE chromaticity diagram of some of the more efficient Ir(III) complexes employed in OLED devices is presented in Fig 1.8 to illustrate the versatility of these complexes. Their chemical structures and emission wavelength are reported in Table 1.1.
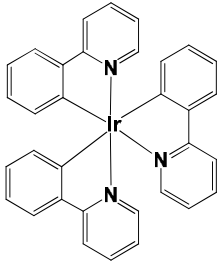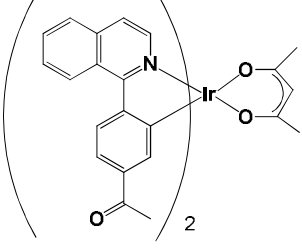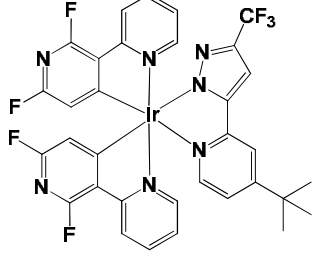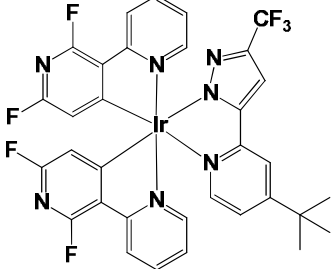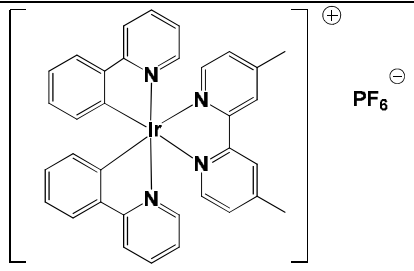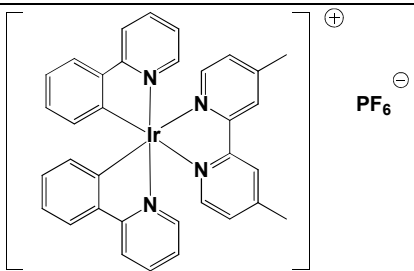
COMPLEX	CHEMICAL STRUCTURE	λmax/nm	Ref.
Fac-[(ppy)₃Ir]		515	31
(4-acetyl-piq)₂Ir(acac)		658	29
(dfpypy)₂Ir(fpbpz)		440	30
[(Fppy)₂Ir(dmb)][PF₆]		522	32
[(ppy)₂Ir(dmb)][PF₆]		580	32
(Fppy)₂Ir(pic)		470	33

Table 1.1. Chemical structures and λ$_{max}$ emission of selected Ir(III) complexes.
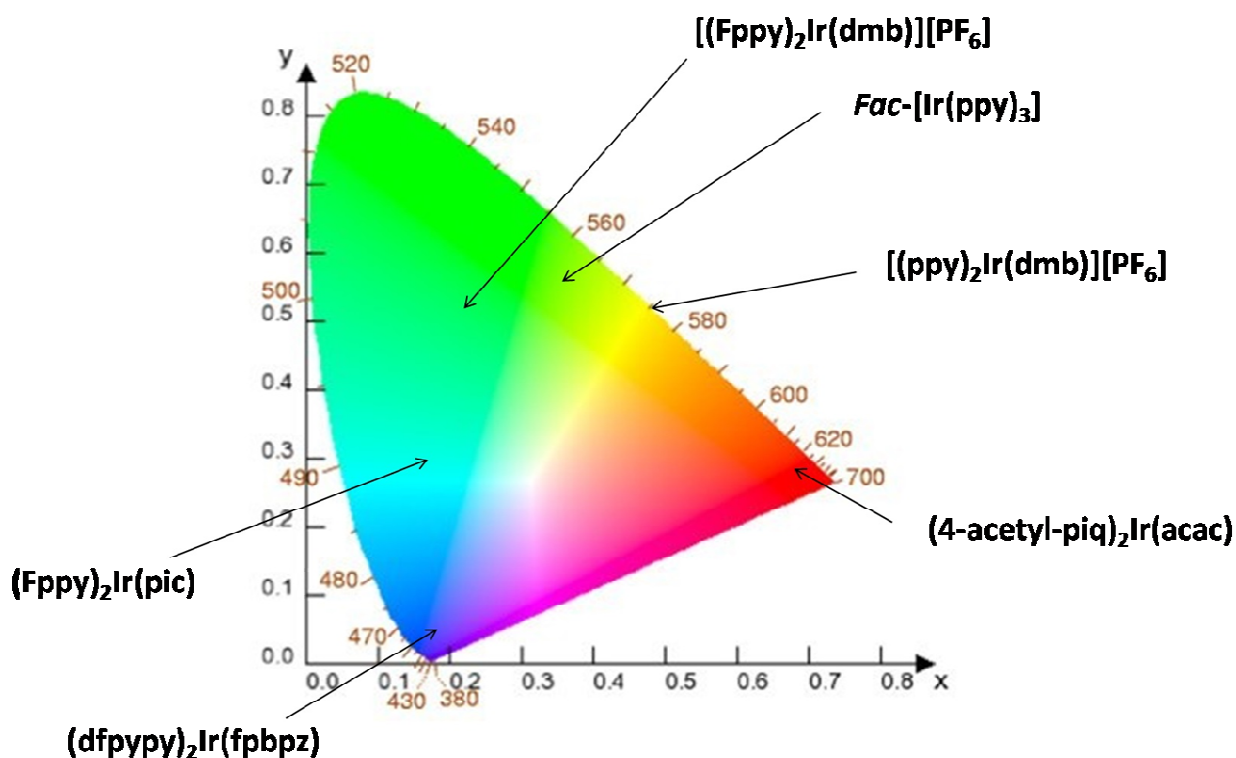
Fig.1.8. Chromaticity diagram with CIE coordinates of selected Ir(III) complexes.

1.3.1.2 LEECs

Due to their ionic nature, charged Ir(III) complexes have been also extensively used for the fabrication of other electroluminescent devices, named light-emitting electrochemical cells (LEECs). LEECs represent a simplified version of OLEDs, consisting in a single-layer device in which the ionic light-emitting material is sandwiched between an anode and a cathode (Fig.1.9).
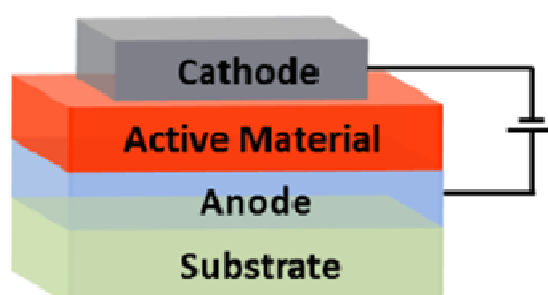
Fig.1.9. A schematic representation of a single-layer LEEC device (from ref. [34])

The working mechanism of these devices has been the subject of many studies,[35-37] and can be summarised in important stages: first, the application of an external electric field allows electrons and holes to be injected from the electrodes respectively into the LUMO and HOMO levels of the active material. Subsequently, the injected charges will be compensated by cations and anions, creating n-type dopants and p-type dopants. The two doped regions will expand over time until ohmic contact will be created, generating a p-n junction. In this domain, holes and electrons will recombine, producing an exciton which will ultimately decay through the emission of a photon.

LEECs devices present many advantages with respect to their OLEDs counterparts, such as the ease of fabrication through spin-coating technique, the higher stability of the low-work-function electrodes used and the requirement of very low voltage of operation.

The light-emitting material can consist either in a polymer[38] or in a transition metal complex (TMC).[39] The polymer-based LEECs require polymer doping with an electrolytic salt, in order to supply the ions necessary to compensate electrons and holes. In a TMC-LEECS, the coordination compound is both responsible for ionic and electronic conductivity.

The first TMC-LEECs devices were based on Ru(II) complexes,[40,41] which, however, offered limited color tuning. Currently, the metal complexes of choice for the preparation of LEECs are ionic Ir(III) coordination compounds, by virtue of their physical and chemical properties, which can lead to high emission efficiency and high color tunability.[42]

Two important parameters of a LEEC system are the device's lifetime, expressed by means of the time lasting for the radiance to decay to halve its maximum value,[43] and the turn-on time, defined as the delay between the device switch on and the achieving of a steady-state light emission, caused by the redistribution of ions.[44] For practical applications, the turn-on time should be close to a few seconds, which is generally not observed. Unfortunately, all the strategies to shorten the turn-on time are at the expense of the device stability.

Rudmann et al. demonstrated the strong dependence of the device turn-on time and lifetime on the nature of the counterion: small counterions, such as BF_4^-, increase ionic conductivity, resulting in a short turn-on time of the device.[45] At the same time, large counterions can enhance device lifetime, therefore, a compromise between turn-on time and lifetime is often needed.[43]

Recently, the fabrication of highly stable and efficient LEECs using cationic Ir (III) complexes bearing 2-phenylpyridine as cyclometalated ligand, arylazole as ancillary

ligands and PF$_6^-$ as counterion was reported.[46] In particular, the introduction of 1-methyl-2-pyridin-2-yl-1H-benzimidazole as ancillary ligand in the complex **[(ppy)₂Ir(pyMebim)]PF₆** led to a yellow light-emitting electrochemical cell, presenting high luminance, great efficiency and high stability (lifetime over 2500h) (Fig.1.10).

Moreover, benzothiazole derivatives, such as **[(ppy)₂Ir(pybth)]PF₆**, have been exploited for the synthesis of red-emitting Ir(III) complexes which have been used as electroluminescent material in LEECs.[47] The devices so manufactured shown very long lifetimes. Blue and green-blue Ir(III) phosphors, as **[(dfppy)₂Ir(phpzpy)]PF₆** have also being incorporated in LEECs devices (Fig.1.10).[48]

[(ppy)₂Ir(pyMebim)]PF₆   [(ppy)₂Ir(pybth)]PF₆   [(dfppy)₂Ir(phpzpy)]PF₆
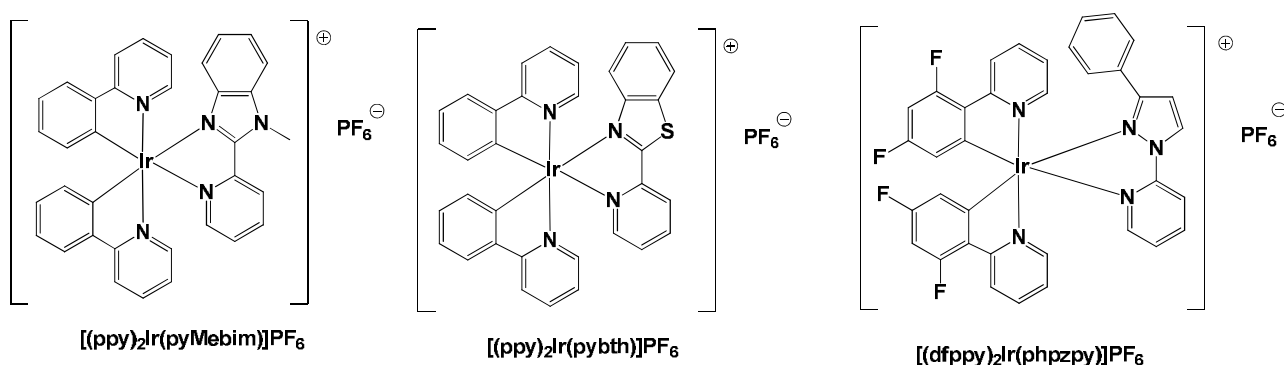
Fig.1.10. Chemical structures of yellow (**[(ppy)₂Ir(pyMebim)]PF₆**), red (**[(ppy)₂Ir(pybth)]PF₆**) and blue (**[(dfppy)₂Ir(phpzpy)]PF₆**) emitters for LEEC devices.

However, the general method to improve the turn-on time involves the addition of an ionic liquid (IL) to the TMC layer, increasing the density of the mobile ions by virtue of their high intrinsic ionic conductivity.[49] In this regard, Costa *et al.* reported the addition of three ILs, 1-ethyl-, 1-butyl-, and 1-hexyl-3-methylimidazolium hexafluorophosphate (EMIM⁺, BMIM⁺ and HMIM⁺ respectively), on the emissive layer of a LEEC consisting of **[(ppy)₂Ir(bpy)]PF₆** (Fig.1.11), demonstrating an optimization of the LEECs turn-on time without sacrificing their stability.[50]
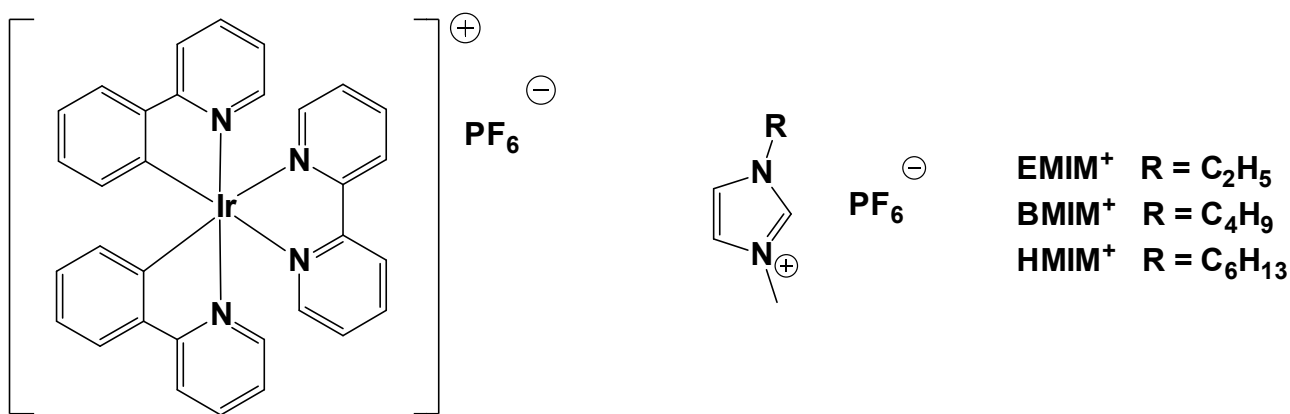
Fig.1.11. Chemical structures of **[(ppy)₂Ir(bpy)]PF₆** (left) and three ILs EMIM⁺, BMIM⁺ and HMIM⁺ (right).[50]

1.3.2 Oxygen sensing and photodynamic therapy (PDT)

The triplet excited state of Ir (III) complexes can efficiently transfer energy to the triplet ground state of molecular oxygen ($^3O_2$), leading to the formation of the singlet excited state of oxygen ($^1O_2$) and to the luminescence quenching of the complex (Fig.1.12).[51]
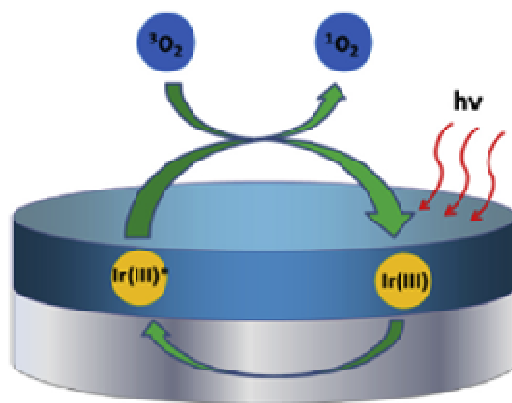
Fig.1.12. A schematic representation of the oxygen sensing mechanism for luminescent Ir (III) complexes (from ref. [51])

The process, illustrated in Fig.1.12, can be simplified as follows:

$$Ir^{III*} + O_2 \longrightarrow Ir^{III} + O_2^*$$
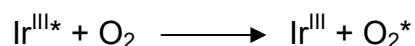
On this basis, Ir (III) phosphors can be actually used as oxygen sensor, measuring O_2 concentration as a function of the change of lumophores photophysical properties.[52,53]

Moreover, singlet oxygen is a reactive oxygen species (ROS), which has a relatively long lifetime, since its return to the ground state is spin-forbidden, although the time decay is highly influenced by the nature of the solvent. By virtue of its high reactivity which gives rise to a pronounced cytotoxic effect, singlet oxygen plays the principal role in photodynamic therapy (PDT).[54-56] PDT constitutes an alternative to chemotherapy for the treatment of some early-stage cancers and it is less invasive than surgery. This treatment involves the use of two components, a photosensitizer (PS) and light, which are combined in order to induce apoptosis and necrosis in tumor cells, via the generation of singlet oxygen.[57] The ideal PS should present some important features, such as low toxicity, high selectivity and should be easily eliminated by the patient.[58] Several studies demonstrated that Ir(III) complexes can be effectively used as photosensitizer in photodynamic therapy by virtue of their high luminescence quantum yield, the long lifetime of the excited state that results in high yield of singlet oxygen, the cell permeability and the ability to generate ROS also under hypoxia conditions.[59-62]

The main disadvantage of using Ir (III) complexes, or in general transition metal complexes, as PSs is the short light wavelength required to activate the compound; indeed, longer wavelengths of activation allow deeper tissue penetration. Ir (III) phosphors generally absorb in the UV/vis region, thus their use in PDT is limited to few cases, such as skin cancers. Very recently, McKenzie *et al.* presented two Ir(III) complexes (Fig.9) bearing 2-phenylpyridine as cyclometalated ligands, bis-benzimidazole and its *N,N*-dimethylated derivative as ancillary ligands and PF_6^- as counterion (**[Ir(ppy)$_2$(bbzH$_2$)]PF$_6$** and **[Ir(ppy)$_2$(bbzMe$_2$)]PF$_6$**) (Fig.1.13).[63] One of these complexes acts as photosensitizer under near-IR (760 nm) two photon excitation (TPE), representing a possibility to overcome the above described limitation of Ir(III) complexes use in PDT.
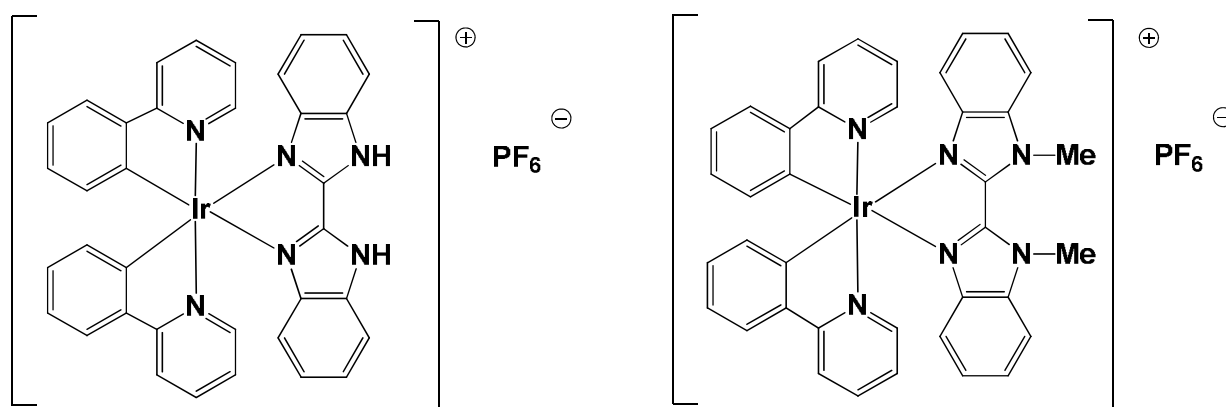
Fig.1.13. Chemical structures of (**[Ir(ppy)$_2$(bbzH$_2$)]PF$_6$** and **[Ir(ppy)$_2$(bbzMe$_2$)]**.[63]

1.3.3 Anticancer agents

Besides their use as PSs in photodynamic therapy, Iridium (III) complexes can exert anticancer activity through several mechanisms, as protein inhibition, targeting of organelles, catalysis of cellular redox reactions, DNA binding and therefore Ir(III) complexes represent an alternative to platinum-based drugs, which actually govern the antitumour market.

For example, Meggers *et al.* described some octahedral iridium complexes able to inhibit the protein kinase Flt4, an important enzyme involved in the generation of new blood vessels.[64] Angiogenesis and lymphangiogenesis are fundamental processes in tumor progression, thus their repression leads to a anticancer activity. The Ir(III) complexes they synthetized bear an unprotected maleimide motif (Fig.1.14). The free maleimide nitrogen atoms are able to form two hydrogen bonds with the hinge region of the ATP binding site of protein kinases, inhibiting it.

COMPLEX	R	X	Y
1	H	Cl	Cl
2	H	CH₃	Cl
3	H	CH₃	SeCN
4	H	CH₃	CH₃
5	H	CF₃	Cl
6	CH₃	Cl	Cl
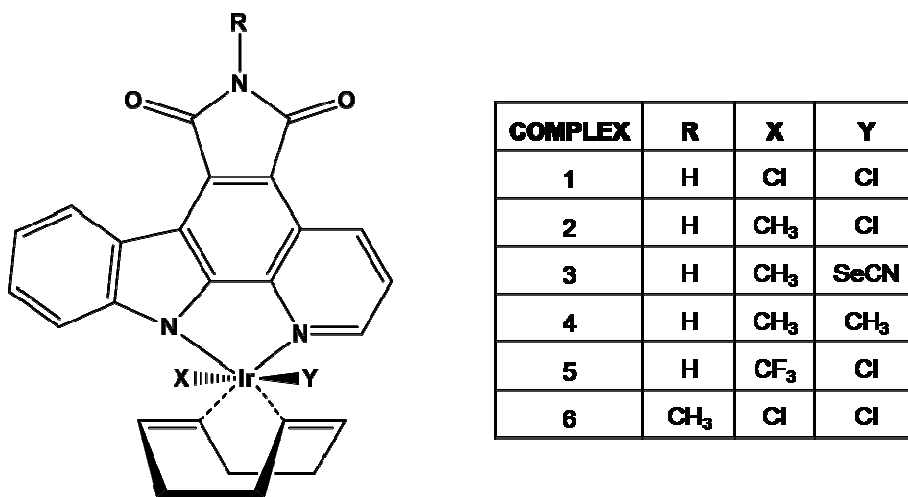
Fig.1.14. Chemical structures of Ir (III) complexes able to inhibit protein kinase Flt4.[64]

Another possible mode of action of Ir(III) antitumor agents is the targeting of subcellular organelles, such as mitochondria and lysosomes, triggering their dysfunctions.

Since mitochondria are indispensable for the survival of eukaryotic cells, their damage can induce cell death, through an apoptotic mechanism. Many Ir(III) coordination compounds can selectively accumulate into mithocondria, causing ROS production, cell cycle changes and apoptosis, as reported for cyclometalated Ir(III) complexes bearing guanidinium groups as ligands (Fig.1.15).[65] Indeed, the guanidinium group acts as hydrogen bonding acceptor and donor, playing an important role in drug design, exhibiting also selectivity towards mitochondria.

18
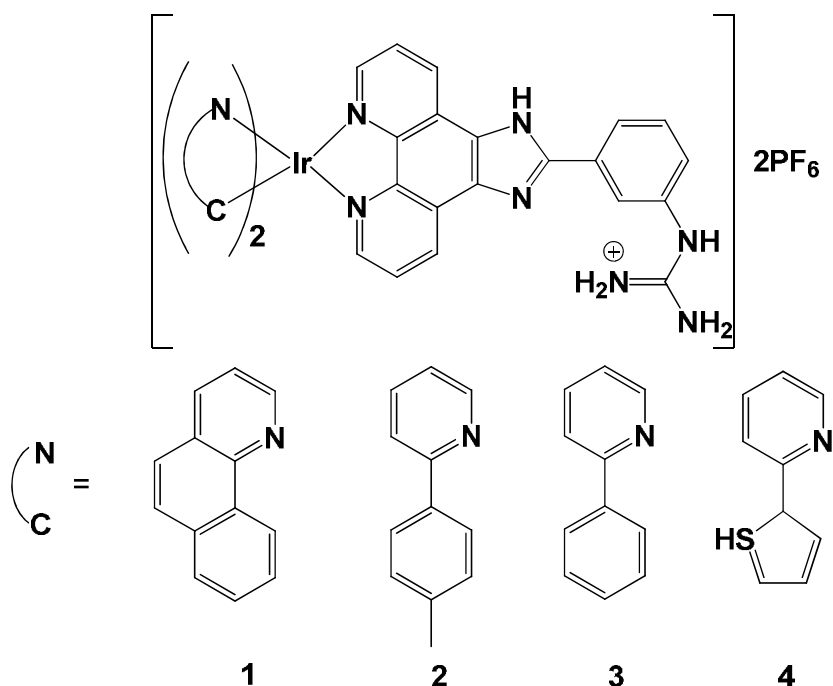
Fig.1.15. Chemical structures of Ir (III) complexes bearing guanidinium group.[65]

Recently, Mao *et al.* described Ir(III) compounds targeting mitochondria and lysosomes which are able to induce apoptosis through reactive oxygen species (ROS) generation and caspase activation upon visible light irradiation.[66]

The cytotoxic effect of Ir(III) compounds can also derive from the catalysis of cellular redox reactions. Some pentamethylcyclopentadienyl (Cp*) Ir (III) complexes, an example of which is reported in Fig.1.16, can exert antitumor effect thanks to their well-known catalytic activity.[67-69] As explained by Sadler, the π-bound negatively charged Cp* ligand, occupies one face of the octahedron (3 coordination sites) and affects the stability of the remaining ligands through modification of their electronic behaviour. Moreover, the functionalization of Cp* ligand with phenyl group may play a role in interactions with a target, for example, by intercalation into DNA base pairs, and the hydrophobicity of the ligand enhances cellular uptake of the complex.[69] Pentamethylcyclopentadienyl (Cp*) Ir (III) complexes can use NADH as an hydride source for hydrogenation reactions, with concomitant NADH oxidation. Following this route, organoiridium compounds, incorporating a Cp* ligand, can reduce many cellular substrates, for example quinones and ketones, with formation of semiquinones and alcohols respectively. The hydride of NADH can be also transferred to oxygen, generating hydrogen peroxide in cells, a strong oxidant. In any case, the resulting effect is the alteration of the cellular redox potentials and of the NADH-mediated cell signalling pathways.[67-69]
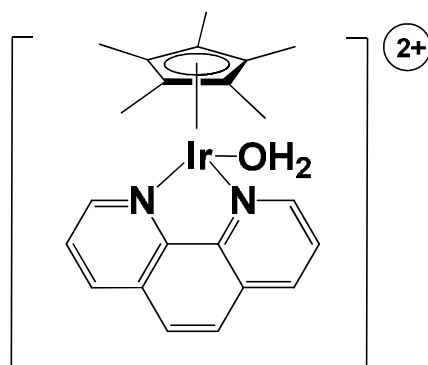
Fig.1.16. An example of aqua-Cp* Ir(III) complex, able to catalyze NADH oxidation.[68]

Finally, Ir(III) coordination compounds can also exert an antitumor effect through the binding in the minor groove of DNA and through inhibition of telomerase, although the mechanism of action had not yet been elucidated.[70-72]

1.3.4 Bioimaging

Iridium (III) lumophores have been widely used in fluorescence cell imaging, owing to their well-known photophysical properties, e.g. large Stokes shift, high emission quantum yield and relatively long emission lifetime, which prevents the interference of the short cell autofluorescence. Besides these photophysical features, a suitable cell probe should exhibit also water solubility, low cytotoxicity, good uptake and high chemical- and photo-stability.[73,74] Many Ir (III) complexes meet some of these requirements, in particular they rarely undergo photobleaching during irradiation.

Even though several Ir(III)-based lumophores show preferential localisation in specific cellular organelles, these complexes can easily be chemically modified or conjugated to biological motifs, in order to address them more specifically to a specific target.

Recently, 1,10-phenanthroline-5,6-dione **(phd)** was introduced in an Ir(III) complex as recognition unit for thiourea, a possible human carcinogen.[75] Upon addition of thiourea (Fig.1.17), this complex changes its photophysical properties, in particular, the luminescence intensity is increased. Hence, this organoiridium compound could be use for the imaging of thiourea in living cells.
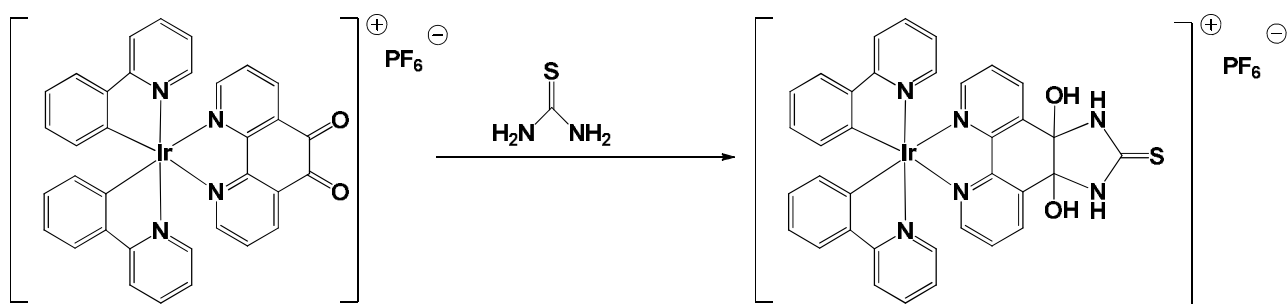
Fig.1.17. The reaction between **[(ppy)₂Ir(phd)]PF₆** and thiourea.[75]

The inclusion of an aldehyde group into an Ir(III) cell probe induces selectivity towards homocysteine (Hcy), an amino-acid considered an important biomarker for the diagnosis and prognosis of several diseases.[76] Indeed, the aldehyde motif can make a cyclization reaction with aminoalkylthiol groups of Hcy. Ir(III) complexes bearing an aldheyde function on the ancillary ligand can effectively be applied to detect and image intracellular Hcy through confocal fluorescence imaging.[77]

Ir (III) complexes have been also conjugated to biological moieties, such as biotin (vitamin H) (Fig.1.18).[78] Biotinylation provides high affinity for the glycoprotein avidin and allows the active transport of the probe into the cells.
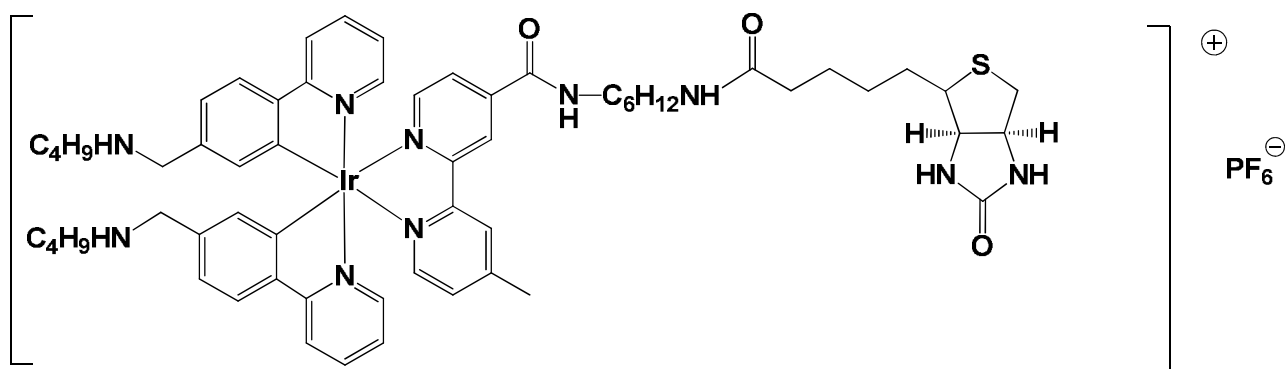
Fig.1.18. Chemical structures of a biotinylated Ir (III) complexes.[78]

Ir (III) phosphors have been also employed to probe enzymes in human cells, as cyclooxygenase-2 (COX-2), which is over-expressed in cancerous cells. The complexes described by Ma *et al*.[79] are able to bind COX-2, through a chemical motif which is a structural analogue of the well-known COX-2 inhibitor indomethacin (Fig.1.19). These complexes can be considered consisting of a "signal unit" conjugated to a "binder unit" via an amide bond linkage. The signal unit is responsible for the generation of an intense luminescence in cancer cells.
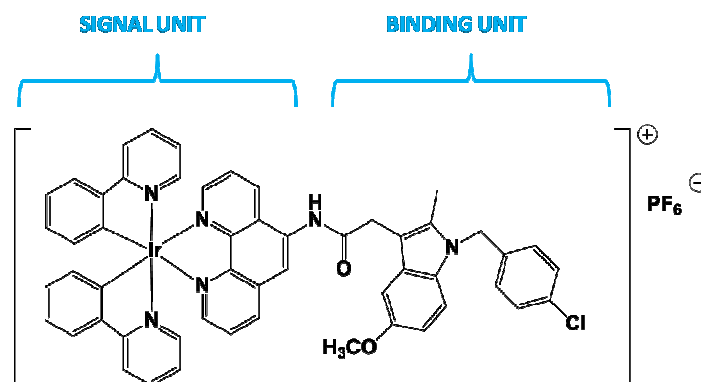
Fig.1.19. Chemical structures of a COX-2 selective Ir (III) complex.[79]

Usually Ir (III) complexes-based luminescent bioprobes show localisation in the cytoplasm, rather than membrane or nucleus, as reported for **[(dfpy)₂Ir(bpy)]PF₆** (Fig.1.20).[80]
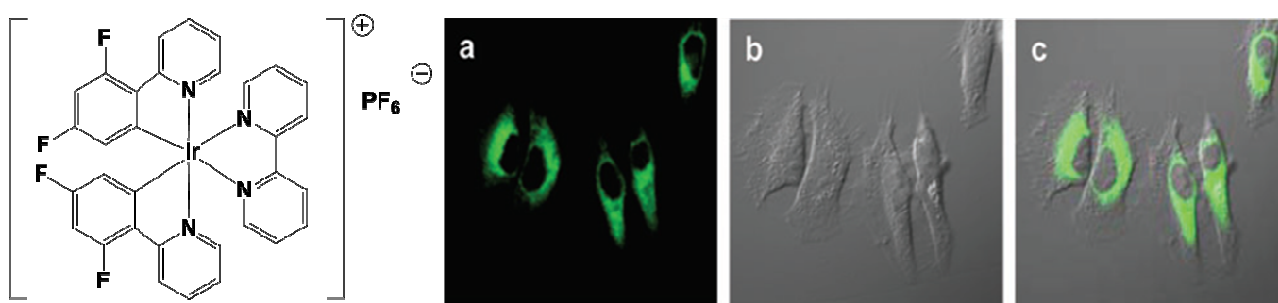
Fig.1.20. Confocal luminescence (a), brightfield (b) and overlay (c) images of HeLa cells incubated with **[(dfpy)₂Ir(bpy)]PF₆** (from ref. [80]).

An exception to this trend is represented by the cyclometalated iridium (III) solvent complex **[Ir(ppy)₂(DMSO)₂]PF₆**.[81] This compound is non-emissive, but after incubation in many cell lines, it accumulates in the nuclei and reacts with histidine/histidine-containing proteins, generating a luminescent adduct, thus through a mechanism which does not involve the nucleic-acid bonding (Fig.1.21).
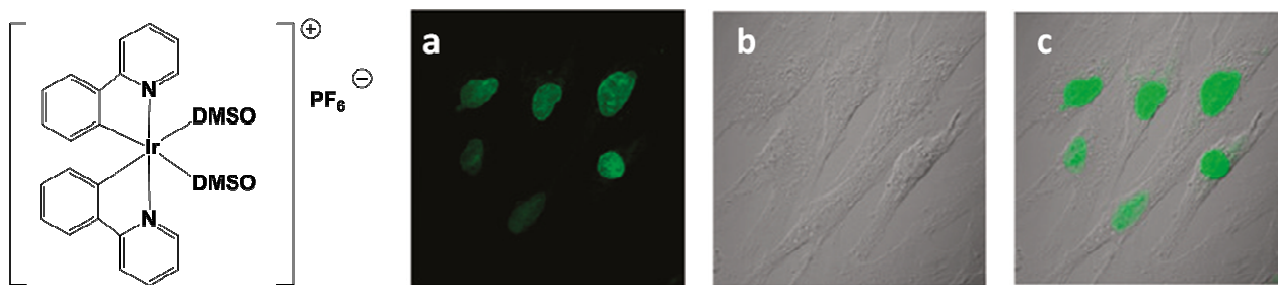
Fig.1.21. Confocal luminescence (a), brightfield (b) and overlay (c) images of MSC cells incubated with **[Ir(ppy)₂(DMSO)₂]PF₆** (adapted from ref. [81]).

1.3.5 G-quadruplex probe

Ir(III) complexes have also been used as G-quadruplex probes. G-quadruplex is a non-canonical four-stranded structure of DNA that can originate in a guanine-rich sequence, via π-π stacking interactions. These motifs are related to many biological processes, such as DNA replication and transcription, thus several studies have focused on the synthesis of luminescent G-quadruplex probes.[82] The interaction of an Ir(III) complex with the G-quadruplex motif has also been exploited for the development of G-quadruplex-based sensing assays. For example, He et al. described an Ir (III) complex, **[(ppy)₂Ir(biq)]PF₆** (Fig.1.22), which is able to bind a guanine-rich single-stranded DNA sequence, generating a weak luminescence signal. The addition of Pb^{2+} ions results in a conformational change of DNA, that creates a G-quadruplex structure with great enhancement of luminescence emission of the Ir (III) probe.[83] The same research group reported the synthesis of another Ir (III) complex **[(ppyr)₂Ir(dip)]PF₆** (Fig.1.22) as selective luminescent probe for parallel quadruplexes and its application for Ca^{2+} ion detection assays.[84]

[(ppy)₂Ir(biq)]PF₆

[(ppyr)₂Ir(dip)]PF₆
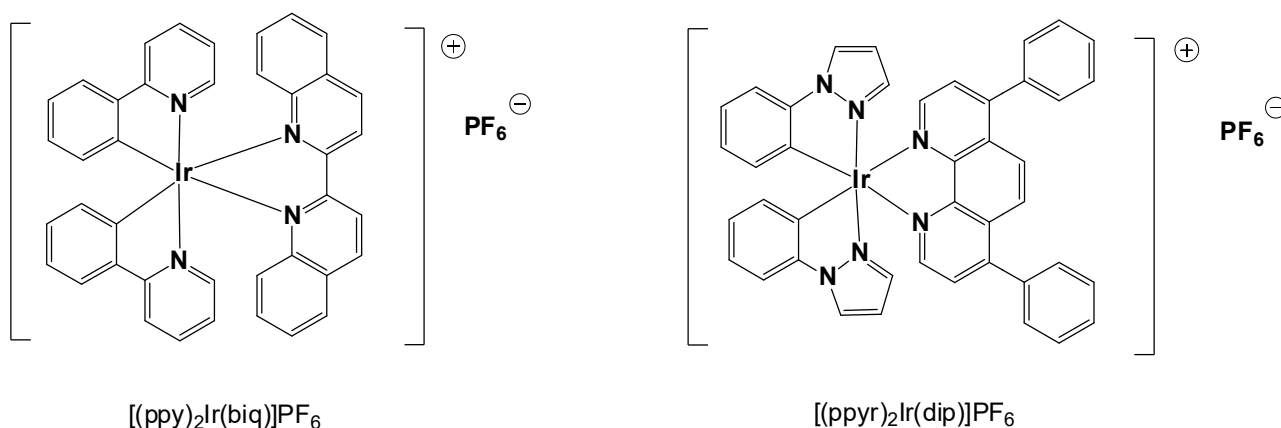
Fig.1.22. Two Ir(III)-based G-quadruplex probes (from ref. [83-84]).

1.3.6 Catalysis

An additional application of Ir (III) complexes which has emerged in the last few years is catalysis. The recent attention to Ir(III)-based catalysts has been triggered by a study published by Bernhard and coworkers in 2008.[85] They described a series of cyclometalated Ir(III) complex, bearing two phenylpyridine ligands and two water molecules, able to catalyze water-oxidation. The archetype compound of these molecules is reported in Fig.1.23.
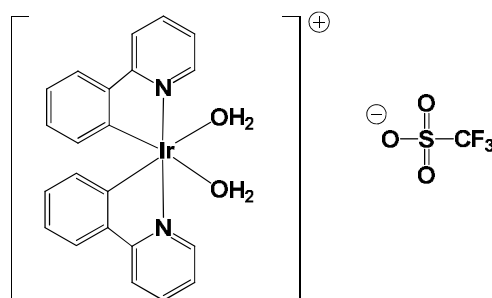
Fig.1.23. Chemical structures of a cyclometalated Ir(III) aquo complex.[85]

Subsequently, the introduction of a pentamethylcyclopentadienyl (Cp*) ligand was exploited for the development of robust Ir(III) catalysts for water-oxidation.[86-87] The strongly electron-donating nature of Cp* ligand plays a beneficial role in allowing high iridium oxidation states to be reached.[88] Although high catalytic performance have been reported for Ir(III) complexes incorporating Cp*, several studies have indicated that the Cp* motif is transformed under catalytic conditions, generating the putative real catalytic species.[88]

Furthermore, at present, Ir (III) metallacycles are employed as catalysts in organic chemical synthesis.[89] In particular, their catalytic activity has been explored for the hydrogenation of imines,[90] asymmetric transfer hydrogenation of ketones,[91] dehydrogenation of primary and secondary alcohols,[92] racemisation of chiral alcohols and amines,[93] and many other organic reactions.

1.4 Dedicated reviews on Ir(III) complexes

The great attention received by Ir(III) complexes is evidenced by the large number of dedicated reviews. The main reviews published in the last five years, concerning the design, the properties and the various applications of Ir(III) complexes, are summarised in table 1.2.

TOPIC	TITLE	YEAR	REF.
Cytotoxic activity, cellular uptake efficiency and mechanisms, and intracellular distribution of Ir(III) complexes	**Iridium(III) complexes as therapeutic and bioimaging reagents for cellular applications**	2012	94
Ir(III) complexes for application in phosphorescent bioimaging of metal ions	**Cyclometalated Iridium(III) Complexes for Phosphorescence Sensing of Biological Metal Ions**	2013	95
Design and development of bioactive Iridium complexes	**Bioactive iridium and rhodium complexes as therapeutic agents**	2013	96
Ir(III) complexes as biolabels and biosensors	**Phosphorescence bioimaging using cyclometalated Ir(III) complexes**	2013	97
Iridium(III) metallacycles for homogeneous catalysis	**Pentamethylcyclopentadienyl Iridium(III) Metallacycles Applied to Homogeneous Catalysis for Fine Chemical Synthesis**	2016	89
Design of Ir(III) emitters for OLED devices	**Strategies for Tuning Emission Energy in Phosphorescent Ir(III) Complexes**	2017	28
Design and photophysical properties of neutral Ir(III) complexes for OLED devices	**Phosphorescent Neutral Iridium (III) Complexes for Organic Light-Emitting Diodes**	2017	98
Design and properties of Ir(III) complexes for OLED and LEC applications	**Recent Progress in Ionic Iridium(III) Complexes for Organic Electronic Devices**	2017	99
Design of cyclometallated iridium(III) complexes for applications in (LECs)	**Over the LEC rainbow: Colour and stability tuning of cyclometallated iridium(III) complexes in light-emitting electrochemical cells**	2017	100

Table 1.2 The main reviews concerning Ir(III) complexes.

1.5 References

1. M. S. Lowry, S. Bernhard, *Chem. Eur. J.*, **2006**, 12, 7970 – 7977.
2. F. Neve, A. Crispini, S. Campagna, S. Serroni, *Inorg. Chem.*, **1999,** *38,* 2250-2258.
3. M. G. Colombo, T. C. Brunold, T. Riedener, H. U. Gudel, *Inorg. Chem.*, **1994,** 33, 545-550.
4. M. S. Lowry, W. R. Hudson, R. A. Pascal, Jr., S. Bernhard*, J. AM. CHEM. SOC.*, **2004**, 126, 14129-141.
5. C. Dragonetti, L. Falciola, P. Mussini, S. Righetto, D. Roberto, R. Ugo, A. Valore, *Inorganic Chemistry,* **2007,** 46, 8533-8547.
6. C.-H. Leung, H.-J. Zhong, H. Yang, Z. Cheng, D. S.-H. Chan, V. P.-Y. Ma, R.n Abagyan, C.-Y. Wong, D-L. Ma, *Angew. Chem. Int. Ed*., **2012**, 51, 9010 –9014.
7. S. Lamansky, P. Djurovich, D. Murphy, F. Abdel-Razzaq, R. Kwong, I. Tsyba, Ma. Bortz, B. Mui, R. Bau, M. E. Thompson, *Inorg. Chem.*, **2001,** 40*,* 1704-1711.
8. V. Fiorini, S. Zacchini, P. Raiteri, R. Mazzoni, V. Zanotti, M. Massi, S. Stagni, *Dalton Trans.*, **2016**, 45, 12884–12896.
9. E. I. Szerb, A. Ionescu, G. Godbert, Y. J. Yadav, A. M. Talarico, M. Ghedini, *Inorg. Chem. Commun*., **2013**, 37, 80–83.
10. A. Ionescu, E. I. Szerb, Y. J. Yadav, A. M. Talarico, M. Ghedini, N. Godbert, *Dalton Trans*., **2014**, 43, 784–789.
11. S. Obara, M. Itabashi, F. Okuda, S. Tamaki, Y. Tanabe, Y. Ishii, K. Nozaki, M. Haga, *Inorg. Chem.*, **2006**, 45, 8907-8921.
12. K. A. King, R. J. Watts, *J. Am. Chem. SOC.,* **1987,** 109*,* 1589-1590.
13. J. Kuwabara, T. Namekawa, E. Sakabe, M. Haga, T. Kanbara, *J Organomet Chem*, **2017**, 845, 189-195.
14. P.-T. Chou, Y. Chi, *Chem. Eur. J.*, **2007**, 13, 380 –395.
15. M. G. Colombo, A. Hauser, H. U. Güdel, *Inorg. Chem.*, **1993***, 32,* 3088-3092.
16. http://260h.pbworks.com/w/page/33532863/Fluorescence%20and%20Phosphorescence
17. A. W. Adamson, *J. Chem. Educ.*, **1983**, 60, 797-802.
18. C. Lee, W. Yang, R. G. Parr, *Phys. Rev. B*, **1998**, 37, 785– 789.
19. A. E. Frisch, M. J. Frisch, Gaussian 98 User's Reference, Gaussian, Inc., Pittsburgh, PA, **1998**.
20. P. J. Hay, *J. Phys. Chem. A,* **2002,** 106*,* 1634-1641.
21. D. Bruce, M. M. Richter, *Anal. Chem*., **2002,** 74, 1340-1342.
22. S. Lamansky, P. I. Djurovich, D. Murphy, F. Abdel-Razzaq, H. E. Lee, C. Adachi, P. E. Burrows, S. R. Forrest, M. E. Thompson, *J. Am. Chem. Soc*., **2001**, 123, 4304-4312.
23. K. Dedeian, J. Shi, S. Nigel, E. Forsythe, D. Morton, *Inorg. Chem*., **2005**, 44, 4445-4447.
24. T. Sajoto, P. I. Djurovich, A. Tamayo, M. Yousufuddin, R. Bau, M. E. Thompson, *Inorganic Chemistry,* **2005**, 44, 7992-8003.
25. D. Wang, Y. Wu, B. Jiao, H. Dong, G. Zhou, G. Wang, Z. Wu, *Organic Electronics*, **2013**, 14, 2233–2242.
26. V. K. Chandra, B. P. Chandra, P. Jha, *Defect and Diffusion Forum,* **2014**, 357, 29-93.
27. https://www.researchgate.net/figure/221909245_fig2_Fig-4-A-schematic-diagram-of-multilayer-structure-of-OLED
28. A. J. Huckaba, M. K. Nazeeruddin*, Comment. Inorg. Chem.*, **2017**, 37, 117–145.
29. F. Ali, P. K. Nayak, N. Periasamy, N. Agarwal, *J. Chem. Sci.*, **2017**, 129, 1391–1398.
30. C.-H. Yang, M.Mauro, F. Polo, S. Watanabe, I. Muenster, R. Fröhlich, L. De Cola, *Chem. Mater*., **2012**, 24, 3684–3695.

31. G. J. Barbante, E. H. Doeven, E. Kerr, T. U. Connell, P. S. Donnelly, J. M. White, T. Lópes, S. Laird, D. J. D. Wilson, P. J. Barnard, C. F. Hogan and P. S. Francis, *Chem. - Eur. J.*, **2014,** 20, 3322-3332.

32. K. P. S. Zanoni, B. K. Kariyazaki, A. Ito, M. K. Brennaman, T. J. Meyer, N. Y. Murakami Iha, *Inorg. Chem.*, **2014**, 53, 4089-4099.

33. A. Endo, K. Suzuki, T. Yoshihara, S. Tobita, M. Yahiro and C. Adachi, *Chem. Phys. Lett.*, **2008**, 460, 155-157.

34. S. Tang, L. Edman, *Top. Curr. Chem. (Z)*, **2016**, 40, 375-395.

35. Q. B. Pei, A. J. Heeger, *Nat Mater*, **2008**, 7, 167.

36. G. G. Malliaras, J. D. Slinke, J. A. DeFranco, M. J. Jaquith, W. R. Silveira, Y.-W. Zhong, J. M. Moran-Mirabal, H. G. Craighead, H. D. Abruna, J. A. Marohn, *Nat Mater*, **2008**, 7, 168.

37. S. van Reenen, P. Matyba, A. Dzwilewski, R. A. J. Janssen, L. Edman, M. Kemerink, *J. AM. CHEM. SOC.*, **201**0, 132, 13776–13781.

38. Q.B. Pei, G. Yu, C. Zhang, Y. Yang, A. J. Heeger, *Science*, **1995**, 269, 1086–1088.

39. R. D. Costa, E. Ort, H. J. Bolink, F. Monti, G. Accorsi, N. Armaroli, *Angew. Chem. Int. Ed.*, **2012**, 51, 8178 – 8211.

40. H. Rudmann, S. Shimada, M. F. Rubner, *J. Am. Chem. Soc.*, **2002**, 124, 4918 – 4921.

41. C. M. Elliott, F. Pichot, C. J. Bloom, L. S. Rider, *J. Am. Chem. Soc.*, **1998**, 120, 6781 – 6784.

42. Iridium(III) in Optoelectronic and Photonics Applications, First Edition. Edited by Eli Zysman-Colman. Published 2017 by John Wiley & Sons Ltd.

43. J. Slinker, D.Bernards, P. L. Houston, H. D. Abruña, S. Bernhard, G. G. Malliaras, *Chem. Commun.*, **2003**, 2392-2399.

44. E. Holder, B. M. W. Langeveld, U. S. Schubert, *Adv. Mater.*, **2005**, 17, 1109-1121.

45. H. Rudmann, S. Shimada, M. F. Rubner, *J. Am. Chem. Soc.,* **2002**, 124, 4918–4921.

46. M. Martínez-Alonso, J. Cerdá, C. Momblona, A. Pertegás, J. M. Junquera-Hernández, A. Heras, A. M. Rodríguez, G. Espino, H. Bolink, E. Ortí, *Inorg. Chem.*, **2017**, 56, 10298–10310.

47. C. D. Ertl, C. Momblona, A. Pertegás, J. M. Junquera-Hernández, M.-G. La-Placa, A. Prescimone, E. Ortí, C. E. Housecroft, E. C. Constable, H, J. Bolink, *J. Am. Chem. Soc.*, **2017**, 139, 3237–3248.

48. C. D. Sunesh, K. Shanmugasundaram, M. S. Subeesh, R. K. Chitumalla, J. Jang, Y. Choe, *ACS Appl Mater Interfaces*., **2015**, 7, 7741–7751.

49. S. T. Parker, J. Slinker, M. S. Lowry, M. P. Cox, S. Bernhard, G. G. Malliaras, *Chem. Mater.*, **2005**, 17, 3187-3190.

50. R. D. Costa, A. Pertegás, Enrique Ortí, H. J. Bolink, *Chem. Mater.*, **2010**, 22, 1288–1290.

51. C. Liu, H. Yu, X. Rao, X. Lv, Z. Jin, J. Qiu, *Dyes Pigments*, 2017,136, 641-647.

52. A. Habibagahi, Y. Mébarki, Y. Sultan, G. P. A. Yap, R. J. Crutchley, *ACS Appl. Mater. Interfaces*, **2009**, 1, 1785–1792.

53. T. Yoshihara, M. Hosaka, M. Terata, K. Ichikawa, S. Murayama, A. Tanaka, M. Mori, H. Itabashi, T. Takeuchi, S. Tobita, *Anal. Chem.*, **2015**, 87, 2710–2717.

54. M. C. DeRosa, R. J. Crutchley, *Coord. Chem. Rev.*, **2002**, 233–234, 351-371.

55. S. Wang, R. Gao, F. Zhou, M. Selke, *J. Mater. Chem.*, **2004**, 14, 487-493.

56. R. R. Allison, H. C. Mota, C. H. Shibata, *Photodiag. Photodyn. Ther.*, **2004**, 1, 263–277.

57. P. Agostinis, K. Berg, K. A. Cengel, T. H. Foster, A. W. Girotti, S. O. Gollnick, S. M. Hahn, M. R. Hamblin, A. Juzeniene, D. Kessel, M. Korbelik, J. Moan, P. Mroz, D. Nowis, J. Piette, B. C. Wilson, J. Golab, *CA Cancer J Clin.*, **2011**, 61, 250–281.

58. R. R. Allison, G. H. Downie, R. Cuenca, X.-H. Hu, C. JH. Childs, C. H. Shibata, *Photodiag. Photodyn. Ther.*, **2004**, 1, 27–42.

59. J. S. Nam, M.-G. Kang, J. Kang, S.-Y. Park, S. J. C. Lee, H.-T. Kim, J. K. Seo, O.-H. Kwon, M. H. Lim, H.-W. Rhee, T. H. Kwon, *J. Am. Chem. Soc.*, **2016**, 138, 10968–10977.

60. W. Lv, Z. Zhang, K. Y. Zhang, H. Yang, S. Liu, A. Xu, S. Guo, Q. Zhao, W. Huang, *Angew. Chem. Int. Ed.*, **2016,** 55, 9947–9951.

61. N. Wu, J.-J. Cao, X.-W. Wu, C.-P. Tan, L.-N. Ji, Z.-W. Mao, *Dalton Trans*., **2017**, DOI: 10.1039/C7DT02477K.

62. H. Xiang, H. Chen, H. P. Tham, S. Z. F. Phua, J.-G. Liu, Y. Zhao, *ACS Appl. Mater. Interfaces*, **2017**, DOI: 10.1021/acsami.7b09506.

63. L. McKenzie, I. Sazanovich, E.h Baggaley, M. Bonneau, V. Guerchais, G. Williams, J. Weinstein, H. E. Bryant, *Chem. Eur. J.*, 10.1002/chem.201604792.

64. A. Wilbuer, D. H. Vlecken, D. J. Schmitz, K. Kraling, K. Harms, C. P. Bagowski, E. Meggers, *Angew. Chem. Int. Ed.*, **2010**, 49, 3839-3842.

65. X.-D. Song, X. Kong, S.-F. He, J.-X. Chen, J. Sun, B.-B. Chen, J.-W. Zhao, Z.-W. Mao, *Eur. J. of Med. Chem.*, **2017**, doi: 10.1016/j.ejmech.2017.06.038.

66. Y. Zheng, L. He, D. Zhang, C. Tan, L. Ji, Z. Mao, *Dalton Trans*., **2017**, DOI: 10.1039/C7DT02273E.

67. P. Zhang, P. J. Sadler, *Eur. J. Inorg. Chem.*, **2017**, DOI: 10.1002/ejic.201600908.

68. S. Betanzos-Lara, Z. Liu, A. Habtemariam, A. M. Pizarro, B. Qamar, P. J. Sadler, *Angew. Chem*., **2012**, 124, 3963 –3966.

69. Z. Liu, P. J. Sadler, *Acc. Chem. Res*., **2014**, 47, 1174−1185.

70. J. Ruiz, C. Vicente, C. de Haro, D. Bautista, *Inorg. Chem.*, **2017**, dx.doi.org/10.1021/ic302219v.

71. Q.-P. Qin, T. Meng, M.-X. Tan, Y.-C. Liu, X.-J. Luo, B.-Q. Zou, H. Liang, *Eur. J. Med. Chem*., **2017**, doi: 10.1016/ j.ejmech.2017.10.035.

72. K. K.-W. Lo, C.-K. Chung, N. Zhu, *Chem. Eur. J.*, **2006**, 12, 1500 − 1512.

73. V. Fernández-Moreira, F. L. Thorp-Greenwood, M. P. Coogan, *Chem. Commun*., **2010**, 46, 186–202.

74. E.Baggaley, J. A. Weinsteina, J.A. Gareth Williams, Coord. Chem. Rev., **2012**, 256, 1762– 1785.

75. W. Wang, Z.-Z. Dong, C. Yang, G. Li, Y.-C. Tse, C.-H. Leung, D.-L. Ma, *Sens Actuators B Chem*, **2017**, 251, 374–379.

76. A. S. Wierzbicki, *Diabetes Vasc Dis Res*, **2007,** 4, 143-149.

77. H. Gao, Z. Li, Y. Zhao, H. Qi, C. Zhang, *Sens Actuators B Chem*, **2017**, 245, 853–859.

78. K. K.-W. Lo, K. Y. Zhang, S.-K. Leung, M.-C. Tang, *Angew. Chem. Int. Ed*., **2008**, 47, 2213- 2216.

79. C. Liu, C. Yang, L. Lu, W. Wang, W. Tan, C. Leung, D. Ma, *Chem. Commun*., **2017**, DOI: 10.1039/C6CC08109F.

80. M. Yu, Q. Zhao, L. Shi, F. Li, Z. Zhou, H. Yang, T. Yia, C. Huanga, *Chem. Commun*., **2008**, 2115-2117.

81. C. Li, M. Yu, Y. Sun, Y. Wu, C. Huang, F. Li, *J. Am. Chem. Soc.*, **2011**, 133, 11231-11239.

82. D.-L. Ma, Z. Zhang, M. Wang, L. Lu, H.-J. Zhong, C.-H. Leung, Chem. Biol., 2015, 22, 812-828.

83. H.-Z. He, K.-H. Leung, H. Yang, D. S.-H. Chan, C.-H. Leung, J. Zhou, A. Bourdoncle, J.-L. Mergny, D.-L. Ma, *Biosens. Bioelectron*, **2013**, 41, 871–874.

84. H.-Z. He, M. Wang, D. S.-H. Chan, C. H. Leung, X. Lin, J.-M. Lin, D.-L. Ma, *Methods,* **2013**, 64, 212–217.

85. N. D. McDaniel, F. J. Coughlin, L. L. Tinker, S. Bernhard, *J. Am. Chem. Soc.*, **2008**, 130, 210–217.

86. J. D. Blakemore, N. D. Schley, D. Balcells, J. F. Hull, G. W. Olack, C. D. Incarvito, O. Eisenstein, G. W. Brudvig, R. H. Crabtree, 2010, *J. Am. Chem. Soc.*, 132, 16017–16029.

87. D. G. H. Hetterscheid, J. N. H. Reek, *Chem. Commun*., **2011**, 47, 2712–2714.

88. I. Corbucci, A. Macchioni, M. Albrecht, Iridium(III) in Optoelectronic and Photonics Applications, First Edition. Edited by Eli Zysman-Colman. 2017 John Wiley & Sons Ltd. Published 2017 by John Wiley & Sons Ltd.

89. C. Michon, K. MacIntyre, Y. Corre, F. Agbossou-Niedercorn, *Chem. Cat. Chem.*, **2016**, 8, 1755 – 1762.
90. B. Villa-Marcos, W. Tang, X. Wu, J. Xiao, *Org. Biomol. Chem.*, **2013**, 11, 6934–6939.
91. N. Pannetier, J.-B. Sortais, J.-T. Issenhuth, L. Barloy, C. Sirlin, A. Holuigue, L. Lefort, L. Panella, J. G. de Vries, M. Pfeffer, *Adv. Synth. Catal.*, **2011**, 353, 2844–2852.
92. K. Fujita, T. Yoshida, Y. Imori, R. Yamaguchi, *Org. Lett.*, **201**1, 13, 2278–2281.
93. T. Jerphagnon, A. J. A. Gayet, F. Berthiol, V. Ritleng, N. Mršić, A. Meetsma, M. Pfeffer, A. J. Minnaard, B. L. Feringa, J. G. de Vries, *Chem. Eur. J.*, **2009**, 15, 12780–12790.
94. K. K.-W. Lo, K. Y. Zhang, *RSC Adv.*, **2012**, 2, 12069–12083.
95. Y. You, S. Cho, W. Nam, *Inorg. Chem.*, **2014**, 53, 1804−1815.
96. C.-H. Leung, H.-J. Zhong, D. Shiu-Hin Chan, D.-L. Ma, *Coord. Chem. Rev.*, **2013**, 257, 1764– 1776.
97. Y. You, *Curr. Opin. Chem. Biol.*, **2013**, 17, 699–707.
98. A. R. Bin Mohd Yusoff, A. J. Huckaba, M. K. Nazeeruddin, *Top Curr Chem* (Z), **2017**, 375:39.
99. D. Ma, T. Tsuboi, Y. Qiu, L. Duan, *Adv. Mater.* **2017**, *29*, 1603253.
100.   C. E. Housecroft, E. C. Constable, *Coord. Chem. Rev.*, **2017**, 350, 155–177.

Chapter 2

Water-soluble Ir(III) complexes

2.1 Introduction

Although the Ir (III) complexes present appealing features, whose general description has been reported in the precedent chapter, their effective use has been limited by their poor solubility in pure water, an essential requisite for many applications, especially biologically-related issues, such as bioimaging and anticancer agents. For example, as reported by Coogan *et al.*, the ideal lumophore for fluorescence imaging applications should display several important features, like low toxicity to the organism at least over the course of the experiment, good uptake into the cells, preferential localisation in a certain organelle of the cell and, above all, the ideal lumophore should be stable and soluble in aqueous buffers.[1] Actually for bioimaging and other related applications, due to their low water solubility, lumophores based on Ir(III) complexes are dissolved in a small amount of dimethylsulfoxide (DMSO), and then diluted in aqueous culture medium. However, it is well known that DMSO is not inert in the cellular environment, as reported by You *et al.*[2] Indeed, thanks to its high polarity, its small and compact structure and its capacity to accept hydrogen bonds, DMSO is not only able to quickly penetrate through biological membranes and cellular barriers, but also capable to enhance the permeability of several low molecular weight solutes across biomembranes.[3] The mechanism of the enhancement of the cell membrane permeability is still controversial, however it probably arises from the ability of DMSO to induce non-lamellar structures in phospholipids.[2] Another mechanism, proposed by Anwar *et al.* through molecular dynamics (MD) simulations, involves the membrane softening induced by DMSO, which would facilitate the membrane fusion and, at high concentration, the induction of water pores in lipid bilayers.[4] According to this model, the DMSO molecules appear to occupy the membrane region just below the headgroup of lipids and act as spacers that enhance lipid-lipid separation, inducing a curving and a softening of the membrane.[4] DMSO is also known to cause protein denaturation, as reported by Henderson *et al.* who suggested that reversible

alterations in protein structure are the major effect of exposure to low DMSO levels at low temperatures, while irreversible denaturation of subunit proteins may be an appreciable effect at higher temperatures and higher DMSO concentrations.[5] The destabilization of the native state of protein systems caused by this organic solvent has been described also by Turner *et al.* who studied the thermal denaturation of ribonuclease in aqueous dimethyl sulfoxide, through Differential Scanning Calorimetry (DSC).[6] Moreovere, You *et al.* also described DMSO as an inducer of cell differentiation, probably by exerting some effect on the genetic regulation.[2] Not so long ago, it was commonly assumed that the described effects on cellular environment did not occur at the low concentrations in which DMSO is generally used for solubilize poorly soluble compounds in cell assays, and, this assumption has led to its ubiquitous use and widespread application. Actually, more recent studies have evidenced that DMSO can exert toxic effects and perturb biomolecules also at very low concentrations. For example, Farber *et al.* reported that in an *in vitro* rat hippocampal culture preparation, DMSO produced neuronal loss at concentrations of 0.5% and 1.0%, probably for a direct cellular effect.[7] Moreover, Salvi *et al.* applied different concentration of DMSO to cochlear organotypic cultures to evaluate its cytotoxic effects on cochlear organotypic cultures, demonstrating that DMSO concentrations of 0.1% and 0.25% caused little or no damage, whereas concentrations between 0.5% and 6% resulted in stereocilia damage, hair cell swelling and a dose-dependent loss of hair cells.[8] Another study supporting the appearance of cellular effects also at very low concentration of DMSO was carried out by Cordeiro *et al.* who reported that DMSO induces retinal apoptosis *in vitro* in a retinal neuronal cell line, at concentrations below 1% (v/v).[9] For all these reasons, in order to test an Ir(III) complex in a cell line for bioimaging, anticancer activity, photosensitizers and other biorelated applications, it would be preferable to avoid the use of DMSO, which could interfere with the cellular environment. In addition, the availability of water-soluble Ir(III)-based drugs, would open the doors also to the possibility of delivering an Ir(III)-based drug by the intravenous and intramuscular route in *in vivo* experiments.

The general technique for inducing water-solubility in Ir(III) complexes consists in functionalizing the ancillary or, occasionally, the cyclometallated ligands with solubilizing groups. For example, recently *Pang et al.*, by means of the introduction of an auxiliary ligand with two carboxylate groups, synthetized an Iridium (III) complex **[(pq)₂Ir(bpy-COOK)]Cl** (where **pq** = 2-phenylquinoline, **bpy-COOK** = potassium 2,2'-bipyridine-4,4'-dicarboxylate) with excellent water solubility (Fig.2.1.1).[10]
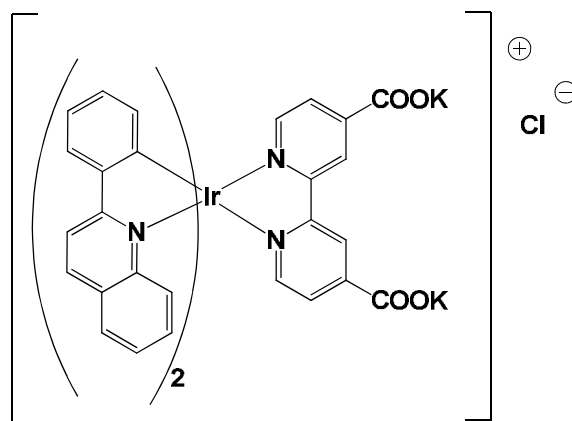
Fig.2.1.1. Chemical structure of the water-soluble **[(pq)$_2$Ir(bpy-COOK)]Cl** complex.[10]

This complex was synthesized by refluxing the dichloro-bridge dimer precursor **[(pq)$_2$Ir(μ-Cl)]$_2$** in CH$_2$Cl$_2$/CH$_3$OH with 2 equivalent of 2,2'-bipyridine- 4,4'-dicarboxylic acid (**bpy-COOH**) and 4 equivalent of KOH under nitrogen atmosphere for 8 h.

Another opportunity to synthetize water-soluble Ir(III) complexes consists in the modification of the ancillary ligand, by embedding it with high soluble fragments. This strategy was exploited by Chen *et al.*, who prepared **[Ir(pq)$_2$(bpy-sugar)]Cl** (Fig.2.1.2).[11]
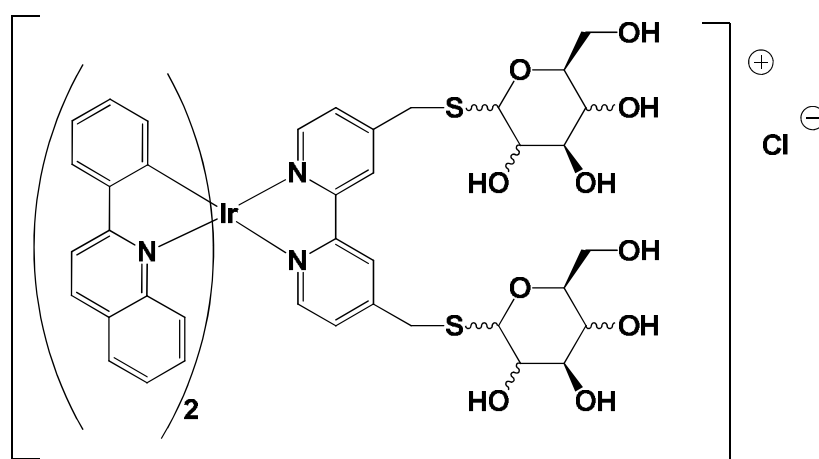
Fig.2.1.2. Chemical structure of the water-soluble **[Ir(pq)$_2$(bpy-sugar)]Cl** complex.[11]

However, the preparation of this sugar-appended ancillary ligand requires long times and several purification steps in order to couple thioglycosidically the carbohydrate residues to bipyridine.[12]

In addition, the water-solubility of the Ir(III) complexes can be realized through the introduction of a quaternary ammonium salt in the N^N ligand.[13] This strategy was described by Ma *et al.*, who synthetized a hydrophilic N^N ligand through nitrification of the 1,10-phenanthroline and subsequent reduction of the nitrate group. The resulting amino-group was then amidated with the chloroacetyl chloride. This N^N ligand was then used in the bridge splitting reaction of a dichloro-bridge dimer precursor. Finally, the reaction of the chloroacetyl group with triethylamine results in the formation of a quaternary amino group (Scheme 2.1.1). Employing this methodology, four completely water soluble complexes were obtained using four different cyclometalated ligands: 2-(2,4-difluorophenyl)pyridine (**dfppy**), 2-(4-(*tert*-butyl)phenyl)pyridine (***t*-buppy**), 2-(thiophen-2-yl)quinoline) (**thq**), 4-(pyridin-2-yl)benzaldehyde (**pba**).
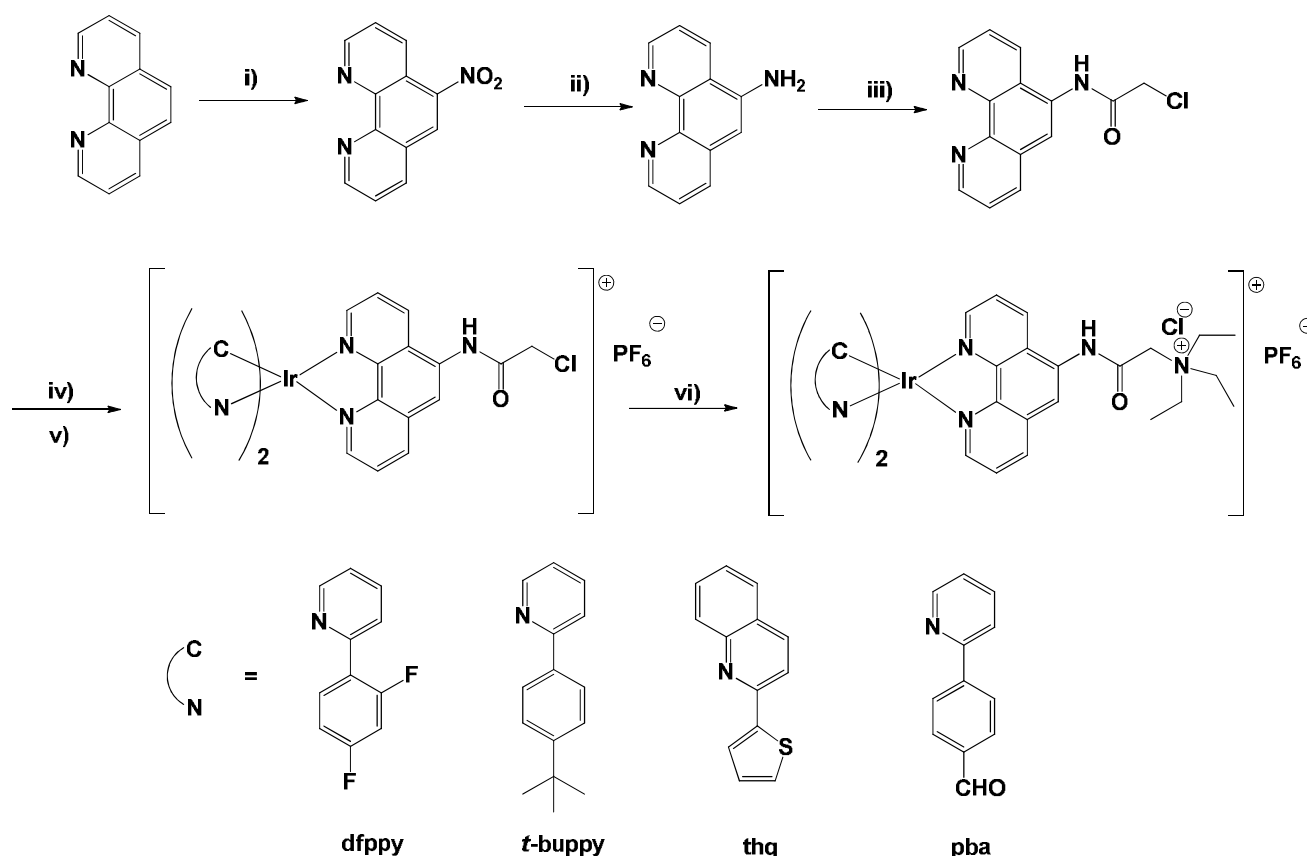
Scheme 2.1.1. Synthetic procedure to obtain water soluble Ir(III) complexes bearing a quaternary amino group. Reaction conditions:(i) H_2SO_4, HNO_3, 160°C−170°C, 2h; (ii) 5% Pd/C, hydrazine hydrate, EtOH, reflux, 5h; (iii) chloroacetyl chloride, triethylamine, R.T., overnight; (iv) **[Ir(C^N)$_2$Cl$_2$]$_2$**, CH_2Cl_2, MeOH, reflux, 4h; (v) KPF$_6$, R.T., 1h; (vi) DMF, triethylamine, 110 °C, 3h. [13]

Although the obtained complexes display good water-solubility, the synthetic pathway implies thorny and expensive procedures which required a long time and several steps.

The introduction of disulfonic groups on the ancillary ligand is another way to increase the hydrophilicity of an Ir(III) complex, hence its solubility in water. In this context, Zhou *et al.* synthetized several anionic Ir(III) compounds incorporating the commercial ancillary ligand disulfonated bathophenanthroline (**DSdip**) and various cyclometalated ligand, in particular 2-phenylpyridine (**ppy**), 2,4-difluorophenylpyridine (**dfppy**), 2-phenylbenzothiazole (**bt**) and 1-phenylisoquinoline (**piq**) (Fig. 2.1.3).[14] However, ancillary ligands incorporating hydrophilic groups are not so frequently commercially available.
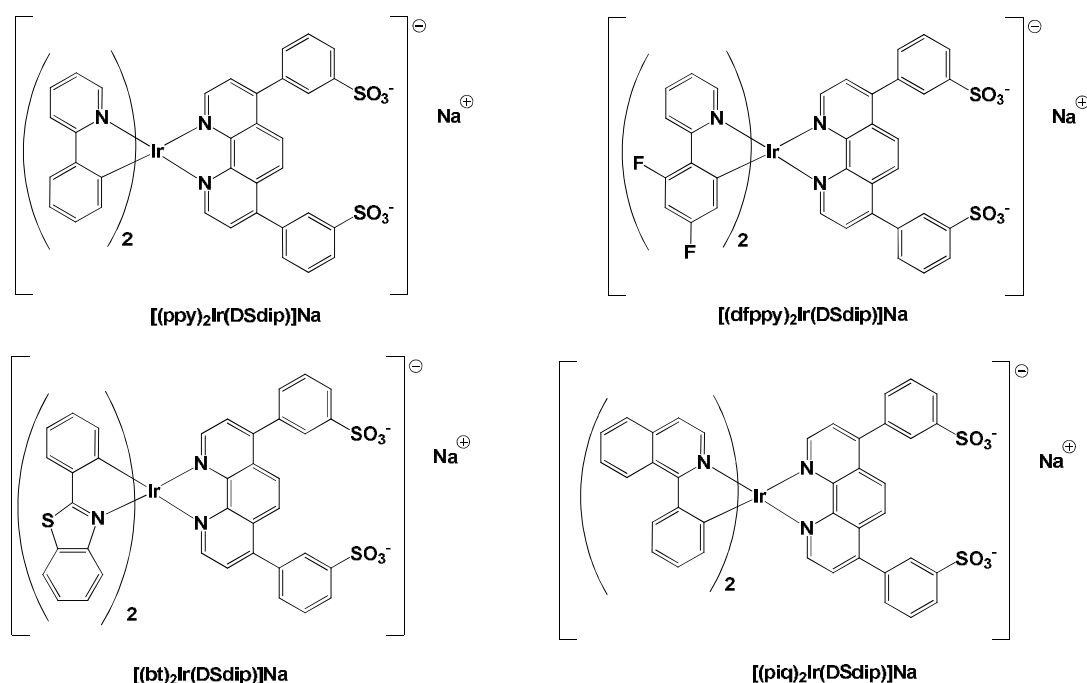
Fig.2.1.3. Chemical structure of the water-soluble **[(ppy)₂Ir(DSdip)]Na**, **[(dfppy)₂Ir(DSdip)]Na**, **[(bt)₂Ir(DSdip)]Na** and **[(piq)₂Ir(DSdip)]Na** complexes.[14]

Another mechanism to induce the water-solubility in an Ir (III) complex is represented by the chemical modification of the cyclometalated ligand. For example, recently, Fan *et al.* described the synthesis of water-soluble Ir(III) compounds bearing a sulfonate-modified bis-benzimidazole-type organic ligand (3,3′-(2,2′-(1,3-phenylene)bis(1H–benzo[*d*]imidazole-2,1-diyl))dipropane-1-sulfonic acid, **MBS**, and different ancillary ligands.[15] The hydrophilic ligand **MBS** was synthesized by introducing sulfonate groups with a propyl chain onto a tridentate N^C^N ligand 1,3-di(1H-benzo[d]imidazol-2-yl)benzene. This reaction is illustrated in Scheme 2.1.2 together with two of the obtained complexes, chosen as examples.
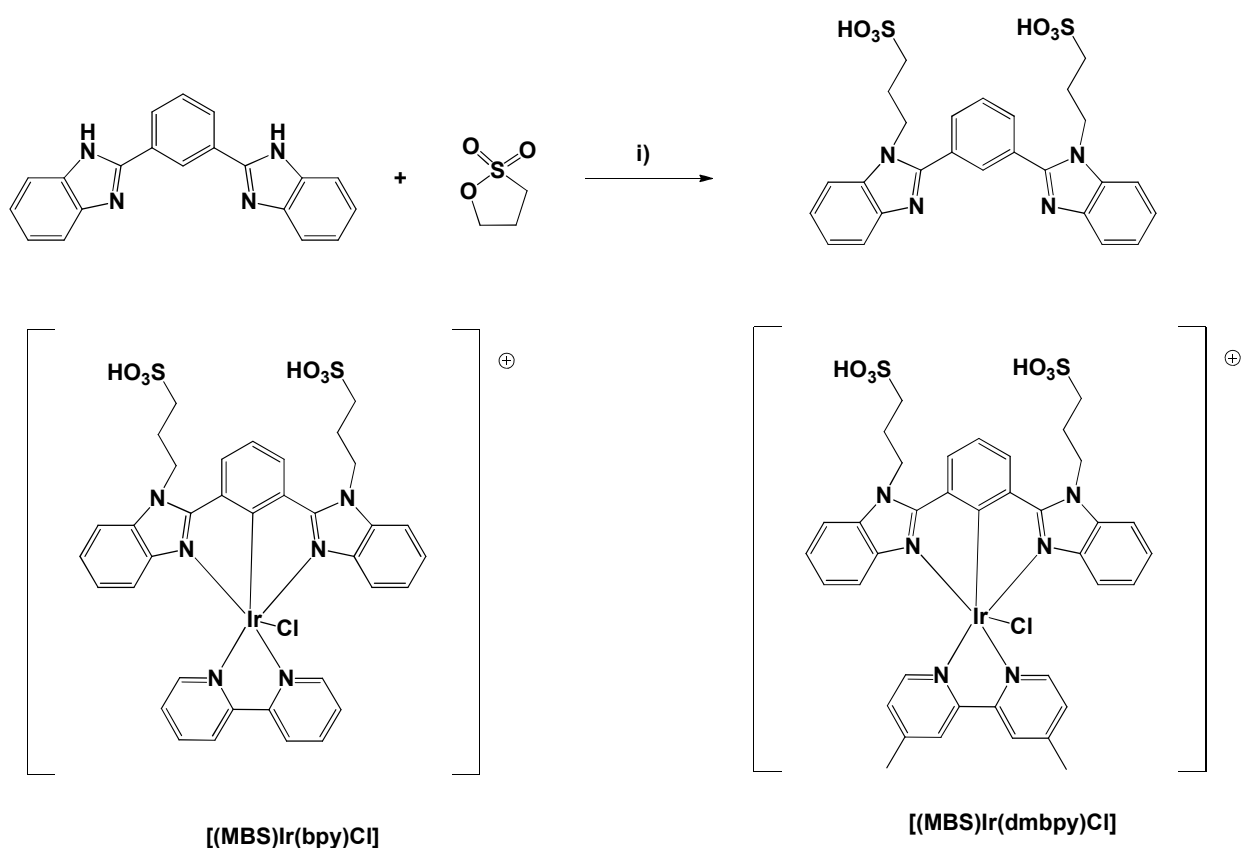
Scheme 2.1.2. Synthesis of the hydrophilic ligand **MBS** (reaction conditions:(i) KOH, Bu$_4$NBr, DMSO/H$_2$O, MW) and chemical structures of compounds **[(MBS)Ir(bpy)Cl]** and **[(MBS)Ir(dmbpy)Cl]**. [15]

Beside sulfonates, also the introduction of carboxylate groups has been exploited in order to prepare water-soluble Ir(III) complexes. In this context, Pope *et al.* used ethyl-2-phenylquinoline-4-carboxylate (**epqc**) as cyclometalated ligand for the synthesis of cationic heteroleptic iridium(III) complexes.[16] The ligand (**Hepqc**) was prepared by dissolving and heating 2-phenylquinoline-4-carboxylic acid (**pqca** or cinchophen) in ethanol with a few drops of concentrated H$_2$SO$_4$. **Hepqc** was then used for the formation of the corresponding Ir(III) bridge-dimer, which, in turn, was employed as precursor for the bridge splitting reaction in the presence of several ancillary ligands (2,2'-bipyridine (**bpy**), 4,4'-dimethyl-2,2'-bipyridine (**dmbpy**), 1,10-phenanthroline (**phen**), 4,7-diphenyl-1,10-phenanthroline (**dip**), dipyridophenazine (**dppz**), benzo[*i*]dipyridophenazine (**dppn**), naphtha[*a*]dipyridophenazine-5,18-dione (**qdppz**)), in order to obtain the corresponding cationic Ir(III) complexes, three examples of which are reported in Fig.2.1.4.
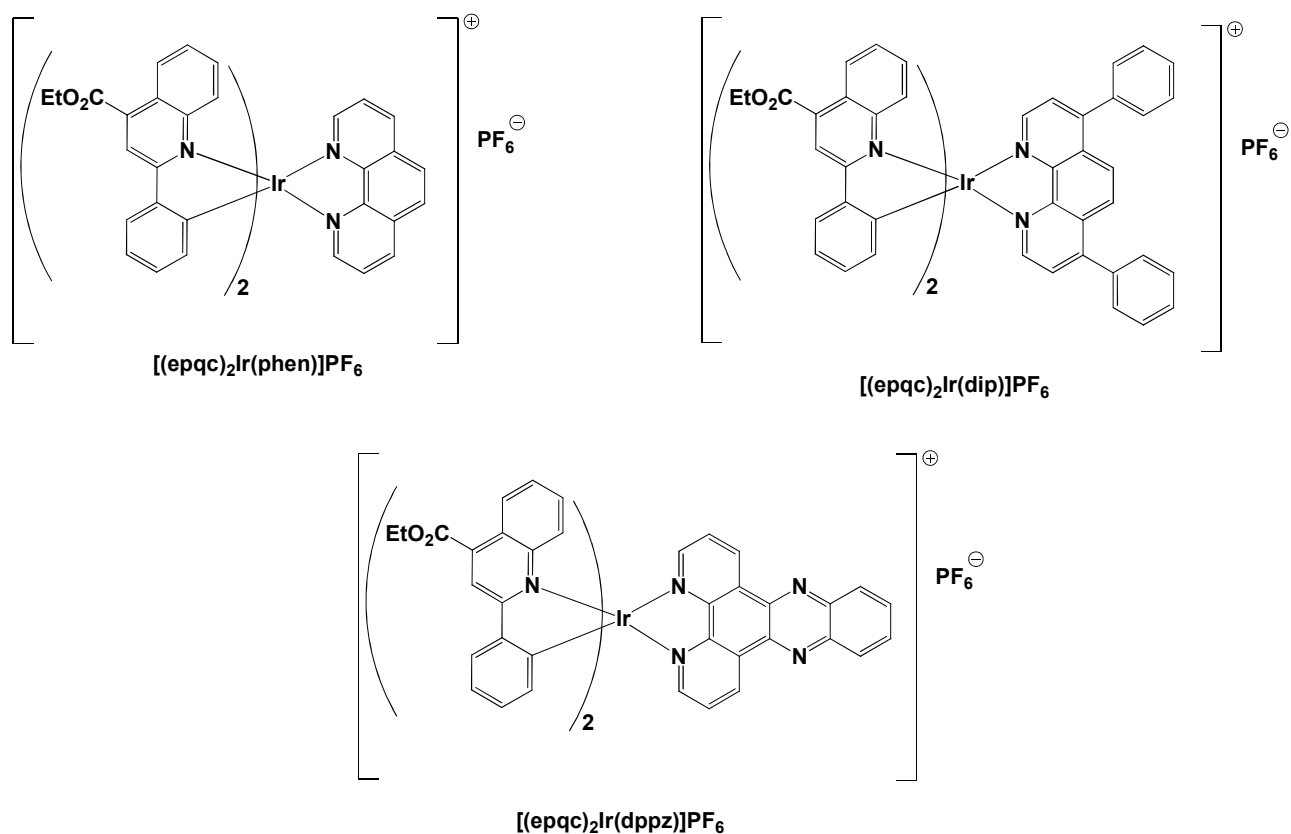
Fig.2.1.4. Chemical structure of three complexes incorporating **epqc** ligand **[(epqc)₂Ir(phen)]PF₆**, **[(epqc)₂Ir(dip)]PF₆** and **[(epqc)₂Ir(dppz)]PF₆**.[16]

Actually, in order to achieve water solubility, further chemical steps are required for these **epqc**-appended Ir(III) complexes. In particular, the conversion of **epqc**-complexes to their corresponding free acids was performed through an hydrolysis reaction in the presence of KOH, followed by neutralisation with HCl, removal of solvent and extraction with methanol (allowing removal of KCl). The corresponding complexes, incorporating phenylquinoline carboxylic acid (**pqca** or cinchophen) as cyclometalated ligand, were obtained as chloride salts, **[(pqca)₂Ir(N^N)]Cl**.[16]

A further reported method for dissolving Ir(III) probes directly in aqueous media is represented by the covalent attachment of the complexes to water-soluble polymers. In this context, Yang *et al.* synthetized a water soluble Ir(III) compound for application in bioimaging, through its functionalization with the biocompatible polymer poly(ethylene) glycol (PEG).[17] The incorporation of PEG polymer chain onto a neutral ligand has been obtained through click chemistry, hence several reaction steps were required (Scheme 2.1.3).
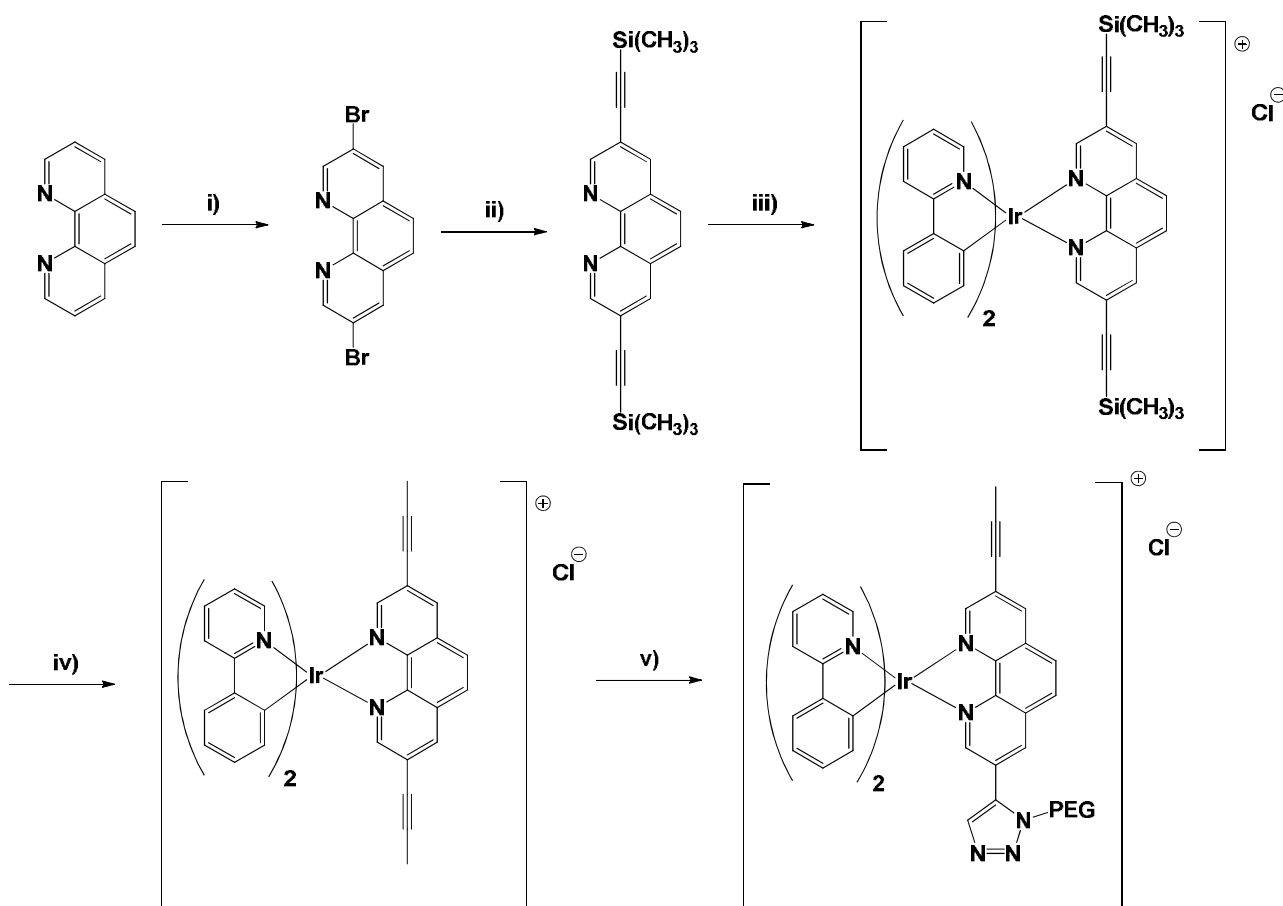
Scheme 2.1.3. Synthesis of the PEG-functionalized Ir(III) complex. Reaction conditions:(i) pyridine, S_2Cl_2, Br_2, 1-chlorobutane, 82°C; (ii) Pd(pph)$_3$, CuI, trimethylsilyacetylene, THF/triethylamine; (iii) **[(ppy)$_2$Ir(μ-Cl)]$_2$**, CH_2Cl_2/MeOH, reflux; (iv) KF·2H$_2$O, MeOH, r.t.; (v) PEG-N$_3$, CuSO$_4$, sodium ascorbate, DMF/H$_2$O, 35°C.[17]

Since requiring a so large number of steps, including also the PEG functionalization with the -N$_3$ chemical motif, this method could not be regarded as a convenient approach for inducing water-solubility into an Ir(III) compound.

Another example of water-soluble polymer containing an Ir(III) complex was given by Huang *et al.* who synthesize a water-soluble phosphorescent probe for homocysteine (Hcy) and cysteine (Cys) in human cells, by the introduction of the Iridium(III) complex **(pba)$_2$Ir(hpa)**, incorporating 4-(2-pyridyl)-benzaldehyde (**pba**) as cyclometalated ligand and 3-hydroxypicolinic acid (**hpa**) as ancillary ligand, into the backbone of water-soluble poly(*N*-isopropylacrylamide) (PNIPAm) (Scheme 2.1.4).[18] Also in this case, many reaction steps are required, making this approach not so simple.
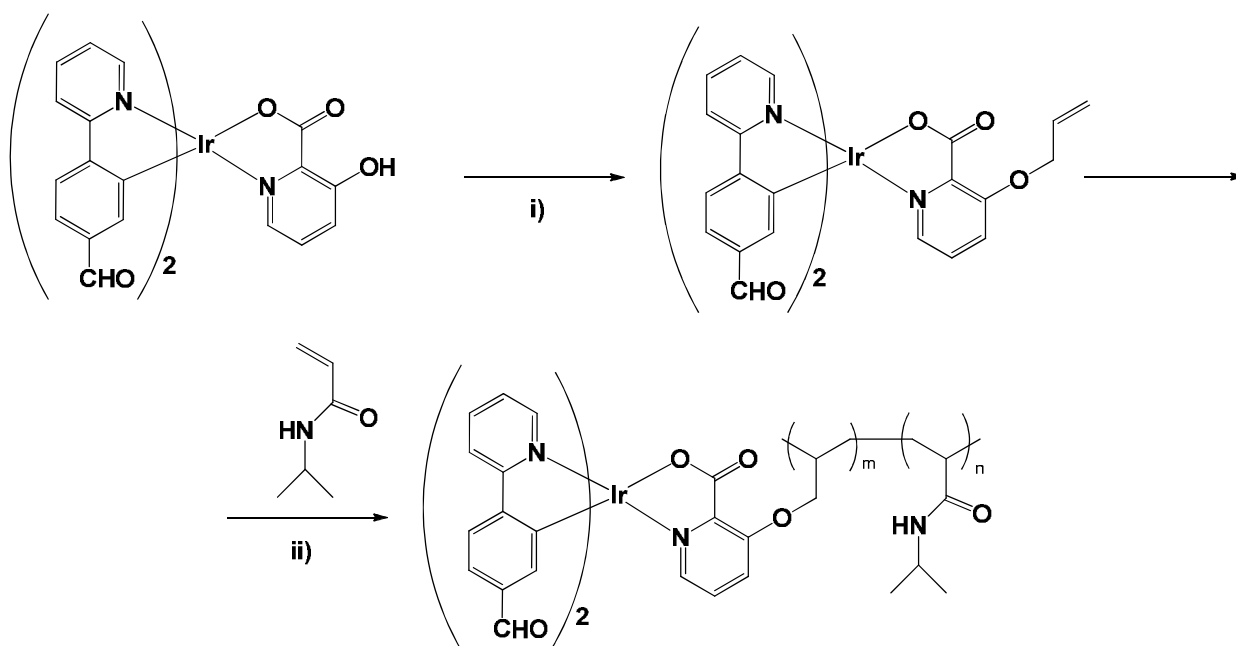
Scheme 2.1.4. Synthesis of the PNIPAm -functionalized Ir(III) complex. Reaction conditions:(i) 3-Bromoprop-1-ene, K$_2$CO$_3$, acetone, 90°C, 12h; (ii) 2,2'-azobis(isobutyronitrile) (AIBN), THF, 70°C, overnight.[18]

In conclusion, the preparation of structurally modified ligands, or dedicated vectors, frequently implies thorny and expensive procedures which commonly require a large number of steps. Furthermore, chemical functionalizations often engender contamination concerns, since these syntheses are generally performed in organic solvents in the presence of toxic reagents, such as metal oxidants used for example for the introduction of carboxylate groups.

In this chapter, an alternative and sustainable approach towards water-soluble luminescent Ir(III) metal complexes, which only requires the choice of the appropriate counter anion, has been exploited.

2.2 Water-soluble [(ppy)$_2$Ir(N^N)]CH$_3$CO$_2$ complexes

In this chapter the synthesis and characterization of several water-soluble Ir(III) complexes are presented. The compounds described herein are Ir(III) octahedral cationic complexes, which bear acetate group as counteranion. The choice of this hydrophilic counterion was crucial for the induction of water-solubility in the synthetized compounds, as recently reported for the cationic complex **[(ppy)$_2$Ir(bpy)]CH$_3$CO$_2$** incorporating 2-phenylpyridine **H(ppy)** as cyclometalated ligand and bipyridine **(bpy)** as ancillary ligand.[19] This complex displays a good solubility in water, differently from the parent complexes **[(ppy)$_2$Ir(bpy)]X** **(X = Cl⁻, PF$_6$⁻)**[20] which are all insoluble in water, confirming that the water solubility is related to the nature of the counteranion. Furthermore, in that case, the water-solubility was accompanied by the formation of supramolecular assemblies in a defined range of concentration. This peculiarity will be the object of chapter 3, which is dedicated to the structural study of the metallogel phases displayed by novel water-soluble Ir(III) complexes.

The water-solubility of an Ir(III) complex can open the doors to its eventual application in biologically-related systems, for example in bioimaging, cellular probes and antitumor agents. Indeed, by virtue of their water-solubility, the above mentioned complex **[(ppy)$_2$Ir(bpy)]CH$_3$CO$_2$**, together with two analogous complexes **[(ppy)$_2$Ir(phen)]CH$_3$CO$_2$** and **[(ppy)$_2$Ir(en)]CH$_3$CO$_2$** respectively bearing 1,10-phenanthroline **(phen)** and ethylenediamine **(en)** as ancillary ligands (Fig.2.2.1), and whose synthesis has been reported by Rossi *et al*[21] and Ricciardi *et al.* respectively,[22] have been preliminary tested as cytotoxic agents towards a pancreatic cancer cell line (MIAPaCa-2) by the group of Prof. Neamati (University of Michigan).[23]

[(ppy)$_2$Ir(bpy)]CH$_3$CO$_2$ [(ppy)$_2$Ir(phen)]CH$_3$CO$_2$ [(ppy)$_2$Ir(en)]CH$_3$CO$_2$
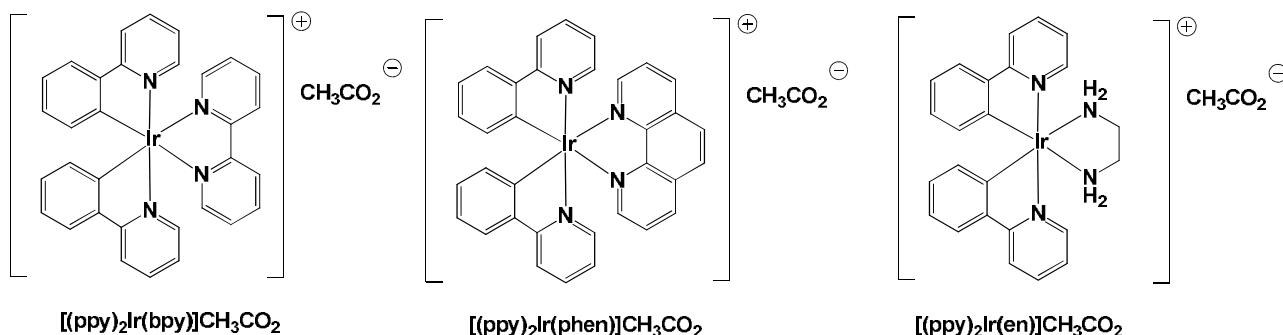
Fig.2.2.1. Chemical structure of **[(ppy)$_2$Ir(bpy)]CH$_3$CO$_2$**, **[(ppy)$_2$Ir(phen)]CH$_3$CO$_2$** and **[(ppy)$_2$Ir(en)]CH$_3$CO$_2$**.

The preliminary results of IC_{50}, defined as the half minimal (50%) cell growth inhibitory concentration (IC) of a substance, are reported in Table 2.2.1 and point out different behaviour of the three complexes.

Complex	Mean IC_{50} (μM)
[(ppy)$_2$Ir(phen)]CH$_3$CO$_2$	0.1
[(ppy)$_2$Ir(bpy)]CH$_3$CO$_2$	0.3
[(ppy)$_2$Ir(en)]CH$_3$CO$_2$	>20

Table 2.2.1. IC_{50} values of **[(ppy)$_2$Ir(phen)]CH$_3$CO$_2$**, **[(ppy)$_2$Ir(bpy)]CH$_3$CO$_2$** and **[(ppy)$_2$Ir(en)]CH$_3$CO$_2$** tested on MIAPaCa-2.

The complexes bearing aromatic ancillary ligands, **bpy** and **phen**, exert a cytotoxic effect towards the cell line MIAPaCa-2 much more larger than the Ir(III) compound which incorporates an aliphatic ancillary ligand, **(en)**.

Taking these preliminary results as starting point, the first objective of the present thesis was to synthesize novel **[(ppy)$_2$Ir(N^N)]CH$_3$CO$_2$** complexes by varying the chemical nature of the N^N ancillary ligand in order to formulate a structure-activity relationship. For this reason, novel aromatic N^N ligands, in particular 2,2'-biquinoline (**biq**), 4,7-diphenyl-1,10-phenanthroline (**dip**), 2,2'-dipyridylamine (**dpa**), 2,2'-dipyridyl ketone (**dpc**), dipyridinoquinoxaline (**dpq)** and dipyridophenazine (**dppz**), have been selected, whose chemical structure is reported in Fig.2.2.2.

Fig.2.2.2. Chemical structure of the N^N ancillary ligands **biq, dip, dpa, dpc, dpq** and **dppz** used for the synthesis of **[(ppy)$_2$Ir(N^N)]CH$_3$CO$_2$** complexes.

The **biq**, **dip**, **dpq** and **dppz** ligands were chosen in order to investigate the effect of the increase of aromaticity, with respect to the **bpy** motif, on the properties of the resulting complexes. Analogous Ir(III) complexes, incorporating these ancillary ligands but different counterions, have been inves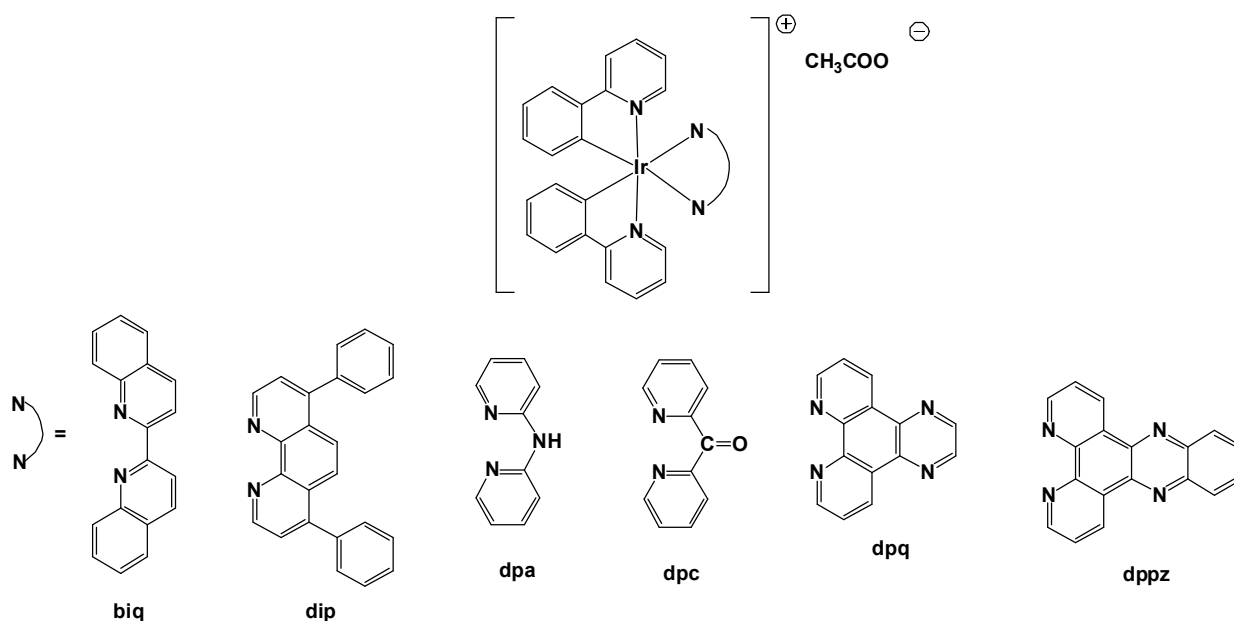tigated for their interesting potential application in biorelated systems. For example, the complex **[(ppy)₂Ir(dip)]PF₆**, analogous to the compounds **3** and **4** presented in this chapter (par. 2.2.2), was tested in human cancer cell lines HeLa, MCF-7 and A549, and was found to induce endoplasmic reticulum stress and mitochondria-mediated apoptosis.[24] This compound, thanks to the high lipophilicity of the N^N ligand, exhibited a high cellular uptake efficiency and a significant cytotoxic activities, with IC_{50} lower than that of cisplatin. However, the compound synthetized by Cao *et al*. was dissolved in a small amount of DMSO and diluted in the cell culture medium in order to be incubated with the cells, since it is not soluble in aqueous solutions.[24]

The **biq** ligand was selected for mainly two reason, first the complex **[(ppy)₂Ir(biq)]PF₆** analogous to compounds **1** and **2** (par. 2.2.2), has received attention by virtue of its ability to inhibit tumor necrosis factor-α (TNF-α), which is a pro-inflammatory cytokine that plays a key role in many biological processes, such as haematopoiesis, immunity, and inflammation.[25] Moreover, as described in paragraph 1.3.5, **[(ppy)₂Ir(biq)]PF₆** can be used as G-quadruplex probe.[26]

The extended **dppz** aromatic ligand has been employed for the synthesis of **[(ppy)₂Ir(dppz)]PF₆**, analogous to compounds **11** and **12** (par. 2.2.2), which demonstrated its ability to trigger both oxidation and reduction of DNA bases.[27] Indeed, thanks to its extended π electron system and its planarity, **dppz** is recognized as an intercalative ligand, thus metal complexes incorporating **dppz** may "bind" DNA. The above mentioned compound **[(ppy)₂Ir(dppz)]PF₆** is effectively able to non-covalently bind DNA, and, upon irradiation, an electron-transfer process occurs, leading to guanine oxidation and thymine reduction.[27] The electron-transfer (ET) process takes place normally between DNA and proteins, but externally triggered ET may result in a cell damage.[28] On this basis, an Ir(III) complex incorporating **dppz** could be tested as cytotoxic agent, justifying the choise of **dppz** as ancillary ligand.

Also the less extended **dpq** ligand may exert an analogous cytotoxic effect, as reported by Lo *et al*. who described the synthesis and characterization of cationic Ir(III) complexes incorporating this N^N ligand (**dpq**), different cyclometalated ligands (phenylpyrazole **ppz**, benzoquinoline **bzq** and phenylquinoline **pq**) and PF₆ as counterion (Fig.2.2.3).[29]
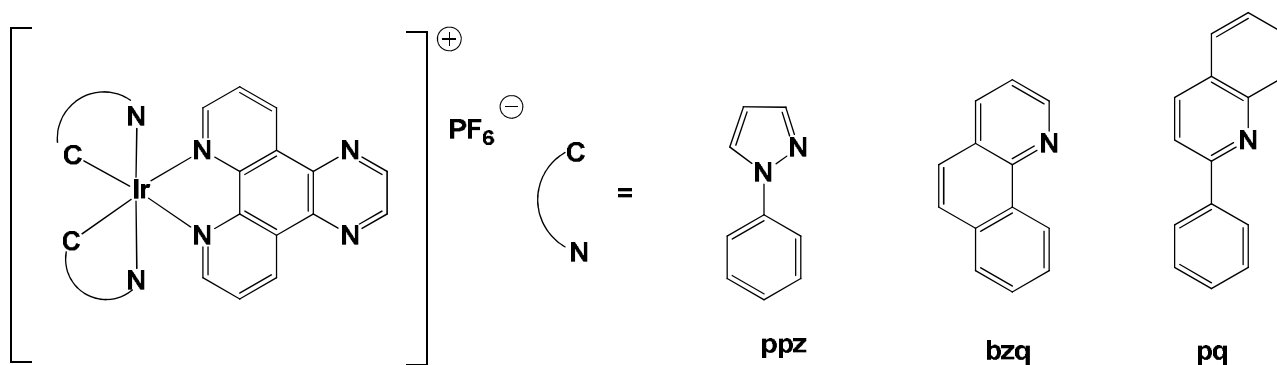
Fig.2.2.3. Chemical structure of **[(ppz)₂Ir(dpq)]PF₆**, **[(bzq)₂Ir(dpq)]PF₆** and **[(pq)₂Ir(dpq)]PF₆**.[29]

Lo *et al.* reported that these **[(C^N)₂Ir(dpq)]PF₆** complexes present a good cellular uptake and are able to bind proteins and intercalate into the base-pairs of double- stranded DNA.[29]

Finally, the **dpa** and **dpc** ligands were chosen by virtue of the presence of the –NH and –CO groups respectively, which could act as sites for hydrogen bonding formation, either as donor or acceptor respectively, resulting in a possible increase of the water-solubility of the resulting complexes.

2.2.1 Synthesis of the precursor [(ppy)₂Ir(*μ*-Cl)]₂ (I)

All the cationic Ir (III) complexes of general formula **[(ppy)₂Ir(N^N)]CH₃CO₂** were obtained starting from the cyclometalated Ir(III) chloro-bridged dimer **[(ppy)₂Ir(*μ*-Cl)]₂ (I)**. The reaction of cyclometalation of nitrogen heterocyclic bases with Iridium (III) was first reported by Nonoyama[30] and is currently recognised as the basic method to form a metal-carbon σ-bond. Since Ir (III) is characterized by the great inertness of its coordination sphere, this reaction requires very drastic conditions in order to substitute the chlorine ligands of the Iridium precursor. Indeed, usually high-boiling-point solvents, such as ethylene glycol derivatives, reflux and long reaction times, ranging from 24h[31] to 32h,[30] are needed. Following previous reports on the use of microwave irradiation to promote cycloplatination[32] and cycloiridation,[33,34] for this research work the reaction of cyclometalation of the ligand 2-phenylpyridine **H(ppy)**, using Iridium (III) chloride as metal source, was achieved by microwave (MW) assisted synthesis in degassed (N₂) 2-ethoxyethanol/water solution at 250 W (Scheme 2.2.1).
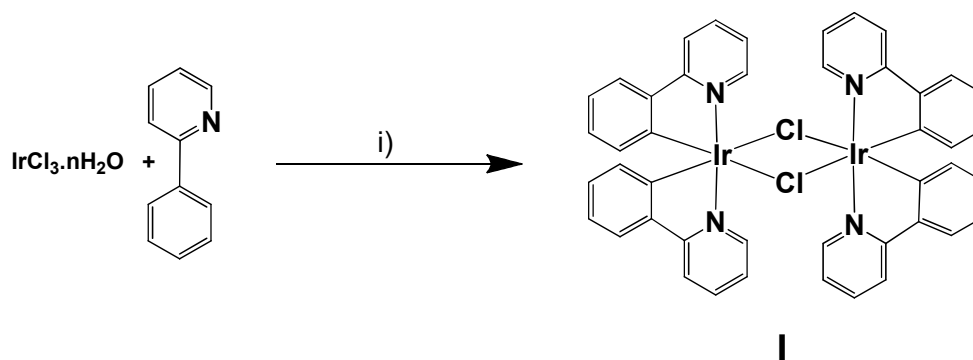
Scheme 2.2.1. Synthesis of the precursor **[(ppy)$_2$Ir(μ-Cl)]$_2$ (I).** Reaction conditions: (i) EtOCH$_2$CH$_2$OH/H$_2$O, 250W, 110 °C, 1 h.

This simple method allows to obtain the chloro-bridged dimer **[(ppy)$_2$Ir(μ-Cl)]$_2$ (I)** in large yield, with high purity and, more importantly, in a shorter time (1h) with respect to conventional heating source. This result arises from the greater efficiency of microwave heating respect to conventional heating source.[35,36] Indeed, microwaves speed up chemical reactions via a dielectric thermal effect which derives from the dielectric polarization of charges in a material and allows a higher temperature homogeneity in the sample. This effect occurs only in substances presenting a permanent dipole moment which are able to align themselves with the direction of the electric field. The fast change in the polarity of the MW radiation electric field leads to a rotation of the molecules in a polar solvent. Since this change is faster than the rotation solvent molecules around their dipole centre, a phase shift occurs, energy is absorbed from the electric field and hot-spots and superheating effect can be induced.

2.2.2 Synthesis of the [(ppy)$_2$Ir(N^N)]CH$_3$CO$_2$ complexes

Several water-soluble cationic Ir(III) complexes have been synthetized. All these Ir(III) coordination compounds incorporate two 2-phenylpyridine as cyclometalated ligands, different N^N ancillary ligands and the acetate (CH$_3$CO$_2^-$) as counterion. All the selected ancillary ligands are commercially available, with the exception of **dppz**, which was synthetized following the procedure reported by Wang *et al.* (Scheme 2.2.2).[37] The synthesis of the **dppz** ligand (**b** in Scheme 2.2.2) involves the oxidation of 1,10-phenanthroline (**phen**) in order to obtain 1,10-phenanthroline-5,6-dione (**a** in Scheme 2.2.2),[38] which was subsequently reacted with benzene-1,2-diamine, recovering the desired product.
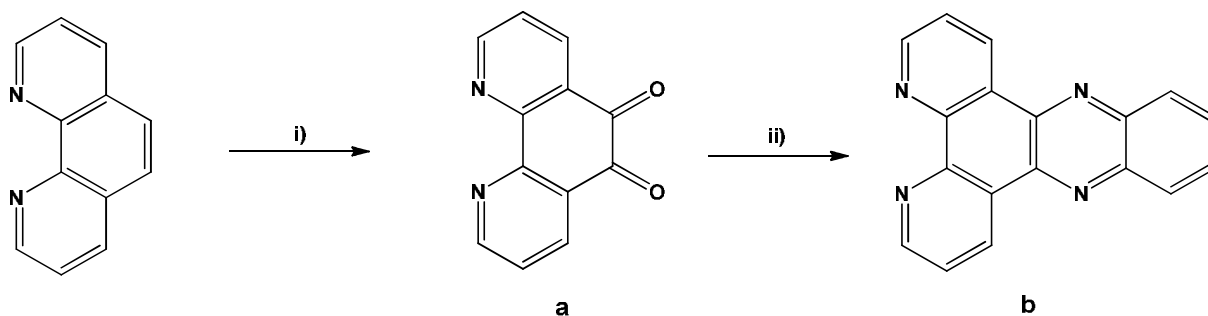
Scheme 2.2.2. Synthesis of the N^N ligand **dppz (b)**. Reaction conditions: i) H_2SO_4, HNO_3, KBr, reflux, 3h; ii) 1.1 eq. of benzene-1,2-diamine, 4-methylbenzenesulfonic acid, EtOH, reflux, 12h..

The synthetic procedure adopted to obtain water-soluble cationic Ir(III) complexes involved two steps: first, a bridge-splitting reaction was performed by the addition of the selected ancillary ligand to the precursor chloro-bridged dimer **[(ppy)₂Ir(μ-Cl)]₂**, obtaining the corresponding complex of general formula **[(ppy)₂Ir(N^N)]Cl**. The bridge-splitting reactions were all performed in MeOH or $MeOH/CH_2Cl_2$ mixtures, under inert atmosphere, for *ca.* 24h. The mixture $MeOH/CH_2Cl_2$ was used in the case of solubility issues encountered in pure MeOH.

The second synthetic step involved an anion-exchange reaction between the complexes bearing chloride ions and silver acetate (CH_3COOAg), which was previously prepared (Scheme 2.2.3), thus the formation of the correspondent water-soluble **[(ppy)₂Ir(N^N)]CH₃CO₂** was achieved (Scheme 2.2.4).

$$CH_3COOH + NaOH \xrightarrow{\text{i)}} CH_3COONa \xrightarrow{\text{ii)}} CH_3COOAg$$
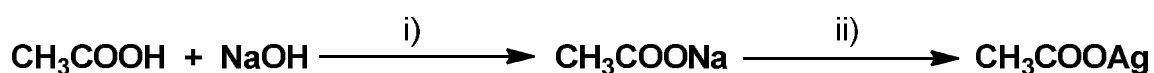
Scheme 2.2.3. Synthesis of silver acetate (CH_3COOAg). Reaction conditions: i) $EtOH/H_2O$, r.t., 2h; ii) $AgNO_3$, r.t., 2h.
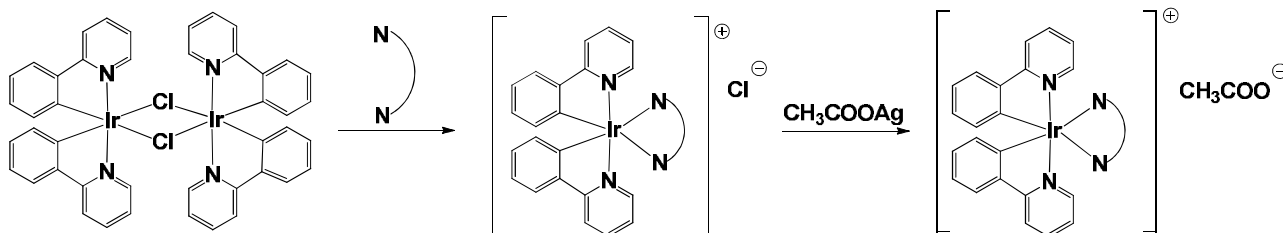
Scheme 2.2.4. The bridge-splitting reaction of **I** followed by the counterion-exchange reaction.

Hence, the anion exchange reaction of compounds **[(ppy)₂Ir(biq)]Cl (1)**, **[(ppy)₂Ir(dip)]Cl (3)**, **[(ppy)₂Ir(dpa)]Cl (5)**, **[(ppy)₂Ir(dpc)]Cl (7)**, **[(ppy)₂Ir(dpq)]Cl (9)** and **[(ppy)₂Ir(dppz)]Cl (11)** allows the formation of the correspondent acetate complexes **[(ppy)₂Ir(biq)]CH₃CO₂ (2)**, **[(ppy)₂Ir(dip)]CH₃CO₂ (4)**, **[(ppy)₂Ir(dpa)]CH₃CO₂ (6)**, **[(ppy)₂Ir(dpc)]CH₃CO₂ (8)**, **[(ppy)₂Ir(dpq)]CH₃CO₂ (10)** and **[(ppy)₂Ir(dppz)]CH₃CO₂ (12)** (Fig. 2.2.4).
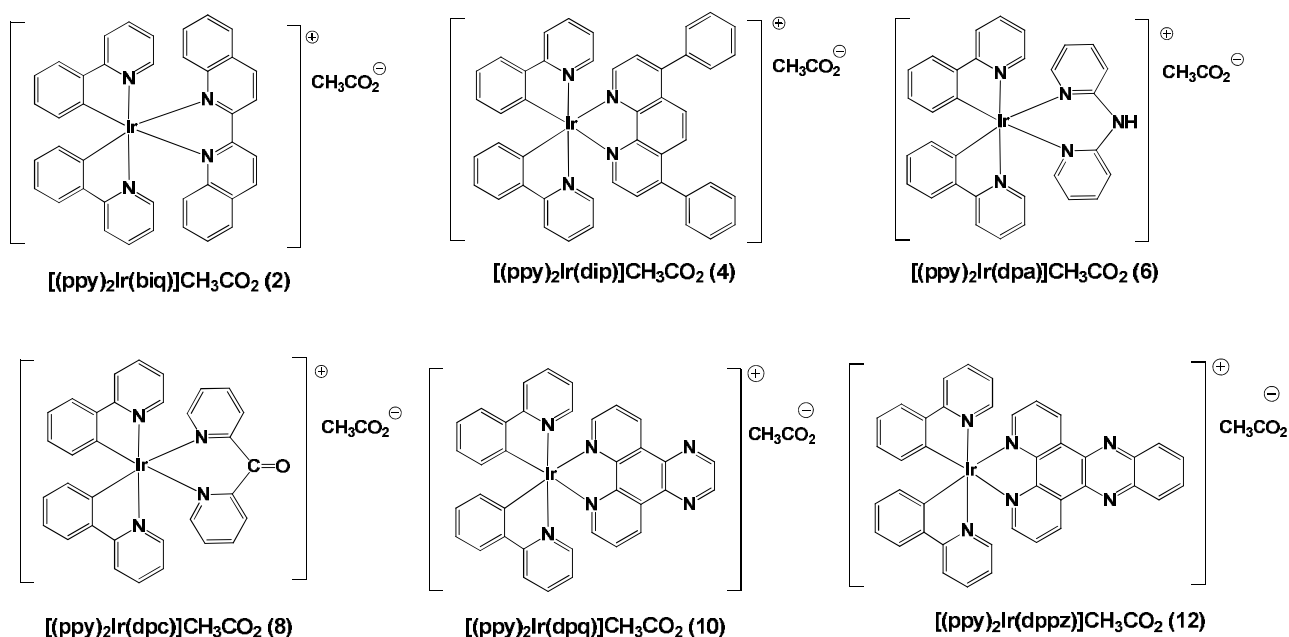
Fig.2.2.4. Chemical structure of compounds **[(ppy)₂Ir(biq)]CH₃CO₂ (2)**, **[(ppy)₂Ir(dip)]CH₃CO₂ (4)**, **[(ppy)₂Ir(dpa)]CH₃CO₂ (6)**, **[(ppy)₂Ir(dpc)]CH₃CO₂ (8)**, **[(ppy)₂Ir(dpq)]CH₃CO₂ (10)** and **[(ppy)₂Ir(dppz)]CH₃CO₂ (12)**.

All the synthetized complexes illustrated in Fig.2.2.4 were soluble in water and their solubility limit were roughly determined (Table 2.2.2). The determination was performed by dissolving increasing amounts of each compound in a fixed volume of water, until a suspension (or a precipitate) was obtained.

Complex	Solubility Limit (g/L)
[(ppy)₂Ir(biq)]CH₃CO₂ (2)	0.83
[(ppy)₂Ir(dip)]CH₃CO₂ (4)	0.80
[(ppy)₂Ir(dpa)]CH₃CO₂ (6)	1.35
[(ppy)₂Ir(dpc)]CH₃CO₂ (8)	10.40
[(ppy)₂Ir(dpq)]CH₃CO₂ (10)	162.80
[(ppy)₂Ir(dppz)]CH₃CO₂ (12)	1.01

Table 2.2.3. Solubility limits of complexes **2, 4, 6, 8, 10** and **12** in water.

Only for **[(ppy)₂Ir(dpq)]CH₃CO₂ (10)** and **[(ppy)₂Ir(dppz)]CH₃CO₂ (12)** was observed the formation of viscous/gel phases when increasing the concentration of the complex in water. A comprehensive structural study of these phases will be presented in chapter 3.

2.2.3 DFT calculations

To provide a quantum chemical insight into all the synthesized complexes, the Density Functional Theory (DFT) method was employed to investigate their ground-state electronic structures and orbital configurations. Calculation were performed starting from the crystal structure, when possible.[39-42] Full geometry optimizations of all Iridium cations in their singlet ground state were performed through DFT calculations using the B3LYP functional[43,44] and the mixed "Double-ζ" quality basis sets, the relativistic effective core potential (ECP) and basis set LANL2DZ[45] was used to treat the heavy metal iridium atom, whilst the basis set 6-31G(d)[46] was employed for the remaining atoms. The relativistic effective core potential (ECP)[47,48] on the Ir atom replaced the inner core electrons leaving the outer core $[(5s)^2(5p)^6]$ electrons and the $(5d^6)$ valence electrons of the Ir(III) metal center. No symmetry constraints were applied during the geometry optimizations, which were carried out with the Gaussian 09 package.[49] This calculation level has widely been used throughout the literature for the computational modellisation of both neutral or ionic Iridium (III) complexes.[50-52] The HOMO-LUMO distributions and the corresponding energy values of the optimized geometries of the Iridium cations **[(ppy)₂Ir(biq)]⁺**, **[(ppy)₂Ir(dip)]⁺**, **[(ppy)₂Ir(dpa)]⁺**, **[(ppy)₂Ir(dpc)]⁺**, **[(ppy)₂Ir(dpq)]⁺** and **[(ppy)₂Ir(dppz)]⁺** are reported in Fig. 2.2.5. For all the cationic motifs, the HOMO is evenly distributed onto the two **ppy** cyclometalated ligands, whereas the LUMO is mainly localized onto the ancillary ligands. Nevertheless the frontier orbitals distribution is similar for all the complexes, slight differences due to electronic effects can be observed in the energy values of the HOMO-LUMO levels, and this effect is more pronounced for the LUMO frontier orbitals. Indeed, while the HOMO energy value ranges from -7.57 eV to -8.00 eV within the series, the LUMO energy values ranges from -4.28 eV to -5.46 eV. Noteworthy, while the band gap HOMO/LUMO is *ca.* 2.8 eV for most of the complexes, only for **[(ppy)₂Ir(dpa)]⁺** and **[(ppy)₂Ir(dpc)]⁺** band values slightly differ (3.54 eV for **[(ppy)₂Ir(dpa)]⁺** and 2.54 eV for **[(ppy)₂Ir(dpc)]⁺**), probably arising from the insertion of the N-H and C=O functional groups respectively within the pseudo-aromatic metallocycles.
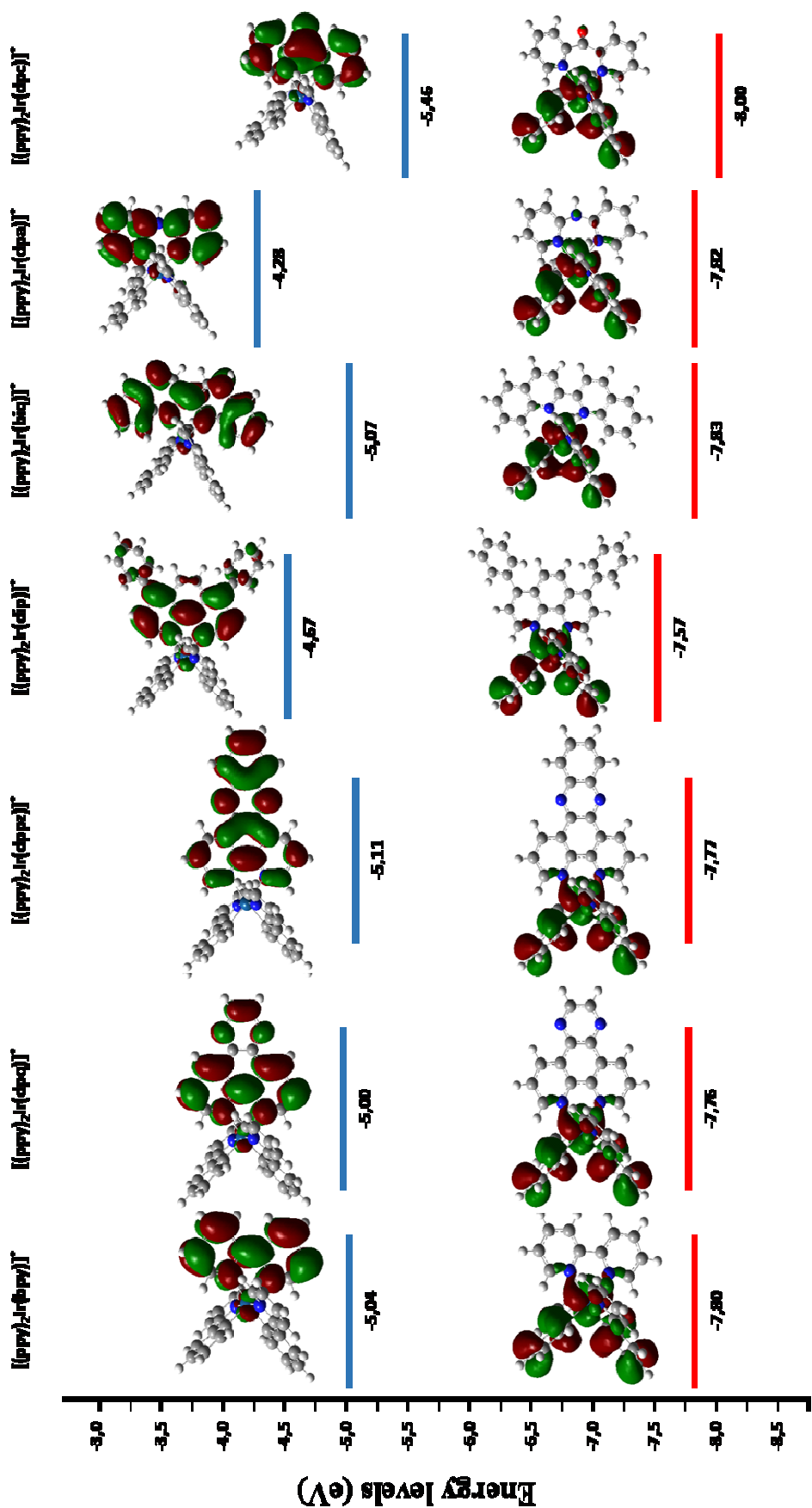
Fig.2.2.5. HOMO-LUMO structures of [(ppy)₂Ir(biq)]⁺, [(ppy)₂Ir(dip)]⁺, [(ppy)₂Ir(dip)]⁺, [(ppy)₂Ir(dpc)]⁺, [(ppy)₂Ir(dpa)]⁺ and [(ppy)₂Ir(dppz)]⁺. All orbital envelopes are drawn at an amplitude of 0.02 (e/Å³)¹ᐟ²

All the atom coordinates of the optimized geometries are reported in the Appendix of this thesis.

Noteworthy, DFT calculations pointed out the distortion of the ancillary ligand **biq** in the cationic motif **[(ppy)₂Ir(biq)]⁺** in a cross shape, as represented in Fig. 2.2.6, due to the steric hindrance exerted by the bulky **biq** ligand to the cyclometalated **ppy** ligands.
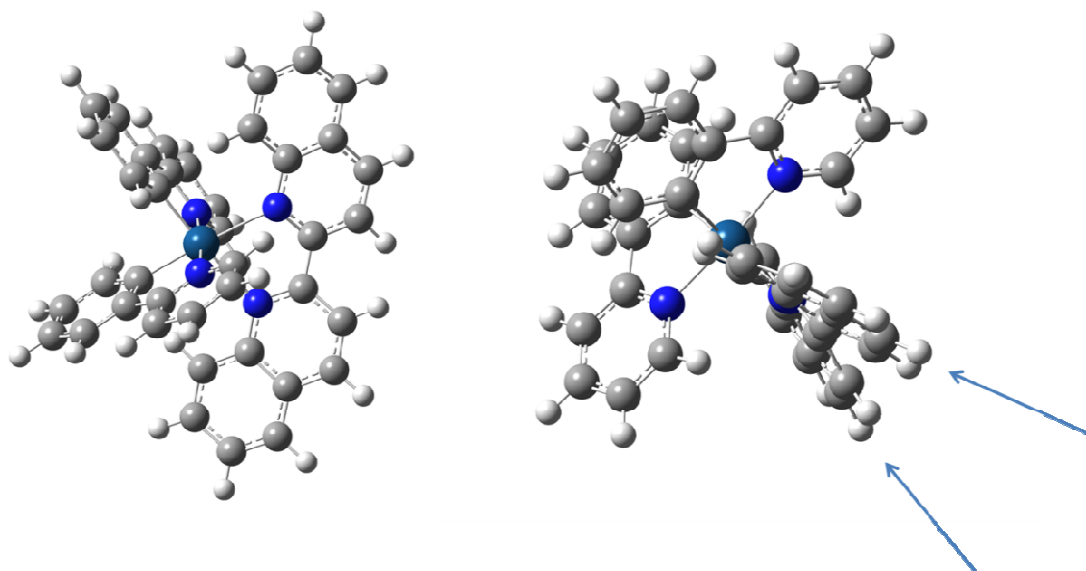
Fig.2.2.6. Two different views of the distortion of the ancillary ligand biq in the complex **[(ppy)₂Ir(biq)]⁺**.

Regarding the **[(ppy)₂Ir(dpa)]⁺** and **[(ppy)₂Ir(dpc)]⁺** cations, the geometry optimization converged towards a structure of the cations in which the N^N ligands **dpa** and **dpc** are V bent, not showing the planarity displayed by all the other N^N ligands of the series (Fig. 2.2.7).
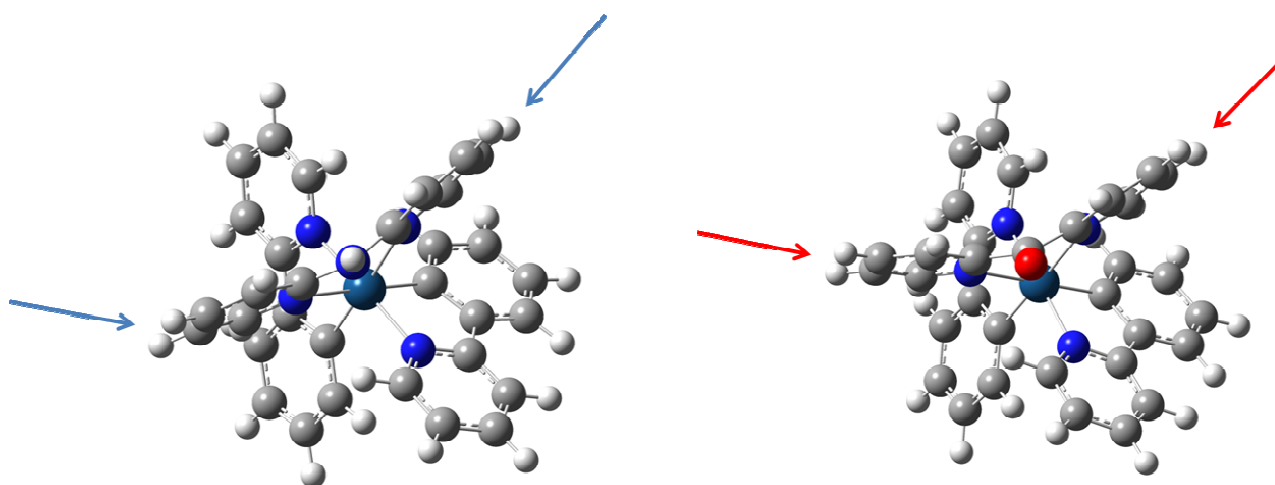
Fig.2.2.7. Distortion of the ancillary ligands dpa in the complex **[(ppy)₂Ir(dpa)]⁺** (on the left) and dpc in **[(ppy)₂Ir(dpc)]⁺**.

2.2.4 Photophysical characterization

The photophysical properties of compounds **2**, **4**, **6**, **8**, **10** and **12** were investigated in diluted water solution (c = $5 \cdot 10^{-6}$M). The absorption spectra of all the complexes are dominated in the UV region (250-350 nm) by intense spin-allowed $^1\pi$-π^* ^{1}LC transitions involving the aromatic ligands; at higher wavelength (350-450 nm) less-intense ^{1}MLCT bands are present (Fig.2.2.8). The absorption spectra are all similar in shape, with the exception of those of compounds **2** and **10**, which present structured and intense bands between *ca.* 240 and 400 nm.
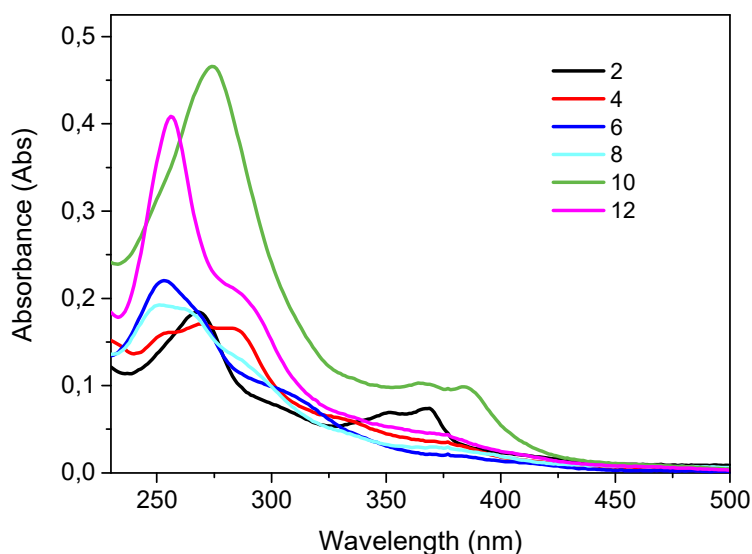
Figure 2.2.8 Absorption spectra of complexes **2, 4, 6, 8, 10 and 12** in water solution.

The emission spectra of compounds **[(ppy)₂Ir(biq)]CH₃CO₂ (2)**, **[(ppy)₂Ir(dip)]CH₃CO₂ (4)**, **[(ppy)₂Ir(dpa)]CH₃CO₂ (6)** and **[(ppy)₂Ir(dpc)]CH₃CO₂ (8)** were recorded in deaerated and aerated water diluted solutions (c = $5 \cdot 10^{-6}$M) and are reported in Fig.2.2.9. The complexes **[(ppy)₂Ir(dpq)]CH₃CO₂ (10)** and **[(ppy)₂Ir(dppz)]CH₃CO₂ (12)** do not emit in these conditions. A structureless intense orange emission is recorded with a maximum centred at 620 nm for the compound **4**, whereas the same emission band results less intense and red-shifted (centered at 670 nm) for the analogous complex incorporating **biq** ligand. On the contrary, the compounds **6** and **8** display structured emission bands with maximum at 479, 509 and 550 nm.
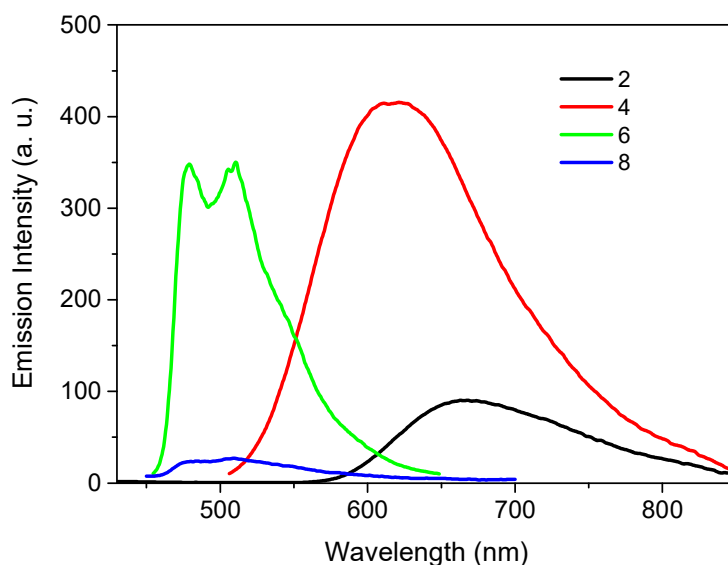
Figure 2.2.9. Emission spectra of complexes **2, 4, 6** and **8** in water solution.

The emission quantum yields for the four compounds range from 0.08% to 8.65% in aerated water solution. Moreover, excited state decays of these compounds show bi-exponential kinetics, whose deconvolution gave τ_1= 67 ns and τ_2= 288 ns values for **2**, τ_1= 86 ns and τ_2= 241 ns values for **4**, τ_1= 293 ns and τ_2= 518 ns values for **6** and τ_1= 12 ns and τ_2= 409 ns values for **8**. The two different lifetimes of the excited states of these emissive complexes can be attributed to two different emissive "species" in solution, corresponding to solvated single molecule and molecular aggregates. All the photophysical data for compounds **2**, **4**, **6** and **8** are reported in table 2.2.3.

Compound	Emission, λ_{max}/nm	Φ (%)*	Lifetime, $\tau(\alpha)$* ns(%)	Φ (%)**	Lifetime, $\tau(\alpha)$** ns(%)
2	670	0.76	67(87.41), 288(12.59)	0.77	67(97.33), 305(2.67)
4	618	2.94	86(92.48), 241(7.52)	2.93	89(84.82), 149(15.18)
6	479, 509, 550	8.65	293(11.26), 518(88.74)	71.5	661(3.16), 2237(96.84)
8	479, 509, 550	0.08	12(4.64), 409(95.36)	0.40	358(9.95), 2233(90.05)

Table 2.2.3. Photophysical data of complexes **2, 4, 6** and **8** in water solution* and deaerated water solution**

The quantum yield and the excited state lifetime remain almost unchanged for compounds **[(ppy)$_2$Ir(biq)]CH$_3$CO$_2$ (2)** and **[(ppy)$_2$Ir(dip)]CH$_3$CO$_2$ (4)** also in deaerated water solution. On the contrary, for complexes **[(ppy)$_2$Ir(dpa)]CH$_3$CO$_2$ (6)** and **[(ppy)$_2$Ir(dpc)]CH$_3$CO$_2$ (8)**, upon degassing, hence upon O$_2$ removal, the two lifetime of the excited state undergo to a substantial increase, giving τ_1= 661 ns and τ_2= 2237 ns values for **6** and τ_1= 358 ns and τ_2= 2233 ns values for **8**. In addition, **[(ppy)$_2$Ir(dpa)]CH$_3$CO$_2$ (6)** in deaerated water solution exhibit a pronounced enhancement of its luminescence quantum yield (71.5%), opening the way to its possible application as O$_2$ sensor and Photodynamic Therapy. Taking into account the excited state lifetime values, it is reasonable to state that the non-radiative decay is much greater for compounds **2** and **4,** leading to shorter lifetime values with respect to the ones of **6** and **8**, although all the de-excitation mechanisms should follow a phosphorescence pathway. The absence of planarity and the V-bending in the N^N ligands of **[(ppy)$_2$Ir(dpa)]CH$_3$CO$_2$ (6)** and **[(ppy)$_2$Ir(dpc)]CH$_3$CO$_2$ (8)** and the presence of the functional group (NH or C=O in **6** and **8** respectively) within the 6 member metallocycle generated by the coordination of the N^N ancillary ligand, with respect to the 5 member metallocycle created for all other complexes, could be responsible of the differences observed in their photophysical behaviour respect to complexes **2** and **4**. Further Time Dependent Density Functional Theory (TD-DFT) calculations could clarify this issue, which are however beyond the immediate scope of this thesis and would require a more specialized analysis.

2.2.5 Conclusion

Six new water-soluble Ir(III) complexes, **[(ppy)$_2$Ir(biq)]CH$_3$CO$_2$ (2), [(ppy)$_2$Ir(dip)]CH$_3$CO$_2$ (4), [(ppy)$_2$Ir(dpa)]CH$_3$CO$_2$ (6), [(ppy)$_2$Ir(dpc)]CH$_3$CO$_2$ (8), [(ppy)$_2$Ir(dpq)]CH$_3$CO$_2$ (10)** and **[(ppy)$_2$Ir(dppz)]CH$_3$CO$_2$ (12)**, have been synthetized starting from the corresponding non-water-soluble chloride analogous, through a simple methodology which involves an anion exchange reaction. With the exception of compounds **10** and **12**, which are able to generate supramolecular assemblies in water, the solubility in water of the synthetized complexes is highly influenced by the nature of the ancillary ligand. In particular, the complexes **6** and **8**, bearing more hydrophilic ligands, display higher water solubility than compound **2** and **4**, that are incorporating ancillary ligands with more extended aromatic systems. The photophysical study of these compounds was performed in water solution, and interesting emission properties were found for **[(ppy)$_2$Ir(biq)]CH$_3$CO$_2$ (2), [(ppy)$_2$Ir(dip)]CH$_3$CO$_2$ (4), [(ppy)$_2$Ir(dpa)]CH$_3$CO$_2$ (6)** and **[(ppy)$_2$Ir(dpc)]CH$_3$CO$_2$ (8)**. In particular, all the emissive complexes are characterized by two different lifetimes of the excited states which can be attributed to two different emissive "species" in solution, corresponding to solvated single molecule and molecular aggregates. Finally, the complexes **[(ppy)$_2$Ir(dpq)]CH$_3$CO$_2$ (10)** and **[(ppy)$_2$Ir(dppz)]CH$_3$CO$_2$ (12)** displayed the ability to generate supramolecular "gel" phases in determined range of concentrations in water, whose structural architectural organization will be comprehensively studied and described in chapter 3.

All these newly synthetized complexes are currently under study through collaboration with Prof. Neamati (University of Michigan, USA) to probe their biological activity as anticancer drugs in various tumour cell lines.

2.3 References

1. V. Fernández-Moreira, F. L. Thorp-Greenwood, M. P. Coogan, *Chem. Commun.*, **2010**, 46, 186–202.

2. Z.-W. Yu, P. J. Quinn, *Biosci. Rep.*, **1994,** 14, 259–281.

3. W. Bunch, C. Edwards, C., *J. Physiol.*, **1969**, 202, 683-697.

4. R. Notman, M. Noro, B. O'Malley, J. Anwar, *J. Am. Chem. Soc.,* **2006,** 128, 13982-13983.

5. T. R. Henderson, R. F. Henderson, *Ann. N. Y. Acad. Sci., USA*, **1975**, 243, 38-53.

6. A. L. Jacobson, C. L. Turner, *Biochemistry*, **1980**, 19, 4534-4538.

7. J. L. Hanslick, K. Lau, K. K. Noguchi, J. W. Olney, C. F. Zorumski, S. Mennerick, N. B. Farber, *Neurobiol. Dis*., **2009**, 34, 1–10.

8. W. Qi, D. Ding, R. J. Salvi, *Hear. Res*., **2008**, 236, 52–60.

9. J. Galvao, B. Davis, M.Tilley, E. Normando, M. R. Duchen, M. F. Cordeiro, *The FASEB J.,* **2017**, 28, 1317-1330.

10. Z. Yang, Y. Zhao, C. Wang, Q. Song, Q. Pang, *Talanta*, http://dx.doi.org/10.1016/j.talanta.2017.01.050.

11. M.-J. Li, P. Jiao, M. Lin, W. He, G.-N. Chena, X. Chen, *Analyst*, **2011**, 136, 205–210.

12. M. Gottschaldt, D. Koth, D. Muller, I. Klette, S. Rau, H. Görls, B. Sch4fer, R. P. Baum, S. Yano, *Chem.-Eur. J.*, **2007**, 13, 10273–10280.

13. Y. Ma, S. Liu, H. Yang, Y. Wu, C. Yang, X. Liu, Q. Zhao, H. Wu, J. Liang, F. Li, W. Huang, *J. Mater. Chem*., **2011**, 21, 18974–18982.

14. L. Yu, Z. Huang, Y. Liu, M. Zhou, *J. Organomet. Chem*., **2012**, 718, 14–21.

15. S.-Y. Yin, S.-S. Sun, M. Pan, Y.-Z. Fan, Y.-X. Chen, H.-P. Wang, Y.-N. Fan, *Inorg. Chem. Comm*., **2017**, 83, 81–83.

16. R. A. Smith, E. C. Stokes, E. E. Langdon-Jones, J. A. James, A. Platts, B. M. Kariuki, A. J. Hallett, S. J. A. Pope, *Dalton Trans*., **2013**, 42, 10347–10357.

17. H. Yang, L. Li, L. Wan, Z. Zhou, S. Yang, *Inorg. Chem. Commun*., **2010**, 13, 1387–1390.

18. S. Liu, W. Qiao, G. Cao, Y. Chen, Y. Ma, Y. Huang, X. Liu, W. Xu, Q. Zhao, W. Huang, *Macromol. Rapid Commun.*, **2013**, 34, 81–86.

19. Y. J. Yadav, B. Heinrich, G. De Luca, A. M. Talarico, T. F. Mastropietro, M. Ghedini, B. Donnio, E. I. Szerb, *Adv. Opt. Mater*., **2013**, 1, 844–854.

20. K. R. Schwartz, R. Chitta, J. N. Bohnsack, D. J. Ceckanowicz, P. Miró, C. J. Cramer, K. R. Mann, *Inorg. Chem.,* **2012**, 51, 5082–5094.

21. C. Oliviero Rossi, C. Cretu, L. Ricciardi, A. Candreva, M. La Deda, I. Aiello, M. Ghedini, E. Ildyko Szerb, *Liquid Crystals*, **2017**, 44, 880-888.

22. L. Ricciardi, T. F. Mastropietro, M. Ghedini, M. La Deda, E. Ildyko Szerb, *J Organomet Chem.*, **2014**, 772–773, 307–313.

23. Unpublished results, studies are still in progress.

24. R. Cao, J. Jia, X. Ma, M. Zhou, H. Fei, *J. Med. Chem*., **2013**, 56, 3636–3644.

25. C.-H. Leung, H.-J. Zhong, H. Yang, Z. Cheng, D. Shiu- Hin Chan, V. Pui-Yan Ma, R. Abagyan, C-Y. Wong, D.- L. Ma, *Angew. Chem. Int. Ed*., **2012**, 51, 9010 –9014.

26. H.-Z. He, K.-H. Leung, H. Yang, D. S.-H. Chan, C.-H. Leung, J. Zhou, A. Bourdoncle, J.-L. Mergny, D.-L. Ma, *Biosens. Bioelectron*, **2013**, 41, 871–874.

27. F. Shao, B. Elias, W. Lu, J. K. Barton, *Inorg. Chem*., **2007**, 46, 10187-10199.

28. Bensasson RV, Land EJ, Truscott TG (1993) Excited states and free radicals in biology and medicine: contributions from flash photolysis and pulse radiolysis. Oxford Press, New York.

29. K. Yin Zhang, S. Po-Yam Li, N. Zhu, I. Wai-Shan Or, M. Shau-Ha Cheung, Y.-W. Lam, K. Kam-Wing Lo, *Inorg. Chem*., **2010**, 49, 2530–2540.

30. M. Nonoyama, *Bull. Chem. Soc. Jpn*., **1974**, 47, 767–768.

31. M. Lepeltier, F. Appaix, Y. Y. Liao, F. Dumur, J.Marrot, T. Le Bahers, C. Andraud, C. Monnereau, *Inorg. Chem*., **2016**, 55, 9586–9595.

32. N. Godbert, T. Pugliese, I. Aiello, A. Bellusci, A. Crispini, M. Ghedini, *Eur. J. Inorg. Chem*., **2007**, 32, 5105–5111.

33. H. Konno, Y. Sasaki, *Chem. Lett.*, **2003**, 32, 252–253.

34. D. L. Davies, M. P. Lowe, K. S. Ryder, K. Singh, S. Singh, *Dalton Trans.*, **2011**, 40, 1028–1030.

35. M. Nüchter, B. Ondruschka, W. Bonrath, A. Gum, *Green Chem* , **2004** , 6 , 128-141.

36. D. M. P. Mingos and D. R. Baghurst, "Applications of Microwave Dielectric Heating Effects to Synthetic Problems in Chemistry", in Microwave Enhanced Chemistry, ed. H. M. Kingston and St. J. Haswell, ACS, Washington, DC, 1997, p. 3.

37. C. Zhou, Q. Wang, *Transition Met. Chem.*, **2010**, 35, 605–611.

38. R. D. Gillard, R. E. E. Hill, R. Maskill, *J. Chem. Soc. A*, **1970**, 1447.

39. M. Ching Tseng, W. Lin Su, Y. Cheng Yu, S. Pin Wang, W. Liang Huang, Inorg. Chim. Acta, **2006**, 359, 4144–4148.

40. H.-C. Su, H.-F. Chen, F.-C. Fang, C.-C. Liu, C.-C. Wu, K.-T. Wong, Y.-H. Liu, S.-M. Peng*, J. Am. Chem. Soc*., **2008**, 130 , 3413-3419.

41. R. D. Costa, E. Ortí, H. J. Bolink, S. Graber, S. Schaffner, M. Neuburger, C. E. Housecroft,; E. C. Constable, *Adv. Funct. Mater*., **2009**, 19, 3456– 3463.

42. K. Kam-Wing Lo, C.-. Chung, N. Zhu, *Chem. Eur. J.*, **2006**, 12, 1500 – 1512.

43. C. Lee, W. Yang, R. G. Parr, *Phys. Rev. B,* **1998**, 37, 785–789.

44. D. Becke, *J. Chem. Phys*. **1993,** 98, 5648–5653.

45. P. J. Hay, W. R. Wadt, *J. Chem. Phys*., **1985**, 82, 299.

46. E. Frisch, M. J. Frisch, Gaussian 98 User's Reference, Gaussian, Inc., Pittsburgh, PA, 1998, and references cited therein.

47. W. Koch, M. C. Holthausen, A Chemist's Guide to Density Functional Theory, Wiley-VCH, Weinheim, Germany, 2000.

48. C. Adamo, B. V. di Matteo, *Adv. Quantum Chem*., **1999**, 36, 4–7.

49. Frisch, M. J.; Trucks, G. W.; Schlegel, H. B.; Scuseria, G. E.; Robb, M. A.; Cheeseman, J. R.; Scalmani, G.; Barone, V.; Mennucci,B.; Petersson, G. A.; Nakatsuji, H.; Caricato, M.; Li, X.; Hratchian, H. P.; Izmaylov, A. F.; Bloino, J.; Zheng, G.; Sonnenberg, J. L.; Hada, M.; Ehara, M.; Toyota, K.; Fukuda, R.; Hasegawa, J.; Ishida, M.; Nakajima, T.; Honda, Y.; Kitao, O.; Nakai, H.; Vreven, T.; Montgomery, J. J. A.; Peralta, J. E.; Ogliaro, F.; Bearpark, M.; Heyd, J. J.; Brothers, E.; Kudin, K. N.; Staroverov, V. N.; Kobayashi, R.; Normand, J.; Raghavachari, K.; Rendell, A.; Burant, J. C.; Iyengar, S. S.; Tomasi, J.; Cossi, M.; Rega, N.; Millam, J. M.; Klene, M.; Knox, J. E.; Cross, J. B.; Bakken, V.; Adamo, C.; Jaramillo, J.; Gomperts, R.; Stratmann, R. E.; Yazyev, O.; Austin, A. J.; Cammi, R.; Pomelli, C.; Ochterski, J. W.; Martin, R. L.; Morokuma, K.; Zakrzewski, V. G.; Voth, G. A.; Salvador, P.; Dannenberg, J. J.; Dapprich, S.; Daniels, A. D.; Farkas, Ö.; Foresman, J. B.; Ortiz, J. V.; Cioslowski, J.; Fox, D. J. Gaussian 09, Revision A.02; Gaussian, Inc.: Wallingford, CT, 2009.

50. X. Gu, T. Fei, H. Zhang, H. Xu, B. Yang, Y. Ma, X. Liu, *Eur. J. Inorg. Chem*., **2009**, 2407–2414

51. E. Baranoff, B. F. E. Curchod, J. Frey, R. Scopelliti, F. Kessler, I. Tavernelli, U. Rothlisberger, M. Grätzel, Md. Khaja Nazeeruddin, *Inorg. Chem*., **2012**, 51, 215–224.

52. J. Sun, F. Zhong, X. Yi, J. Zhao, *Inorg. Chem*., **2013**, 52, 6299–6310.

Chapter 3

Supramolecular Gels and Metallogels

3.1 Introduction

Gels represent a very wide category of soft materials, and giving a precise definition remains a rather difficult task. In 1949 Hermans[1] defined a gel as a colloidal disperse systems of at least two components which exhibits mechanical properties characteristic of the solid state. The dispersion medium could be a gas in an aerogel or a liquid in a common gel. The dispersed component and the dispersion medium form together a continuous system.

In 1974, Flory[2] provided a more precise description, according to which a gel can be considered as a dispersion of a liquid, the major component (usually above 90 wt %), within a fibrillar solid network. Although they are mainly composed by a liquid, gels do not flow in the steady-state and have a solid-like rheology, meaning that they respond to deformations as elastic bodies. Actually, a substance is still classified as a gel by observing its characteristic flow through a typical test tube experiment[3] or through the dropping ball method,[4] which can be referred as crude rheological measurements. In the first method the tubes in which gels are prepared at increasing concentrations are turned upside down until no flow is observed, allowing the determination of the minimum gel concentration. In the second method, a small metal ball is placed on the top of the gel and its behaviour is observed: ideally, the ball should be immobile in the gel, but move downward in the sol.

Furthermore, Flory classified gels in four main categories on the basis of structural criteria:

(1) well-ordered lamellar structures, including gel mesophases which are arranged in parallel and present a long-range order (*e.g.*, soap gels and phospholipids);

(2) covalent polymeric networks, which exhibit a disordered continuous structure provided by a three-dimensional network of structural units covalently linked (*e.g.*, vulcanized rubbers, condensation polymers containing polyfunctional groups, phenolic resins and paint films);

(3) polymer networks formed through physical aggregation, which display a predominantly disordered structure with the exception of some regions of local order (*e.g.*, gelatin);

(4) particulate, disordered structures composed of highly anisotropic particles or reticular networks of fibers (*e.g.*, V_2O_5 gels or gels formed by aggregation of proteins).

A further class of gels, that can be considered as a subgroup of the last category, is represented by "supramolecular gels", called also physical gels.[5] They derive from the self-assembly, in a specific solvent, of small molecules, called Low Molecular Weight Gelators (LMWG), through non-covalent interactions. Depending on the nature of the solvent, supramolecular gels can be distinguished in organogels, if the liquid component is an organic solvent, and hydrogels, if it is water. The main feature of supramolecular gels is the reversibility of the sol-gel transition allowed by the noncovalent nature of the interactions between molecular building blocks, responsible for the generation of the 3D gel network.

3.1.1 Mechanism of physical gel formation

The most common used method for the preparation of physical gels implies the dissolution of the gelator in the suitable heated solvent and the cooling of the resulting solution below the T_{gel} (gelation temperature).[6]
The gelator concentration is expressed as percentage by weight and is usually comprised in a range between 1% and 10% w/w. Molecules that create gel-phase below concentration of 1% w/w are called "supergelators".
In an appropriate solvent, the gelator molecules establish non-covalent interactions, generating first small aggregates, tipically fibers. These structures become gradually bigger and entangled, generating a 3D network which traps solvent molecules via surface tension effect (Fig.3.1.1).
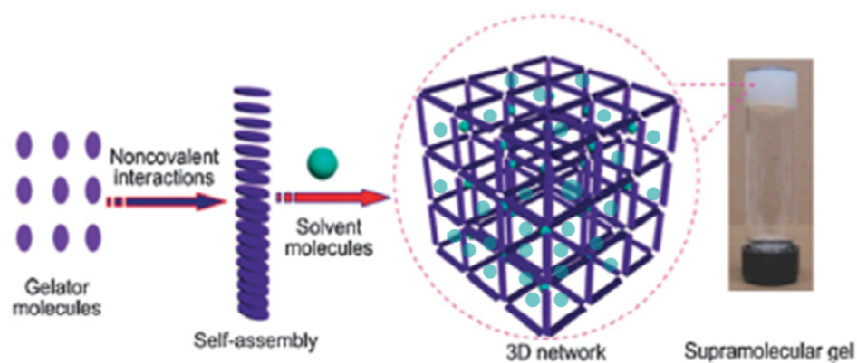
Fig.3.1.1. Schematic representation of a supramolecular gel formation (adapted from Ref.[7]).

Usually in an organogel, the driving force for the self-assembly is represented by hydrogen-bonds within the gelator molecules, whereas in a hydrogel the formation of the solid network is induced by hydrophobic interactions and π-π stacking between the starting molecules.

In order to achieve gel formation, there must be a precise balance between solubilization and phase separation. Moreover, gelation is a hierarchical process that comprises a number of steps:[8]

1. Interaction between two adjacent molecules to form a dimer;
2. Oligomerization of dimers by interaction with other molecules;
3. Lengthening of oligomers and generation of strands;
4. Bundling of strands to form fibers;
5. Interconnection of fibers and creation of a 3D continuous network;
6. Immobilization of solvent molecules in the fibers matrix.

In a fascinating description, Hamilton[6] compared gel formation with the genesis of proteins. Indeed, gelation is characterized by hierarchical levels, much like the primary, secondary and tertiary structures of a protein (Fig.3.1.2). The anisotropic aggregation of gelator molecules represents the primary structure; the growth of these aggregates gives rise to fibers, ribbons, sheets or micelles, considered the secondary structure; lastly, the interaction between the secondary structures generates the 3D system, that is the tertiary structure.
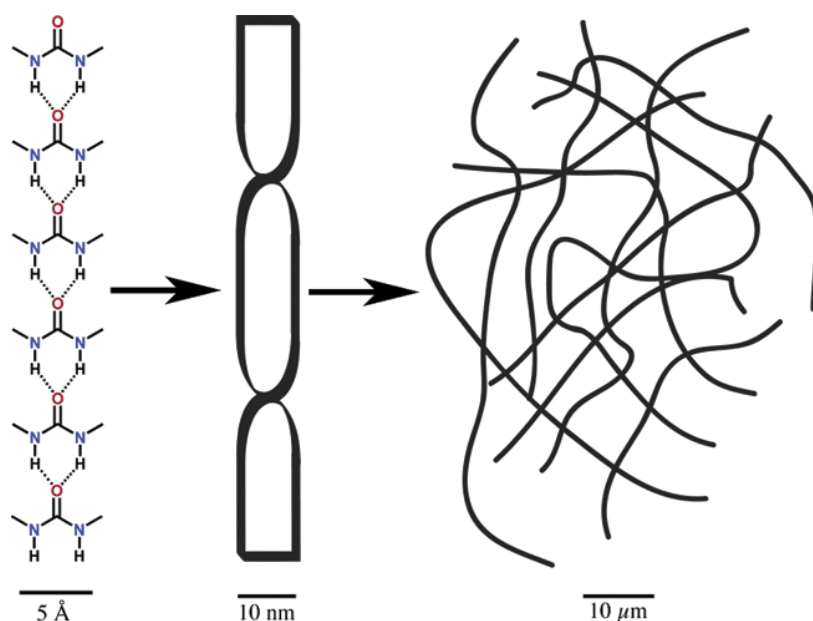
Fig.3.1.2. Schematic representation of the three hierarchical levels of organization in a supramolecular gel (from Ref.[6]).

3.1.2 Characterization of supramolecular gels

Since gels can be considered as an intermediate state of matter, being not quite solid, neither liquid, similar to liquid crystals, their characterization is not straightforward. Many of the common laboratory techniques used are generally adopted for solid or liquid materials, so need to be adapted to the analysis of gels. In other cases the interpretation of the results may imply some approximations.

Anyhow, the possible techniques are manifold, ranging from microscopy to rheology, depending on the scale to which the investigation is performed. For example, Simmons *et al.* studied some phenolic organogels, employing different techniques.[9] They managed to elucidate the gel molecular architecture at three length scales, using NMR, SAXS and AFM: single strands with a diameter of *ca.* 2nm self-assemble into fibers with hexagonal symmetry, which, in turn, self-organize into bundles (Fig.3.1.3).

Fig.3.1.3. Schematic representation of the three levels of organization of a gel and the methods employed that allowed to characterized the supramolecular architecture(from Ref.[9]).
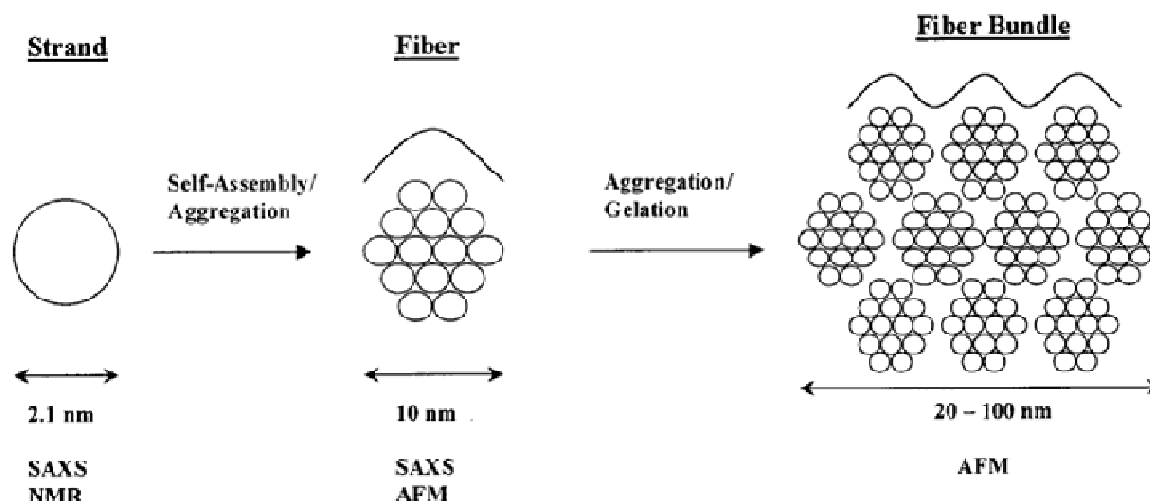
The most frequently used observational methods to investigate supramolecular gels are listed below and briefly described.

3.1.2.1 Nuclear Magnetic Resonance (NMR)

Solution-state ^{1}H-NMR is often used to investigate gel phases, although it presents several limitations arising from the low mobility of gelator molecules in this condition. Indeed, the resulting spectra are characterized by very broad peaks and therefore by inadequate spectral resolution.[7] Nevertheless, the broadening of NMR peaks, the changes in their chemical shifts and sometimes their appearance/disappearance which occur with temperature variations, could be exploited for the study of the noncovalent interactions (hydrogen bonds, π-π stacking) that lead to the gel formation. For example, Jung *et al*. acquired ^{1}H-NMR spectra at different temperatures of a sugar appended hydrogelator, observing the chemical shift and the appearance of the aromatic peaks upon heating, thus moving from the gel phase to the sol state (Fig.3.1.4).[10] They explained the difference in chemical shift between the aromatic protons and their manifestation in the sol state as a result of the breaking of π-π stacking and hydrogen-bond interactions.

61
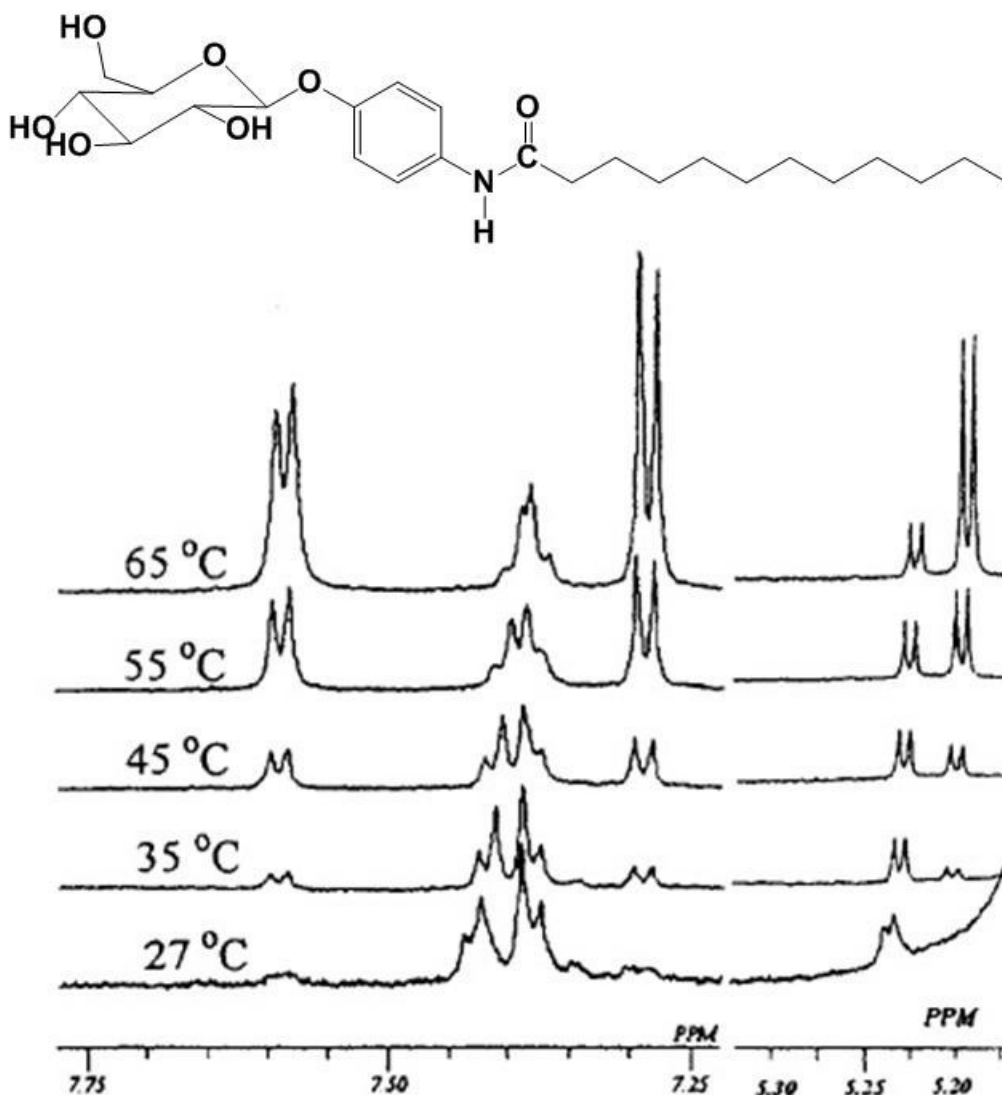
Fig.3.1.4 Chemical structure of a sugar-based gelator and its ^{1}H-NMR spectra in D$_2$O and methanol-d$_4$ (1:1 v/v) registered at different temperatures (adapted from Ref.[10]).

Other possibilities are solid-state NMR experiments[11] and relaxation time measurements (T1 and T2).[12] However, solid state NMR of gels presents several disadvantages, especially, due to high spinning speed. The significant centrifugal force generated upon spinning can result in the disintegration of gels. Therefore, low spinning speeds are generally recommended, which shall determine poor resolution of the NMR spectrum.[11]

Indeed, longitudinal relaxation time T1 and the NMR transverse relaxation time T2, have been measured during volume phase transition in PMMA gels,[12] but the analysis of these parameters is not straightforward.

3.1.2.2 Other spectroscopic techniques

Supramolecular gels which incorporate chromophores or fluorophores can be characterized through UV-vis spectroscopy and fluorescence spectroscopy. The comparison between spectra recorded in the sol phase and in the gel phase could provide information about the change in the surrounding environment polarity of the single gelator molecule, hence suggestions about the possible molecular packing could be extracted.

Moreover, FTIR spectroscopy is a useful method to monitor the formation of physical interactions. For example, Wegner *et al*. correlated the FTIR spectra of amphiphilic diblock codendrimers organogelators in solution (toluene was used as solvent), gel phase and solid state (Fig.3.1.5). They did not found significant differences between the gel phase and the solid state, but they observed the shift of the bands corresponding to the C=O stretching, the N-H bending, the C-N stretching and the N-H stretching after gelation from solution, which indicates that upon gelation the amide or urethane groups become strongly hydrogen bonded.[13]
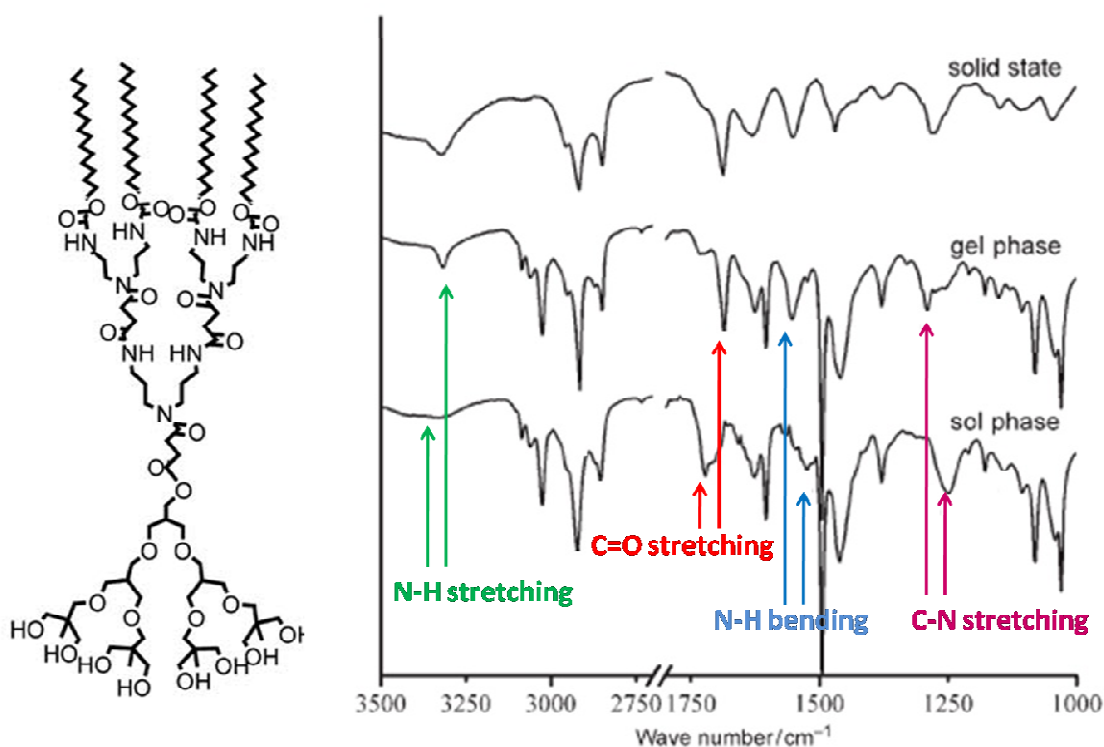

Fig.3.1.5 Chemical structure of codendrimers organogelator and its FTIR spectra in solid state, gel phases and solution (adapted from Ref.[13]).

3.1.2.3 Microscopy techniques

Electron microscopies (SEM and TEM) are the more suitable techniques to get a deep insight of the gel-phases morphology. These methods allow to determine, with resolution up to 0.2 nm, the dimension and the shape of the supramolecular aggregates which form the 3D network. Unfortunately, SEM and TEM measurements are carried out under high vacuum conditions, so they require the complete drying of the sample, either under ambient conditions or under vacuum. Thus, the observed samples are xerogels, rather than gels, implying that the detected structure is not completely identical to the native one. However, it is commonly assumed that the variations in the gel architecture are rather minimal. These limitations can be overcome through cryo-electron microscopies (cryo-SEM and cryo-TEM), in which the gel samples are rapidly frozen in liquid nitrogen. Usually cryo-EM micrographs exhibit more expanded and solvated matrixes, in which the solvent is immobilized in the interstitial cavities (Fig.3.1.6).[14]
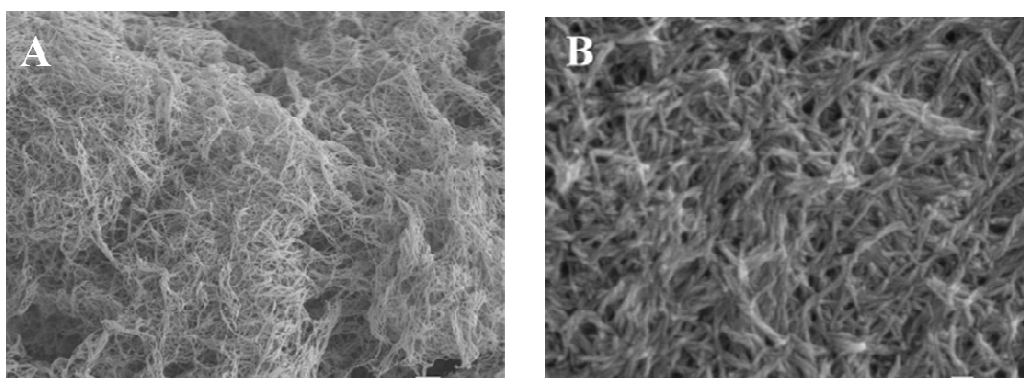
Fig.3.1.6 Cryo-SEM (A) and SEM (B) of a dendritic gel in bromobenzene. The length of the white bar is 100 nm for micrograph A and 1 μm for B (adapted from Ref.[14]).

Furthermore, gel phases could be examined with polarized optical microscope (POM), similarly to liquid crystalline phases. Although there are only few examples of supramolecular gels POM images,[15-17] these materials could show birefringent textures indicating an anisotropic arrangement of molecules and of their aggregates (Fig.3.1.7).
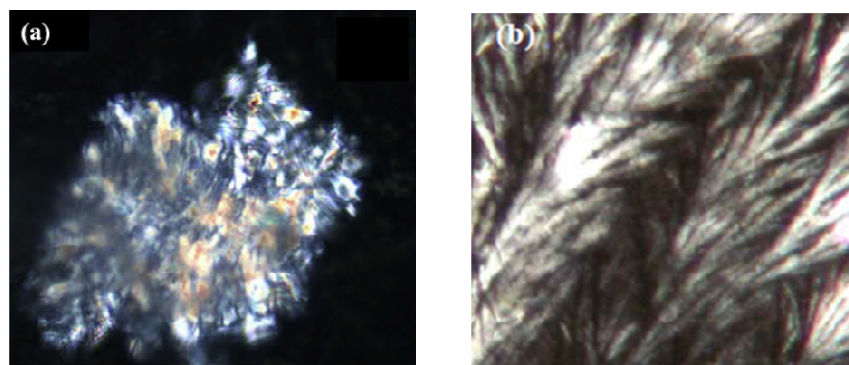
Fig.3.1.7 POM images of an alanine-derivative organogel (a)[17] and a tripeptide-based hydrogel (b).[16]

3.1.2.4 Differential scanning calorimetry (DSC)

DSC is a useful technique to analyze the response of a physical gel to temperature variations. This method has been used to determine the thermal stability and thermoreversibility of the sol-gel transition in many gel phases. Usually, in a DSC curve the gel-sol transition appears as an endothermic peak, whereas an exothermic peak can be monitored during the sol-gel transition. The integration of these peaks provides the direct measure of the phase-change enthalpy ($\Delta H_{gel-sol}$).[18,19] For example, Sundararajan *et al.* investigated the sol-gel transition of organogelators based on octadecyl carbamates with alkyl side chains of different lengths through DSC experiments.[19] The DSC heating curve of the carbamate gelator $C_{18}H_{37}(NHCOO)C_8H_{17}$ (alkyl chain of 8 carbon atoms) exhibits an endothermic peak ($\Delta H = 6.1$ J/g) due to the transition from gel to solution, whereas the DSC cooling curve exhibits an exothermic peak ($\Delta H = -5.8$ J/g) due to the transition from solution to gel (Fig.3.1.8). The transition temperature from gel to solution was found to be 8-10 °C higher than that from the solution to gel. Repeated heating and cooling showed similar transition behaviour, indicating thermoreversibility of the sol-gel transition in this gel.
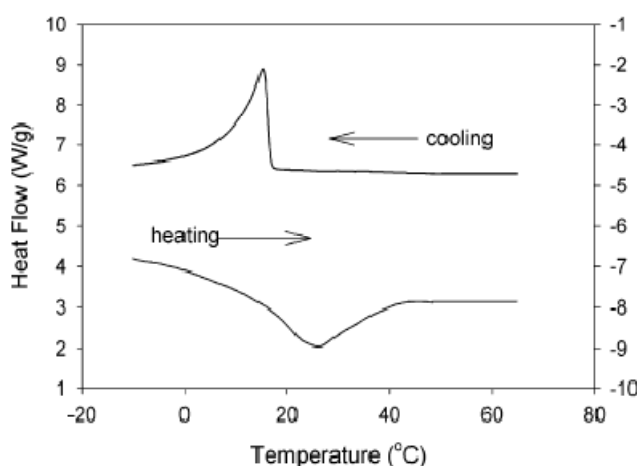
Fig.3.1.8 DSC curves of an octadecyl carbamate gelator (from ref.[19])

3.1.2.5 X-ray techniques

Wide Angle X-ray Scattering (WAXS) is frequently used in order to check the possible presence of an ordered structure within the gel. However, since a gel is mainly composed by a liquid, the interpretation of its XRD pattern is not straightforward, due to a strong interference of the liquid part. Therefore, the XRD analysis of these materials is often carried out on the dried samples, thus in the corresponding xerogels. This means that results must be treated with care, as samples drying could induce some morphological

changes, but it is commonly assumed that these variations are negligible. The indexation of gels/xerogels XRD patterns has led to the identification of well-organized supramolecular structures, usually characterized by lamellar[20,21] or columnar[22] packing mode, as liquid crystals (Fig.3.1.9). Usually, the organization of molecules in the gel/xerogel phase differs from the one in the solid-state, with just few exceptions.[19,23]
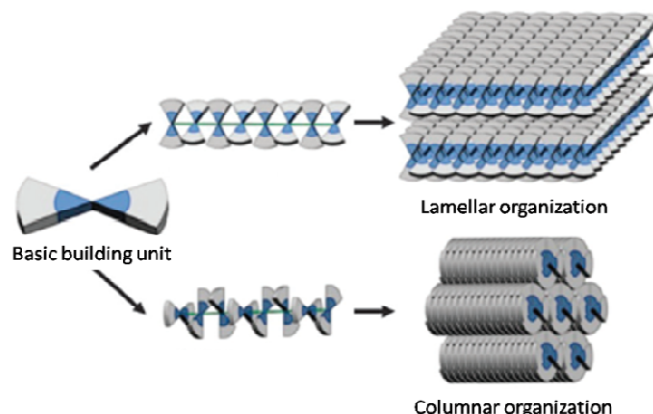
Fig.3.1.9. Schematic representation of the lamellar and columnar organizations in a supramolecular gel (adapted from Ref.[24]).

Small Angle X-ray Scattering (SAXS) can be employed in the characterization of supramolecular gels. Important parameters of the aggregates, such as maximum intermolecular distance, size, shape and the packing mode, can be extracted from SAXS profiles. For example, by a SAXS experiment, Shinkai *et al*. studied the supramolecular arrangement of a sugar-appended organogelator in its gel phase at different temperatures.[23] Below T_{gel} SAXS profile exhibits a lattice scattering, indicating that an ordered lattice is present in the gel state (Fig.3.1.10). For hexagonally packed cylinders, the lattice peak position for the Miller index of (k,l) is given by:

$$q_{kl} = 2\pi a^{-1}(2/\sqrt{3})\sqrt{k^2 + kl + l^2}$$ eq. 3.1.1

where q_{kl} is the peak position corresponding to (k,l) and *a* is the distance between the nearest adjacent lattices. Considering the quite-perfect accordance between peaks positions in the SAXS profile and the values calculated through equation 3.1.1, they demonstrated that the gelator and the solvent (xylene) molecules cooperated generating hexagonally packed fibrils.
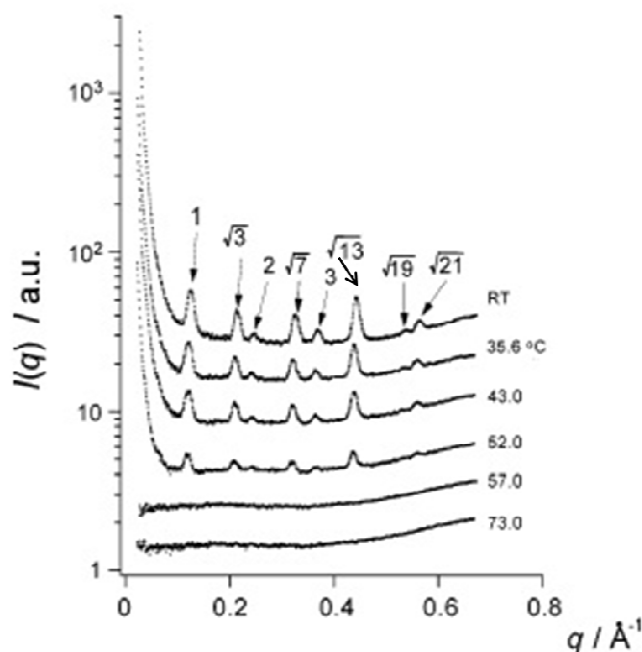
Fig.3.1.10 SAXS profiles of a sugar-appended organogel at different temperatures. The numbers attached to the peaks show the values of the square root in eq.3.1.1 (adapted from ref.[23])

3.1.2.6 Rheology

The mechanical behaviour of a gel can be investigated through rheometry. By using this technique, the elastic modulus (G'), which is defined as the ability of a material to regenerate its initial shape upon deformation, and the elastic loss modulus (G''), designated as the ability of the material to flow under stress, can be determined under oscillatory shear. These parameters serve as an indication of some potential applications of supramolecular gels, in particular for self-healing materials.[25]

3.1.3 The design of a supramolecular gelator

Physical gelation of a solvent is a very sensitive process, which depends on the delicate balance between the dissolution and the aggregation of gelator molecules. Indeed, nowadays it is commonly accepted the principle whereby, in order to achieve gelation, the gelator molecules must be partially soluble in the selected solvent, but not too soluble,

otherwise a solution may eventually be obtained; at the same time the gelator must be partially insoluble in this solvent, but not too insoluble, otherwise precipitation may occur. Thus, the design of a gelator is a challenging and difficult task and relies on the correct balance between its hydrophylicity and hydrophobicity, which can be achieved for example introducing into the molecule skeleton several functional groups able to form multiple noncovalent interactions.[8] Many structural motifs with the ability to generate supramolecular gels have been identified, including lipids, peptides, carbohydrates, etc. For example, Sodium Deoxycholate (SDC), a bile salt with a rigid steroid structure (Fig.3.1.11), creates a biocompatible hydrogel through the formation of a three dimensional network of helical aggregates.[26]
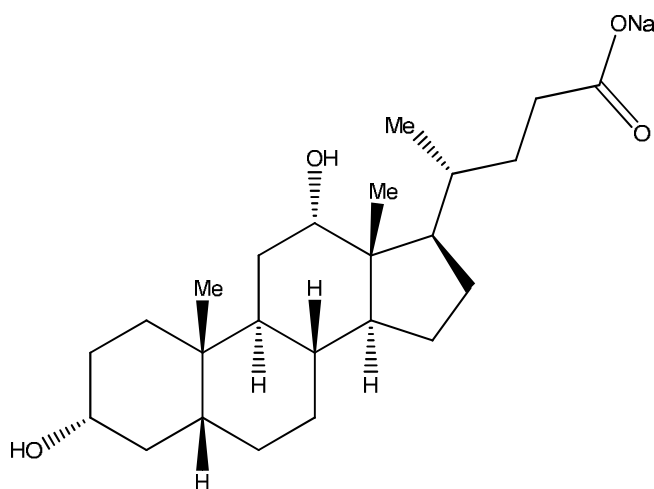
Fig.3.1.11 Chemical structure of SDC gelator (from Ref.[26]).

Similarly, using natural derivative products known to gelate different solvents, Bhattacharya synthesized tetrameric sugar derivatives containing azobenzene core, capable of gelate water at very low concentration and very stable to pH variations (Fig.3.1.12).[27] Employing UV-vis and FTIR spectroscopies he demonstrated that the driven force for gelation is the combination of the π-π stacking of the azobenzene groups and the hydrogen bonding of the sugar groups.
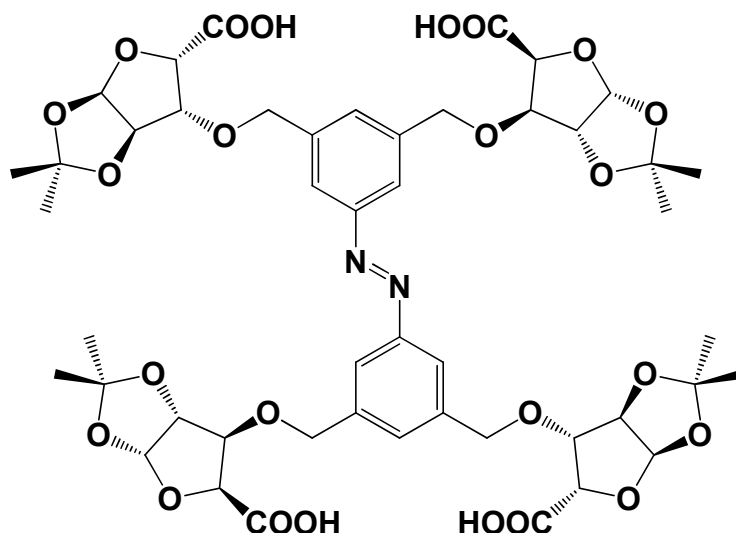
Fig.3.1.12 Chemical structure of a tetrameric sugar derivative containing azobenzene core able to gelate water (from Ref.[27]).

Also, N-protected amino acids bearing aromatics groups have been exploited as low molecular weight hydrogelators. An example is Fmoc (fluorenylmethyloxycarbonyl)-protected pentafluorophenylalanine (F_5-Phe) which self-assembles into entangled fibers in water via hydrophobic interactions involving the aromatic groups (Fig.3.1.13).[28]
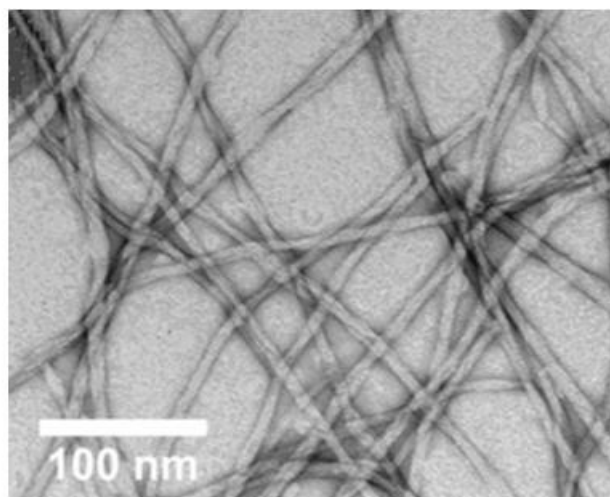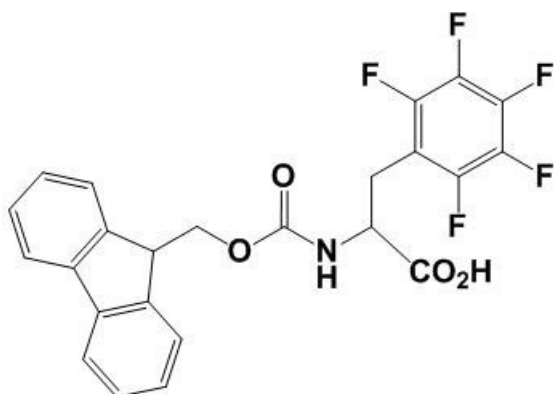
Fig.3.1.13 Chemical structure of Fmoc protected F_5-Phe and TEM micrograph of its gel phase in water (adapted from Ref.[28]).

Even the urea and bisurea functionalities have been introduced in many molecules in order to induce the formation of a physical gel in water. These chemical groups provide sites for strong hydrogen bonds and the possibility of a 1D growth of their aggregates.[21]

Although considerable progress have been made in the gel design area, gelators are often discovered serendipitously.[29,30]

3.1.4 A special class of gel: Supramolecular Metallogels

Among supramolecular gels, a special class known as metallogels has received particular attention over the last few years. The term metallogel is generally referred to gel incorporating metal ions. The presence of metal ions in the gel network can introduce new interesting properties, such as catalytic, redox, optical and magnetic properties. Metallogels can be classified into two main categories: gels in which the metal atom acts as a linker between ligands, inducing the formation of a coordination metallopolymer, and gels in which the metal atom is part of a discrete metal complex. In the former class, the metal-ligand interactions are the primary force in the formation of 3D gel networks, which consist of metal ions spaced by organic bridging ligands.[5] The commonly used ligands are multidentate, thus they display the ability to link together two metal ions. A metallopolymer usually does not exhibit a reversible sol-gel transition and once it is prepared, it cannot be redissolved,[31] as recently reported by Maitra *et al.*, who described the formation of a thermo-irreversible metallo-hydrogel by the addition of Indium ion ($InCl_3$) to sodium cholate (Na-Ch) and sodium deoxycholate (Na-DCh) solutions (Fig.3.1.14).[32]
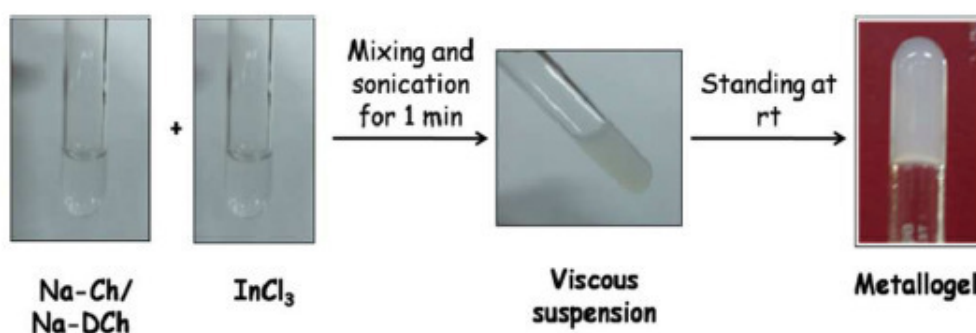
Fig.3.1.14 Preparation of a thermo-irreversible Indium metallogel (from Ref.[32]).

In the second class, the metal atom is part of a coordination complex and usually is not directly involved in the formation of the 3D gel matrix. Since the complex molecules self-assemble through hydrogen bonds, van der Waals forces, π-π interactions, etc., these metallogels are effectively physical gels.

The rational design of metallogelators is subject to the same rules as the design of supramolecular gelators and then presents the same difficulties. The general synthetic approach entails the introduction of functional groups able to form multiple intermolecular weak interactions.

For example, Kishimura *et al.* synthesized a trinuclear Au(I) pyrazolate complex bearing long alkyl chains (Fig.3.1.15).[22] This complex is able to self-assemble in hexane through the van der Waals forces exerted by the octadecyloxy chains coupled with Au(I)-Au(I) metallophilic interactions, generating a supramolecular gel consisting of rectangular columns.
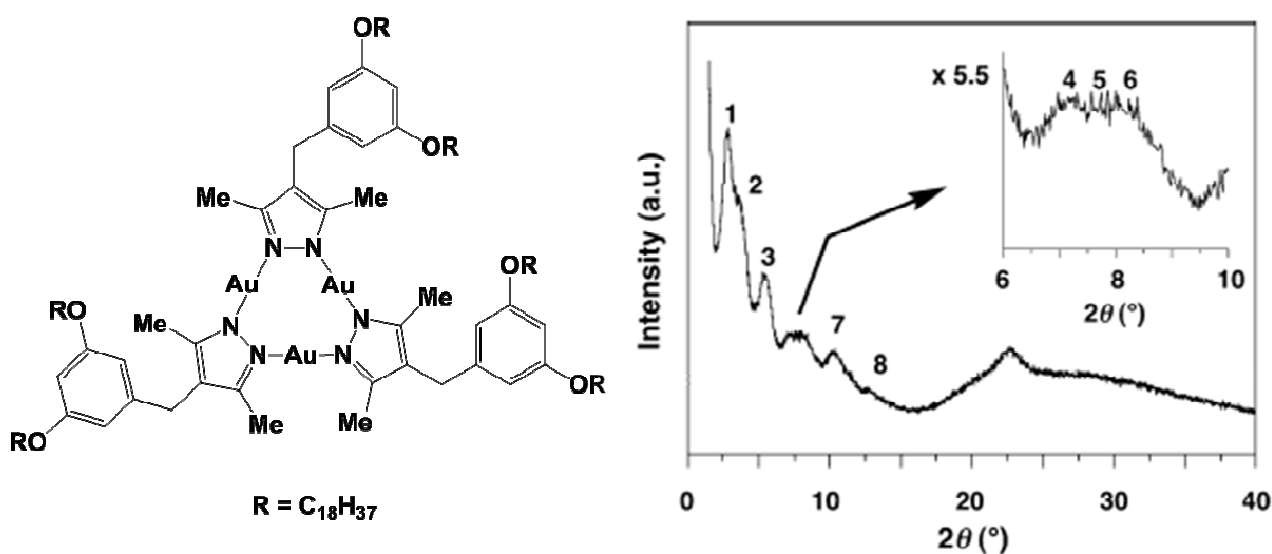
Fig.3.1.15. Chemical structure of a gold(I) metallogelator and the PXRD pattern of its xerogel. The observed peaks were indexed as a 2D columnar system with rectangular *c2mm* symmetry.[22]

Zhang *et al.* reported the synthesis of metallohydrogelator consisting of a Ru(II) tris-bipyridine complex incorporating a tripeptide derivative.[15] This molecular motif is able to promote the self-organization in water of the complex via π-π stacking between the phenyl and/or naphthyl groups, and via hydrogen bonds formed by amide groups and hydroxyl groups. These interactions allow the supramolecular chains to hold a considerable amount of water, producing a luminescent and birefringent gel (Fig.3.1.16).
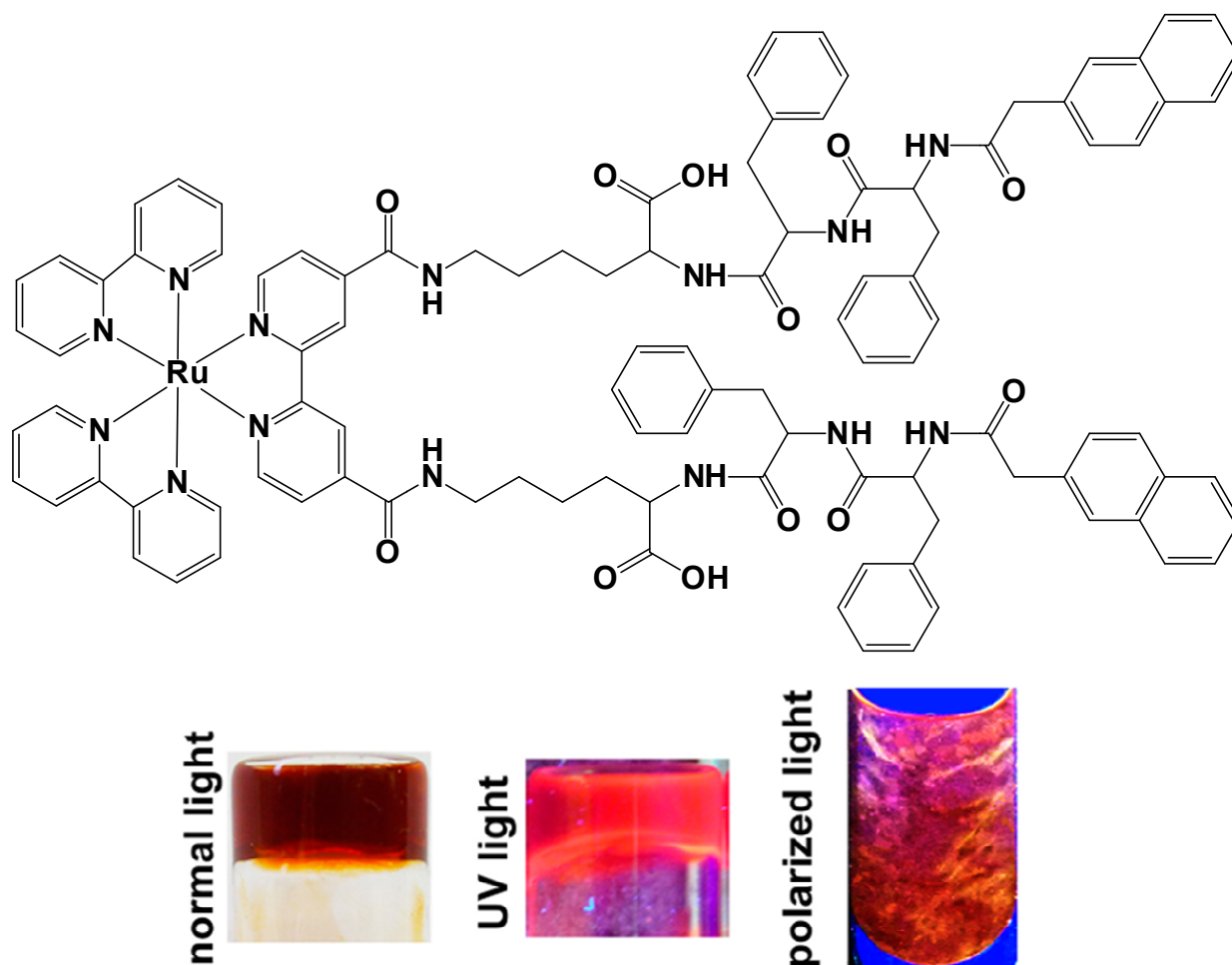
Fig.3.1.16. Chemical structure of a tripeptide functionalized [Ru(bpy)₃]²⁺ and images of its hydrogel phase under normal light, UV light and polarized light (adapted from ref.[15]).

As previously mentioned, another functional group favouring gelation is urea and it has been exploited by Steed *et al*. for the preparation of some Pt metallogelator (Fig.3.1.17).[33] In these Pt(II) complexes, the metal atom is bound to pyridine-based ligands bearing urea motifs and dodecyl chains. The gelation of many organic solvents (xylene, toluene, chloroform) is achieved through several noncovalent interactions, such as intermolecular bonding of the urea moieties, van der Waals forces among the alkyl chains, π-π interactions involving the pyridyl rings and Pt-Pt interactions, which contribute synergistically to the formation of a network of entangled fibers.

m = 0, 1, 3
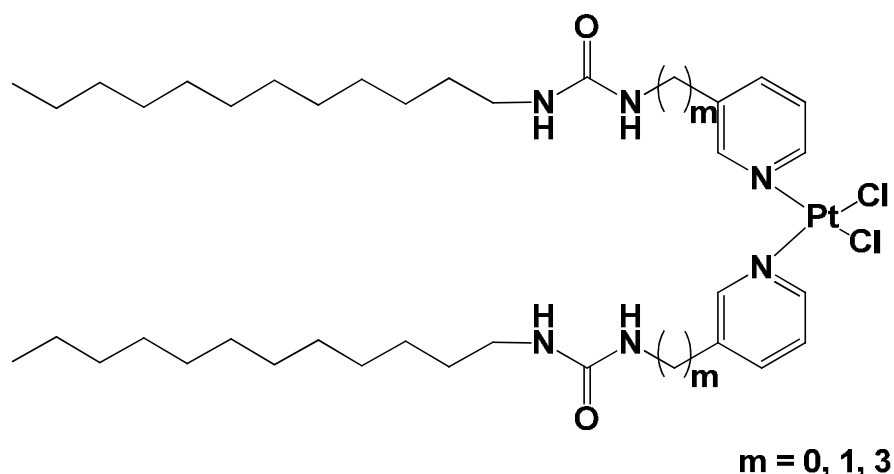
Fig.3.1.17 Chemical structure of some Pt(II) metallogelators. [33]

Supramolecular metallogels have also been obtained using cholesterol-appended ferrocene derivatives.[34] The use of steroids is a well-known expedient to induce gelation of several solvents[35] and, in this case, the additional presence of amide groups strengthens the gel scaffold through the instauration of hydrogen bonds.

3.1.5 Applications of supramolecular gels

Supramolecular gels are promising materials with potential applications in many fields, mainly depending on the special features displayed by the gelator molecules constituting the gel matrix.

Physical gels can find application in photovoltaic and light-emitting devices, as light-harvesting and energy transfer materials, since these phenomena are affected by supramolecular organization of donor and acceptor molecules and could benefit from an almost fixed and ordered spacing between them. In this regard, organogels based on some oligo(phenylenevinylene)s derivatives (OPV), wherein Rhodamine B was dispersed, provide an efficient donor-acceptor system.[36] This system displays an effective fluorescence-resonance energy transfer (FRET), which disappears upon heating as a consequence of the gel matrix collapse.

Another attracting feature of supramolecular gels is their possible use as medium for crystal growth.[33] The high viscosity of these materials allows to slow down the diffusion of substrates and the local ordering of gel fibers could be transferred to the growing crystal. Biocompatible hydrogels are also interesting candidates for drug delivery systems[37] and for biomaterials to use in regenerative medicine.[38]

Among all the potential applications of supramolecular gels, their most intensively exploited uses are as sensing agents and templating agents. These two employments of physical gels are briefly described in the following paragraphs.

3.1.5.1 Sensing agents

The noncovalent nature of the interactions between molecular building blocks, responsible for the formation of the gelator 3D arrangement, makes the sol-gel transition thermally reversible, therefore supramolecular gels are appealing materials for thermosensing applications, for example taking advantage of a colour change. Indeed, Kimizuka reported the preparation and characterization of organogels derived from lipophilic Co(II)-1,2,4-triazole complexes (Fig.3.1.18).[39] A blue gel phase is formed at room temperature and displays the characteristic color of cobalt (II) in the tetrahedral coordination. Unlike most gel phases, a pale pink solution is obtained upon cooling, pointing out the conversion to the octahedral geometry. On this premise, these gels proved to be interesting thermoresponsive materials.
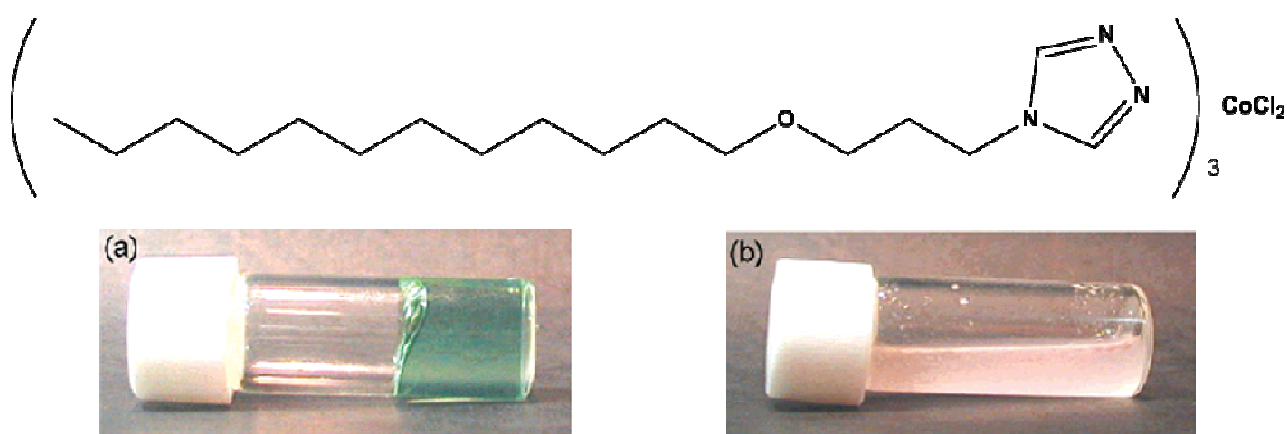
Fig.3.1.18 Chemical structure of a metallogelator based on a Co(II) triazole complex. Images of the complex in chloroform: (a) a blue gel-like phase at 25 °C; (b) a pale pink solution at 0 °C (from ref.[39]).

Supramolecular assemblies retain the chemical and physical properties of the starting gelator molecules, hence the incorporation of a gelator motif into a specific molecule can lead to smart materials that respond to several external stimuli, such as pH,[40] gases and ions,[41] light,[42] oxidation/reduction,[15] etc.

For example, a yellow organogel of an asymmetric bisphenazine turns into a red solution upon addition of a small amount of an acid, demonstrating to be a pH responsive material (Fig.3.1.19).[40]
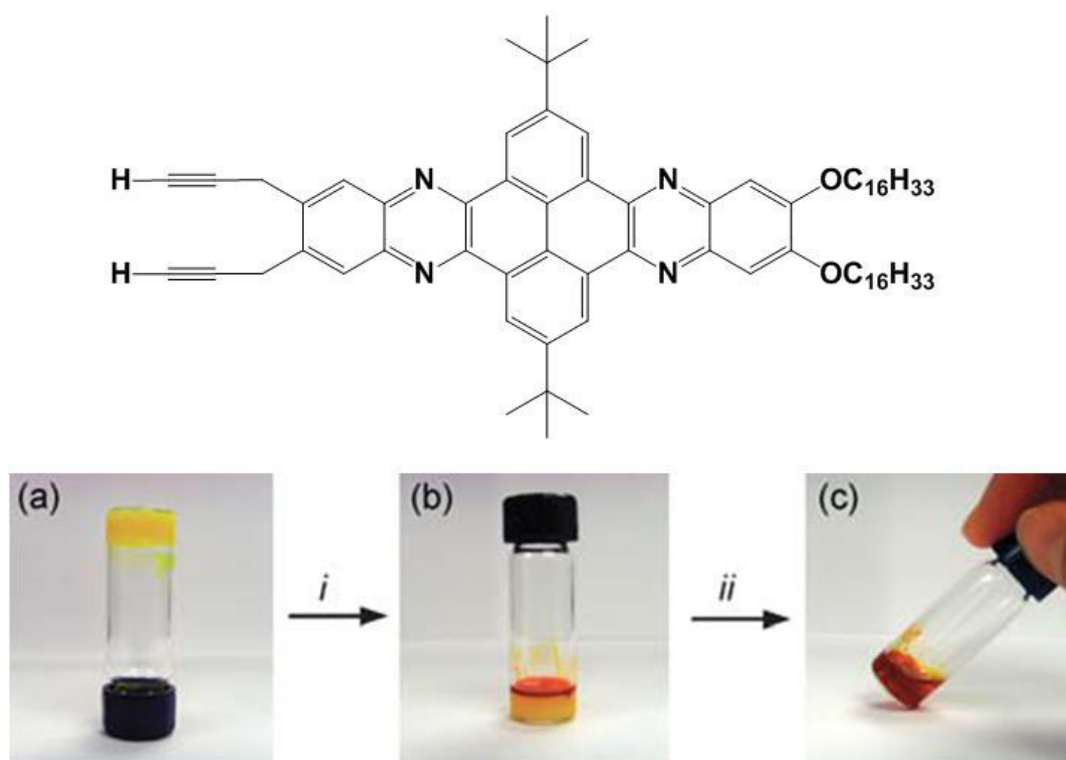
Fig.3.1.19 Chemical structure of an asymmetric bisphenazine organogelator and images of: (a) its yellow gel phases in 1,1,1-trichloroethane, (b) immediately after the addition of one drop of trifluoroacetic acid, and (c) the red solution formed 4h after the addition of trifluoroacetic acid (from ref.[40]).

The observation of the sol-gel transition could be also a useful method to visually monitor the presence of some substances, such as anions and CO_2.[41]

In addition, a multistimuli responsive supramolecolar gel have been described by Liu and coworkers.[42] The gelator (Azo-G3) has a dendritic structure, incorporating an azobenzene group as photoresponsive motif. This molecule is able to gelate most of the organic solvents through heating-cooling cycles and, unexpectedly, it gelates also some polar solvent as a response to a sonication treatment. Furthermore, the sol-gel transition could be triggered by light: UV irradiation induces the disruption of the gel fibrous network, by photoisomerization of the azobenzene motif from trans-to-cis isomer, generating a

solution; this solution could turn again into gel-phase via visible light irradiation (Fig.3.1.20).
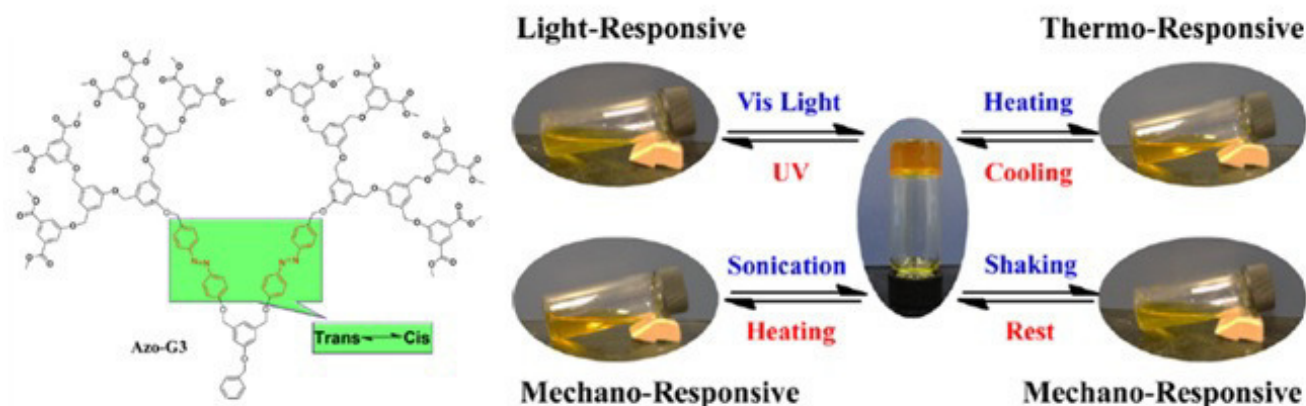
Fig.3.1.20. Chemical structure of the Azo-G3 gelator and its reversible sol-gel transition triggered by several stimuli (from Ref.[42]).

3.1.5.2 Templating agents

Since supramolecular gels exhibit several shapes such as fibers, rods, helices, ribbons or tubes, probably the most promising application of supramolecular gels is their use as templates for nanostructured inorganic materials, because these inorganic nanostructures could resemble the gel network.[43]

SiO_2, TiO_2, ZrO_2, ZnO and WO_3 nanotubes were prepared employing a tripodal-cholamide-based hydrogel.[44] The metal salts precursors were dissolved in a warmed water solution of the gelator, and the mixture was left to rest at room temperature. The metal precursors reacted around the just formed gel fibers, creating metal oxide nanotubes. The gel template was then removed through calcination.

Generally, the gelators used as agents directing the structure of inorganic nanomaterial are positively charged in order to electrostatically attract the negative charged precursors (Fig.3.1.21).
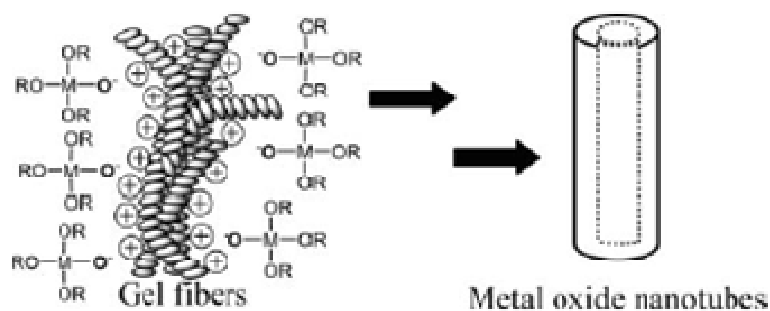
Fig.3.1.21. Schematic representation of metal oxide nanotubes around positively charged gelators(adapted from Ref.[45]).

In addition, metal and metal oxide nanoparticles can be effectively prepared employing a supramolecolar gel scaffold as Structural Directing Agent (SDA).[18,45,46] For example, Hanabusa *et al*. reported the fabrication of TiO_2 nanoparticles using a negative charged L-lysine based organogelator (2) (Fig.3.1.22).[45] On the contrary, employing an uncharged L-lysine gelator (1) they obtained TiO_2 nanotubes of different diameters depending on the solvent used.
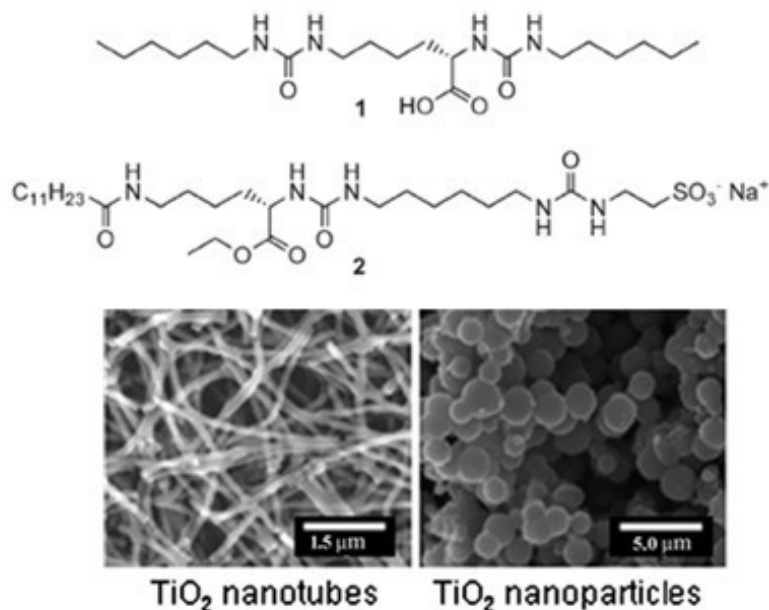
Fig.3.1.22 Chemical structures of L-lys based organogelators. FE-SEM images of TiO_2 nanotubes template with organogel of (1) in 1-buthanol and TiO_2 nanoparticles template with organogel of (2) in 1-buthanol (from ref.[45]).

Finally, metal helical nanowires have been successfully synthesized taking advantage of chiral organogelators; as a result, right- and left-handed metal nanohelices were produced.[47]

However, up to now, to the best of our knowledge, the use of a metallogel as a direct metal source for the synthesis of a metal nanostructured oxides has not yet been reported.

3.1.6 Dedicated reviews on supramolecular gels and metallogels

To emphasize the importance of this research field in material chemistry, the main reviews published in the last 15 years concerning the design, the characterization and the applications of supramolecular gels and metallogels are summarised in table 3.1.1.

TOPIC	TITLE	YEAR	REF.
Design and characterization of hydrogels	Water Gelation by Small Organic Molecules	2003	6
Applications of supramolecular gels	High-Tech Applications of Self-Assembling Supramolecular Nanostructured Gel-Phase Materials: From Regenerative Medicine to Electronic Devices	2008	38
Design, characterization and applications of metallogels	Metal- and Anion-Binding Supramolecular Gels	2010	5
Co-assembling gelators	Supramolecular gels formed from multi-component low molecular weight species	2012	48
Applications of supramolecular gels	Control of molecular gelation by chemical stimuli	2013	49
Design of metallogelators	Metal-organic gels: From discrete metallogelators to coordination polymers	2013	31
Synthesis and properties of metallogelators	Recent advances in metallogels	2013	50
Characterization of physical gels	Characterization of supramolecular gels	2013	7
Design and application of organogelators	Functional π- Gelators and Their Applications	2014	51
Design and applications of supramolecular gels	Multistimuli-Responsive Supramolecular Gels: Design Rationale, Recent Advances, and Perspectives	2014	52
Design of metallogelators	Metallogels from Coordination Complexes, Organometallic, and Coordination Polymers	2016	53

Table 3.1.1 The main reviews concerning supramolecular gels and metallogels.

3.2 Metallo-hydrogels based on Ir(III) complexes

A large proportion of the research work described in this thesis was devoted to the synthesis and characterization of some Iridium (III) complexes with the ability to self-assemble in water. The compounds described herein are Ir(III) octahedral ionic complexes, embedded with hydrophilic counterions, and they are able, in defined ranges of concentrations, to form supramolecolar metallo-hydrogels.

This work was inspired from the observation of the gel phases formation from the octahedral Ir(III) complexes bearing **ppy** as cyclometalated ligands, **bpy** as ancillary ligands and carboxylate counterions with different alkyl chains.[54] Since the parent complexes **[(ppy)$_2$Ir(bpy)]X** (X=Cl$^-$, PF$_6$$^-$)[55] are insoluble in water and also unable to self-organize into supramolecular structures, clearly the nature of the counteranion plays an important role into the self-assembly property of the compound. Indeed, carboxylate anions are non-innocent motifs that can strengthen a supramolecular assembly through the formation of hydrogen-bonds, as reported for many physical gels.[56-60]

However, it is worth noting that, despite the Ir (III) complexes described in the previous chapter incorporate acetate as counterion, only **[(ppy)$_2$Ir(dppz)]CH$_3$CO$_2$** and **[(ppy)$_2$Ir(dpq)]CH$_3$CO$_2$** are capable of creating supramolecular organizations, displaying "gel" phases in water. Therefore, a synergy effect between the counterion and the ligands should be involved in the self-assembly properties of this kind of coordination compounds.

As previously reported, the complexes **[(ppy)$_2$Ir(bpy)]X** (X = CH$_3$CO$_2$, C$_2$H$_7$CO$_2$, C$_5$H$_{11}$CO$_2$) are able to self-assemble in water and were defined chromonic-like physical gels.[54] Szerb *et al.* observed the formation of viscous luminescent gels at room temperature and at low concentrations and the appearance of textures similar to chromonic phases studied under polarized optical microscopy. They investigated these supramolecular materials through WAXS, SAXS and SANS, supposing the presence of polyelectrolytic strands which self-organize into a columnar superstructure through non-covalent interaction (Fig.3.2.1). However, a precise classification of these Ir(III) complexes into a definite class of compounds forming supramolecular organization in water was not made unequivocally.
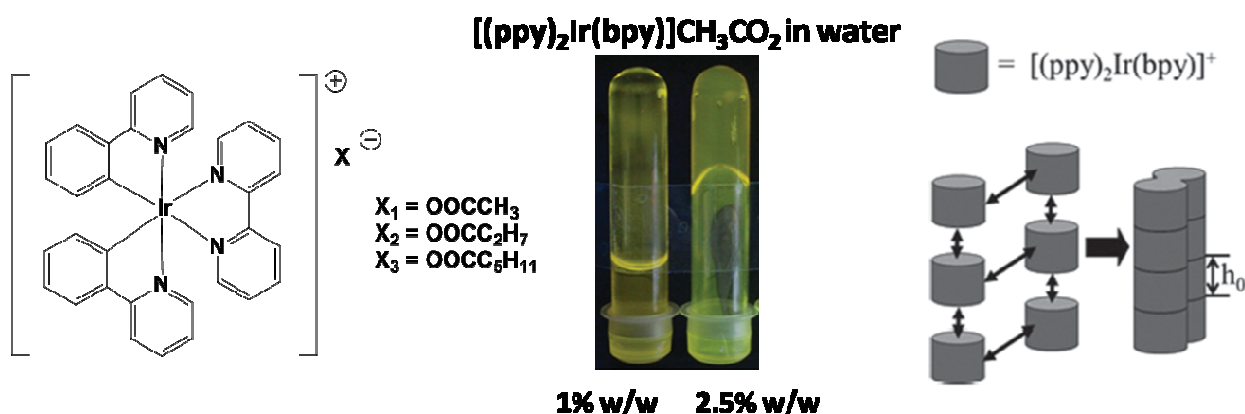
Fig.3.2.1. From the left: chemical structure of Ir(III) octahedral ionic complexes bearing carboxylates as counterions; test-tube experiment of the gel-like phase originated from **[(ppy)₂Ir(bpy)]CH₃CO₂** in water; the supposed organization of these Ir (III) complexes in the gel-like phase.[54]

During the course of this thesis, Szerb *et al*. reported the rheological investigation of the complex **[(ppy)₂Ir(bpy)]CH₃CO₂** together with the synthesis and characterization of the analogous **[(ppy)₂Ir(phen)]CH₃CO₂** bearing 1,10-phenanthroline (**phen**) as ancillary ligand.[61] The ability to generate birefringent supramolecular structures was also proved for the latter complex (Fig.3.2.2). Moreover, they reported through rheological study, that increasing the aromaticity of the N^N ancillary ligand, passing from **bpy** to **phen**, leads to the formation of smaller and more symmetrical shape aggregates.
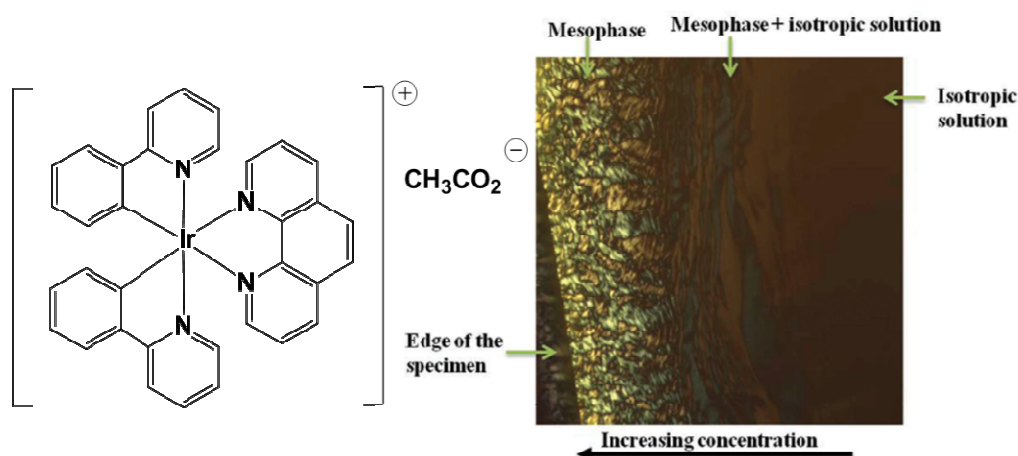
Fig.3.2.2. Chemical structure of **[(ppy)₂Ir(phen)]CH₃CO₂** and its birefringent textures in water at r.t. in concentration gradient observed under POM.[61]

Noteworthy, the replacement of the N^N aromatic ancillary ligand **bpy** from the cationic motif **[(ppy)₂Ir(N^N)]⁺** by ethylenediamine (**en**) or 2-picolylamine (**pam**) yielded water

soluble complexes, **[(ppy)₂Ir(en)]CH₃CO₂** and **[(ppy)₂Ir(pam)]CH₃CO₂** respectively, that are unable to self-assemble into organized superstructures (Fig. 3.2.3).[62] The loss of the self-assembling ability in these complexes, can be explained by the high increase of their water-solubility, considering that, as explained in paragraph 3.1.1, in order to achieve gelation, there must be a precise balance between solubilization and phase separation.

[(ppy)₂Ir(en)]CH₃CO₂
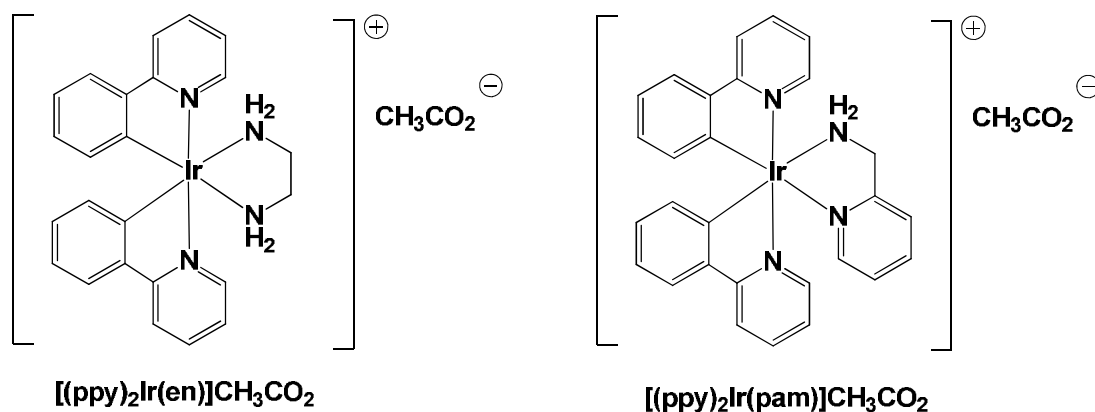
[(ppy)₂Ir(pam)]CH₃CO₂

Fig.3.2.3. Chemical structure of **[(ppy)₂Ir(en)]CH₃CO₂** and **[(ppy)₂Ir(pam)]CH₃CO₂**.[62]

Within this context, it is therefore not surprising that the Ir(III) complexes **[(ppy)₂Ir(dpq)]CH₃CO₂ (10)** and **[(ppy)₂Ir(dppz)]CH₃CO₂ (12)**, whose synthesis has been described in the previous chapter, were found to form supramolecular assemblies in water, both presenting a further increase in the aromaticity of the ancillary ligands with respect to the analogous complexes bearing **bpy** and **phen**. The self-assembling properties in water of the compounds **10** and **12** were investigated through several experimental techniques, including POM, TEM, PXRD and DSC in order to get a deeper insight on the supramolecular architecture of the gel.

3.2.1 Supramolecular phase of [(ppy)₂Ir(dpq)]CH₃CO₂

The Ir(III) compound **[(ppy)₂Ir(dpq)]CH₃CO₂ (10)** shows the ability to gelate water in a large well-defined range of concentration from 3% to 14% w/w.
The gel-phases were prepared dissolving the opportune quantity of complexes in warm distilled water. The mixtures were then heated and shaken in a closed tube until clear solutions were obtained. Subsequently, the solutions were slowly cooled down to room temperature. The formation of gel phases was determined through a typical inversion test

tube experiment: tubes of increasing concentration were turned upside down until no flow was observed (Fig.3.2.4).
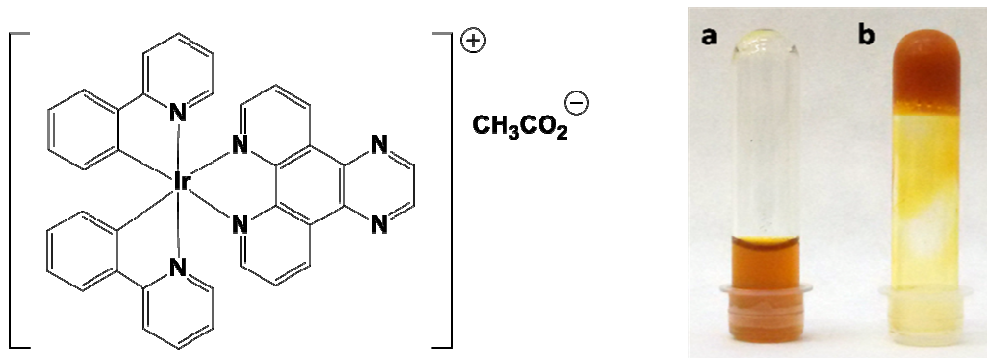
Fig.3.2.4. Chemical structure of compound **10** and the test tube experiments, below (a) and above (b) its critical gel concentration.

3.2.1.1 POM analysis

As reported for the analogous complexes **[(ppy)$_2$Ir(bpy)]CH$_3$CO$_2$**[54] and **[(ppy)$_2$Ir(phen)]CH$_3$CO$_2$**,[61] the water gel phases of compound **10** at different concentrations were observed under a Polarizing Optical Microscope. The samples were placed in closed cells in order to avoid evaporation of the solvent, hence to prevent a change of the gel concentration during observation. Surprisingly, the gel phases at concentrations within the range of 3%-8% w/w presents elongated fibers, already visible through the 10x objective of an optical microscope (Fig.3.2.5_a). Up to now, examples of supramolecular aggregates, in particular gel fibers, large enough to be detected with an optical microscope, have not yet been reported. Indeed, generally, in order to analyze the morphology of supramolecular assemblies, electron microscopy is required. The superstructures observed for the 3%-8% w/w gel phases of **[(ppy)$_2$Ir(dpq)]CH$_3$CO$_2$** are birefringent and appear as a tangle of wires (Fig.3.2.5_c and.3.2.5_d). Furthermore, these birefringent fibers acquire great mobility and start to flow upon heating (Fig. 3.2.5_e), until the temperature of *ca*. 45°C has been reached. At this temperature these aggregates disappear and a liquid isotropic phase is observable. Lastly, a subsequent cooling of the specimen leads to the reappearance of the birefringent fibers, which self-organize in structures resembling braided hair (Fig. 3.2.5_f).
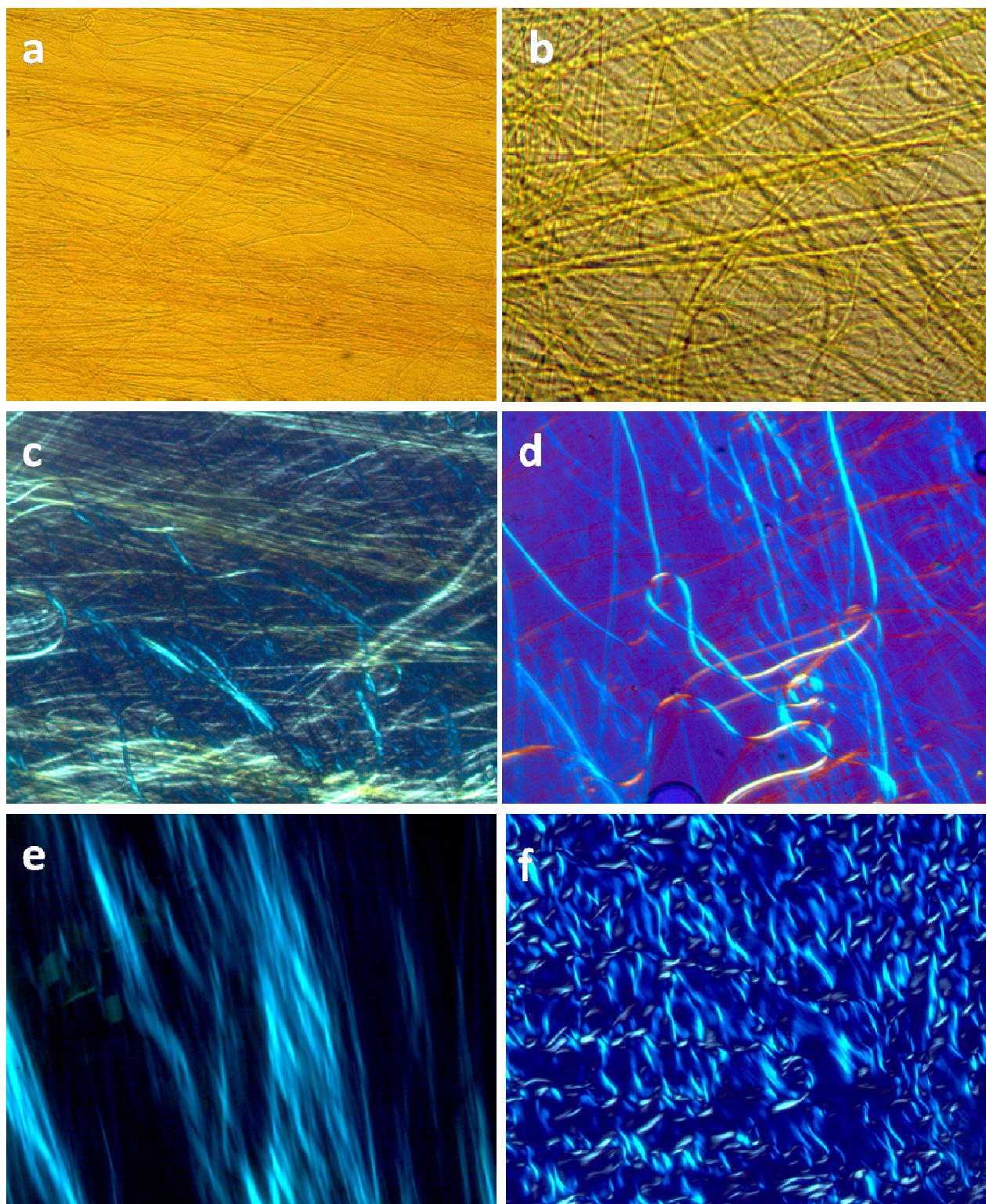
Fig.3.2.5. POM micrographs of the gel phases originated by **[(ppy)₂Ir(dpq)]Ac** in water: (a) 3% w/w, r.t., 10x microscope objective (MO); (b) 3% w/w, r.t., 50x MO; (c) 3%w/w, r.t., 20x MO; (d) 6% w/w, r.t., 20x MO; (e) 4% w/w, 37°C, 20x MO; (f) 4% w/w, 28°C, 20x MO. Images **c, d, e** and **f** were acquired between two crossed polarizators.

Furthermore, the gel phases of **[(ppy)$_2$Ir(dpq)]CH$_3$CO$_2$ (10)** in the range of concentrations between 9% and 14% w/w, exhibit intense and homogeneous birefringent textures under POM (Fig.3.2.6_a). The most concentrated gel phase (14% w/w) was selected as example and its POM micrographs are reported in Fig.3.2.6. In these 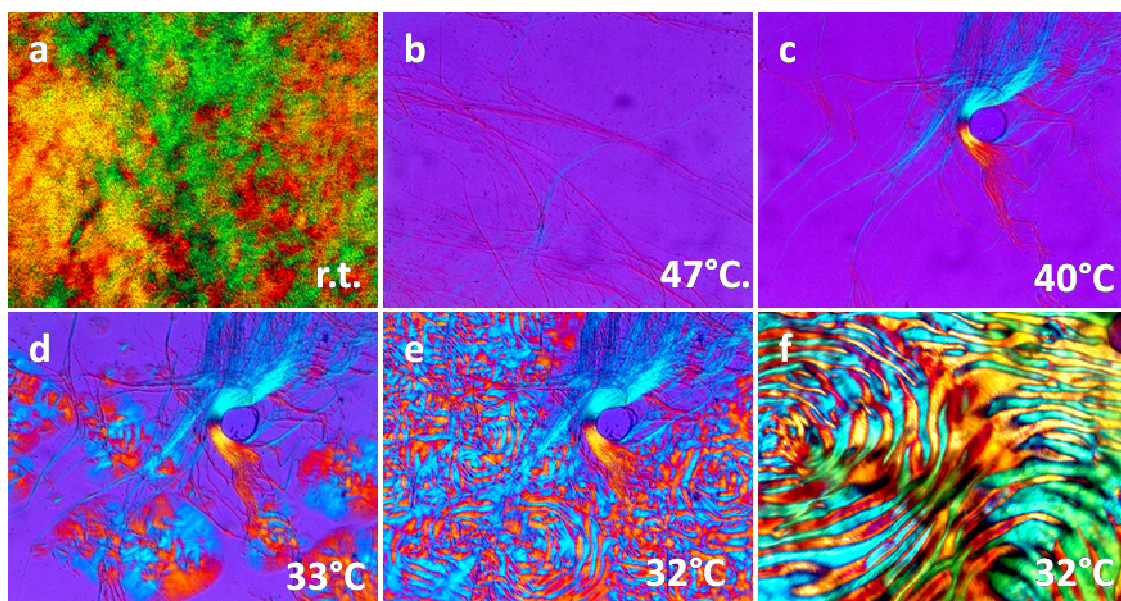most concentrated samples, the supramolecular fibers are no longer visible at room temperature. This could be explained considering that in these highly viscous specimens the superstructures are too close and packed together to be clearly distinguished. However, the presence of these supramolecular wires was confirmed by their appearance upon heating (Fig.3.2.6_b). Indeed, the birefringent texture of the 14% w/w gel phase disappears at *ca.* T = 47°C (T$_i$, isotropic transition temperature), indicating the transition from the gel phase to the sol state, thus the achievement of the isotropic condition. However, during the texture vanishing, the birefringent fibers become well visible and persist in the sample up to the temperature of 49°C, after which they fade. Upon cooling, at *ca.* 40°C the re-assembly of the molecules into wires occurs (Fig.3.2.6_c), and, by continuing to reduce the temperature, a new birefringent tiger-skin texture emerges at 33°C (T$_{gel}$, temperature of gelation) (Fig.3.2.6_d), which becomes gradually more defined (Fig.3.2.6_e and Fig.3.2.6_f). Furthermore, a second heating-cooling cycle was performed in order to better investigate the anisotropic arrangement of molecules in these samples. During this second increase of temperature, the same trend experienced during the first cycle was observed, thus at *ca.* 47°C the texture dissolving occurred, followed by the disappearance at *ca.* 49°C of the wires. In the course of the second cooling, at first the birefringent fibers appear (Fig.3.2.6_g) which gradually enlarge themselves (Fig.3.2.6_h) and which are evident also without the crossed polarizers (Fig.3.2.6_i). However, surprisingly, a focal conic fan texture started to form in some regions of the sample (Fig.3.2.6_k), becoming well-defined by leaving the sample to rest at room temperature (Fig.3.2.6_j and Fig.3.2.6_l).

Since focal conic fan textures have been reported for several of discotic liquid crystals,[63-66] a two-dimensional columnar organization of the molecular building blocks in the concentrated gel phases of **[(ppy)$_2$Ir(dpq)]CH$_3$CO$_2$**, can be assumed.

Fig.3.2.6. POM micrographs of the 14% w/w gel phases originated by **[(ppy)₂Ir(dpq)]CH₃CO₂** in water: (a) r.t; (b) first heating, 47°C; (c) first cooling, 40°C; (d) first cooling, 33°C (e) first cooling, 32°C; (f) magnification of (e); (g) second cooling, 40°C; (h) and (i) second cooling, 40°C, with and without crossed polarizers, respectively; (j) second cooling, 33°C; (k) second cooling, 32°C; (l) second cooling, r.t.

Moreover, similar to lyotropic liquid crystals (LLCs), the dried gel samples, *i.e.* the xerogel, obtained leaving water to evaporate from a gel sample deposited onto a glass slide, do not retain the starting birefringent texture under POM. Indeed, an important feature of lyotropic liquid crystals is the role played by the solvent, which provides fluidity to the system, filling

the space around the compounds. Indeed, a LLC undergoes its phase transitions by adding or removing the solvent. Usually, when solvent is removed from a lyomesophase, the supramolecular architecture can be totally or partially destroyed, in the latter case with just loss of some degree of order, as demonstrated by the signals broadening in the dried-film XRD spectra.[67] Generally, the orientationally order of lyotropic phases, thus birefringence and characteristic diffraction patterns, can be retained in a dried film if the sample in the LC state has been aligned before solvent evaporation.[68,69]

3.2.1.2 PXRD analysis

The PXRD pattern of the gel phase (10% w/w) was acquired between 5 and 50° (2θ). Unfortunately, due to the limitation of the diffractometer that has been used which does not allow to observe the low-angle region of the spectra, the detection of useful reflection peaks in the small-angle region was not possible. Anyhow, the presence of interesting signals in the medium-angle region of the PXRD pattern allowed to determine the supramolecular architecture of the gel-phase. Taking into account the characteristic focal conic fan texture observed under POM, that are often indicative of a columnar mesophase, this system was successfully indexed using LCDixRay program,[70] a recently developed free software for the indexation of PXRD patterns of columnar liquid crystals. The indexation performed suggests a columnar rectangular lattice exhibiting cell parameters of a_r = 18.46 Å and b_r = 28.04 Å, with a *p2mm* space-group. According to the extinction rules governing 2D rectangular lattices, the *p2mm* is the only possible space-group, since the indexation revealed the presence of d_{hk} reflection peaks with odd values both for h and k, ruling out all other possible symmetries.[70] The PXRD spectra, the indexation and the supramolecular model proposed for the gel phase of **[(ppy)₂Ir(dpq)]CH₃CO₂** (10% w/w) are reported respectively in Fig.3.2.7, Table 3.2.1 and Fig.3.2.8.
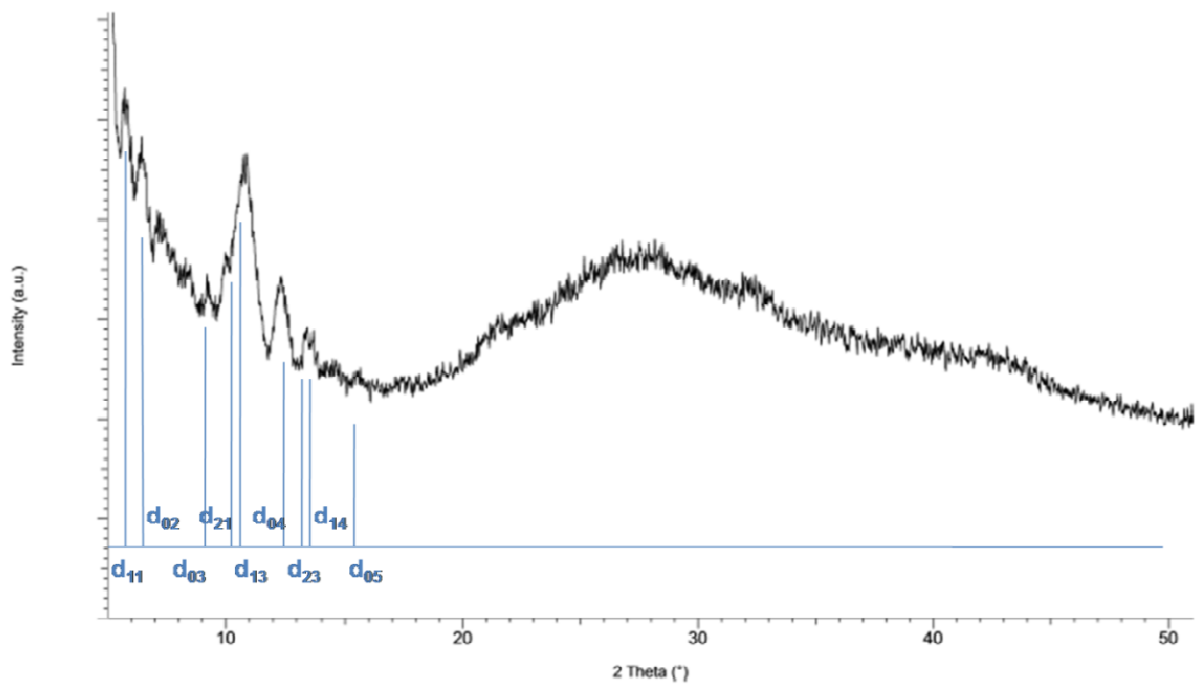
Fig. 3.2.7. PXRD pattern of the gel phase of **[(ppy)$_2$Ir(dpq)]CH$_3$CO$_2$** (10% w/w) with relative indexation.

d_{obs} (Å)	d_{hk}	d_{calcd} (Å)[a]	Cell parameters
15.42	d_{11}	15.42[b]	
14.02	d_{02}	14.02[b]	
9.53	d_{03}	9.35	**Col$_r$**
8.84	d_{21}	8.77	**a_r = 18.46 Å**
8.24	d_{13}	8.34	**b_r = 28.04 Å**
	d_{22}	7.71[c]	
7.17	d_{04}	7.01	
6.57	d_{23}	6.57	
6.55	d_{14}	6.55	
5.65	d_{32}	5.63	
	d_{05}	5.61[c]	

Table 3.2.1. Indexation of PXRD spectra of the gel phase of**[(ppy)$_2$Ir(dpq)](CH$_3$CO$_2$)** [a] Calculated data were obtained using LCDixRay program.[70]   [b] Data chosen for calculations. [c] possible overlapped reflection peaks
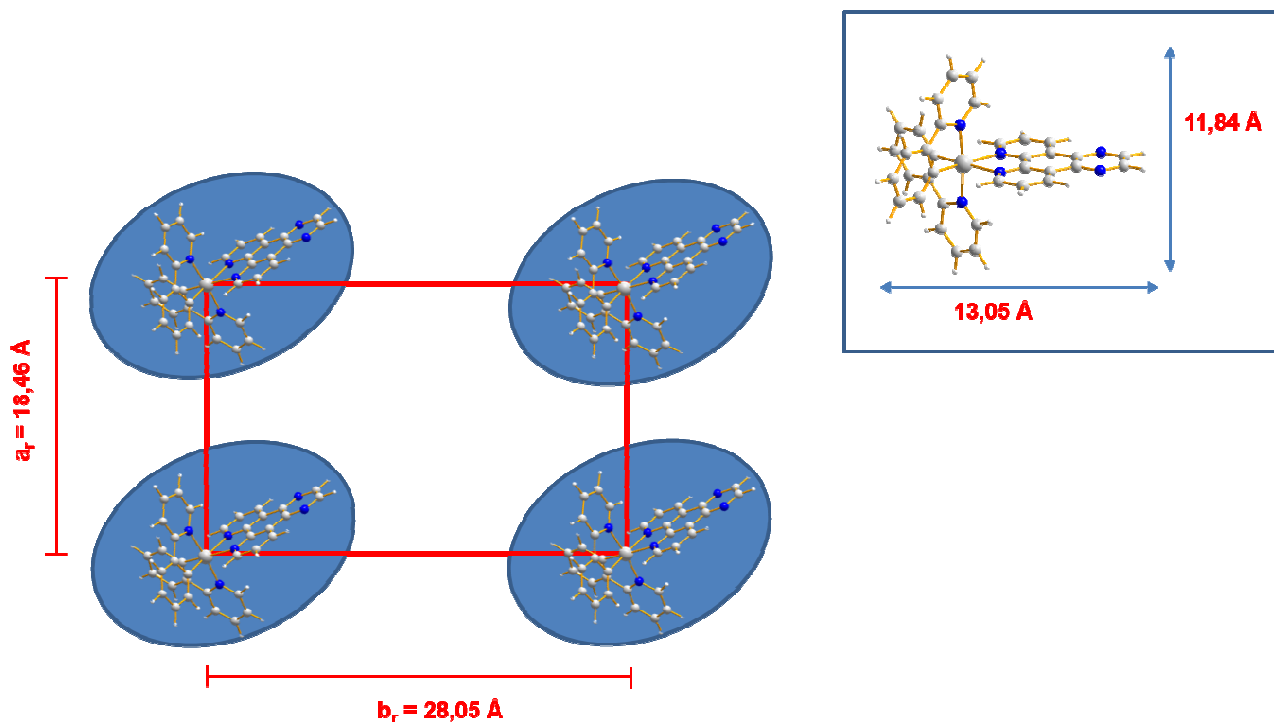
Fig. 3.2.8. Proposed model for the Col_r structure (*p2mm* symmetry) of the supramolecular phase of **[(ppy)$_2$Ir(dpq)]CH$_3$CO$_2$**.

The PXRD analysis performed on the dried gel samples*, i.e*. the xerogel, obtained by leaving water to evaporate from a gel sample cast onto the sample holder of the diffractometer, corroborates the experimental evidences seen under POM observation. Indeed, the PXRD spectra of the xerogel derived from the **[(ppy)$_2$Ir(dpq)]CH$_3$CO$_2$** gel phase (10% w/w) shows the total absence of useful reflection peaks and the presence of broad halos attributable to a completely amorphous material (Fig.3.2.9). The solvent evaporation from the highly organized gel phase leads to the loss of the anisotropic supramolecular architecture, as it is often observed in the case of lyotropic liquid crystals.
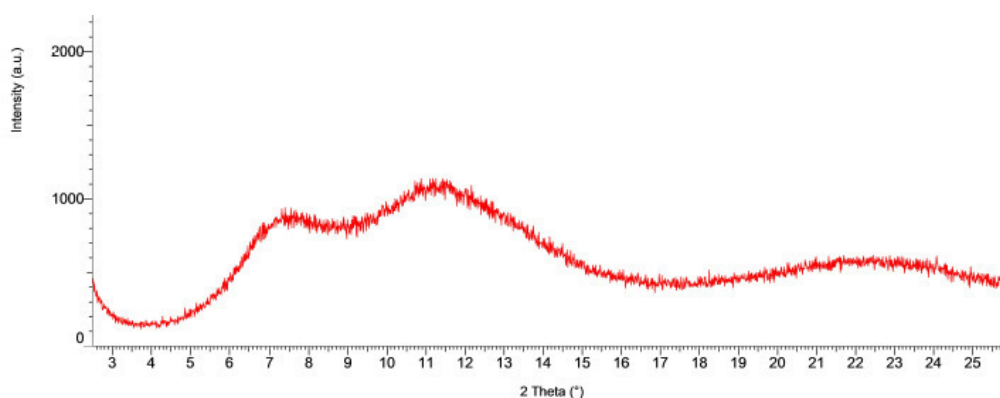
Fig.3.2.9 PXRD patterns of the xerogel derived from the **[(ppy)$_2$Ir(dpq)]CH$_3$CO$_2$** gel phase (10% w/w).

3.2.1.3 Thermal analysis

In order to determine more accurately the thermoreversibility of the sol-gel transition in the supramolecular phases originated by **[(ppy)₂Ir(dpq)]CH₃CO₂** in water, DSC measurements were carried out, both in diluted and concentrated samples. The DSC analysis were performed between 10°C and 60°C, with a scan rate of 5°C/min, in hermetic aluminium pans. Unfortunately, the DSC curves of the diluted 3-10% w/w gel phases do not exhibit any transitions (the DSC curve of the 4% w/w gel phase is reported as example in Fig. 3.2.10). This could be explained considering the small quantity of compound present in these samples with respect to the quantity of water, which probably renders any transition below the detection limit of the instrument.
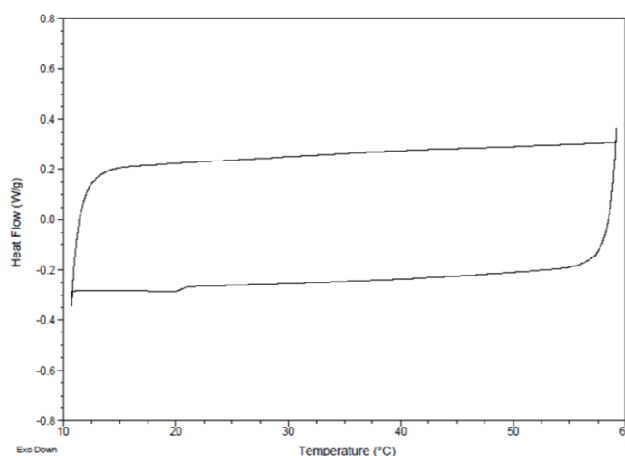
Fig.3.2.10 DSC curve of 4% w/w gel sample of **[(ppy)₂Ir(dpq)]CH₃CO₂**.

However, the DSC curves of the concentrated 11-14% w/w gel phases present well-defined peaks, that can be attributed to the sol-gel transition. The DSC curve of the 14% w/w sample is reported in Fig.3.2.11 as example.
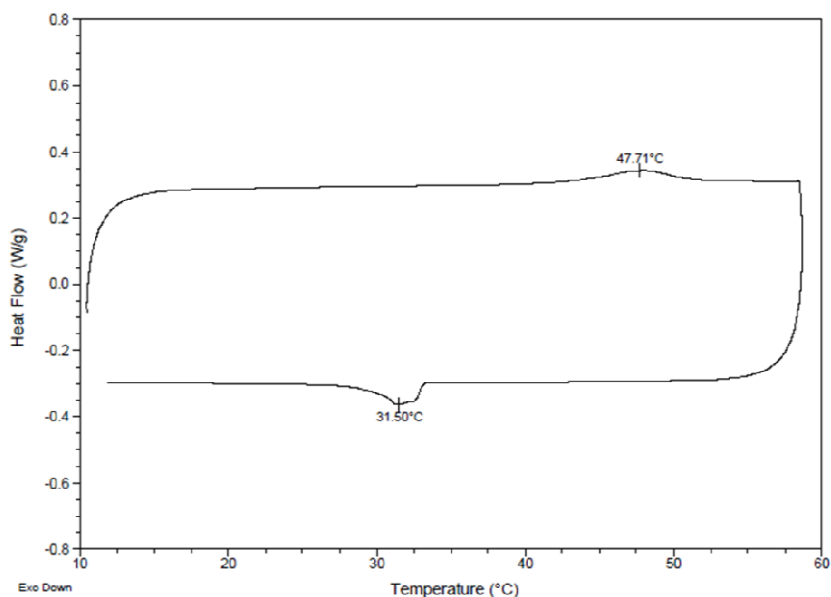
Fig.3.2.11 DSC curve of 14% w/w gel sample of **[(ppy)₂Ir(dpq)]CH₃CO₂**.

The heating DSC curve of the 14% w/w sample shows an endothermic peak, indicative of the gel-sol transition. This peak presents its maximum at *ca*. 47°C, in perfect agreement with the T_i detected through POM observation. The cooling DSC curve shows an exothermic peak, assigned to the sol-gel transition. The peak maximum falls at *ca*. 32°C, once again in accordance with the observation performed through POM. It is worth noting that the two opposite curves present a hysteresis feature, probably arising from the sluggishness of the exothermic transition, as reported for many gel phases[18,19] and for liquid-crystalline phases.[71] Furthermore, the integration of these signals provides the direct measurement of the phase-change enthalpy (ΔH), whose value is *ca.* 2.3 J/g.

The heating-cooling cycles were repeated three times, demonstrating the reversibility of the transitions and the stability of the sample (Fig.3.2.12). Indeed, the three consecutive heating curves and the three consecutive cooling curves are almost superposable, presenting quasi-identical values of the transition temperatures and of the correlated ΔH (Table 3.2.2).
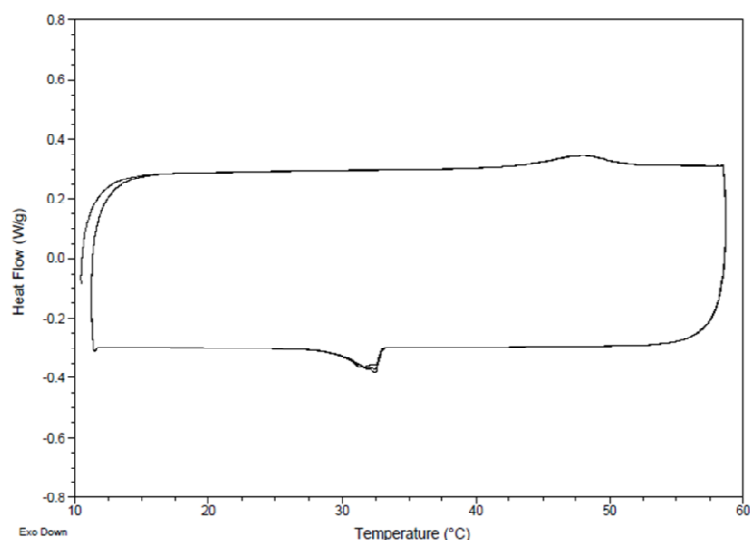
Fig.3.2.12 DSC curve of 14% w/w gel sample of **[(ppy)$_2$Ir(dpq)]CH$_3$CO$_2$**, repeated three times.

CYCLE	T$_{max}$ gel-sol transition (°C)	ΔH gel-sol transition (J/g)	T$_{max}$ sol-gel transition (°C)	ΔH sol-gel transition (J/g)
1	47.71	2.364	31.5	2.231
2	47.93	2.238	32.45	2.359
3	47.85	2.165	32.49	2.257

Table 3.2.2 Parameters of the transitions observed in three consecutive heating-cooling DSC cycles of 14% w/w gel sample of **[(ppy)$_2$Ir(dpq)]CH$_3$CO$_2$**.

Noteworthy, no additional transition to the isotropic ones were observed, indicative of a unique supramolecular organization in water.

3.2.1.4 Confocal microscopy

The **[(ppy)$_2$Ir(dpq)]CH$_3$CO$_2$** diluted gel phase was investigated also through confocal microscopy. The confocal images of the 5% w/w sample are reported in Fig.3.2.13 as example. Surprisingly, even though the gelator molecules do not exhibit luminescence emission in high diluted water solution (5x10^{-6} M, Chap.2), luminescent supramolecular structures are generated in water gel phases. This luminescence allowed to observe the

wire-shaped superstructures under a confocal microscope. When excited at 488 nm, the gel fibers showed an intense emission and the presence of three-dimensional fiber bundles.
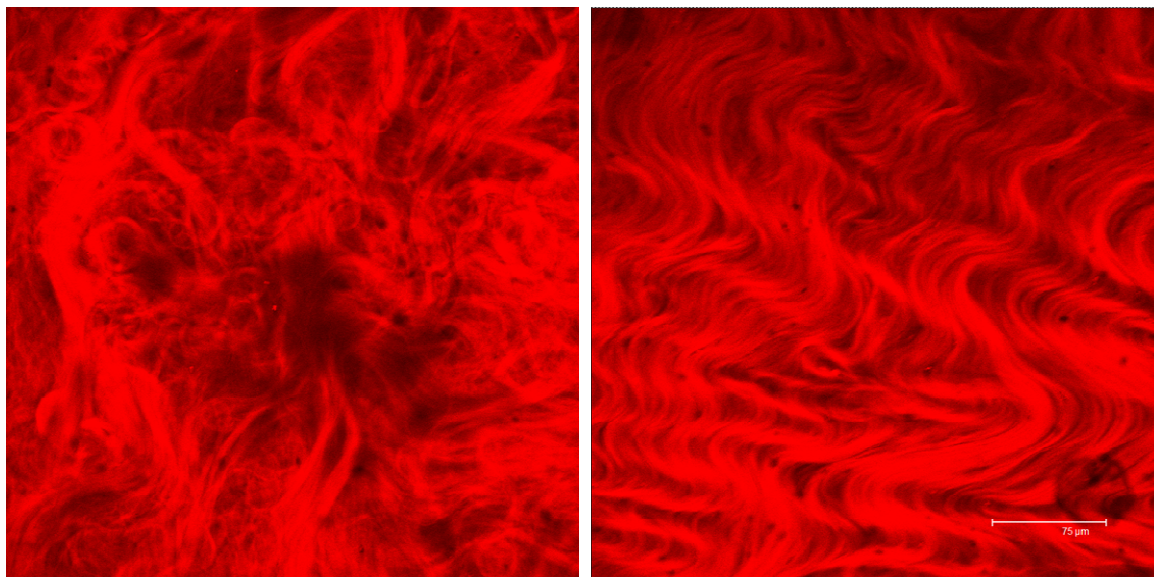
Fig.3.2.13. Confocal images of the 5% w/w gel phases originated by **[(ppy)₂Ir(dpq)]Ac** in water.

This is a clear example of AIPE (Aggregation-Induced Phosphorescnce Enhancement), which is an extraordinary phenomenon for whom non- or weakly emissive molecules are induced to emit efficiently through aggregate formation.[72] Up to now, many Ir(III) complexes, able to originate this effect, have been reported.[72] For example, Park *et al.* described an Ir(III) compound, reported in Fig.3.2.14, which is weakly emissive in solution, but exhibits high phosphorescence in the solid state, showing AIPE activity.[73] This feature was explained considering that in solution, the Ir(III) has a non-radiative rotational relaxation channel for the excited state to decay. In the solid state, aggregates are generated and the rotation is restricted due to the physical constraint, thus the excited state deactivated radiatively.
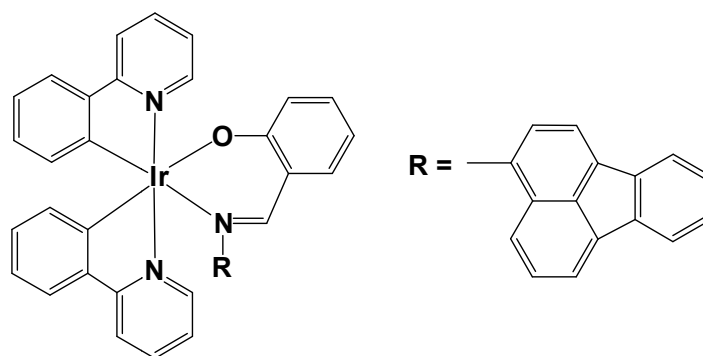
Fig.3.2.14. Chemical structure of an Ir(III) complex exhibiting AIPE feature.[73]

3.2.1.5 TEM microscopy

A deep insight of the fiber-shaped superstructures was provided by TEM analysis of gel samples. The 6% w/w gel sample was diluted with distilled water (dil. 1/1000) and was left to dry at room temperature. The so obtained xerogel was examined through TEM. TEM micrographs clearly show the presence of the supramolecular wires even in the xerogel film (Fig.3.2.15_a). Moreover, every macro-fiber is actually composed by a variable number of smaller wires which twist around each other, as displayed in magnified TEM images (Fig.3.2.15_b).
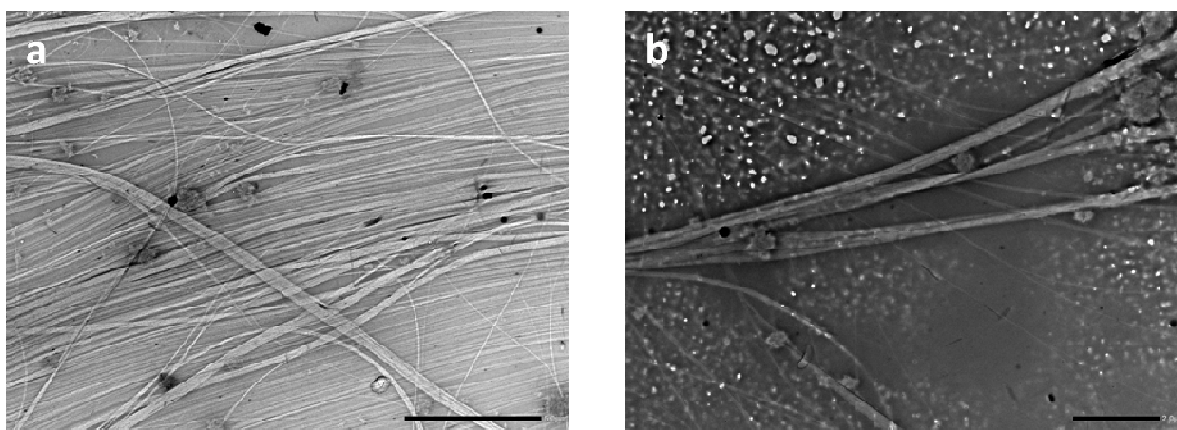
Fig.3.2.15. TEM images of the xerogel originated from a 5% w/w gel phase of **[(ppy)$_2$Ir(dpq)]CH$_3$CO$_2$**.

Although TEM micrographs elucidate the presence of fiber-shaped superstructures also in the dried samples, *i.e.* in the xerogel, which is a common feature of gel phases (paragraphs 3.1), the observed features of the water-phase is also close to the ones displayed by LLCs. Indeed, POM and PXRD analysis performed on the supramolecular phases derived from **[(ppy)$_2$Ir(dpq)]CH$_3$CO$_2$** in water allowed to demonstrate that their nature is very similar to lyomesophases, despite the fact that the chemical structure of compound **10** is highly different from conventional LCCs, that are generally characterized by a polar head and a long lipophilic chain. [74,75]

3.2.2 Supramolecular phase of [(ppy)$_2$Ir(dppz)]CH$_3$CO$_2$

The Ir(III) compound **[(ppy)$_2$Ir(dppz)]CH$_3$CO$_2$ (12)** (Fig.3.2.16), differently from compound **10**, is not capable to generate genuine gel phases which do not flow in a typical test tube experiment. However, its highest reachable concentrated water solution, which corresponds to the 1% w/w solution (solubility limit), displays an elevated viscosity, which could suggest the generation of some supramolecular assemblies. In order to prove this

hypothesis, POM, TEM and PXRD investigations have been carried out on the viscous solution and on the corresponding xerogel, obtained through complete dehydration of the first.
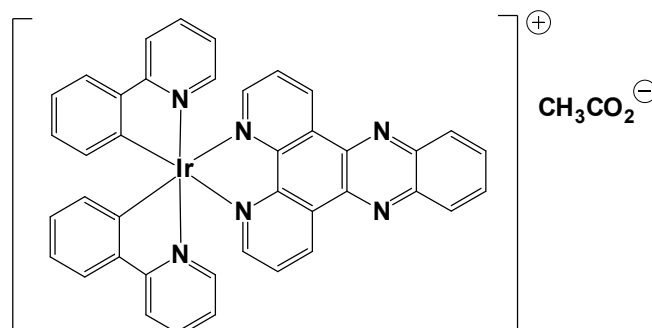
Fig.3.2.16. Chemical structure of **[(ppy)$_2$Ir(dppz)]CH$_3$CO$_2$ (12)**.

3.2.2.1 POM analysis

The viscous 1% w/w solution of **[(ppy)$_2$Ir(dppz)]CH$_3$CO$_2$ (12)** was observed under a Polarizing Optical Microscope. Also for this phase, an intense birefringence was observed (Fig.3.2.17_a), hence the presence of an anisotropic organized superstructure can be assumed. Moreover, differently from the gel phases originated by compound **10**, after the complete dehydration of this viscous phase, obtained leaving the sample at room temperature for several days, the birefringent texture was preserved. Indeed, the POM micrograph of the xerogel derived from **[(ppy)$_2$Ir(dppz)]CH$_3$CO$_2$** in water (1% w/w) (Fig.3.2.17_b), shows the same colours and shapes features of the texture displayed by the starting sample.
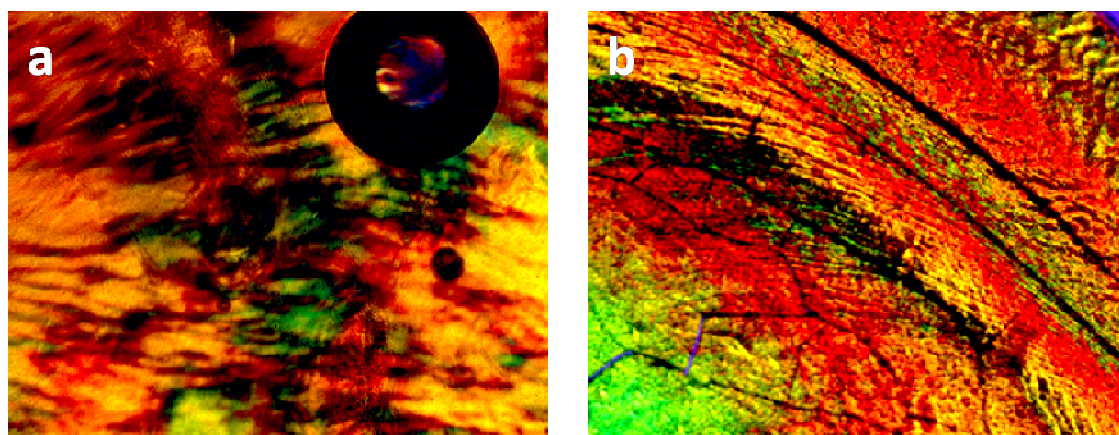
Figure 3.2.17. POM micrographs of the viscous phase in water of **12** (1 % w/w) (a) and the corresponding xerogel obtained after complete dehydration (b).

On this basis, with a good approximation, as already reported,[76,77] the persistence in the xerogel of a quasi-identical supramolecular organization to the starting viscous phase of complex **12** can be assumed.

3.2.2.2 TEM analysis

The presence of supramolecular assemblies in the water phase of **[(ppy)₂Ir(dppz)]CH₃CO₂** was unequivocally revealed by the TEM images acquired on its xerogel phase (Fig. 3.2.18).
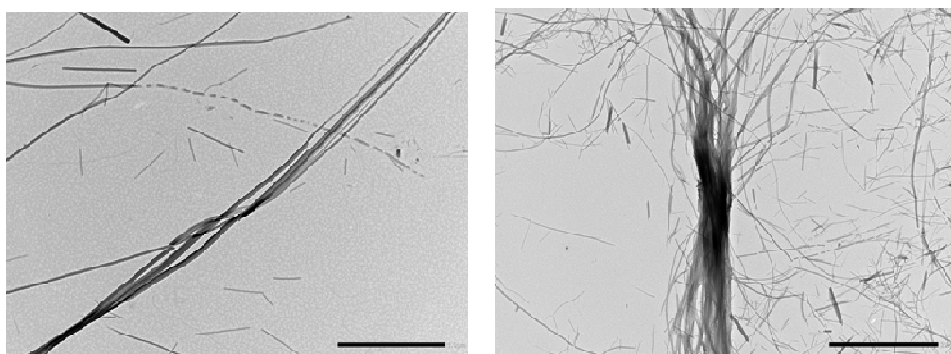
Fig.3.2.18. TEM images of the xerogel originated from the dilution of a 1% w/w water solution of **[(ppy)₂Ir(dppz)]CH₃CO₂**.

Similar to the xerogel originated from complex **10**, the dried samples derived from the dilution of the 1% w/w viscous water solution of compound **12**, present elongated aggregates wrapped in fiber bundles. However, in this case, the fiber-length distribution is wider than in the xerogel of **[(ppy)₂Ir(dpq)]CH₃CO₂**. Indeed, as shown in Fig.3.2.18, the supramolecular aggregates generated by **[(ppy)₂Ir(dppz)]CH₃CO₂** present different sizes, ranging from short needle-like aggregates to genuine long wires. The generation of smaller assemblies upon increasing the aromaticity of the N^N ligand, is in line with the observation of Szerb *et al.*[61] In any case, the formation of elongated fiber-shape aggregates demonstrates the tendency of these compound to self-assemble into columnar-like structures.

3.2.2.3 PXRD analysis

The observation of birefringent textures in the viscous solution and xerogel films led to the investigation of the supramolecular architecture of **[(ppy)₂Ir(dppz)]CH₃CO₂ (12)**, both in viscous water solution and in xerogel films, through Powder X-Ray Diffraction (PXRD) analysis. Unfortunately, the PXRD pattern of the quasi-gel 1% w/w phase does not exhibit any reflection peaks, but just the liquid background. Indeed, in this sample, the amount of water is far too high to allow the detection of any useful signals. For this reason, and assuming that the dried sample preserves the supramolecular architecture of the corresponding starting phase, the PXRD analysis was carried out on the xerogel film.
The PXRD patterns of the crude polycrystalline powder of **12** and of the xerogel obtained through complete dehydration of its water "gel" phase (prepared at *ca.* 1% w/w), are presented in Fig.3.2.19.
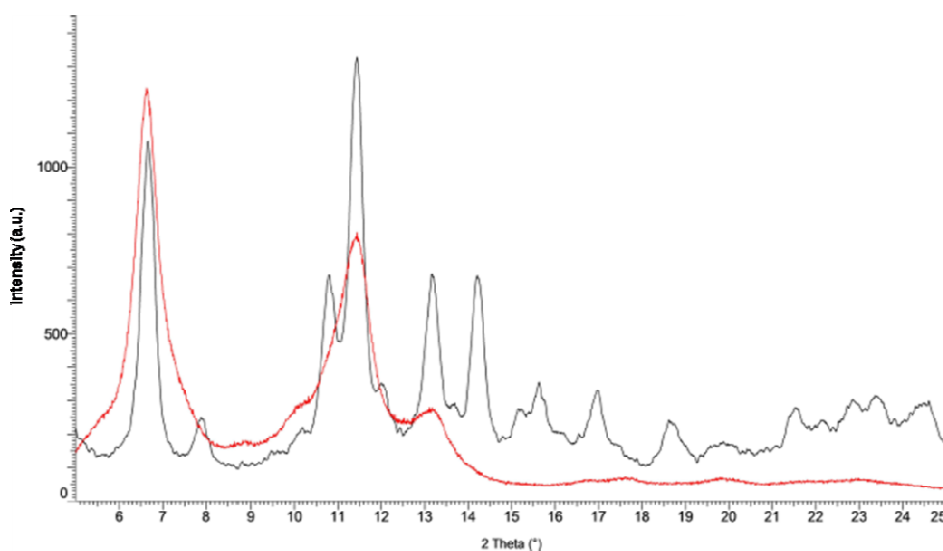
Fig.3.2.19. PXRD patterns of the crude powder (in black) and of the xerogel (in red) of complex **12**.

Although if two main peaks are present in both patterns at *ca.* 2θ = 13.2 ° and 2θ = 7.7 °, the PXRD are clearly not superimposable, ruling out the possibility of recrystallization of the xerogel into the polycrystalline form of the crude product. Furthermore, the relative intensities of these two common peaks are different between the patterns, displaying a quasi-inverse proportion. Consequently, the diffraction pattern of the xerogel can be indexed as a new organized solid form.

The PXRD pattern of the xerogel (Fig.3.2.20) presents 3 intense peaks in the small-medium angle region (2θ = 13.311, 7.753 and 6.750 °) and three smaller ones into the high angle region (2θ = 5.04, 4.46 and 3.86 °).
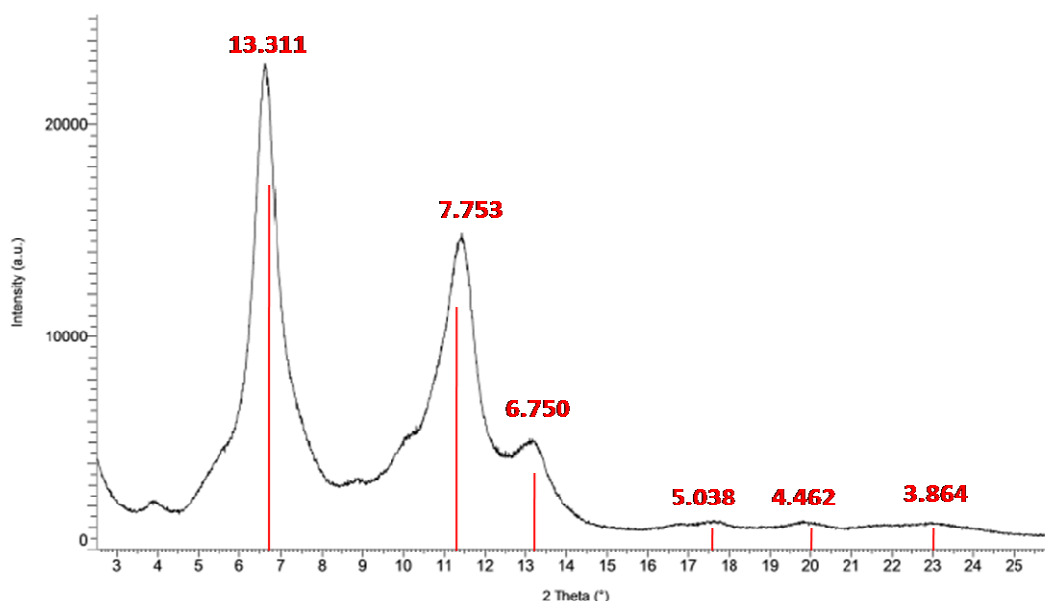
Fig.3.2.20. PXRD patterns of the xerogel originated from the water viscous solution of complex **12,** and relative d values.

Interestingly, the relative position of these peaks coupled with the continuous decrease of intensity with the increase of reflection angle, remembers the typical PXRD profile displayed by a columnar liquid crystal. Correlating this observation with the presence of fibrils within the xerogel, observed through TEM microsopy, that implies a high tendency of the complex to self-organize into columnar assemblies, an attempt of indexation of the PXRD pattern of the xerogel was performed by using LCDixRay.[70] Interestingly, a complete indexation of the PXRD pattern of the xerogel was successful, corresponding to a columnar hexagonal lattice (Col$_h$) with a cell parameter of a$_h$= 15.46 Å. Indeed, for hexagonally 2D systems, the lattice peak position for the Miller index of (h,k) is given by eq.3.2.1 and the positions of all the peaks are proportional to the first d$_{10}$ observed peak with the ratio reported in table 3.2.3.

$$\frac{1}{d_{hk}^2} = \frac{4}{3}\left(\frac{h^2 + hk + k^2}{a_h^2}\right)$$ eq. 3.2.1

Peak	d$_{10}$	d$_{11}$	d$_{20}$	d$_{21}$	d$_{30}$	d$_{22}$	d$_{31}$	...	d$_{hk}$	...
Ratio	1	$\frac{1}{3^{1/2}}$	$\frac{1}{2}$	$\frac{1}{7^{1/2}}$	$\frac{1}{3}$	$\frac{1}{12^{1/2}}$	$\frac{1}{13^{1/2}}$	...	$\frac{1}{(h^2 + hk + k^2)^{1/2}}$	...

Table 3.2.3 Characteristic ratios between the observed peaks of a PXRD pattern of a Col$_h$ 2D system.[27]

The indexation of the PXRD pattern of the xerogel originated from the water viscous solution of complex **12** is reported in table 3.2.4.

d_{obs}	*hk*	d_{calcd}[a]	d_{cacd} after refinement	System and Cell parameters
13.311	d_{10}	13.311[b]	13.39	
7.753	d_{11}	7.685	7.731	Col_h
6.750	d_{20}	6.655	6.695	
5.038	d_{21}	5.031	5.061	a_h= 15.46 Å
4.462	d_{30}	4.437	4.463	
3.864	d_{22}	3.843	3.865	

Table 3.2.4 Indexation of PXRD spectra of the xerogel of **[(ppy)$_2$Ir(dppz)]CH$_3$CO$_2$**. [a] Calculated data were obtained using LCDixRay program. [70] [b] Data chosen for calculations.

Noteworthy the value of cell parameter a_h= 15.46 Å, determined through PXRD analysis, is comparable to the length value of the cation **[(ppy)$_2$Ir(dppz)]$^+$** (a = 15.12 Å) determined via geometry optimization performed through DFT calculations (Chapter 2). On this basis, a model for the Col_h structure of the xerogel derived from compound **12** has been proposed and it is reported in Fig.3.2.21.
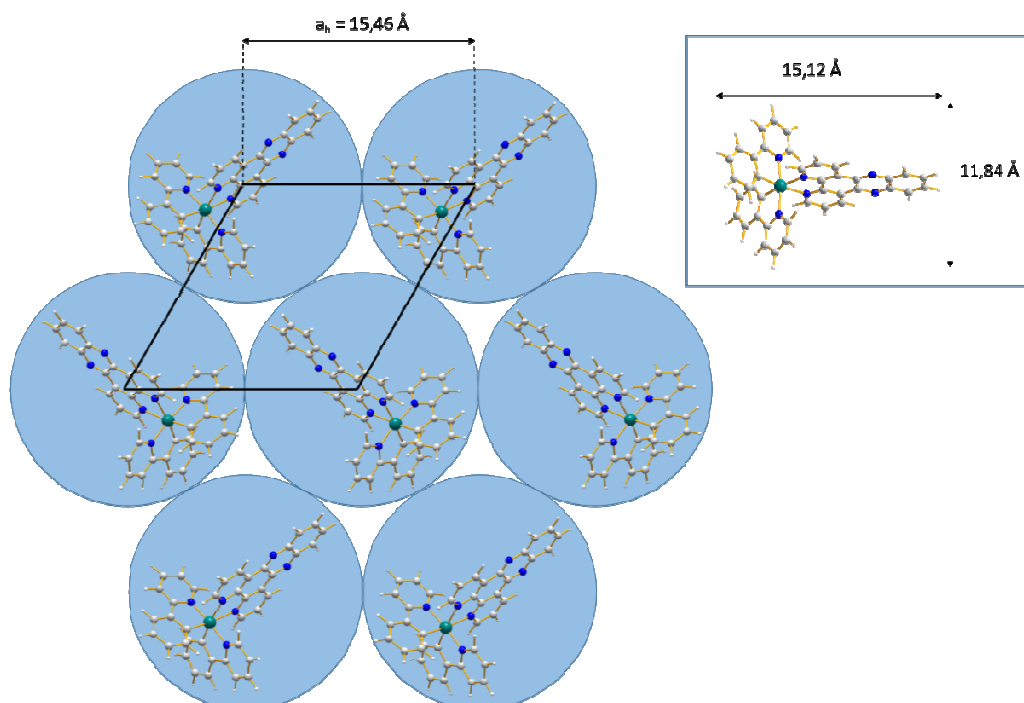
Fig. 3.2.21. Proposed model for the Col_h structure of the xerogel of **[(ppy)$_2$Ir(dppz)]CH$_3$CO$_2$**. Note that the orientation of the moleculaes within the circles are unknown, chosen in this representation only for clarity of the figure. In inset the molecular dimensions determined on the optimized geometry obtained through DFT calculations.

In conclusion, the water viscous 1% w/w solution of **[(ppy)₂Ir(dppz)]CH₃CO₂** is characterized by an ordered bidimensional architecture, pointed out by the birefringent textures and the PXRD pattern. However, the presence of this extended aromatic ancillary ligand **dppz** led to a decrease in the water solubility of compound **12** with respect to the parent complexes **[(ppy)₂Ir(bpy)]CH₃CO₂**, **[(ppy)₂Ir(phen)]CH₃CO₂** and **[(ppy)₂Ir(dpq)]CH₃CO₂**, and to the inability to generate a genuine gel phase.

3.2.3 Synthesis of novel [(ppy)₂Ir(bpy)]X metallo-hydrogelators

In order to synthesize further Ir(III) complexes able to generate organized self-assembled structures, a feature displayed by many compounds,[78-81] the inclusion of other hydrophilic counterions into the archetype cationic Iridium (III) complex **[(ppy)₂Ir(bpy)]⁺** was performed, taking into account that the analogous **[(ppy)₂Ir(bpy)]CH₃CO₂** creates gel-phases in water. The compounds **[(ppy)₂Ir(bpy)]X (X = EtO⁻, OH⁻, EtOCH₂CO₂⁻, MeOCH₂CO₂⁻)** were obtained, and they are effectively Ir(III)-based metallo-hydrogelators, able to form luminescent physical gel phases with a well-ordered supramolecular architecture.

Furthermore, the presented materials retain the same organized structure also after complete evaporation of the liquid component, thus in the corresponding xerogels.

3.2.3.1 Synthesis of [(ppy)₂Ir(μ-OH)]₂ (II)

All the complexes of type **[(ppy)₂Ir(bpy)]X**, described in this chapter, were obtained starting from a versatile and very reactive precursor, the *μ*-dihydroxy bridged dimer **[(ppy)₂Ir(*μ*-OH)]₂ (II)**. This binuclear complex has been already used for the synthesis of meridional tris-cyclometalate Ir(III) complexes at low-temperatures, but, in that case, it was prepared using a synthetic procedure which involved the transition from an intermediate Ir(III) complex coordinated to two molecules of acetonitrile.[82]

[(ppy)₂Ir(*μ*-OH)]₂ was chosen as precursor for a subsequent bridge-splitting reaction with the archetype 2,2-bipyridine (**bpy**) ligand in order to introduce the OH⁻ as counterion in the ionic complex **[(ppy)₂Ir(bpy)]⁺**, similarly to what happens with the split of the chloro-

bridged dimer **[(ppy)₂Ir(μ-Cl)]₂** with a N^N ligand, which leads to the corresponding cationic Ir(III) complex bearing Cl⁻ as counterion.

The dinuclear intermediate (**II**) was obtained in high yield and high purity through the metathesis reaction of **[(ppy)₂Ir(μ-Cl)]₂ (I)** under strong basic conditions, which allowed the opening of the chloro bridge (Scheme 3.2.1).
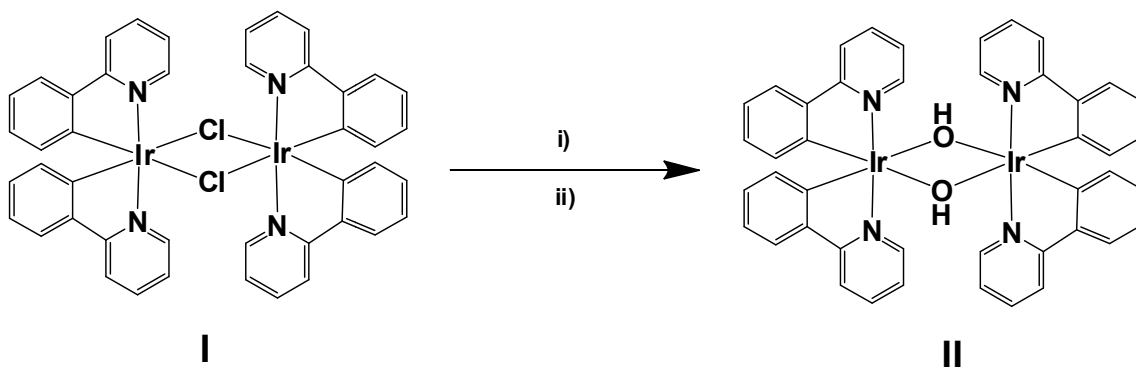
Scheme 3.2.1. Synthesis of the precursor **[(ppy)₂Ir(μ-OH)]₂(II)**. Reaction conditions: (i) KOH, EtOCH₂CH₂OH/THF, r.t., 48 h; (ii) KOH, THF, r.t., 3h.

The binuclear complex **II** was first identified by its characteristic ¹H-NMR distinctive signal of the *μ*-OH bridge proton at δ = -1.62 ppm, indeed this peak is shifted to very high field, due to strong-fielding effect (Fig.3.2.22).[83] Furthermore, the total absence of chlorine atoms, thus the confirmation of the completeness of the metathesis reaction, was determined through scanning electron microscopy coupled with energy-dispersive X-ray spectroscopy (SEM/EDX) performed on the crushed powder of (**II**).
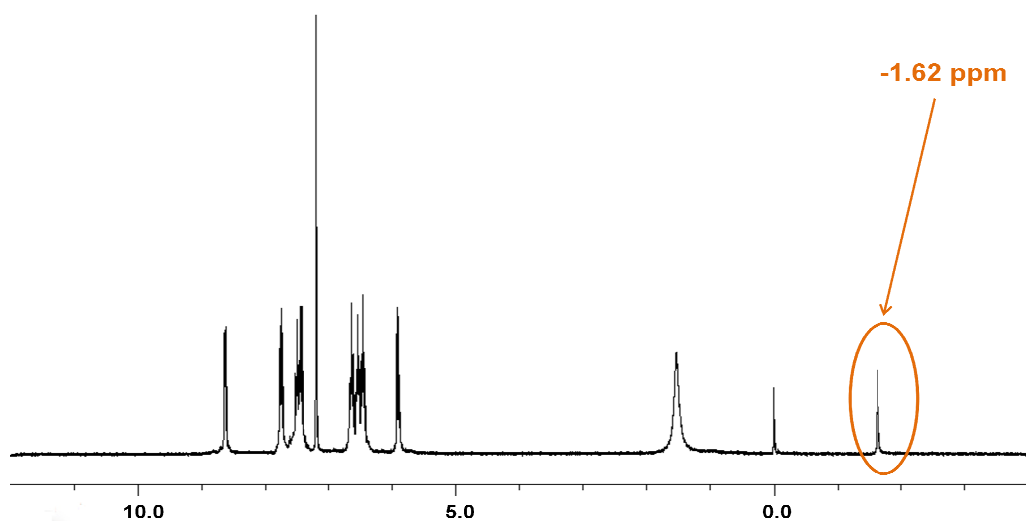
Figure 3.2.22 ¹H- NMR spectra of compound (**II**).

3.2.3.2 Synthesis of [(ppy)₂Ir(bpy)]EtO (13)

The dimeric precursor **(II)** was initially used in a bridge-splitting reaction with the archetype 2,2'-bipyridine (**bpy**) ligand to synthesize the ionic complex formed by the tris-chelated cation **[(ppy)₂Ir(bpy)]⁺** and the OH⁻ anion. This reaction was performed in absolute ethanol. Unexpectedly, the formation of the complex **[(ppy)₂Ir(bpy)](EtO)** was observed instead of the predictable **[(ppy)₂Ir(bpy)](OH)**. The ethoxide anion was clearly identified through ¹H- and ¹³C-NMR spectroscopies. The incorporation of the ethoxide group (EtO⁻) as counter-anion in the Ir(III) cationic complex can only be attributable to the deprotonation of some solvent molecules. The basic behaviour of the hydroxy-bridged dimer **(II)** was already reported by Mann,[82] who found that this precursor promotes the deprotonation of the cyclometalating carbon atom in the ligands 2-phenylpyridine (**ppy**) and 2,2'-thienylpyridine (**thpy**), observing the formation of tris-cyclometalated species. Probably, the compound **(II)** acts as source of OH⁻ anions, which in turn exerts a basic action on some ethanol molecules.
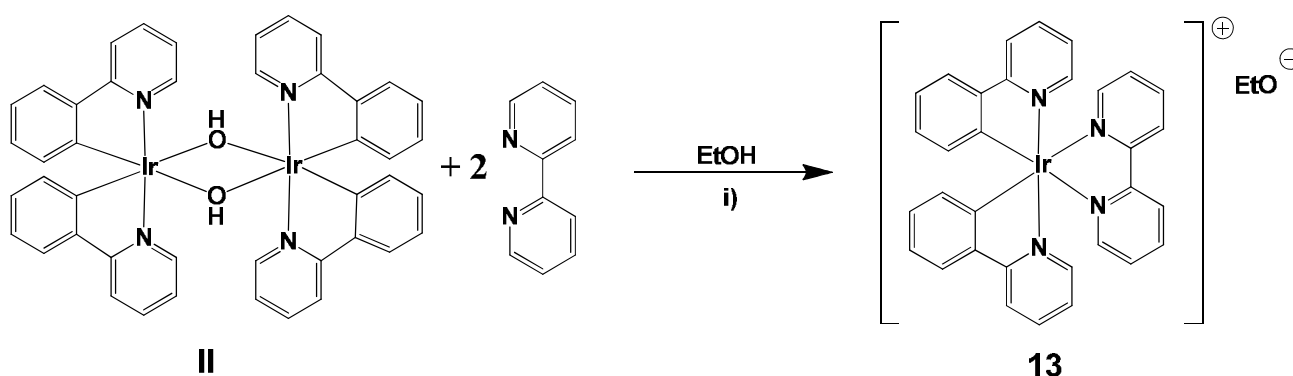
Scheme 3.2.2. Synthesis of the complex **[(ppy)₂Ir(bpy)]EtO (13)**. Reaction conditions: (i) EtOH, reflux, N₂, 72h.

3.2.3.3 Synthesis of [(ppy)₂Ir(bpy)]OH (14)

The hydroxide complex **[(ppy)₂Ir(bpy)]OH (14)** was obtained through two different reactions (Scheme 3.2.3).
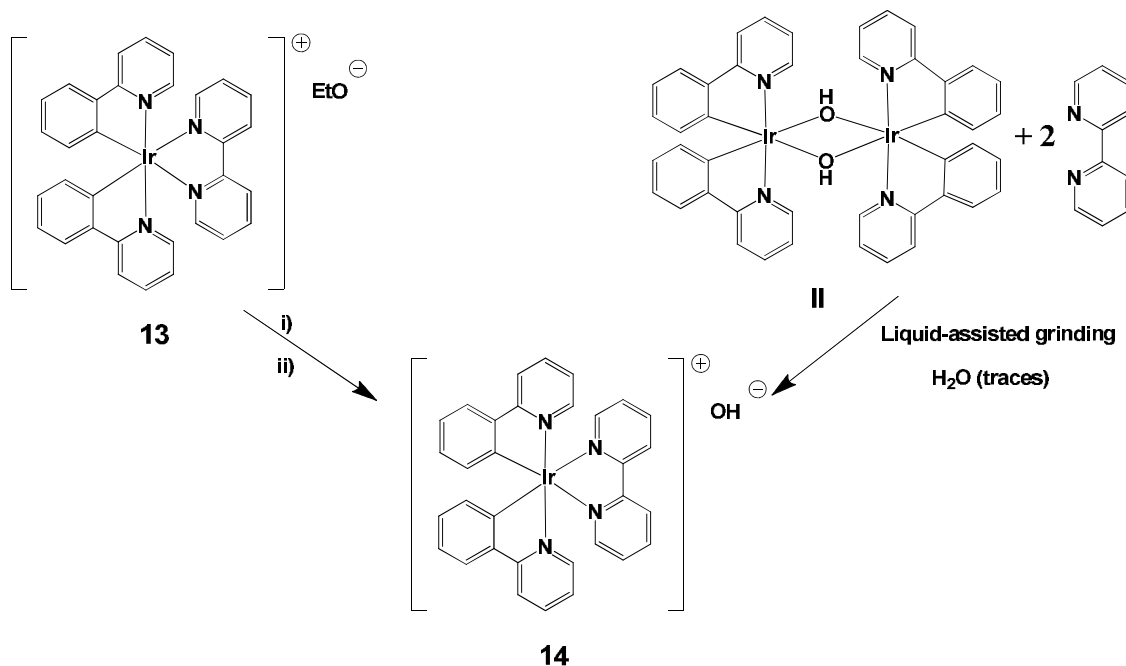
Scheme 3.2.3. Synthesis of the complex **[(ppy)₂Ir(bpy)]OH (14)**. Reaction conditions: (i) THF/H₂O; (ii) Et₂O.

First, **(14)** was recovered in almost quantitative yield by hydrolysis of the ethoxy anion of **(13)** in water/tetrahydrofuran solution and subsequent re-precipitation in diethyl ether. Indeed, the conjugate base of EtOH is strong enough to deprotonate water, generating EtOH and OH⁻ ions. The latter replace ethoxide as counterion of the cationic **[(ppy)₂Ir(bpy)]⁺** motif.

The complex **(14)** was also directly synthesized from the hydroxyl-bridged dimer (**II**) via a solid state reaction by liquid-assisted grinding (LAG) in the presence of a small amount of water. LAG is a widely used mechanochemical technique based on the grinding of the reactants in solid powders in the presence of a very small amount of solvent.[84-86] Liquid-assisted grinding reactions are generally performed in a ball mill and are often faster and more selective than solvent-based reactions. Furthermore, the use of a minimum quantity of solvent results in reduced environmental pollution, making this method attractive for industrial applications.

The synthesis of **[(ppy)₂Ir(bpy)]OH** was performed by LAG, precisely in order to avoid the use of a solvent other than water. After acquiring powder X-ray diffraction (PXRD) patterns

of the precursors (**II**) and **bpy**, the progress of the reaction was followed by PXRD between 5° and 40° (2θ) (Fig.3.2.23).
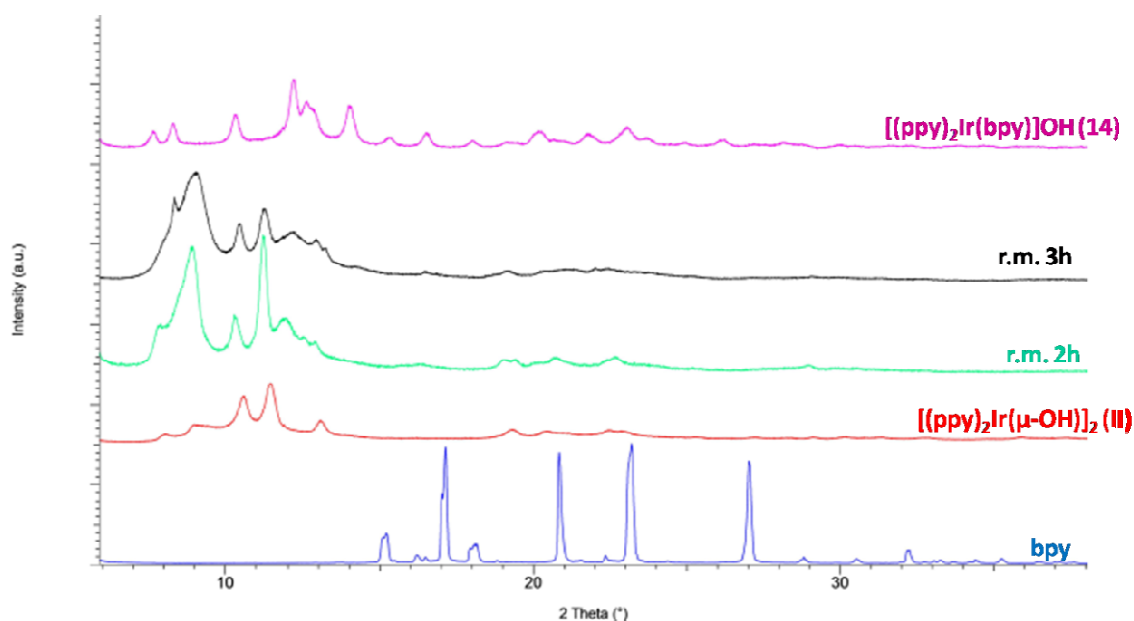
Fig.3.2.23. Comparison between PXRD patterns of **bpy**, **[(ppy)₂Ir(μ-OH)]₂ (II),** the reaction mixture (r.m.) after 2h of grinding, the r.m. after 3h of grinding and the final product **[(ppy)₂Ir(bpy)]OH (14).**

After 4h of grinding, the pure final product was recovered from water by slow dehydration. The PXRD pattern of the compound (**14**), obtained through solid state reaction, was compared to the PXRD pattern of the same complex, recovered via hydrolysis of **[(ppy)₂Ir(bpy)]EtO (13)** (Fig.3.2.24). The two patterns are perfectly superposable. The uncontroversial chemical equality of the two solids was confirmed by ^{1}H-NMR analysis.
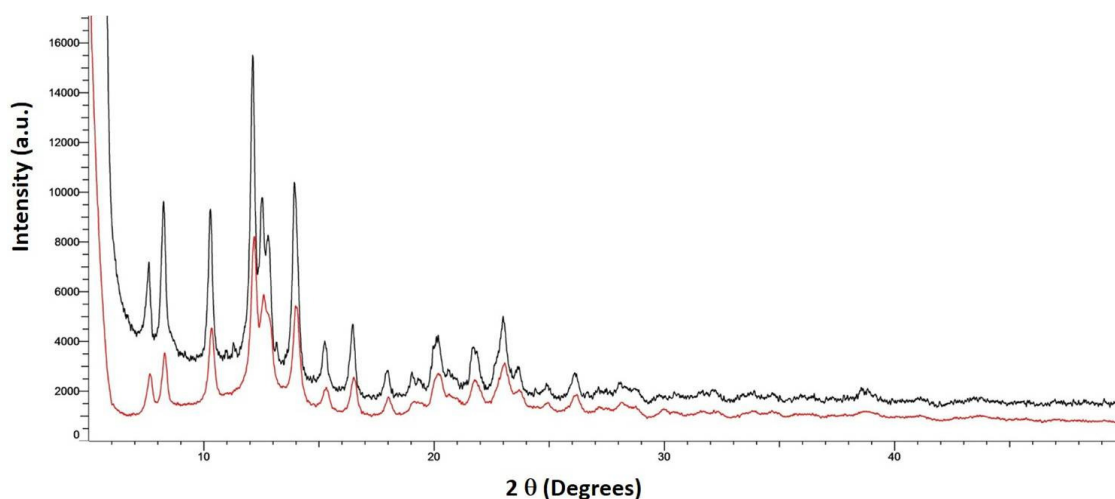
Fig.3.2.24. PXRD patterns of (**14**) (in black from hydrolysis of (**13**), in red from solid state synthesis).

Compound **14** was also used as precursor for the synthesis of complexes **17** and **18,** incorporating **CH₃CO₂** and **BrCH₂(CH₂)₄CO₂** respectively as counter-anions (paragraph 3.2.3.5), demonstrating its versatility.

3.2.3.4 Synthesis of [(ppy)₂Ir(bpy)]EtOCH₂CO₂ (15) and

[(ppy)₂Ir(bpy)]MeOCH₂CO₂ (16)

The reaction between compound (**II**) and the ancillary ligand **bpy** was performed also in deoxygenated 2-ethoxyethanol. Taking into account the strong basic character of the precursor hydroxyl-bridged dimer (**II**), which in ethanol led to the formation of EtO⁻ as counterion of the **[(ppy)₂Ir(bpy)]⁺** motif (complex **13**), in the presence of 2-ethoxyethanol as solvent, the generation of the anion $EtOCH_2CH_2O^-$ was expected. However in this case, the hydroxy-bridge splitting reaction of (**II**) results in the formation of complex **[(ppy)₂Ir(bpy)](CH₃CH₂OCH₂CO₂) (15)**, presenting as counterion the corresponding carboxylate anion originating from the in situ oxidation of the solvent (Scheme 3.2.4).
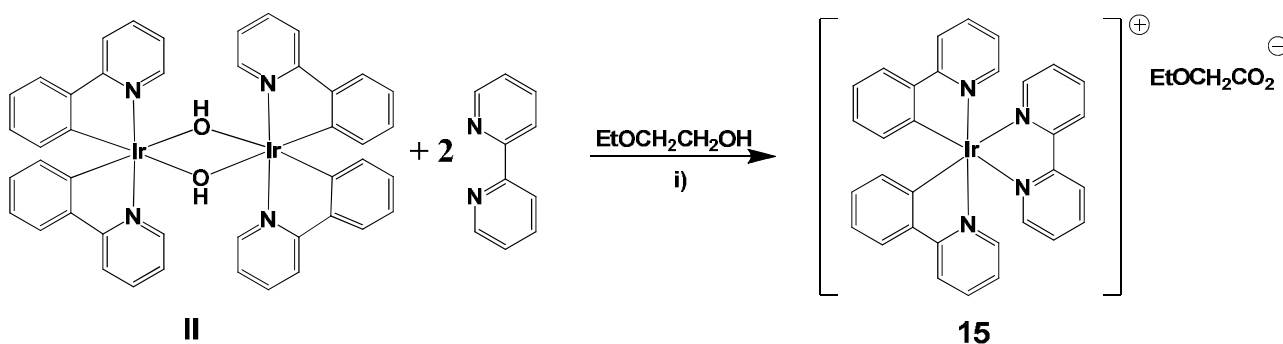
Scheme 3.2.4. Synthesis of the complex **[(ppy)₂Ir(bpy)]EtOCH₂CO₂ (15)**. Reaction conditions: (i) 2-EtOCH₂CH₂OH, reflux, N₂, 72h.

The presence of this unexpected counterion was identified through several techniques, including electrospray ionization mass spectrometry and NMR spectroscopy. The mass spectra in positive and negative ion modes show the peaks corresponding to the cation (ESI+, direct infusion) m/z = 657 (100% **[(ppy)₂Ir(bpy)]⁺**) and the anion (ESI−, direct infusion) m/z = 103 (100% **[EtOCH₂CO₂]⁻**), respectively (Fig.3.2.25).
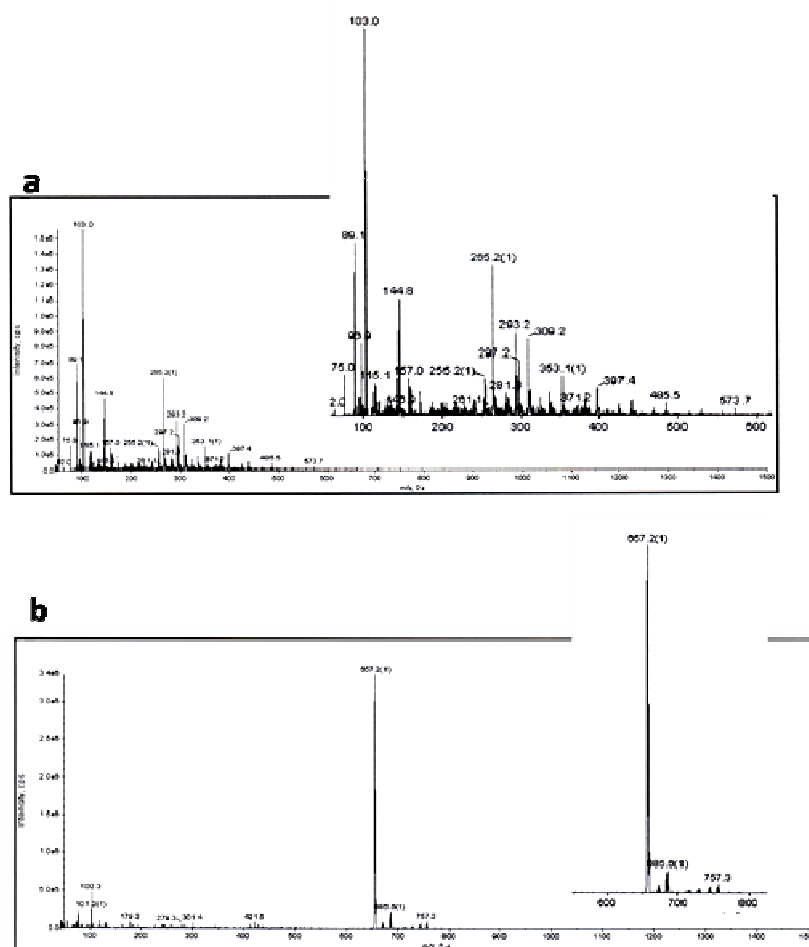
Figure 3.2.25. Mass spectra of complex **(15)** in negative (a) and positive modes (b) .

The ^{1}H-NMR spectrum of complex **15**, recorded in CDCl$_3$ (Fig.3.2.26), shows a triplet, a quartet and a singlet in the aliphatic region, which can be attributed only to the 2-ethoxyacetate counteranion of complex **15**. In particular, the triplet is associated to the methyl protons, the quartet to the methylene protons close to the methyl group, and the singlet is associated to the methylene protons between the ether oxygen and the carboxylate chemical function. The value of these protons integrals allowed to demonstrate that the reaction in 2-ethoxyethanol leads exclusively to an equimolar amount of carboxylate anions for each Ir(III) metal center. Furthermore, the presence of a carboxylic carbon atom signal (δ = 171 ppm) and of the other aliphatic carbon atoms within the counterion are observable in the ^{13}C-NMR spectra of complex **(15)** (Fig.3.2.27).
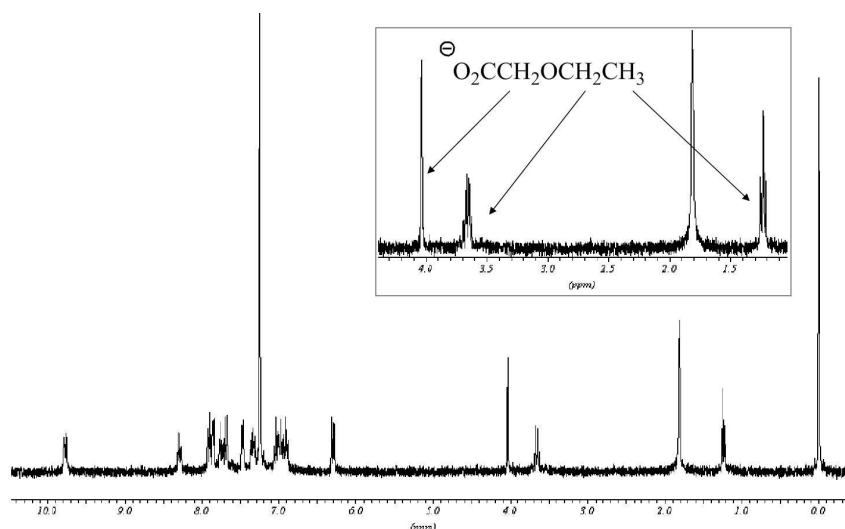
Figure 3.2.26. ^{1}H- NMR spectra of complex **(15)**.
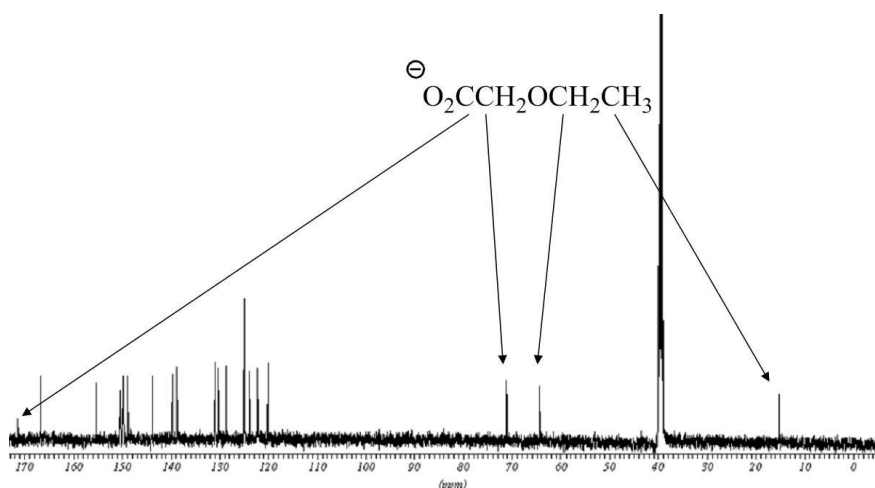
Figure 3.2.27. ^{13}C-NMR spectra of complex **(15)**.

Moreover, the precursor **(II)** was refluxed in deoxygenated 2-ethoxyethanol for 72h under inert atmosphere in the absence of the ancillary ligand, **bpy**. In this case, the hydroxyl-bridged dimer remained unreacted and no solvent oxidation was observed, thus the presence of the ligand, involved in the splitting of the hydroxyl bridge, is necessary to expose the OH function, which should play an important role in the solvent oxidation.

The surprising oxidation of 2-ethoxyethanol might be correlated with the peculiar reactivity of the μ-dihydroxy bridged dimeric Ir(III) complex **II**, as found out by Schubert.[83] Indeed, he used this reactive compound as precursor for the synthesis of several Ir(III) complexes bearing a phenyl-hydroxymethyl-triazole derivatives as ligands. In his work, the observation of the oxidation of the alcoholic function of the ligand to carboxylate was reported.

The hypothesis considered is that the *μ*-dihydroxy-bridged dimer probably acts as a source of OH$^\bullet$ radicals. Oxidation of glycol ethers by OH$^\bullet$ radicals has been reported by many groups.[87-90] In particular, Stemmler *et al.*[87,88] used an apparatus, filled with air containing NO, in which hydroxyl radicals were generated from the photolysis of methyl nitrite. However, in this case, the oxidation of 2-ethoxyethanol led to the formation of ethyl formate and ethoxyacetaldehyde as main products, thus the reaction stopped before the generation of the corresponding carboxylic acid.

Consequently, in our case, the oxidation of the alcohol up to the carboxylate anion is still puzzling and the in situ "formation" of radicals may not be sufficient to elucidate this complete oxidation, suggesting a more complicated oxidation pathway.

The reaction between **[(ppy)$_2$Ir(μ-OH)]$_2$ (II)** and the ancillary ligand **bpy** was carried out also in another glycol-ether, 2-methoxyethanol, following the same experimental conditions of **(15)**. Once again, the in situ oxidation of the solvent was obtained and the complex **[(ppy)$_2$Ir(bpy)](CH$_3$OCH$_2$CO$_2$) (16)** was formed. Therefore, it can be concluded that the oxidizing activity of the hydroxyl-bridged dimer **(II)** is exerted only on glycol ether, thus the ether oxygen present in these compounds should play some role in this synthetic pathway.

3.2.3.5 Synthesis of [(ppy)$_2$Ir(bpy)]CH$_3$CO$_2$ (17) and
[(ppy)$_2$Ir(bpy)]BrCH$_2$(CH$_2$)$_4$CO$_2$ (18)

The complex **[(ppy)$_2$Ir(bpy)](OH) (14)** was used as precursor for the synthesis of analogous compounds bearing a carboxylate as counterion, **[(ppy)$_2$Ir(bpy)]CH$_3$CO$_2$ (17)** and **[(ppy)$_2$Ir(bpy)]BrCH$_2$(CH$_2$)$_4$CO$_2$ (18)** (Scheme 3.2.5). The synthesis of complexes **17** and **18** were performed by dissolution of the precursor **14** in CH$_2$Cl$_2$ and subsequent addition of acetic acid (CH$_3$COOH) for **17** and 6-Bromohexanoic acid (BrCH$_2$(CH$_2$)$_4$COOH) for **18**. The correspondent carboxylates, CH$_3$COO$^-$ for **17** and BrCH$_2$(CH$_2$)$_4$COO$^-$ for **18**, were formed in a very short time (*ca*. 30 min), through reaction with the OH$^-$ ion of the precursor **14**.
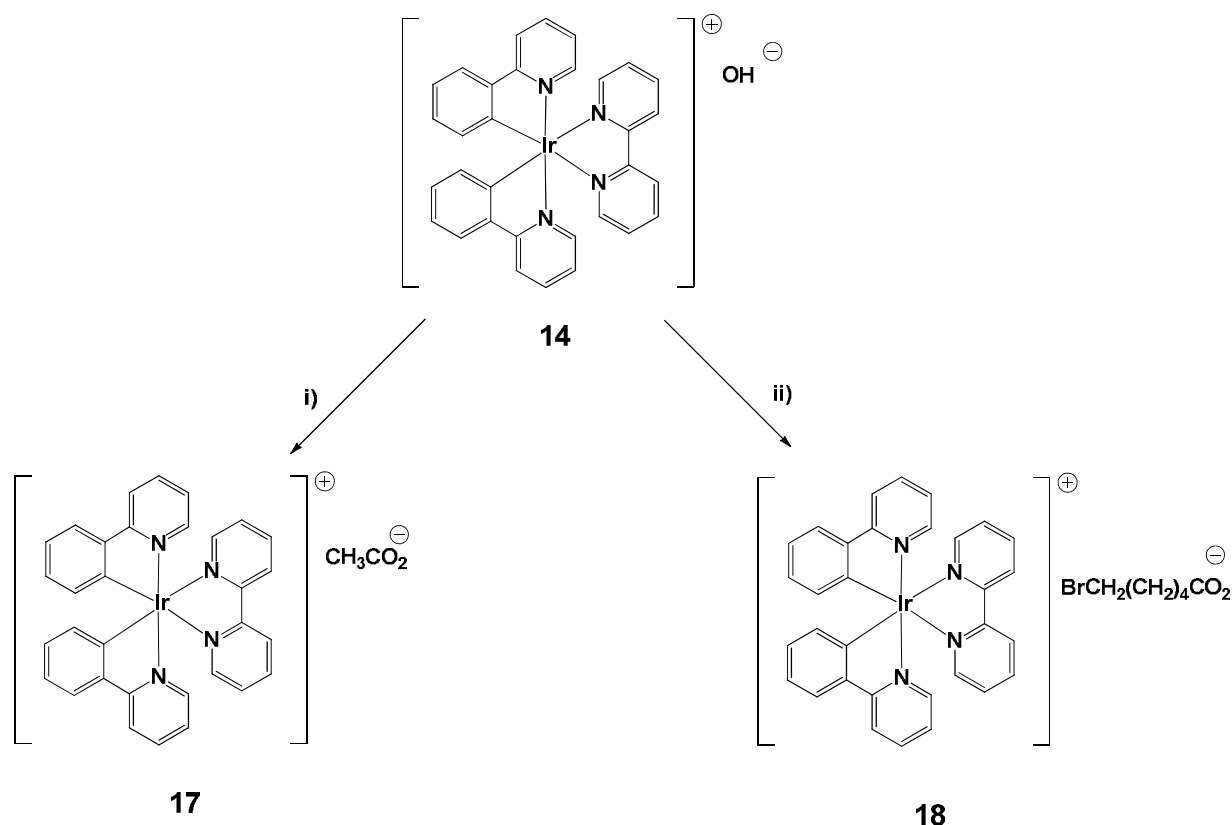
Scheme 3.2.5. Synthesis of the complexes **[(ppy)₂Ir(bpy)]CH₃CO₂ (17)** and **[(ppy)₂Ir(bpy)]BrCH₂(CH₂)₄CO₂ (18)**. Reaction conditions: (i) CH₃COOH, CH₂Cl₂, 30 min., r.t.; (ii) BrCH₂(CH₂)₄COOH , CH₂Cl₂, 30 min., r.t.

Noteworthy, the synthesis of compound **17**, has already been reported, although employing the anion exchange method with silver acetate.[54]

This method demonstrates the versatility of complex **[(ppy)₂Ir(bpy)](OH) (14)** as precursor for the synthesis of further water-soluble Ir(III) cationic complexes, incorporating potentially any carboxylate anion. Noteworthy, this synthetic approach avoids the use of *ad-hoc* prepared silver salts.

3.2.4 Gel-phases derived from [(ppy)₂Ir(bpy)]X complexes

3.2.4.1 Gel preparation

All the newly synthetized Ir(III) complexes **[(ppy)₂Ir(bpy)]X (X = EtO⁻, OH⁻, EtOCH₂CO₂⁻, MeOCH₂CO₂⁻)** are highly soluble in water up to concentrations of *ca*. 6% w/w. As already reported for the analogous **[(ppy)₂Ir(bpy)](CH₃CO₂)** complex,[54] a gel-phase formation is observable in a well-defined range of concentration.

The gel-phases were prepared by using the same method reported for compound **10** (paragraph 3.2.1), thus dissolving the opportune quantity of complexes in warm distilled water and cooling down to room temperature the resulting solutions The formation of gel phases was determined through the typical inversion test tube experiment.

This method allowed also to estimate the critical gel concentration, meaning the minimal gelator concentration required to generate a gel-phase, for all the complexes (**13, 14, 15, 16**). Moreover, the maximum gel concentrations were determined by examining the gel samples of increasing concentrations under a microscope. The appearance of insoluble particles fixed the solubility limit of the compound, and consequently the maximum gel concentration. For these four complexes (**13, 14, 15, 16**) derived from **[(ppy)$_2$Ir(μ-OH)]$_2$ (II)**, the range of concentrations in which the generation of gel-phases occurs is reported in table 3.2.5.

Complex	Critical gel concentration (w/w , mol.L^{-1})	Solubility limit (w/w , mol.L^{-1})
13	2.3 %, 3.35 x 10^{-2}	5.0 %, 7.30 x 10^{-2}
14	2.2 %, 3.35 x 10^{-2}	4.5%, 6.84 x 10^{-2}
15	2.8 %, 3.79 x 10^{-2}	6.0%, 8.12 x 10^{-2}
16	2.4 %, 3.30 x 10^{-2}	5.2 %, 7.14 x 10^{-2}

Table 3.2.5. Critical gel concentrations and solubility limit of complexes **13-16** in water.

The four metallo-hydrogels, originated from the four corresponding Ir(III) metallogelators (**13**, **14**, **15** and **16**), exhibit quasi-identical features in terms of supramolecular structures, POM textures, sol-gel transition temperatures, etc. This observation is in line with the quasi-identical chemical structures of the four compounds, which present the same cationic motif and slightly different counterions (EtO$^-$, OH$^-$, EtOCH$_2$CO$_2^-$, MeOCH$_2$CO$_2^-$). For this reason, in this chapter, the full characterization of only one complex is reported. In particular, since the most concentrated gel phase is achievable with complex **15**, this compound was chosen as archetype of this class of Ir(III) metallogelators.

3.2.4.2 Sol-gel transition

The transition between the gel phase and the sol state is observable from a macroscopic point of view through the test-tube experiment. However, in order to extract more detailed

information on the temperature values at which this transition occurs, hydrogel phases of complex **15** at different concentrations (3%, 4%, 5% and 6% w/w) were prepared and examined under a polarizing microscope equipped with a heating stage. The gel phases are characterized by an intense birefringence, which disappear in the isotropic state. Heating/cooling cycles were carried out on the gel phases placed under sealed coverslips to avoid dehydration, and therefore to avoid a concentration change. The transition to the isotropic condition (no birefringence observed) depends on the concentration of the gelator molecule. In particular, the most diluted gel (3 % w/w) displays an isotropic transition temperature at *ca.*44 °C. This value increases quasi-linearly with concentration, to reach *ca*. 55 °C for the most concentrated gel (6 % w/w) (Fig.3.2.28). This behaviour can be explained with the instauration of an increasing number of secondary interactions upon increasing concentration of the gel phases; these interactions are responsible for the higher thermal stability of the supramolecular structure.
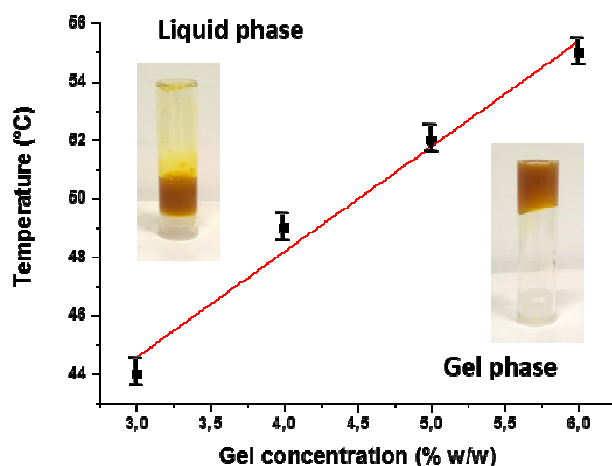
Fig. 3.2.28. Variation of the isotropic temperature with increase of the gelator **[(ppy)$_2$Ir(bpy)]EtOCH$_2$CO$_2$ (15)** concentration.

3.2.4.3 Polarizing optical microscope (POM) analysis

The gel-phases, derived from the complexes **13**, **14**, **15** and **16**, were placed in closed cells and observed under a polarizing optical microscope (POM). The gel state of all these four Ir (III) compounds displayed an intense and homogeneous birefringent texture, which is indicative of the presence of ordered anisotropic supramolecular structures. Similarly to

liquid crystalline phases, these gel phases can exhibit changes in the birefringence colour and in textures, upon heating and cooling cycles, indicating a change in their supramolecular arrangements. The typical POM textures of the gel phases of complex **15**, 4 % w/w in water, deposited in a closed cell, are illustrated in Fig.3.2.29. At room temperature, the gel phase exhibits a pristine texture, composed of aligned string-shaped structures (Fig.2.2.29_a). This observation could suggest the presence of anisotropic fibrous aggregates within the gel matrix. These structures disappear upon heating at *ca*. 40°C, indicating an architectural change induced by the rise in temperature (Fig.3.2.29_b). When temperature reaches 49°C, the transition to the isotropic solution (sol) occurs and no birefringence was observed. Upon cooling the sol below T_{gel}, first a thread-like texture, similar to those of nematic liquid crystals, appears (Fig.3.2.29_c), and, after the return to room temperature, the sample displays in some regions a herringbone texture, which resembles the M-phase of chromonic liquid crystals (Fig.3.2.29_d).[91,92]
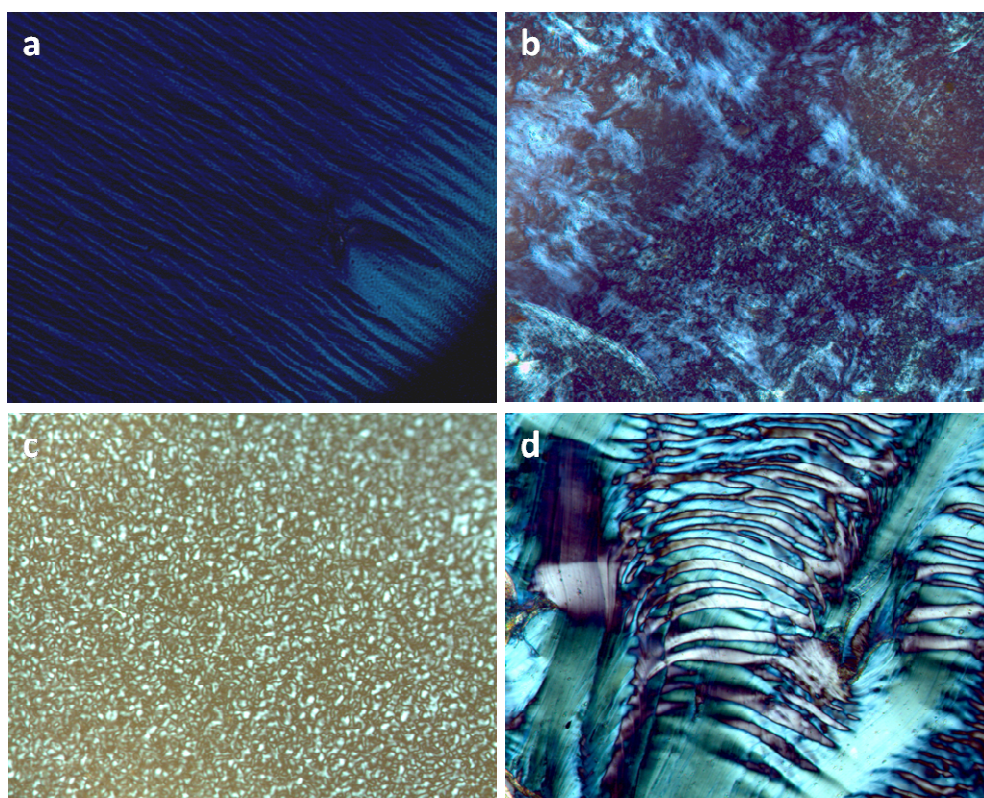
Figure 3.2.29. POM micrographs of the gel phases textures of **15** at a concentration value of 4 % w/w in water: a) r.t.; b) upon heating at *ca*. 40°C; c) upon cooling at *ca*. 35°C; d) after return to r.t.

Although birefringence was reported for some gel phases,[15-17] the appearance of these intense birefringent textures may create confusion in the attribution of these materials to either the classes of supramolecular gels and/or lyotropic liquid crystals (LLCs). However, the synthetized Ir(III) complexes have a chemical structure very different from the conventional lyotropic mesophases, which usually consist of a flexible lipophilic chain and a polar head.[74,75] Moreover, LLCs are able to build up aggregates, generally in the shape of micelles, in a defined range of concentrations and in presence of a solvent. The critical micelle concentration and the Kraff-point are characteristic parameters for these materials[93] and are not displayed by the compounds **13**, **14**, **15** and **16**, in a similar way to a particular class of lyotropic liquid crystals, named chromonic LCs. The chromonic systems are formed by soluble aromatic compounds, usually in water, and present two distinct mesophases: a low concentrated N phase and a high concentrated M phase.[91,92] The uncontroversial identification of a chromonic system is based on the observation of a distinctive phase diagram and of a unique X-ray diffraction pattern. The latter exhibits, for both N and M mesophases, a high angle axial reflection (3.4 Å), corresponding to the π-π stacking between aromatic rings, and a low-angle equatorial reflection, which appears diffuse in a N phase and splits in two separated signals in a M phase. However, the concentrated samples originated from the Ir (III) complexes **13**, **14**, **15** and **16** do not present two different phases, thus carry out a phase diagram for these systems is impossible. Furthermore, their XRD patterns differ from those of chromonic LCs, as described in the next paragraph.

Moreover, as described in paragraph **3.2.1.1**, in a lyotropic liquid crystal when the solvent is removed from the lyomesophase, the supramolecular architecture can be totally or partially destroyed, thus birefringence and characteristic diffraction patterns can be lost after solvent evaporation.[68,69]

A different trend was observed for the supramolecular phases generated from the self-assembly of the Ir(III) compound **13**, **14**, **15** and **16**. The defined texture displayed by the sample in the gel phase is retained also after its complete dehydration, without the need for pre-treatments of the specimen. The POM micrograph of a 5% w/w gel of complex **15** is illustrated in Figure 3.2.30_a, whereas the POM image of the corresponding xerogel, obtained leaving the gel sample several hours on a warm hot-stage (30°C), in order to undergo complete dehydration, is reported in Figure 3.2.30_b. The sample, before and after removal of the solvent, displays identical features in texture with exception of well defined cracks due to partial shrinkage that occurred during drying of the gel phase.
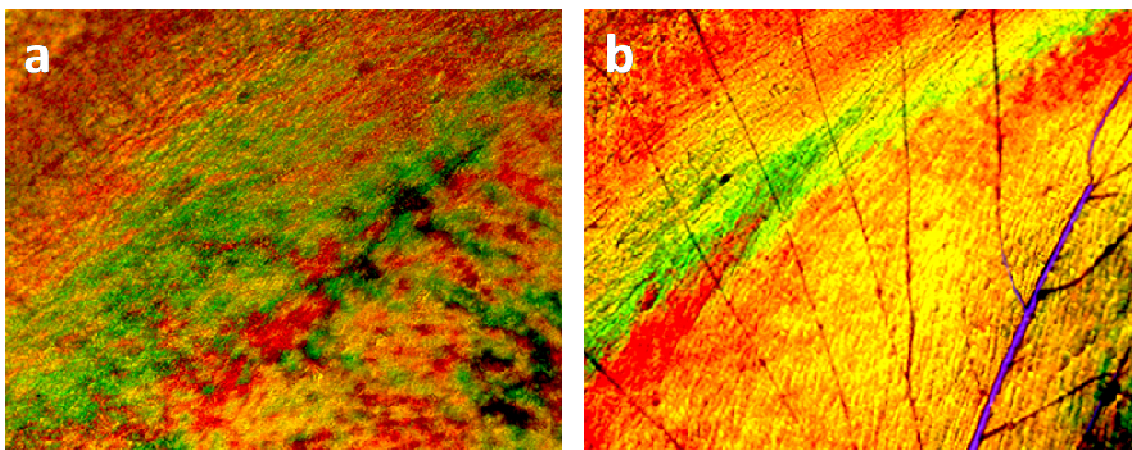
Figure 3.2.30. POM micrographs of the gel phase in water of **15** at a concentration value of 5 % w/w (a) and the corresponding xerogel obtained after complete dehydration on the warm hotplate (b).

For all the above mentioned reasons, and considering the low maximum concentration at which a supramolecular phase is obtainable for these systems, the compounds **13**, **14**, **15** and **16** can be labelled as hydro-metallogelators.

3.2.4.4 Transmission Electron Microscopy (TEM) analysis

As described in paragraph 3.1.1, the supramolecular gelator molecules, in a defined solvent and range of concentration, are able to self-assemble through non-covalent interaction, generating a 3D network of entangled fibers.

In order to verify the presence of these aggregates, the gel phases formed by compounds **13**, **14**, **15** and **16**, were examined under a transmission electron miscroscope (TEM). The samples were prepared depositing high diluted droplets of these gel phases on a copper grid and letting them dry for several days. Indeed, the TEM images (Fig.3.2.31) revealed the presence of the fibrous matrix typical of gel phases, with filaments of *ca*. 20-30 nm of diameter. Although the deposition was effectuated at concentration well-below gelification, the slow evaporation of the solvent induces rise in the concentration of the complex molecules, which exhibit their high tendency to self-assemble into ordered fibrous structures. Noteworthy, the TEM image taken at the edge of the residual droplets (Figure 3.2.31_b) reveals an efficient stacking of the fibers in the preferential direction of the droplet borders giving rise to a highly ordered texture.
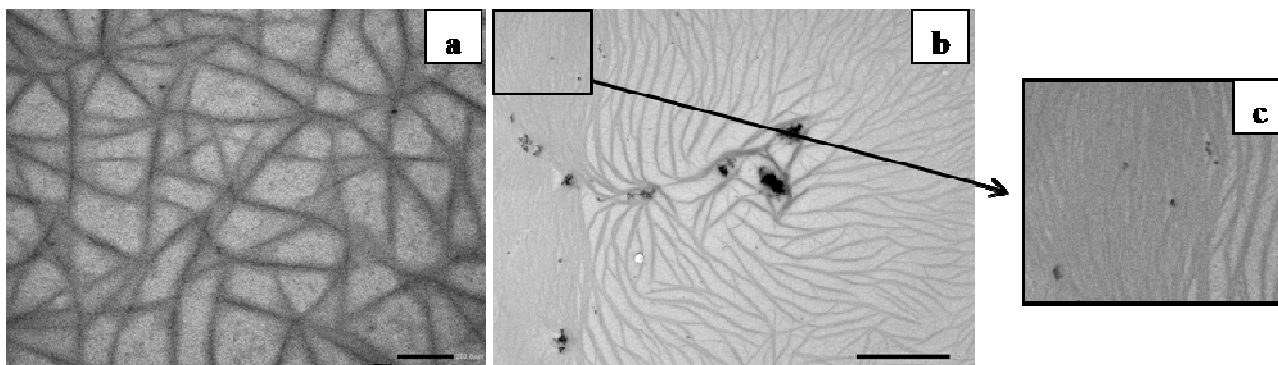
Figure 3.2.31. TEM micrographs of a dried droplet of water solution of complex **[(ppy)₂Ir(bpy)](CH₃CH₂OCH₂CO₂)** taken in the middle (a) and on the edge (b) of the residual droplet, with insert (c) showing magnification of the region in which fibers self-align.

3.2.4.5 Powder X-Ray Diffraction (PXRD) analysis

The observation of birefringent textures in the gel phase and xerogel films, originated from the metallogelators **[(ppy)₂Ir(bpy)]X** (X = EtO⁻, OH⁻, EtOCH₂CO₂⁻, MeOCH₂CO₂⁻), offers some insight into the presence of ordered anisotropic structures. For this reason, the supramolecular architecture of these materials was investigated through Powder X-Ray Diffraction (PXRD) analysis.

First, PXRD pattern were acquired for the gel phases of complex **[(ppy)₂Ir(bpy)]EtOCH₂CO₂ (15)** at different concentrations (3%, 4%, 5% and 6% w/w) (Fig.3.2.32).
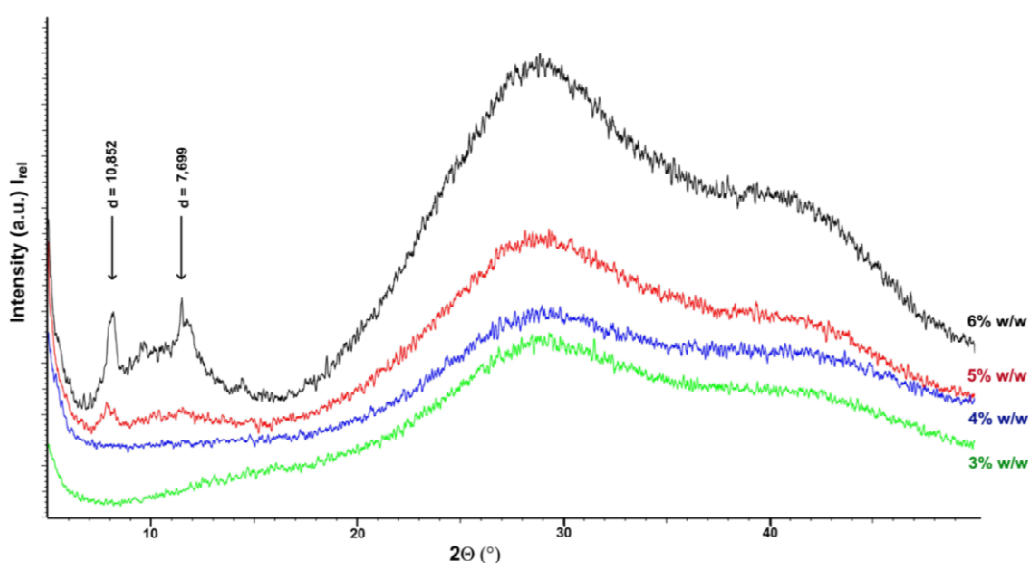
Figure 3.2.32. PXRD patterns of gel phases of compound **15** (3%, 4%, 5%, 6% w/w from bottom to top).

As expected, the medium and wide angle regions of all the four spectra are characterized by broad halos, due to a strong interference of water. Indeed, it should be pointed out that gels are binary systems, in which the solvent is the component present in higher proportions (> 94%). Moreover, in the PXRD profiles of the gel phases at 3% and 4% w/w, the liquid part completely precludes the visualization of useful reflection peaks also in the small-medium region of the spectrum, despite birefringence is noticeable even at these low concentrations. The PXRD pattern of the sample at 5% w/w exhibits some emerging reflections in the small-medium region. These peaks become well-defined in the most concentrated gel phase (6% w/w) and correspond to the interplanar spacing distances of 10.85 Å and 7.70 Å. In order to exclude the presence of solid particles of the gelator, the PXRD spectrum of the polycrystalline powder of complex **15** was acquired and compared to the profile of the 6% w/w gel sample (Fig.3.2.33). The comparison reveals the absence of overlap between the signals belonging to the two different spectra and allows to demonstrate that the reflection peaks emerged in the 6% w/w gel pattern result from a new molecular arrangement.
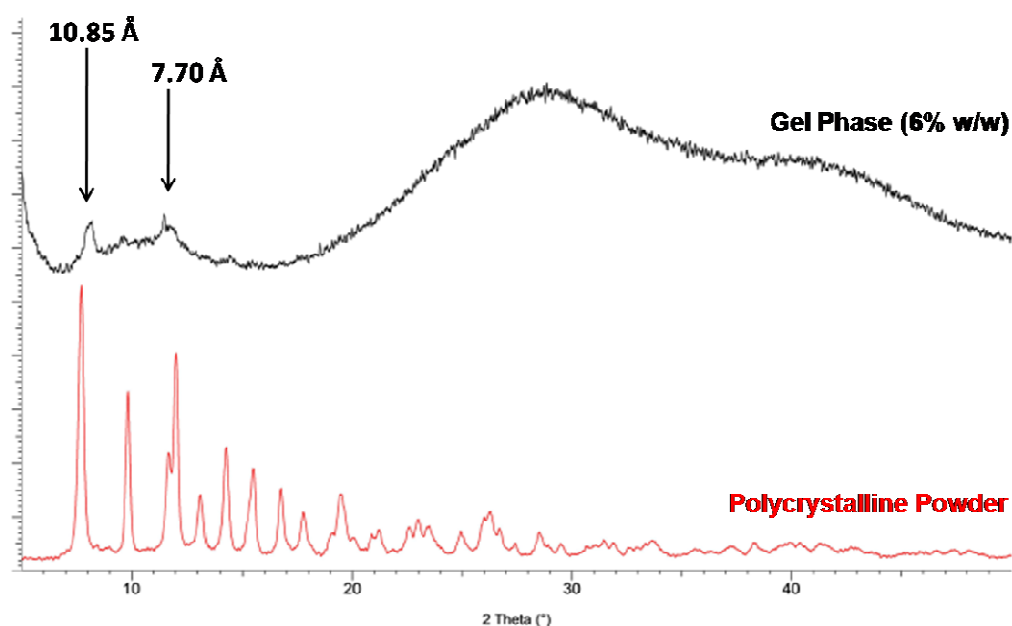
Fig.3.2.33. Comparison between PXRD spectra of polycrystalline powder (red) and 6% w/w gel sample of compound **15** (black).

Taking into account the TEM analysis performed in these samples, showing the high tendency of the complex to self-assemble into elongated fibers, which, in turn, can reflect a columnar aggregation of gelator molecules, the two observed reflections are in agreement with a simple columnar tetragonal 2-D system (Col_t). For a tetragonal 2D system, the interplanar distances d_{hk} are given by:

$$\frac{1}{d_{hk}^2} = \frac{h^2 + k^2}{a_t^2} \qquad \text{eq. 3.2.2}$$

The first reflection peak (d = 10.85 Å) can be correlated to the d_{10} interplanar distance, while the second reflection (d = 7.70 Å) can be associated with the d_{11} distance. Indeed, due to the high symmetry of the *p4mm* space group, for a Col_t system the d_{11} value is correlated to the d_{10} value through the relation $d_{11} = d_{10}/\sqrt{2}$, which is perfectly fitting in this case (Table 3.2.6).

d_{obs} (Å)	d_{hk} (system)	d_{calcd} (Å)[a]	Cell parameters Col_t a_t = 10.85 Å
10.85	$d_{10}(Col_t)$	10.85 [b]	
7.70	d_{11} (Col_t)	7.68	

Table 3.2.6. Indexation of PXRD spectra of **[(ppy)$_2$Ir(bpy)](CH$_3$CH$_2$OCH$_2$CO$_2$)** in 6% w/w gel phase. [a] Calculated data were obtained using LCDixRay program. [70] [b] Data chosen for calculations.

The strong predisposition of compound **15**, and of the other related complexes, to self-assemble through non-covalent interaction generating soft materials, precluded the formation of single crystals, suitable for X-ray crystallography technique. Nevertheless, crystallographic data of the parent complexes **[(ppy)$_2$Ir(bpy)](Cl)**,[94] **[(ppy)$_2$Ir(bpy)](PF$_6$)**[95] and **[(ppy)$_2$Ir(bpy)][B(C$_6$F$_5$)$_4$]**,[96] incorporating the same cationic part of **15**, have been reported. Within the crystal structures of all the above mentioned compounds can be recognized tetrameric motifs in which the distances separating two Iridium atoms fall within the range 7,919 Å<$d_{Ir...Ir}$< 13,333 Å. These experimental data support the hypothesis of the presence of tetragonal columnar structures within the gel phase of **[(ppy)$_2$Ir(bpy)](CH$_3$CH$_2$OCH$_2$CO$_2$) (15)**. Furthermore, the lattice parameter a_t=10.85 Å of the Col_t phase is comparable in value to the distances Ir-Ir observed in the complexes **[(ppy)$_2$Ir(bpy)](Cl)**, **[(ppy)$_2$Ir(bpy)](PF$_6$)** and **[(ppy)$_2$Ir(bpy)][B(C$_6$F$_5$)$_4$]** (Fig.3.2.34).
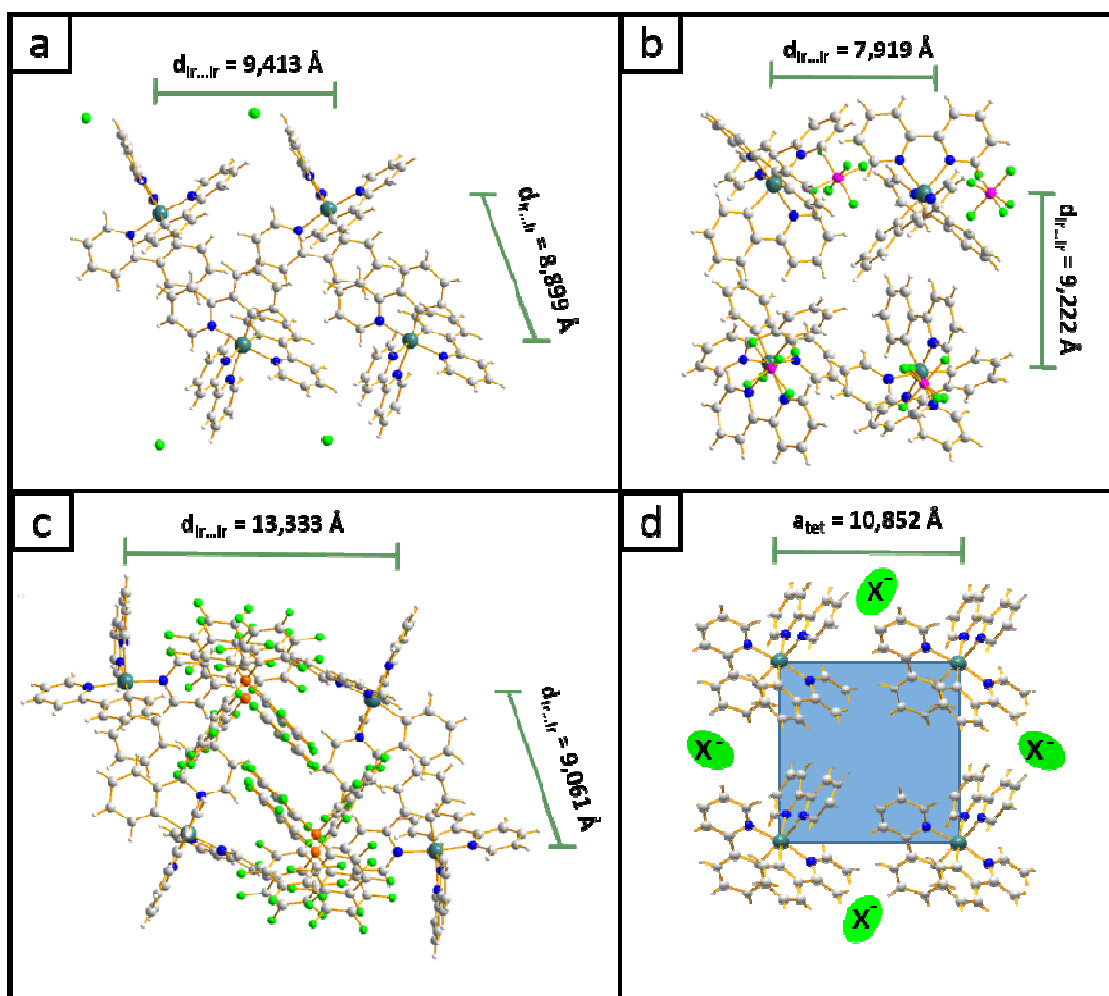
Figure 3.2.34. Tetrameric motifs in the crystal structures of a):**[(ppy)$_2$Ir(bpy)](Cl)**[94], b) **[(ppy)$_2$Ir(bpy)](PF$_6$)**[95] and c)**[(ppy)$_2$Ir(bpy)][B(C$_6$F$_5$)$_4$]**.[96] d) Hypothesized Col$_t$ lattice for **[(ppy)$_2$Ir(bpy)](CH$_3$CH$_2$OCH$_2$CO$_2$)** in gel phase.

It is commonly assumed that the xerogel phase retains quasi-identical supramolecular organization than the relative gel phase.[76] This hypothesis in the present case is also corroborated by the similarities of textures observed under POM of the two phases (Fig.3.2.30). For this reason the PXRD study of the xerogels were carried out. This analysis allows a deeper insight of the supramolecular structure of the gel, by removing the strong solvent interference from the PXRD spectra.

For all gel concentration solutions (3% to 6% w/w), the PXRD patterns of the obtained xerogels are all identical. The PXRD pattern of the xerogel generated from the 6% w/w gel phase is reported in Figure 3.2.35 together with the PXRD spectrum of the polycrystalline powder of complex **15**, in order to rule out a partial crystallization of the gelator which could occur during solvent evaporation. Figure 3.2.35 shows the absence of overlap

between the signals belonging to the two different spectra, indicating that the xerogel PXRD pattern results from a new molecular arrangement. In Fig.3.2.36 a match-up between PXRD spectra of xerogel and 6%w/w gel phase of complex **15** is provided.
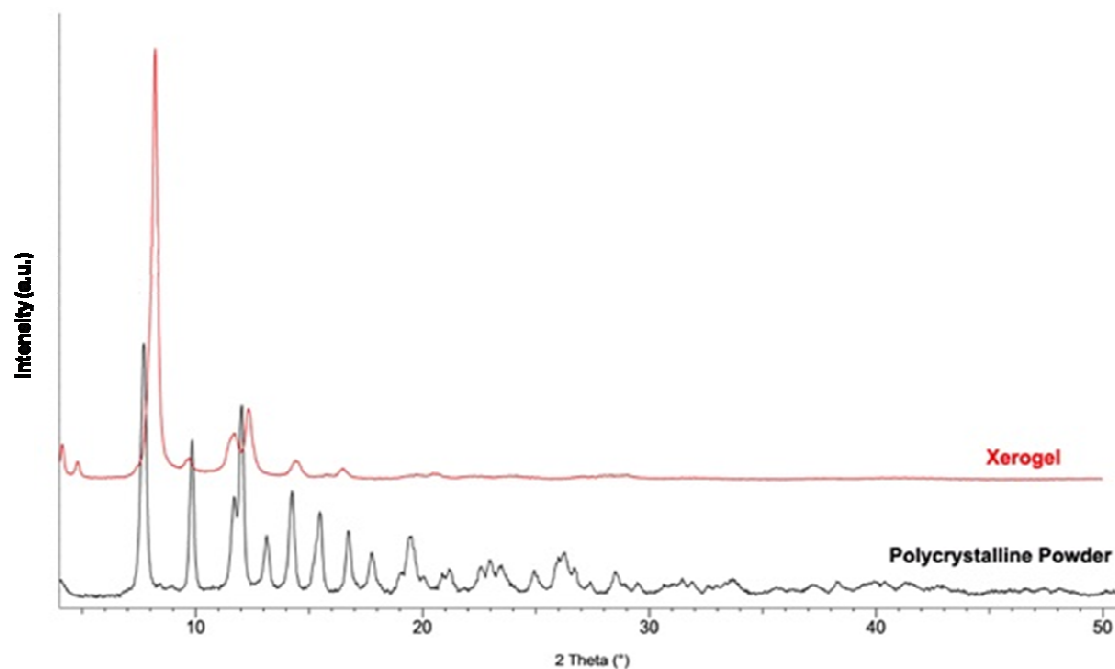
Figure 3.2.35 PXRD patterns of the xerogel (in red) and of the polycrystalline powder (in black).
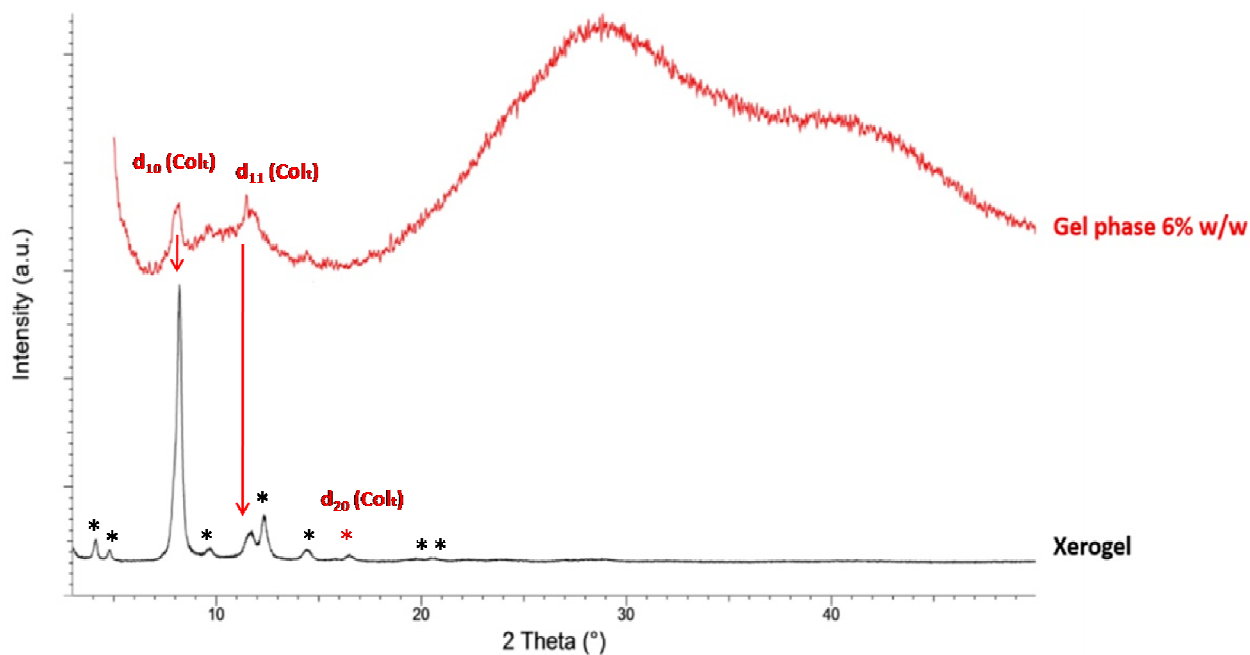
Figure 3.2.36 PXRD patterns of the xerogel (in black) and of the 6% w/w gel phase (in red) of compound **15**.

The two reflection peaks found in the PXRD pattern of the most concentrated gel phase (6% w/w), corresponding to the d_{10} and d_{11} interplanar distances of a Col_t system, can be retrieved in the PXRD spectrum of the xerogel at d = 10.75 Å and d = 7.56 Å respectively. These values are slightly lower than those measured in the pattern of the gel phase (10.85 Å and 7.70 Å) probably for a shrinkage effect of the columnar lattice occurring during evaporation of the solvent. The same effect is responsible for the appearance of well defined cracks into the xerogel films observed under POM (Fig.3.2.30). The disappearance of the water-induced broadening background allows the detection of another reflection peak (indicated with the red * in Fig.3.2.36), that can be assigned to the Col_t system, which falls at d = 5.37 Å and corresponds to the d_{20} interplanar distance. However, many other signals (indicated with black * in Fig.3.2.36) are evident in the xerogel PXRD pattern and cannot be relative to the Col_t lattice.

A similar case was reported by Resta *et al.*[76] who described the XRD analysis of a xerogel derived from a triphenilene-derivative gel in methanol. They indexed the XRD pattern as a simple hexagonal 2D system with an intercolumnar distance of 49 Å. Since this value shall be presumed to be too high for a simple stacking of triphenilene units and since the intensities of the reflections corresponding to d_{11} and d_{21} of the Col_h system were too elevated, they suggested that each column with hexagonal symmetry is built up by four columns of individual triphenilene motifs self-organized in a 2D tetragonal lattice.

Drawing inspiration from this study, the additional reflection peaks found in the PXRD pattern of the xerogel of complex **15** have been indexed as a second supramolecular ordered structure. In particular, using LCDiXray, all new peaks can be indexed through a columnar oblique (Col_o) system built up by four columns of complexes molecules arranged in the Col_t sub-unit system (Figure 3.3.37 and Table 3.2.7).

For an oblique 2D system, the interplanar distances d_{hk} are given by:

$$\frac{1}{d_{hk}^2} = Ah^2 + Bk^2 + Chk \qquad \text{eq. 3.2.3}$$

$$A = 1/(a_o^2 sin^2\gamma); \ B = 1/(b_o^2 sin^2\gamma); \ C = -2cos\gamma/a_o\, b_o\, sin^2\gamma$$
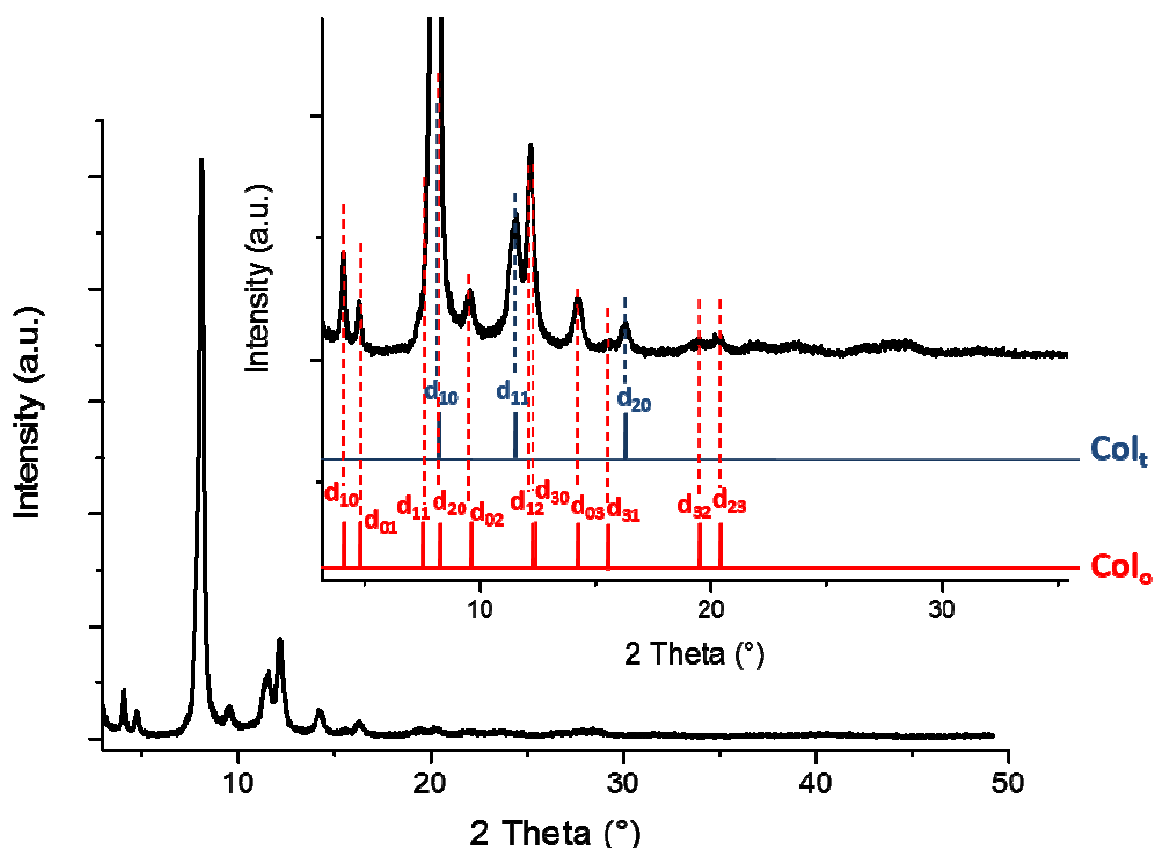
Figure 3.2.37. PXRD pattern of **[(ppy)₂Ir(bpy)](CH₃CH₂OCH₂CO₂)** in the xerogel phase and relative indexation.

d_{obs} (Å)	d_{hk} (system)	d_{calcd} (Å)[a]	Cell parameters
21.43	$d_{10}(Col_o)$	21.43[b]	
18.38	$d_{01}(Col_o)$	18.38[b]	Col_t
10.75	$d_{10}(Col_t)$	10.75	a_t = 10.75 Å
	d_{11} (Col_o)	11.28[c]	
	d_{20} (Col_o)	10.71[c]	Col_o
9.12	d_{02} (Col_o)	9.19	a_o = 25.40 Å
7.56	d_{11} (Col_t)	7.60	b_o = 21.79 Å
7.17	d_{12} (Col_o)	7.17[b]	γ = 57.5 °
	d_{30} (Col_o)	7.14[c]	
6.14	d_{03} (Col_o)	6.13	
5.68	d_{31} (Col_o)	5.70	
5.37	d_{20} (Col_t)	5.38	
4.55	d_{32} (Col_o)	4.80	
4.33	d_{23} (Col_o)	4.39	

Table 3.2.7. Indexation of PXRD spectra of the xerogel of **[(ppy)₂Ir(bpy)](CH₃CH₂OCH₂CO₂)** [a] Calculated data were obtained using LCDixRay program. [70] [b] Data chosen for calculations. [c] possible overlapped reflection peaks.

Furthermore, the relative intensities and the slight broadening of specific peaks (d = 10.75 Å and d = 7.17Å) can also be rationalized due to the possible overlapping of signals coming from the two columnar systems.

All PXRD data reported in Tables 3.2.5 and 3.2.6, together with the calculated interplanar distances, were obtained through LCDiXRay program.[70]

Noteworthy, a carefull inspection of the PXRD pattern of the 6% w/w gel phase (Figure 3.2.38) allows to notice, in addition to the two well defined Col_t reflection peaks, less distinguishable reflection peaks at 2θ = 9.6° (d = 9.16 Å) and 2θ = 14.4° (d = 6.15 Å), that could be relative to the d_{02} = 9.19 Å and d_{03} = 6.13 Å reflections of the Col_o lattice that are observed more accurately in the PXRD pattern of the xerogel. The presence of these supplementary peaks in the PXRD pattern of the gel phase would indicate that both Col_t and Col_o organizations are present within the gel phase. An in-plane view and a 3D view of the supramolecular highly ordered architecture of the gel phase are shown in Figure 3.2.39.
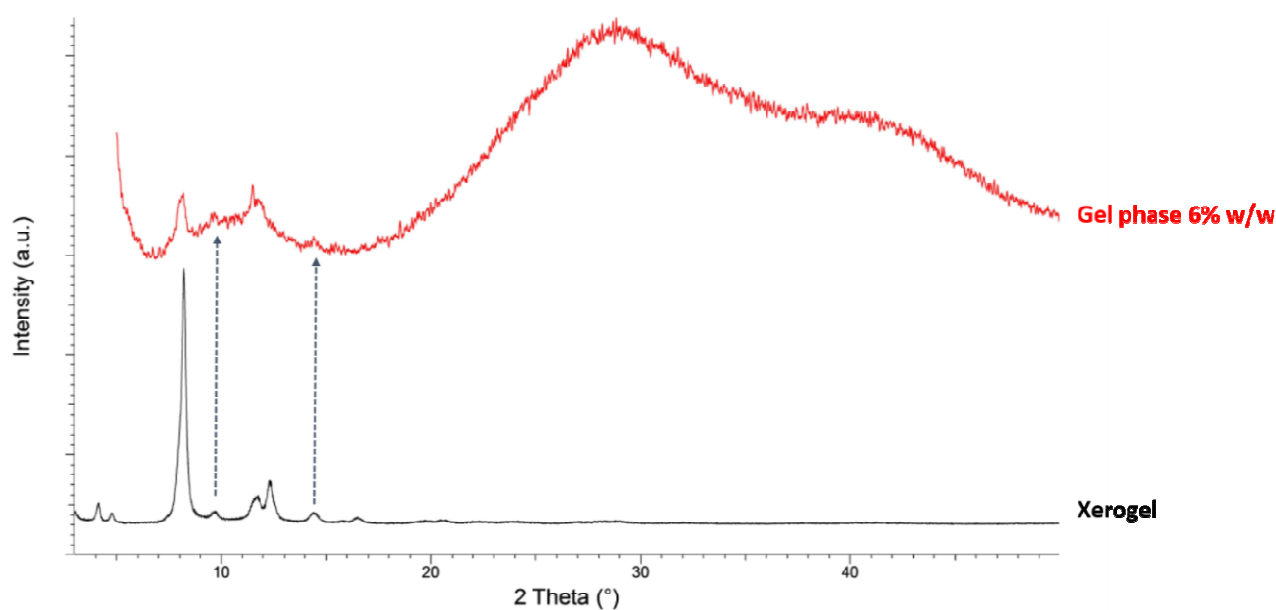
Figure 3.2.38. PXRD patterns of the 6%w/w gel phase (in red) and of the xerogel (in black).
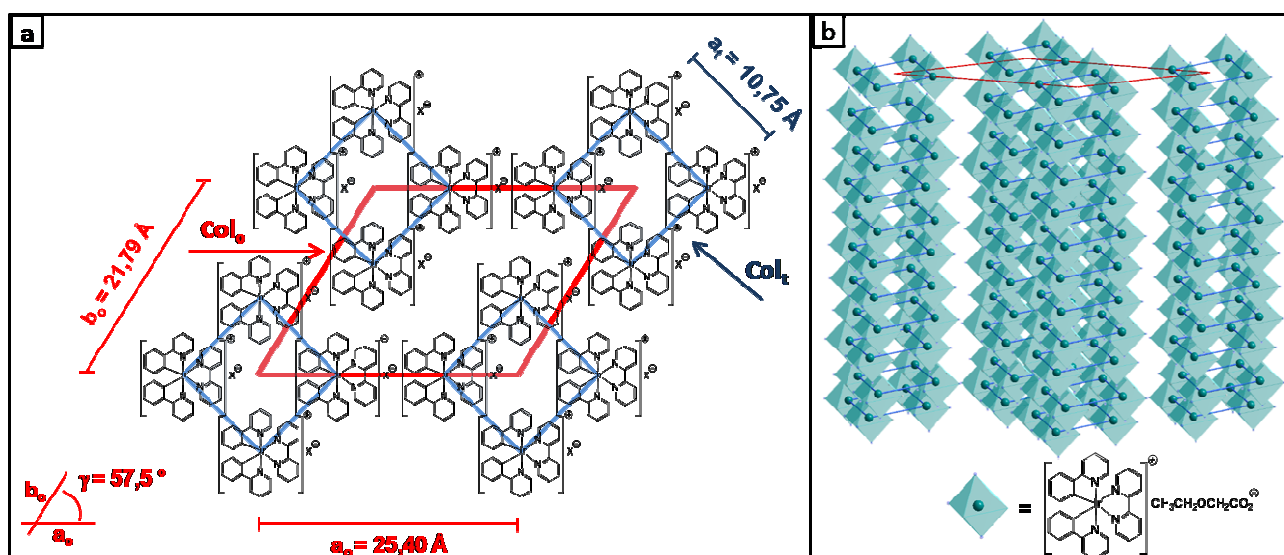
Figure 3.2.39. Assumed self-assembled supramolecular structure for the gel phase in water of **[(ppy)₂Ir(bpy)](CH₃CH₂OCH₂CO₂)**, an in-plane view (a) and a 3D sketch (b).

In the case of compound **16** a similar trend was observed, since this compound differs only minimally from complex **15**. The PXRD pattern of the xerogel derived from the 5% gel phase of **[(ppy)₂Ir(bpy)](CH₃OCH₂CO₂)** is reported in Fig.3.2.40 together with its indexation (Table 3.2.8). Similar to the PXRD spectra of xerogel of **15**, several reflection peaks can be observed in the small- and medium-angle region of the spectra, which can be attributed to a double symmetrical system, consisting of tetragonal columns, in turn self-organized in an oblique columnar configuration. However, in this case, the cell parameters both of the tetragonal and oblique systems, a_t = 10.05 Å (for the Col$_t$), a_o = 25.27 Å, b_o = 21.32 Å, γ = 128.6 °(for the Col$_o$), respectively, are slightly lower than those observed in the architecture of the xerogel derived from compound **15**, a_t = 10.75 Å, a_o = 25.40 Å, b_o = 21.79 Å, γ = 57.5 °. This could be explained by the smaller size of the counter-anion present in **16** (CH₃OCH₂CO₂⁻) with respect to the one of **15** (CH₃CH₂OCH₂CO₂⁻). Note that γ = 128.6 ° is approximately the complementary angle of γ = 57.5 °. The 2D structures of the supramolecular phases originated from **15** and **16** are confronted in Fig.3.2.41.
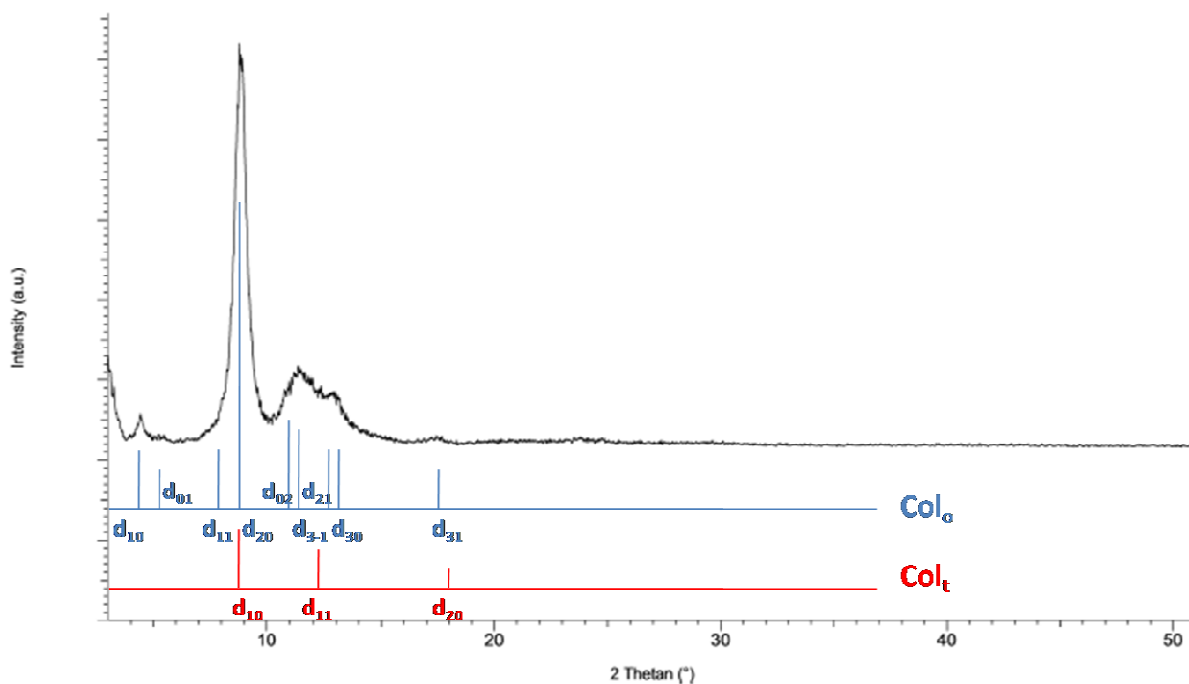
Figure 3.2.40. PXRD pattern of **[(ppy)$_2$Ir(bpy)](CH$_3$OCH$_2$CO$_2$)** in the xerogel phase and relative indexation.

d$_{obs}$ (Å)	d$_{hk}$ (system)	d$_{calcd}$ (Å)[a]	Cell parameters
19.89	d$_{10}$(Col$_o$)	19.89[b]	
16.79	d$_{01}$(Col$_o$)	16.79[b]	**Col$_t$**
10.12	d$_{11}$(Col$_o$)	10.12	**a$_t$ = 10.05 Å**
	d$_{2-2}$ (Col$_o$)	10.24[c]	
	d$_{10}$(Col$_t$)	10.05[c]	**Col$_o$**
9.94	d$_{20}$ (Col$_o$)	9.94	**a$_o$ = 25.27 Å**
8.20	d$_{02}$(Col$_o$)	8.39	**b$_o$ = 21.32 Å**
7.72	d$_{3-1}$ (Col$_o$)	8.10	**γ = 128.6 °**
7.26	*d$_{11}$ (Col$_t$)*	7.10	
6.85	d$_{21}$ (Col$_o$)	6.89	
6.66	d$_{30}$ (Col$_o$)	6.63	
5.17	d$_{31}$ (Col$_o$)	5.17	
5.03	*d$_{20}$ (Col$_t$)*	5.02	

Table 3.2.8 Indexation of PXRD spectra of the xerogel of **[(ppy)$_2$Ir(bpy)](CH$_3$OCH$_2$CO$_2$)** [a] Calculated data were obtained using LCDixRay program. [70] [b] Data chosen for calculations. [c] possible overlapped reflection peaks.
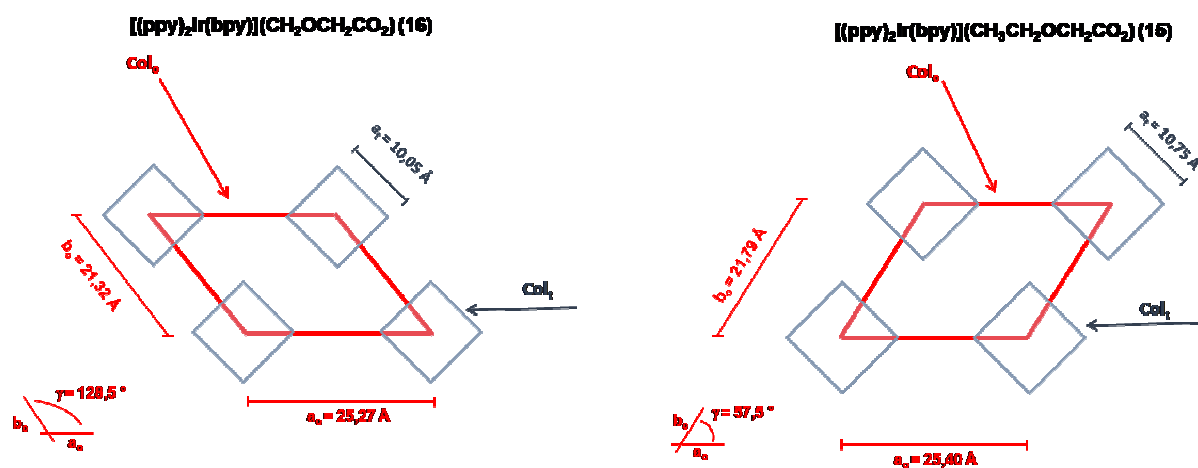
Figure 3.2.41. Comparison between the 2D supramolecular structures of complexes **16** (on the left) and **15** (on the right).

3.2.5 Photophysical characterization of [(ppy)₂Ir(bpy)]X metallo-hydrogelators

The photophysical properties of all the synthetized metallo-hydrogelator complexes, **13**, **14**, **15** and **16**, were investigated, both in solution and gel phase, through UV-vis, fluorescence and time-resolved spectroscopy.

The photophysical study in solution was performed in dichloromethane, as well as water, in order to compare the photoluminescence properties of compounds **13**, **14**, **15** and **16** with the parent complex **[(ppy)₂Ir(bpy)]Cl**. This parallelism allowed to evaluate the potential influence of hydrophilic counter-anions on the photoluminescence properties of the photoactive **[(ppy)₂Ir(bpy)]⁺** cation.

In dichlorometane solution, the absorption spectra of complexes **13–16** are consistent with the reference **[(ppy)₂Ir(bpy)]Cl** complex (Fig. 3.2.42).
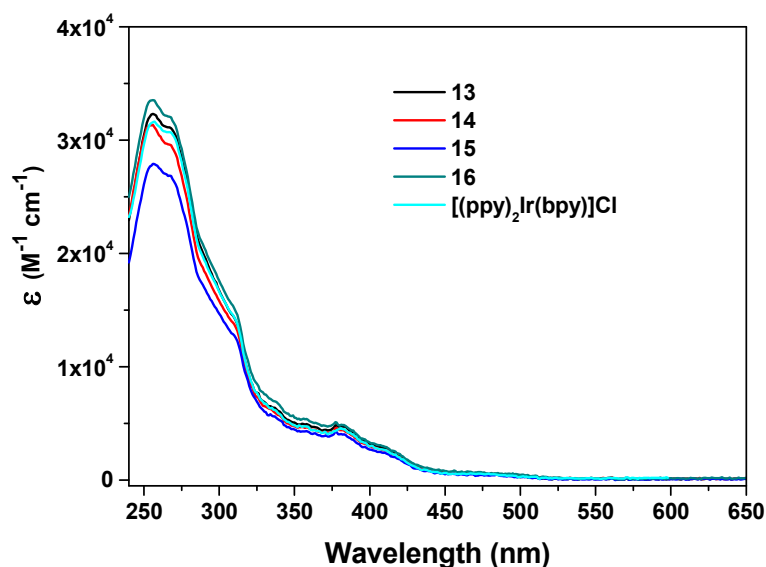
Fig.3.2.42 Absorption spectra of complexes **13**–**16** and **[(ppy)₂Ir(bpy)]Cl** in deaerated CH_2Cl_2 solution (5.0 × 10^{-6} M).

The spectra are dominated by two intense and partially overlapping absorption bands, with $\varepsilon = 10^4$ $M^{-1}cm^{-1}$, at 256 nm and 267 nm arising from spin-allowed $^1\pi$–π^* ^{1}LC transitions involving the (**ppy**) and (**bpy**). As reported by Zysman-Colman[97] *et al*. and Ko *et al*.,[98] these high energy intraligand (^{1}IL) transitions, corresponding to those of the cyclometalated ligands and the ancillary ligands, are characteristic of polyimine Ir(III) complexes. At higher wavelengths (310–430 nm), meaning lower energies, less-intense absorption bands are present. The nature of these bands have been recently investigated by Colman *et al*.[97], with the aid of theoretical calculations. They attributed these bands to an admixture of spin-allowed charge-transfer (^{1}CT) transitions that comprise both $d\pi$ - π^*_{bpy} metal-to-ligand (^{1}MLCT) and π_{ppy}- π^*_{bpy} ligand-to-ligand (^{1}LLCT) transitions. Additionally, very low intensity bands around 450 nm are assigned to spin-forbidden ^{3}MLCT and ^{3}LLCT transitions induced by the large spin–orbit coupling of Ir. All compounds **13-16** exhibit similar photophysical properties, the cation **[(ppy)₂Ir(bpy)]⁺** being the site of the explored electronic transitions.

In water, only complexes **14-16** have been investigated. Indeed, ethoxy complex **13** is completely converted into the hydroxyl complex **14** when dissolved in water, as reported in paragraph **3.2.1.3**, consequently the absorption spectra of both complexes in water solution are identical (Fig.3.2.43_a). The absorption spectra of complexes **14-16** in deaerated water solution are shown in Fig.3.2.43_b.
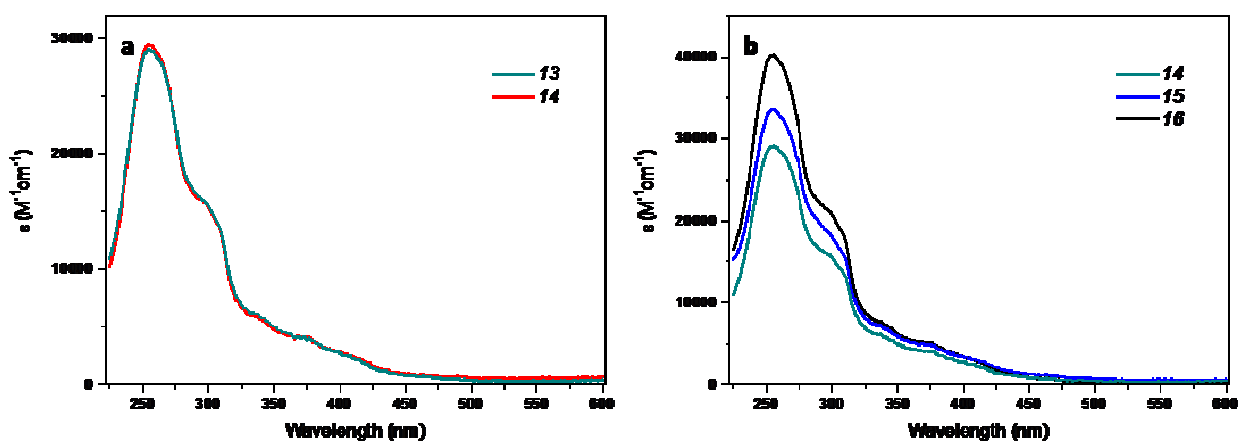
Figure 3.2.43. Absorption spectra of complexes **13** and **14** in deaerated water solution (a) and of complexes **14**, **15** and **16** in deaerated water solution (b).

When highly diluted in water (c = 5.0 × 10^{-6} M), the absorption spectra of **14**–**16** are practically superimposable with the spectra obtained in dichloromethane.

All the synthetized Ir (III) metallo-hydrogelators **13-16** emit in the orange region of the visible spectrum. The cationic motif of the complexes **[(ppy)₂Ir(bpy)]$^{+}$** is responsible for the emission, as well as for the absorption properties, and the dynamics of its excited states has been recently studied through time-resolved spectroscopy and theoretical calculations.[99] In this study, Chen *et al*. attributed the triple phosphorescence in blue, green and orange bands, to the possible emissive states, ^{3}LLCT, ^{3}MLCT$_{ppy}$ and ^{3}MLCT$_{bpy}$, respectively. Therefore, the observation of orange emission for compounds **13-16** was ascribed to the radiative deactivation to the ground state of lowest triplet excited state ^{3}MLCT$_{bpy}$.

Unlike the absorption spectra, the emission profiles of the **[(ppy)₂Ir(bpy)]X** complexes recorded in dichlorometane and water solution (Fig.3.2.44_a and Fig.3.2.44_b, respectively) show some substantial differences.
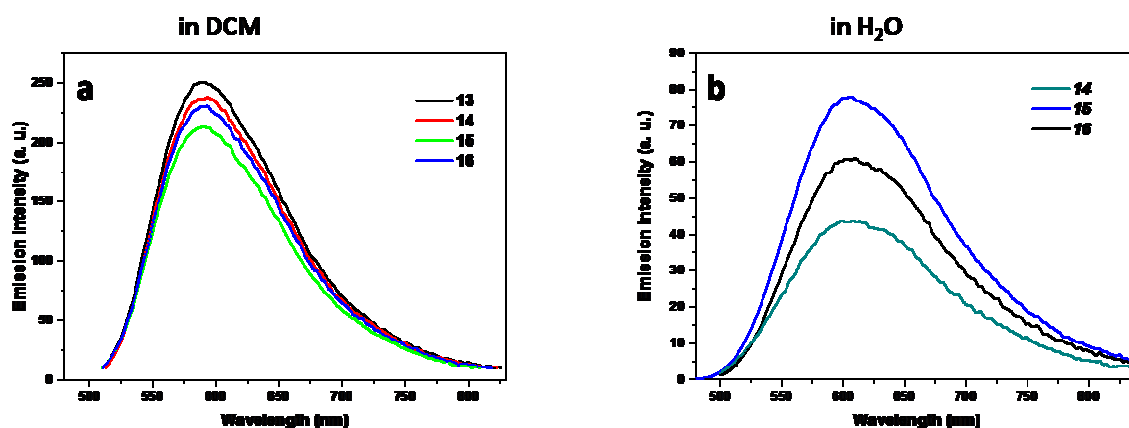
Figure 3.2.44. Emission spectra of complexes **13-16** in CH_2Cl_2 solution (a) and of compounds **14-16** in water solution (b).

A structureless orange emission is recorded with a maximum centred at 606 nm for the compound **14-16** in water solution, whereas the same emission bands are narrowed and blue-shifted (centered at 593 nm) in CH_2Cl_2. The photoluminescence quantum yield (ɸ) varies from 1.9 to 2.2% in water, thus are lower than the ones registered in dichlorometane (16.2 < ɸ < 18.5 %). Moreover, excited state decays of all complexes show bi-exponential kinetics in water solution, with a preeminent lifetime value of 40 ns and a secondary more lasting value ranging from 126 to 531 ns, whereas decay times can be fitted by a single exponential function in CH_2Cl_2 solution and cover a values range from 485.0 to 549.3 ns. The maximum absorption and emission wavelengths (λ_{max}), the photoluminescence quantum yields (ɸ) and lifetimes of the excited states (τ), in water and CH_2Cl_2 diluted solutions, are reported in Table 3.2.9.

	Deaerated dichlorometane solution (5.0 x 10^{-6} M)			
	Absorption λ_{max}/nm(ε/M^{-1}cm^{-1})	Emission λ_{max}/nm	Φ/%	Lifetime τ/ns
13	256(32310)-267(31150)-311(14080)-338(6250)-380(4750)-410(2820)-475(575)	593	18.5	549.3
14	256(31345)-267(29590)-311(13485)-338(5870)-380(4425)-410(2655)-475(570)	593	18.0	533.6
15	256(27915)-267(26875)-311(12550)-338(5500)-380(4065)-410(2420)-475(455)	593	18.0	530.9
16	256(33530)-267(32080)-311(14875)-338(6900)-380(4825)-410(2960)-475(660)	593	16.2	485.0
[(ppy)₂Ir(bpy)]Cl	256(31615)-267(30750)-311(13980)-338(6025)-380(4585)-410(2700)-475(535)	590	14.9	448.1
	Deaerated water solution (5.0 x 10^{-6} M)			
	Absorption, λ_{max}/nm(ε/M^{-1}cm^{-1})	Emission, λ_{max}/nm	Φ/%	Lifetime, τ/ns(α/%)
14	255(29080)-295(16000,sh)-336(6095)-373(4100)-415(2100,sh)-465(740)	606	1.9	39.0(97.2),362.0(2.8)
15	255(33555)-295(18900,sh)-336(7295)-373(4965)-415(2800,sh)-465(1150)	606	2.2	40.9(91.9),531.0(8.1)
16	255(40125)-295(21300,sh)-336(7740)-373(5130)-415(2600,sh)-465(790)	606	2.1	39.0(97.6),126.5(2.4)

Table 3.2.9. Photophysical data of complexes **13-16** and the analogous **[(ppy)₂Ir(bpy)]Cl** in dichlorometane and water diluted solutions.

The overall behaviour can be explained by considering the difference in the polarity of the two solvents and the formation of aggregates in water, whose the second lifetime value observed in this solvent can be attributed. In CH$_2$Cl$_2$, the single lifetime decays derives from the non-aggregated **[(ppy)₂Ir(bpy)]X** ionic pairs and the lifetime values measured are almost invariant within the series of complexes, thus do not depend on the anion. The short lifetime observed in water, accounting for most of the luminescence decay (92–97%), is also unaffected by the type of anion, therefore it can be assigned to the isolated cationic species **[(ppy)₂Ir(bpy)]⁺**. Indeed, in high diluted water solution, ionic compounds **14–16** are mainly solvated and basically exist as isolated species. On the contrary, the additional longer decay observed in high diluted water solution clearly depends on the type of anion, displaying the values of 362 ns for complex **14**, 531 ns for **15** and 126 ns for **16**, but represent the smallest proportion of the luminescence decay (2.4 - 8.1%). Despite the fact that the concentration value (i.e. 5x10^{-6}M) is very far from the critical gel concentrations of compounds **13-16**, the estimation of the longer lifetime could be related to the pre-generation of supramolecular assemblies.

Moreover, the difference between the primary lifetime values measured in water (*ca.*40 ns) and the lifetime value registered in CH$_2$Cl$_2$ (*ca.* 520 ns) is due to the difference in the

polarity of the two solvents, as already observed by Chen *et al.*[99] Indeed, lifetime decays dramatically decrease with the increase of solvent polarity (normalising the values of relative polarity[100]). This is further confirmed by comparing the data registered in water solution with those reported for a series of **[(ppy)₂Ir(bpy)]X** complexes ($X^- = Cl^-$, PF_6^- or CH_3COO^-) in solvents with different polarity values (Fig.3.2.45, Table 3.2.10). Indeed the radiative decays of the excited isolated **[(ppy)₂Ir(bpy)]⁺** cation decrease from т = *ca.* 520 ns in CH_2Cl_2, *ca.* 350 ns in CH_3CN,[101,102] *ca.* 260 ns in CH_3OH[54,101] and *ca.* 40 ns in H_2O (Table 5). In tandem with the decrease of the excited state lifetimes, a reduction of the associated photoluminescence quantum yield (Φ) occurs (from *ca.* 18% in CH_2Cl_2, 9% in CH_3CN,[101,102] 8% in CH_3OH[54,101] and 2% in H_2O respectively). These two trends further confirm the attribution of the short time decay in water to the isolated **[(ppy)₂Ir(bpy)]⁺** cation.
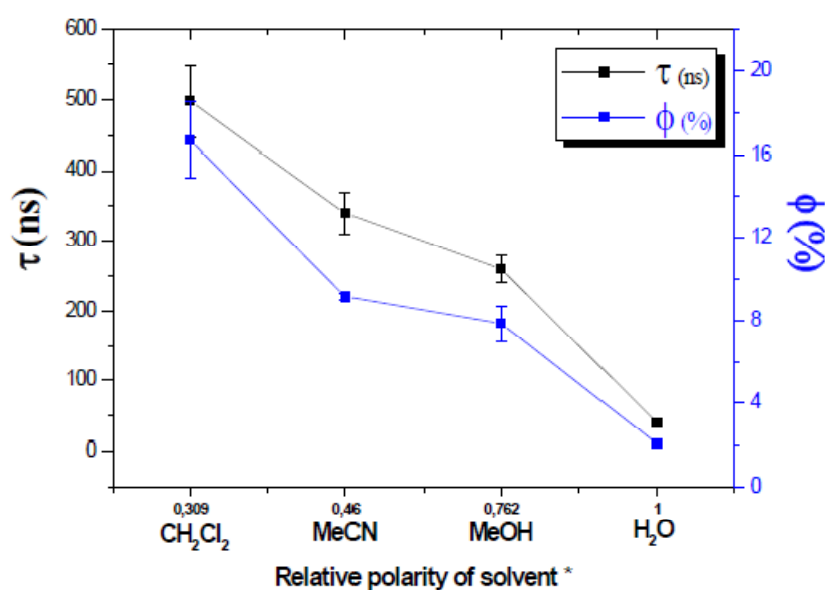
Fig. 3.2.45. Life time decay (т, ns) and luminescence quantum yield (ϕ, %) of the exited state of the cation **[(*ppy*)₂Ir(*bpy*)]⁺** with increase of solvent polarity.

Deaerated acetonitrile solution				
	Emission, λ_{max}/nm	Φ/%	Lifetime, τ/ns	Ref.
[(*ppy*)$_2$Ir(*bpy*)]PF$_6$	588	9.3	370	101
[(*ppy*)$_2$Ir(*bpy*)]Cl	585	9	310	102

Deaerated methanol solution				
	Emission, λ_{max}/nm	Φ/%	Lifetime, τ/ns	Ref.
[(*ppy*)$_2$Ir(*bpy*)]PF$_6$	588	8.7	280	54
[(*ppy*)$_2$Ir(*bpy*)](CH$_3$CO$_2$)	585	7	240	101

Table 3.2.10. Photophysical data of **[(*ppy*)$_2$Ir(*bpy*)]X** complexes in acetonitrile and methanol solutions.

In order to shed light onto the nature of the second longer lifetime decay observed in high dilution condition in water, the photophysical study of the gel phases originated from complexes **14-16** (3% w/w in water) has been performed (Fig.3.2.46). The emission spectra of compounds **14-16** in gel state show a maximum at λ ranging from 567 to 580 nm, thus a blue shift of the emission maxima with respect to the diluted water solution occurs. Even this effect may be assigned to the change in polarity experienced by the cation **[(ppy)$_2$Ir(bpy)]$^+$**. The dependence of the MLCT emission bands from the solvent polarity have been already reported for Ir (III) ortho-metalated complexes by Watts *et al*.[103] The creation of supramolecular assemblies in the gel phase can be viewed as a change in the enclosing polarity of the cations **[(ppy)$_2$Ir(bpy)]$^+$**, which are now surrounded by many other complex molecules rather than water molecules.
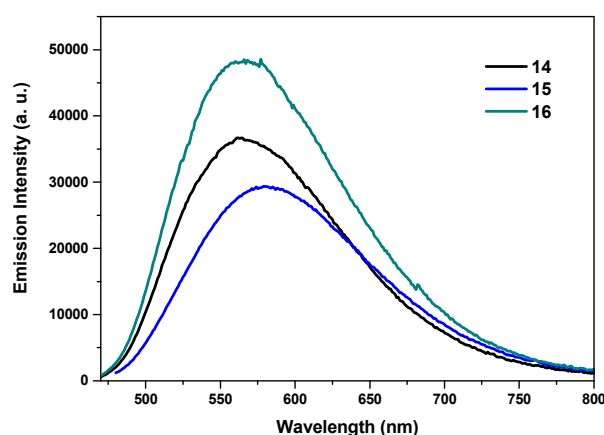
Figure 3.2.46. Emission spectra of complexes **14-16** in gel phase (3% w/w in deaerated water) at room temperature.

The excited state lifetime values for complexes **14-16** were fitted by three-exponential functions in the gel phase, thus the presence of three different lifetimes was observed (Table 3.2.11).

Complex	Emission,λ_{max}/nm	Lifetime, τ/ns(α/%)
14	567	39.5 (14.2), 125.4 (56.3), 377.1 (29.5)
15	580	28.5 (17.2), 115.9 (55.0), 336.4 (27.8)
16	567	31.9 (12.6), 120.7 (47.9), 247.1 (39.5)

Table 3.2.11. Photophysical data of complexes **14-16** in deaerated gel phase (3% w/w).

In particular, the short lifetime ranges from 28.5 to 39.5 ns and it is similar to all compounds. These values are almost identical to those reported for diluted water solution (39.0 - 40.9 ns). The observation of this lifetime shows the presence of isolated cations within the gel phase, although its low weight in the function-fitting decay (13–17%) indicates a minor quantity of these species with respect to the major quantity of the aggregated ones. Taking into account the supramolecular architecture of compounds **15** in its gel phase, elucidated through PXRD analysis, the moderate and long lifetime decays can be correlated with the establishment of different interaction modes between aggregated **[(ppy)₂Ir(bpy)]⁺** cations that are present within the gel. Indeed, the molecules self-assemble into tetragonal strands, which, in turn, generate larger columnar oblique systems. The longest lifetime decay, already observed under high dilution conditions, is highly dependent on the nature of the anion and can be correlated to the formation of the smaller **[(ppy)₂Ir(bpy)]⁺** strands surrounded by the counter-anions. The stability of these strands is influenced by the surrounding polarity, hence by the nature of the counter-anion, explaining the disparities in lifetime decays and weight within the series of complexes **14-16** (247.1 - 377.1 ns). The moderate lifetime decay, on the contrary, is unvaried within the series (*ca.* 120 ns). This decay can be associated with the coming nearer of single strands, which generate the tetragonal columns and the oblique systems. Therefore, additional interactions are established within the core of the resulting assemblies, which are reasonably less influenced by the polarity of the surrounding anions.

However, the establishment of both these interactions takes place at a concentration well below gelification, as demonstrated through the photophysical study of **15** in water solution with the progressive increase of concentration (Table 3.2.12 and Fig. 3.2.47).

Concentration (mol·L^{-1})	Emission, λ_{max}/nm	Lifetime, τ/ns (α/%)
5·10^{-6}	606	40.9 (91.9) 531.0 (8.1)
1.3·10^{-5}	593	39.4 (81.57), 444.7 (18.43)
1.3·10^{-4}	592	33.9 (60.72), 77.2 (34.44), 275.0 (4.84)
1.2·10^{-3}	590	30.2 (47.27), 83.5 (45.85), 277.8 (6.87)
4.0·10^{-2} (gel phase)	580	28.5 (17.2), 115.9 (55.0), 336.4 (27.8)

Table 3.2.12. Photophysical data of complex **15** in deaerated water solution at various concentrations.
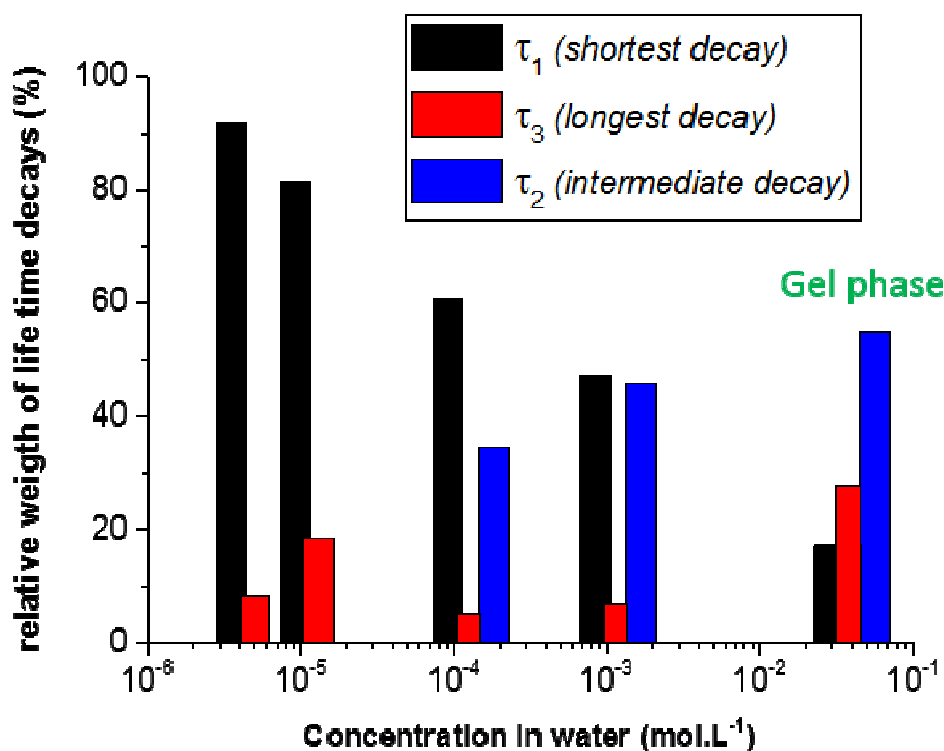
Fig. 3.2.47. Variation of the relative weight of lifetime decays of **15** in water with the progressive increase of concentration.

The shorter lifetime decay (τ_1) relative to the isolated **[(ppy)$_2$Ir(bpy)]$^+$** cations linearly decreases with the increase of concentration. The strands of cations, characterized by their longest lifetime decay (τ_3), are always present, indicative of the high self-assembling tendency of the cations. Interactions between strands, characterized by the moderate lifetime decay (τ_2) are already observable at *ca.* 10^{-4} M and their number increases with further increase of concentration until gelification.

3.3 Conclusions

In this chapter, several Ir(III) cationic complexes, in particular **[(ppy)₂Ir(dpq)]CH₃CO₂**, **[(ppy)₂Ir(dppz)]CH₃CO₂** and **[(ppy)₂Ir(bpy)]X (X = EtO⁻, OH⁻, EtOCH₂CO₂⁻, MeOCH₂CO₂⁻)**, able to generate supramolecular assemblies through the instauration of non-covalent interactions, have been presented. The compound family of the **[(ppy)₂Ir(bpy)]X** type was obtained through a newly devised synthetic pathway, summarized in Scheme 3.2.6. In addition, the complex **14** has been successfully employed as precursor of further water-soluble compounds **[(ppy)₂Ir(bpy)]CH₃CO₂ (17)** and **[(ppy)₂Ir(bpy)]BrCH₂(CH₂)₄CO₂ (18)**, incorporating two carboxylates as counterions, showing the versatile use of the hydroxide complex **14** as an efficient precursor to prepare any carboxylated derivative by a straightforward acid-base reaction effectuated upon simple addition of the corresponding carboxylic acid.
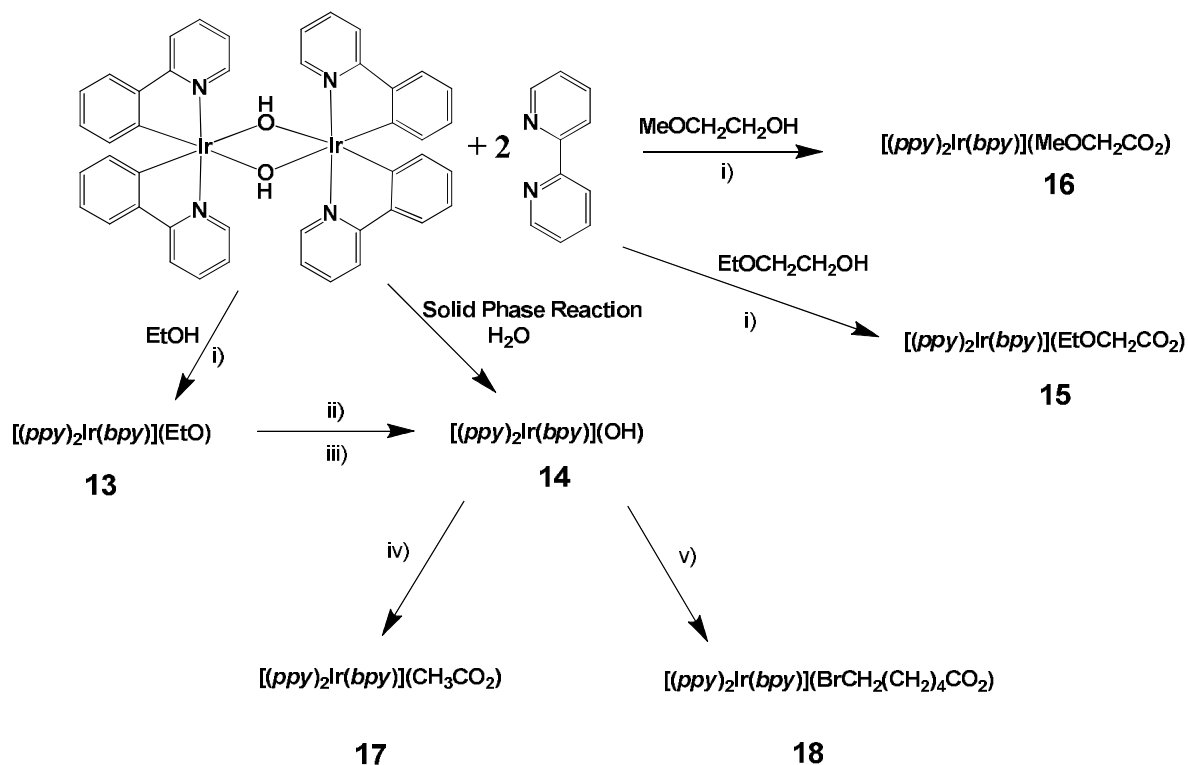
Scheme 3.2.6. Synthesis of complexes **13-16**. Reaction conditions: i) reflux, 72h, N₂; ii) THF/H₂O; iii) Et₂O; iv) CH₃COOH, CH₂Cl₂, 30 min., r.t.; (v) BrCH₂(CH₂)₄COOH , CH₂Cl₂, 30 min., r.t..

The small variation in the aromaticity of the ancillary ligand provided a great change in the supramolecular features of these compounds. In particular, passing from the **bpy** ligand to the more aromatic **dpq** ligand (Fig.3.2.48), an enhancement of the self-assembling abilities is observed, demonstrated firstly from the wider range of concentration in which self-

assembly occurs. However, a further increase in the aromaticity, exploited through the extended **dppz** ligand, almost procures the annihilation of the self-organization capacity of the corresponding complex.
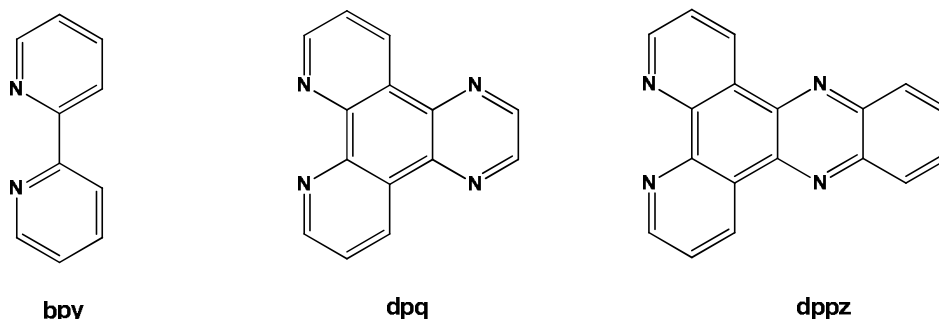
Fig. 3.2.48. Chemical structures of the **bpy, dpq** and **dppz** ligands.

Furthermore, the incorporation of these differently aromatic ligands in **[(ppy)₂Ir(N^N)]X** complexes (X = CH_3CO_2 or the other hydrophilic counterions EtO^-, OH^-, $EtOCH_2CO_2^-$, $MeOCH_2CO_2^-$), generates different types of soft materials. More specifically, the introduction of the **bpy** ligand in the above mentioned complexes, provides effective metallo-hydrogelators, that display all the special features of this class of materials, such as the presence of an entangled fibers network within the gel sample, the responsiveness to the test tube experiment, the persistence of the starting supramolecular organization also after evaporation of the solvent. Contrary, the extreme case of the ligand **dppz** led to a complex **[(ppy)₂Ir(dppz)]CH₃CO₂** (**12**) that it is no longer a genuine gelator, having lost the crude rheological properties of the last category, but, at the same time, its ability to generate organized supramolecular structures was proved. Finally, the complex **[(ppy)₂Ir(dpq)] CH₃CO₂** cannot be classified as a simple gelator, by virtue of the important role played by the solvent in its supramolecular-phase, whose removal determines the loss of the organization. Moreover, its well-defined birefringent texture resemble those of true liquid crystalline phases.

The precise classification of the above presented compound still remains controversial, however by simple playing with the nature of the ancillary ligand, complexes with self-assembling properties can be devised. These complexes can behave either more like true lyotropic liquid crystals or true metallogelators, representing highly interesting building blocks for the supramolecular chemistry and soft matter research field.

3.4 References

1. P.H. Hermans, *Colloid Science*. Vol. **11,** H. R. Kruyt (Ed.), Elsevier Publishing Company, Inc., Amsterdam, **1949,** p. 483.
2. P. J. Flory, *Faraday Discuss. Chem. Soc.*, **1974**, 57, 7-18.
3. *Gels Handbook, The Fundamentals.* Edited by:Yoshihito Osada, Kanji Kajiwara, Takao Fushimi, Okihiko Irasa, Yoshitsugu Hirokawa, Tsutomu Matsunaga, Tadao Shimomura, Lin Wang and Hatsuo Ishida. ISBN: 978-0-12-394690-4. Vol. 1, chapter 2, section 2.
4. A. Takahashi, M. Sakai, T. Kato, *Polym. J.*, **1980**, 12, 335-341.
5. M.-O. M Piepenbrock, G. O. Lloyd, N. Clarke, J. W. Steed, *Chem. Rev.* **2010**, 110, 1960–2004.
6. L. A. Estroff, A. D. Hamilton, *Chem. Rev.* **2004**, 104, 1201-1216.
7. G. Yu, X. Yan, C. Han, F. Huang, *Chem. Soc. Rev.,* **2013**, 42, 6697—6722.
8. Smith, D. K. In Organic Nanostructures; Atwood, J. L., Steed, J. W., Eds.; Wiley-VCH: Weinheim, Germany, 2008; p 111.
9. B. A. Simmons, C. E. Taylor, F. A. Landis, V. T. John, G. L. McPherson, D. K. Schwartz, R. Moore, *J. Am. Chem. Soc.*, **2001**, 123, 2414-2421.
10. J. H. Jung, G. John, M. Masuda, K. Yoshida, S. Shinkai, T. Shimizu, *Langmuir*, **2001**, 17, 7229-7232.
11. Nonappa, E. Kolehmainen, *Soft Matter,* **2016**, 12, 6015-6026.
12. K-T. Yung, *Magn. Reson. Imaging,* **2003**, 21*,* 135–144.
13. M. Yang, Z. Zhang, F. Yuan, W. Wang, S. Hess, K. Lienkamp, I. Lieberwirth and G. Wegner, *Chem.–Eur. J.*, **2008**, 14, 3330-3337.
14. A. R. Hirst, D. K. Smith, *Langmuir*, **2004**, 20, 10851–10857.
15. Y. Zhang, B. Zhang, Y. Kuang, Y. Gao, J. Shi, X. X. Zhang, B. Xu, *J. Am. Chem. Soc.,* **2013**, 135, 5008–5011.
16. B. Adhikari, G. Palui, A. Banerjee, *Soft Matter,* **2009**, 5, 3452–3460.
17. T. Patra, A. Pal, J. Dey, *J. Colloid Interf. Sci.*, **2010**, 344, 10–20.
18. H. Basit, A. Pal, S. Sen and S. Bhattacharya, *Chem.–Eur. J.*, **2008**, 14, 6534-6545.
19. M. Moniruzzaman, P. R. Sundararajan, *Langmuir*, **2005**, 21, 3802-3807.
20. J. H. Jung, G. John, M. Masuda, K. Yoshida, S. Shinkai, T. Shimizu, *Langmuir*, **2001,** 17*,* 7229-7232.
21. F. Rodrìguez-Llansola, D. Hermida-Merino, B. Nieto-Ortega, F. J. Ramìrez, J. T. Lòpez Navarrete, J. Casado, I. W. Hamley, B. Escuder, W. Hayes, J. F. Miravet, *Chem. Eur. J.*, **2012**, 18, 14725 – 14731.
22. A. Kishimura, T. Yamashita, T. Aida, *J. Am. Chem. Soc.*, **2005**, 127, 179-183.
23. K.Sakurai, Y. Jeong, K. Koumoto, A. Friggeri, O. Gronwald, S. Sakurai, S. Okamoto, K. Inoue, S. Shinkai, *Langmuir*, **2003**, 19, 8211-8217.
24. C. Park, J. Lee, C. Kim, *Chem. Commun.*, **2011**, 47, 12042–12056.
25. Y. Zhang, B. Yang, X.Zhang, L. Xu, L. Tao, S. Li, Y. Wei, *Chem. Commun.*, **2012**, 48, 9305–9307.
26. N. F. Goldshleger, A. S. Lobach, V. E. Baulin, A. Yu. Tsivadze, *Russ. Chem. Rev.*, **2017**, 86, 269-297.
27. A. Srivastava, S. Ghorai, A. Bhattacharjya, S. Bhattacharya, *J. Org. Chem,* **2005**, 70, 6574 –6582.
28. D. M. Ryan, S. B. Anderson, F. T. Senguen, R. E. Youngman, B. L. Nilsson, *Soft Matter*, **2010**, 6, 475-479.
29. J. W. Steed, *Chem. Commun.,* **2011**, 47, 1379–1383.
30. N. M. Sangeetha, U.Maitra, *Chem. Soc. Rev.*, **2005**, 34, 821–836.
31. J. Zhang, C.-Y. Su, *Coord Chem Rev*, **2013**, 257, 1373–1408.
32. M. Maity, U. Maitra, *Dalton Trans.*, **2017**, DOI: 10.1039/C7DT02177A.

33. A. Dawn, K. S. Andrew, D. S. Yufit, Y. Hong, J. P. Reddy, C. D. Jones, J. A. Aguilar, J. W. Steed, *Cryst. Growth Des,* **2015**, 15, 4591–4599.

34. J. Liu, P. He, J. Yan, X. Fang, J.Peng, K. Liu, Y. Fang, *Adv. Mater*., **2008**, 20, 2508–2511.

35. M. Zinic, F. Vogtle, F. Fages, *Top. Curr. Chem*., **2005**, 256, 39-76.

36. A. Ajayaghosh, S. J. George, V. K. Praveen, *Angew. Chem. Int. Ed*., **2003**, 42, 332-335.

37. Y. Song, J. Gao, X. Xu, H. Zhao, R. Xue, J. Zhou, W. Hong, H. Qiu, *Mater. Sci. Eng., C*, **2017**, 75, 706–713.

38. A. R. Hirst, Be. Escuder, J. F. Miravet, D. K. Smith, *Angew. Chem. Int. Ed*., **2008**, 47, 8002 – 8018.

39. K. Kuroiwa, T. Shibata, A. Takada, N. Nemoto, N. Kimizuka, *J. Am. Chem. Soc.*, **2004**, 126, 2016-2021.

40. D.-C. Lee, K. K. Grath, K. Jang, *Chem. Commun*., **2008**, 3636–3638.

41. X. Zhang, S. Lee, Y. Liu, M. Lee, J. Yin, J. L. Sessler, J. Yoon, *Scientific Reports*, **2014**, 4, 4593. DOI: 10.1038/srep 04593.

42. Z.-X. Liu, Y. Feng, Z.-C. Yan, Y.-M. He, C.-Y. Liu, Q.-H. Fan, *Chem. Mater*., **2012**, 24, 3751–3757.

43. M. Llusar, C. Sanchez, *Chem. Mater.* **2008**, *20*, 782–820.

44. G. Gundiah, S. Mukhopadhyay, U. G. Tumkurkar, A. Govindaraj, U. Maitra, C. N. R. Rao, *J. Mater. Chem.*, **2003**, 13, 2118–2122.

45. M. Suzuki, Y. Nakajima, T. Sato, H. Shirai, K. Hanabusa, *Chem. Commun*., **2006**, 377–379.

46. C. S. Love, V. Chechik, D. K. Smith, K. Wilson, I. Ashworth, C. Brennan, *Chem. Commun*., **2005**, 1971–1973.

47. C. L. Chan, J. B.Wang, J. Yuan,H.Gong, Y. H. Liu, M. H. Liu, *Langmuir*, **2003**, 19, 9440–9445.

48. L. E. Buerkle, S. J. Rowan*, Chem. Soc. Rev.,* **2012**, 41, 6089–6102.

49. M. D. Segarra-Maset, V. J. Nebot, J. F. Miravet, B. Escuder, *Chem. Soc. Rev.,* **2013**, 42, 7086-7098.

50. A. Yiu-Yan Tam, V. Wing-Wah Yam, *Chem. Soc. Rev.,* **2013**, 42, 1540-1567.

51. S. Santhosh Babu, V. K. Praveen, A. Ajayaghosh, *Chem. Rev.,* **2014**, 114, 1973–2129.

52. Z. Sun, Q. Huang, T. He, Z. Li, Y. Zhang, L. Yi, *ChemPhysChem,* **2014**, 15, 2421 – 2430.

53. P. Dastidar, S. Ganguly, K. Sarkar, Chem. Asian J. **2016**, 11, 2484 – 2498.

54. Y. J. Yadav, B. Heinrich, G. De Luca, A. M. Talarico, T. F. Mastropietro, M. Ghedini, B. Donnio, E. I. Szerb, *Adv. Opt. Mater*., **2013**, 1, 844–854.

55. K. R. Schwartz, R. Chitta, J. N. Bohnsack, D. J. Ceckanowicz, P. Miró, C. J. Cramer, K. R. Mann, *Inorg. Chem.,* **2012**, 51, 5082–5094.

56. T. Imae, N. Hayashi, T. Matsumoto, T. Tada, M. Furusaka, *J. Colloid Interface Sci*., **2000**, 225, 285-290.

57. T. Imae, Y. Takahashi, H. Muramatsu, *J. Am. Chem. Soc*., **1992**, 114, 3414-3419.

58. C. K. Siew, P. A. Williams, *Biomacromolecules*, **2005,** 6, 963-969.

59. O. Esue, S. Kanai, J. Liu, T. W. Patapoff, S. J. Shire, *Pharm. Res.*, 2009, 26, 2478-2485.

60. J. Makarević, M. Jokić, B. Perić, V. Tomišić, B. Kojić-Prodić, M. Žinić, *Chem. Eur. J.*, **2001**, 7, 3328-3341.

61. C. Oliviero Rossi, C. Cretu, L. Ricciardi, A. Candreva, M. La Deda, I. Aiello, M. Ghedini, E. Ildyko Szerb, *Liquid Crystals*, **2017**, 44, 880-888.

62. L. Ricciardi, T. F. Mastropietro, M. Ghedini, M. La Deda, E. Ildyko Szerb, *J Organomet Chem.*, **2014**, 772–773, 307–313.

63. C. Cuerva, J. A. Campo, P. Ovejero, M. R. Torres, M. Cano, *Dalton Trans*., **2014**, 43, 8849–8860.

64. O. D. Lavrentovich, Handbook of Liquid Crystals, 2014, pp.1-53, DOI:0.1002/9783527671403.hlc027.

65. S. Laschat, A. Baro, N. Steinke, F. Giesselmann, C. Hägele, G. Scalia, R. Judele, E. Kapatsina, S. Sauer, A. Schreivogel, M. Tosoni, *Angew. Chem. Int. Ed*., **2007**, 46, 4832–4887 and references cited therein.

66. B. R. Kaafarani, *Chem. Mater.,* **2011**, 23, 378-396 and references cited therein.

67. Y. Chen, Z. Zhao, Z. Bian, R. Jin, C. Kang, X. Qiu, H. Guo, Z. Du, L. Gao, *ChemistryOpen*, **2016**, 5, 386 – 394.

68. T. Schneider, A. Golovin, J. C. Lee, O. D. Lavrentovich, *J. Inf. Disp*., **2004**, 5, 27-38.

69. J. F. Dreyer, *J. Phys. Colloq*., **1969**, 30 (C4), 114-116.

70. N. Godbert, A. Crispini, M. Ghedini, M. Carini, F. Chiaravalloti, A. Ferrise, *J. Appl. Cryst*., **2014**, 47, 668-679.

71. Advances in Liquid Crystals, Volume 113 (eBook) Jagdish K. Vij (Herausgeber), John Wiley & Sons (Verlag) 978-0-470-14225-7 (ISBN), 2009.

72. V. Sathish, A. Ramdass, P. Thanasekaran, K.-L. Lu, S. Rajagopal, *J. Photochem. Photobiol. C: Photochem. Rev*., **2015**, 23, 25–44 and references cited therein.

73. Y. You, H.S. Huh, K.S. Kim, S.W. Lee, D. Kim, S.Y. Park, *Chem. Commun*., **2008**, 3998–4000.

74. S. Friberg, Naturwissenschaften, **1977**, 64, 612-618.

75. B. Donnio, *Curr. Opin. Colloid. Interface Sci.,* **2002**, 7, 371-394.

76. I. Muñoz Resta, V. E. Manzano, F. Cecchi, C.C. Spagnuolo, F. D. Cukiernik, P. H. Di Chenna, *Gels*, **2016,** 2(1), 7; doi:10.3390/gels2010007.

77. Y. Yu, N. Chu, X. Y. Li, N. Song, C. Liu, L. N. Yu, B. Li, C. Wang, Z. G. Zhao, Y. N. Zhao, Y. G. Sheng, C. S. Wang, *Russ. J. Phys. Chem. B,* **2017**, 11, 121–128.

78. J. H. Jung, G. John, M. Masuda, K. Yoshida, S. Shinkai, T. Shimizu, *Langmuir*, **2001,** 17*,* 7229-7232.

79. D. K. Kumar, D. A. Jose, P. Dastidar, A. Das, *Langmuir*, **2004**, *20,* 10413-10418.

80. A. Sànchez-Ferrer, I. Bräunlich, J. Ruokolainen, M. Bauer, R. Schepper, P. Smith, W. Caseri, R. Mezzenga, *RSC Adv*., **2014**, 4, 60842-60852.

81. T. Giorgi, F. Grepioni, I. Manet, P. Mariani, S. Masiero, E. Mezzina, S. Pieraccini, L. Saturni, G. P. Spada, G. Gottarelli, *Chem. Eur. J*., **2002**, 8, 2143-2152.

82. K. A. McGee, K. R. Mann, *Inorg. Chem*., **2007**, 46, 7800–7809.

83. B. Beyer, C. Ulbricht, A. Winter, M. D. Hager, R. Hoogenboom, N. Herzer, S. O. Baumann, G. Kickelbick, H. Görlsf, U. S. Schubert, *New J. Chem*., **2010**, 34, 2622– 2633.

84. S. L. James, C. J. Adams, C. Bolm, D. Braga, P. Collier, T. Friscic, F. Grepioni, K. D. M. Harris, G. Hyett, W. Jones, A. Krebs, J. Mack, L. Maini, A. G. Orpen, I. P. Parkin, W. C. Shearouse, J. W. Steed, D. C. Waddel, *Chem. Soc. Rev*., **2012**, 41, 413–447.

85. M. Juribasic, I. Halasz, D. Babic, D. Cincic, J. Plavec, M. Curic, *Organometallics*, **2014**, 33, 1227–1234.

86. A. L. Garay, A. Pichon, S. L. James, *Chem. Soc. Rev*., **2007**, 36, 846–855.

87. K. Stemmler, W. Mengon, J. A. Keer, *Environ. Sci. Technol*., **1996**, 30, 3385–3391.

88. K. Stemmler, D. J. Kinnison, J. A. Kerr, *J. Phys. Chem*., **1996**, 100, 2114–2116.

89. P. Dagaut, R. Liu, T. J. Wallington, M. J. Kurylo, *J. Phys. Chem*., **1989**, 93, 7838–7840.

90. E. J. Strojny, R. T. Iwamasa, L. K. Frevel, *J. Am. Chem. Soc.*, **1971**, 93 , 1171–1178.

91. J. Lydon, *J. Mater. Chem*., **2010**, 20, 10071–10099.

92. J. Lydon, *Liq. Cryst*., **2011**, 38, 1663-1681.

93. Hiltrop K. (1994) Lyotropic Liquid Crystals. In: Stegemeyer H., Behret H., Deutsche Bunsen-Gesellschaft für Physikalische Chemie e.V. (eds) Liquid Crystals. Topics in Physical Chemistry, vol 3. Steinkopff, Heidelberg.

94. G. E. Schneider, H. J. Bolink, E. C. Constable, C. D. Ertl, C. E. Housecroft, A. Pertegàs, J. A. Zampese, A. Kanitz, F. Kesslerd, S. B. Meie, *Dalton Trans*., **2014**, 43, 1961–1964.

95. R. D. Costa, E. Ortí, H. J. Bolink, S. Graber, S. Schaffner, M. Neuburger, C. E. Housecroft,; E. C. Constable, *Adv. Funct. Mater.*, **2009**, 19, 3456– 3463.

96. D. Ma, Y. Qiu, L. Duan, *Adv. Funct. Mater.*, **2016**, 26, 3438–3445.

97. S. Ladouceur, E. Zysman-Colman, *Eur. J. Inorg. Chem.*, **2013**, 17, 2985–3007.

98. K. C. Chan, W. K. Chu, S. M. Yiu, C. C. Ko, *Dalton Trans.*, **2015**, 44, 15135–15144.

99. S.-H. Wu, J.-W. Ling, S.-H. Lai, M.-J. Huang, C. H. Cheng, I.-C. Chen, *J. Phys. Chem. A*, **2010**, 114, 10339–10344.

100. K. K.-W. Lo, J. S.-W. Chan, L.-H. Lui, C.-K. Chung, *Organometallics*, **2004**, 23, 3108–3116.

101. A. Ionescu, E. I. Szerb, Y. J. Yadav, A. M. Talarico, M. Ghedini, N. Godbert, *Dalton Trans.*, **2014**, 43, 784–789.

102. Christian Reichardt, Solvents and Solvent Effects in Organic Chemistry, Wiley-VCH Publishers, 3rd ed., 2003.

103. A. P. Wilde, R. J. Watts, *J. Phys. Chem.*, **1991**, 95, 622– 629.

Chapter 4

Nanostructured Iridium Oxide

4.1 Introduction

Iridium Oxide (IrO_2) is a noble metal oxide with a rutile crystalline structure,[1] analogous to the TiO_2 rutile polymorph, with a space group P4$_2$/*mnm*. The rutile structure is characterized by a tetragonal unit cell in which every Iridium atom is coordinated to six Oxygen atom (Fig.4.1.1).
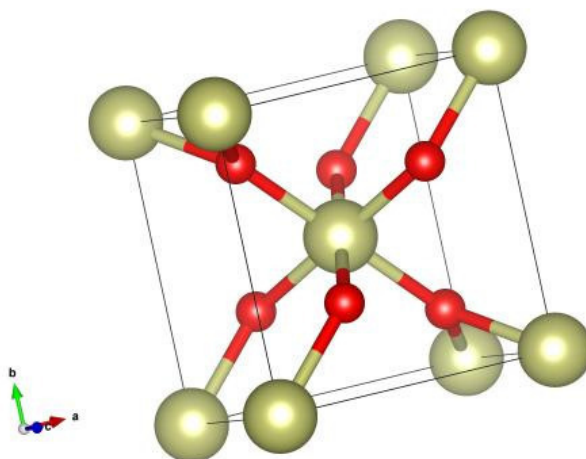
Fig. 4.1.1. The unit cell of IrO_2 rutile. Here, Ir atoms are yellow and O atoms are red. [2]

4.1.1 Properties

Unlike other transition metal oxides, IrO_2 shows a metallic type conductivity (~10^4 S·cm^{-1}).[3] The reason of this property has been first investigated by Gillson *et al*.[4]: IrO_2, like other dioxides with a rutile-related structure, have incompletely filled d shells [IrO_2 (5d^5)]. Later, Verbist et al.[5], by using X-ray Photoelectron Spectroscopy (XPS), confirmed the presence in IrO_2 of a partially filled electron band, with a d character, just at the Fermi level, which could be responsible of the high conductivity of the metal oxide.

IrO_2 presents attractive properties and can be synthesized in the form of various types of nanostructures, as nanosheets,[6] nanotubes,[7] nanorods,[8] nanowires,[9,10] nanoparticles[11] and nanoporous films.[12,13] Nanostructuration of IrO_2, as well as for other transition metal oxides, can enhance its intrinsic properties with respect to the bulk material. Indeed, 1D nanostructures exhibit electrical, mechanical, chemical and optical properties modified respect to the corresponding bulk material, and they can be used as building blocks in optoelectronic devices.[14,15] Indeed, devices made of well-defined and ordered metal oxides architectures display better performances in many applications.[16-18]

4.1.2 Applications

4.1.2.1 Electrocatalysis for Oxygen Evolution Reaction (OER)

In recent years, many methodological and research efforts have been made for the production of molecular hydrogen, as an energy source in alternative to fossil fuels. The cleanest method to produce molecular hydrogen is water electrolysis, a process in which water is split into hydrogen and oxygen gases, by means of the passing of an electric current (Fig.4.1.2).

Anodic reaction: $2H_2O_{(l)} \longrightarrow O_{2(g)} + 4H^+_{(aq)} + 4e^-$

Cathodic reaction: $4H^+_{(aq)} + 4e^- \longrightarrow 2H_{2(g)}$
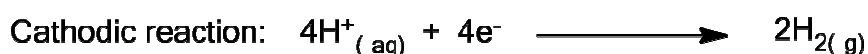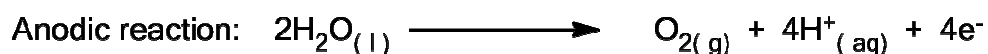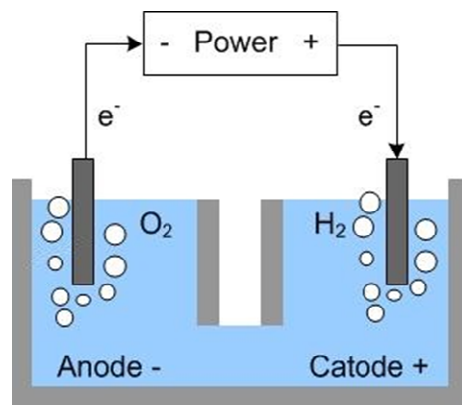
Fig.4.1.2. A schematic representation of a water electrolyzer and the half reactions taking place in a water electrolyzer (adapted from ref.[19]).

The efficiency of the water electrolysis in acidic conditions is limited by the energy barrier of the Oxygen Evolution Reaction (OER), the anodic reaction of this process.[20-22] The cell voltage, and therefore the energy consumption of the process, is governed by this reaction. To overcome this problem, an efficient and stable electrocatalyst is required. Ir and Ru oxides are considered the best electrocatalysts for OER, showing the lowest overpotential in acidic media.[23]

Electrochemical and XPS studies[24,25] demonstrated that IrO_2 surface in contact with water undergoes to a partial hydroxylation, showing hydroxide sites which coexist with the oxide sites. During OER, the hydroxide sites are converted into oxide sites, passing through an OOH as intermediate. Furthermore, the simultaneous formation of some Ir (V) centres was verified, which could be responsible of the catalytic activity of IrO_2 toward OER, since its subsequent two-electrons reduction to Ir (III) can be sufficient to oxidize water in an Oxygen molecule.

IrO_2 is slightly less active than RuO_2, but presents a greater long-term stability in strong acidic media, proving its corrosion and poisoning resistance.[26] In order to achieve a comparable OER activity with RuO_2, it is necessary to improve the morphology and the surface area of IrO_2.[27] A possible strategy is the nanostructuration of IrO_2, hence the increase of surface area which results in an enhancement of electrocatalytic and sensing activities, due to an increased number of active sites on the material.[12] The improved accessibility for reactive species can also reduce the overpotential of OER, determining a better catalytic performance.[28] Recently nanosheets of IrO_2 (Fig.4.1.3) have been prepared via exfoliation of layered iridic acid, showing an OER activity six times higher than that of IrO_2 nanoparticles, making such thin films highly attractive candidates for the development of new electrode materials and efficient electrocatalysts.[6]
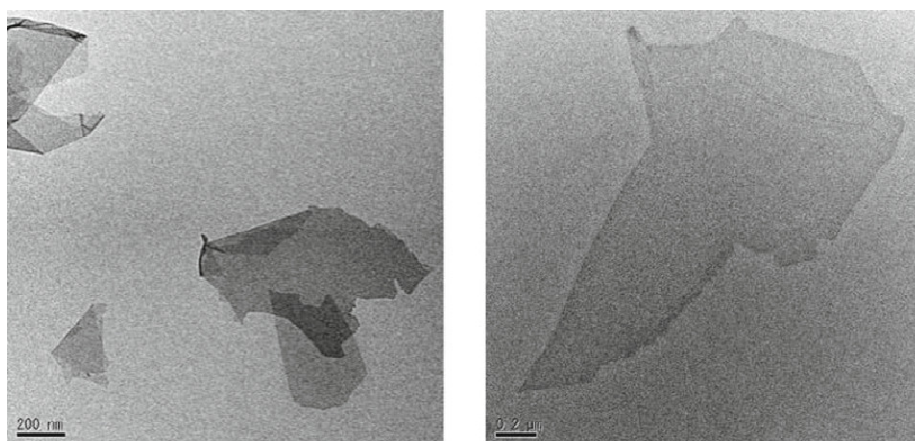
Fig.4.1.3. TEM images of IrO_2 nanosheets (from ref.[6]).

4.1.2.2 Electrochromic Material

An electrochromic device (EC) changes its optical properties upon application of a voltage and could find application in smart windows, a promising topic for energy saving technology. It consists essentially of an electrochromic material layer and two conducting and transparent electrodes separated by an electrolyte layer (Fig.4.1.4).
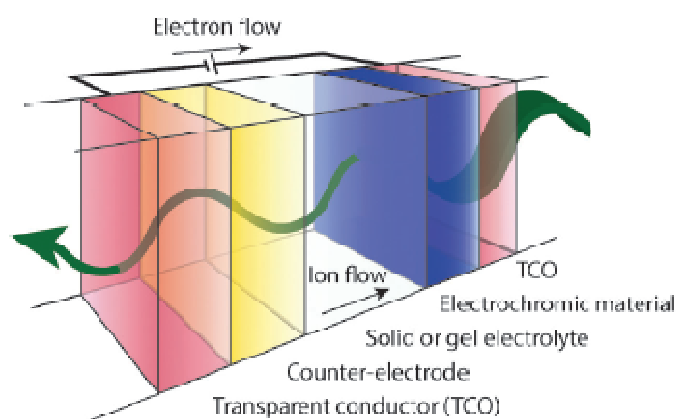
Fig. 4.1.4. A schematic representation of an electrochromic device (From Ref.[29])

Iridium oxide is an electrochromic (EC) material, displaying a reversible and persistent colour change as a result of the application of an external electric field. The change in its optical properties may be ascribed to the following reaction:[30]

$$\text{Ir (OH)}_n \rightleftharpoons \text{IrO}_x(\text{OH})_{n-x} + x\text{H}^+ + x\text{e}^-$$
$$\text{transparent} \qquad\qquad \text{blue-black}$$
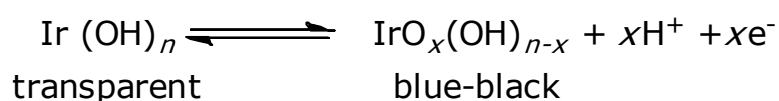
During colouring, electrons and protons are removed from the material by application of an anodic potential, whereas during bleaching electrons and protons are injected into the substrate.[31] In its lower oxidation states [Ir(II) and Ir(III)], IrO_2 is transparent, while in its higher oxidation state [Ir(IV)] is blue-black due to a strong absorption in the visible spectral region.[30] Iridium oxide presents several ideal features for an EC material, such as fast colour change, good open-circuit memory and long last durability (more than 10^7 cycle lives) [30,32], which promote its application in EC devices. [33-36]

The eventual nanostructuration of the EC layer could bring significant benefits to the device performance. Indeed, the high surface-to-volume ratio could also speed up the transition between the oxidation states of Ir (II/III to IV), resulting in a faster colour change in an electrochromic device.[30]

4.1.2.3 Other applications

The transition between two oxidation state [Ir(III) and Ir(IV)] is exploited also for the fabrication of Iridium Oxide based pH sensors. [7,9, 37,38] IrO_2 provides a fast potentiometric response to pH change, thanks to its high conductivity. IrO_2-based electrodes present useful properties, such as high stability in a wide range of temperature,[39] linear response in a broad pH range,[40] great chemical stability and low impedance,[41] and the pH response is not affected by most anions and complexing agents.[42] Furthermore, Food and Drug Administration (FDA) approved IrO_2 as high biocompatible material, facilitating its application in biosensors[43] and stimulating and recording electrodes,[44] thanks also to its high charge capacity: for a given applied voltage pulse, IrO_2 injects a very high charge density.[45]

By virtue of its conductive nature, high chemical stability, low surface work function (4.23 eV) and stability under influence of high electric fields, Iridium Oxide has been used as field emitter cathode in vacuum microelectronics.[46-49] Indeed, IrO_2 doesn't suffer from the eventual presence of residual oxygen in these devices, contrary to other metals, as Mo, that reacts quickly with O_2 forming an insulating layer of oxide.[50]

Further applications of Iridium Oxide include electrode material for direct methanol fuel cell,[51] for supercapacitors,[52] and for neural stimulation.[53]

4.1.3 Nanostructures of IrO_2

Various methods have been employed to prepare Iridium Oxide nanostructures (nanoparticles, nanotubes, nanorods, nanowires, nanosheets and nanostructured films).

4.1.3.1 IrO$_2$ nanoparticles

Several methods to synthesize IrO$_2$ nanoparticles have been experimented. In 2005 Marshall [54] introduced a modification to the well-known polyol method.[55] This procedure consists of dissolving or disperding the metallic precursor, usually hexachloroiridic acid (H$_2$IrCl$_6$·nH$_2$O), in a polyol, such as ethylene glycol, which acts both as solvent and as reducing agent. Upon refluxing of the reaction mixture, a metallic precipitate, composed by nanoparticles with an average size of about 3 nm, is formed (Fig.4.1.5), which is then filtered and dried. The colloid is finally calcinated in order to oxidize to IrO$_2$ the metallic powder obtained.
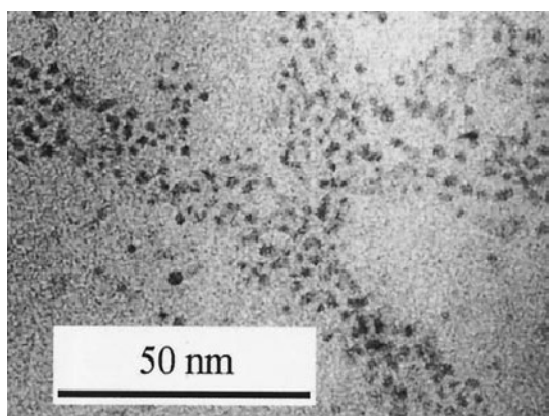
Fig.4.1.5. TEM micrograph of Ir nanopowder obtained through the polyol method (from ref.[55]).

Another approach is represented by the Adam fusion method,[56] in which the metallic precursor is melted with NaNO$_3$. The possible reactions that may occur during the process are shown in Scheme 4.1.1.

$$H_2IrCl_6 + 6NaNO_3 \longrightarrow 6NaCl + Ir(NO_3)_4 + 2HNO_3$$

$$Ir(NO_3)_4 \longrightarrow IrO_2 + 4NO_2 + O_2$$
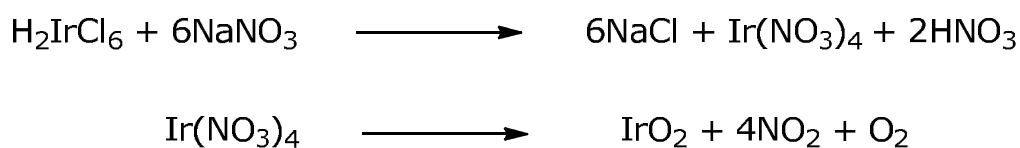
Scheme 4.1.1. The hypothesized reactions taking place in the Adam fusion method.[54]

After cooling, the mixture is washed with water to remove salt residues, nitrites and nitrates. Anyway, sodium traces may remain in the metal oxide powder.

Nanosized IrO$_2$ powder can also be synthesized through the colloidal method.[20,57] This process involves the addition of NaOH to a water solution of the Iridium precursor,

($H_2IrCl_6 \cdot nH_2O$) in order to induce the formation of an Ir-hydroxide. The resulting colloidal solution is then washed, dried and calcinated, obtaining colloidal IrO_2, composed by IrO_2 nanoparticles with an average size of *ca*. 7 nm. However, since the final product is a colloid, the nanoparticles are all aggregated to each other as shown in the reported TEM micrograph (Fig.4.1.6).
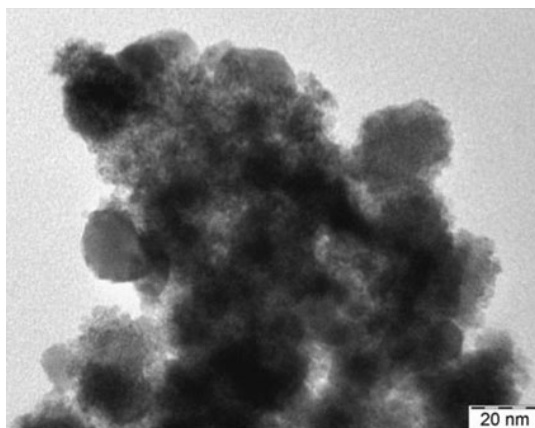
Fig.4.1.6. TEM micrograph of colloidal IrO_2 obtained through the colloidal method (from ref.[57]).

In addition, the hard-templating route has been adapted to the preparation of IrO_2 nanoparticles. In this case, colloidal SiO_2 microspheres were immersed in an ethanolic solution of ($H_2IrCl_6 \cdot nH_2O$) to allow the impregnation of the Iridium precursor within the template, then the suspension was dried and calcinated, and the template was removed by using a concentrated HF solution.[20] Chen *et al.* demonstrated that using SiO_2 microspheres with a mean diameter of 330 nm and very low polydispersity (*ca*. 0.5%), macroporous IrO_2, displaying an ordered honeycomb array of macropores, can be obtained (Fig.4.1.7).[20] The macropores are typically 300 nm in diameter, which is slightly smaller than the size of SiO_2 microspheres, probably as a consequence of the contraction of the template during the heat treatment process. The main drawback of this synthetical method is the drastic acidic condition (concentrated HF solution) required in order to remove the templating SiO_2 agent.
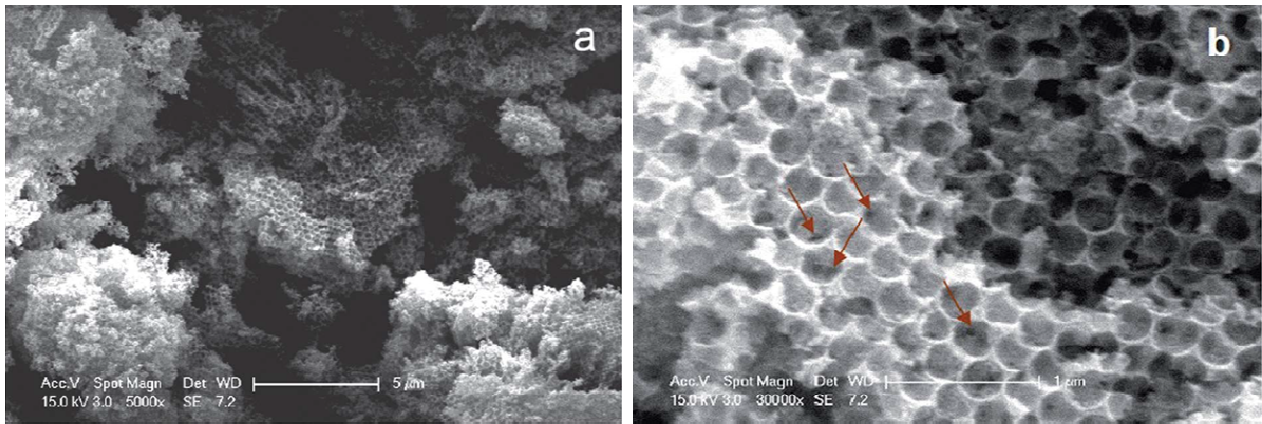
Fig.4.1.7. (a) Low and (b) high magnification SEM images of macroporous IrO$_2$ prepared by the hard-template method (from ref.[20]).

4.1.3.2 1D nanostructures: nanotubes, nanorods, nanowires

Beside IrO$_2$ nanoparticles, also IrO$_2$ nanotubes have been built using a hard-templating route coupled with electrodeposition (Fig.4.1.8).[7] Practically, an anodic aluminium oxide (AAO) layer with controlled pore diameters was first fabricated through the sputtering of an aluminium layer on a silicon substrate, followed by an anodization process. IrO$_x$ was electrodeposited on this template layer, generating nanotubes along the walls of the AAO nanopores. At the end of the process, the AAO template was removed by dissolution in concentrated KOH solution.
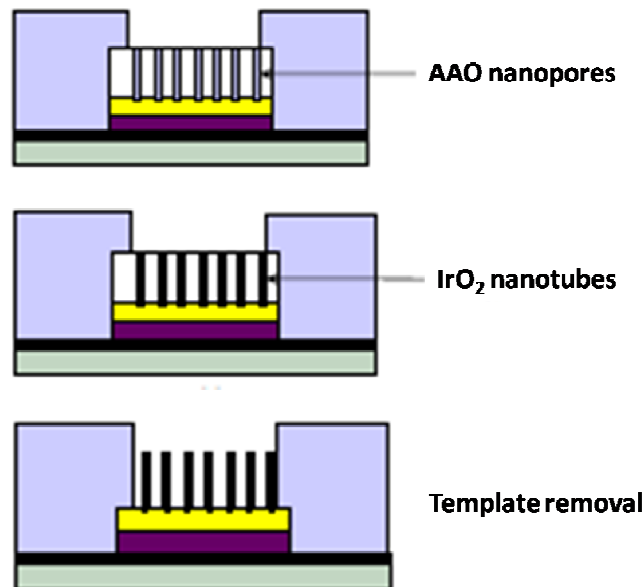
Fig. 4.1.8. A schematic representation of the hard-template route for the synthesis of IrO$_2$ nanotubes (From Ref.[7])

As reported by Chiao *et al.*, the shape and the length of the nanotubes prepared through this method depend on the morphology of the nanoporous AAO template, whereas the wall thickness of nanotubes is specified by the electrodeposition time.[7] The nanotubes obtained present a diameter of 50 nm and length of around 750 nm. However, the not uncommon presence of defective nanopores in the AAO template results in the formation of incomplete and collapsed nanotubes together with hollow nanotubes (Fig.4.1.9).
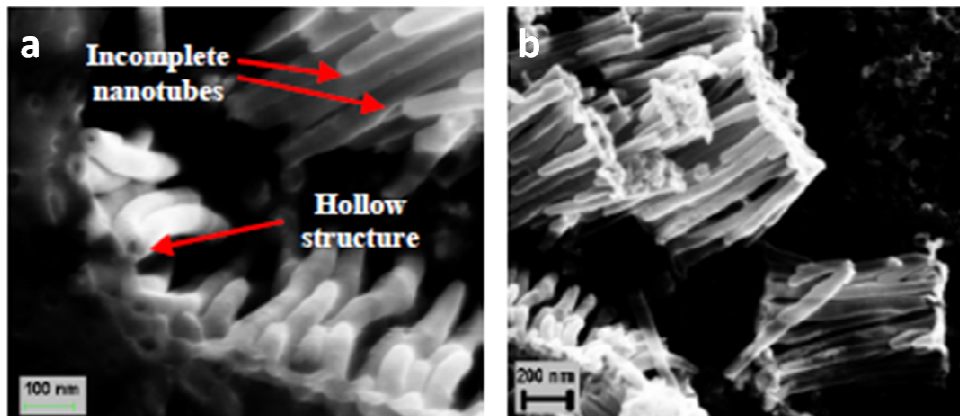
Fig. 4.1.9. SEM micrographs of: (a) hollow-wall and incomplete IrO_2 nanotubes; (b) side-view of collapsed IrO_2 nanotubes (from Ref.[7]).

IrO_2 nanorods were produced through several techniques, including the "molten salt" method,[58] Metalorganic Chemical Vapor Deposition (MOCVD)[8] and the hard-template route.[59] In the "molten salt" method the Iridium precursor ($IrCl_4$) is grinded with NaCl and KCl and then calcinated at high temperature (600°C) for 12 hours.[58] Through this procedure, Mao *et al*. obtained nanostructures with an average diameter of 15 nm and length of *ca.* 200 nm (Fig.4.1.10). [58] However, this method required long purification and drying processes.
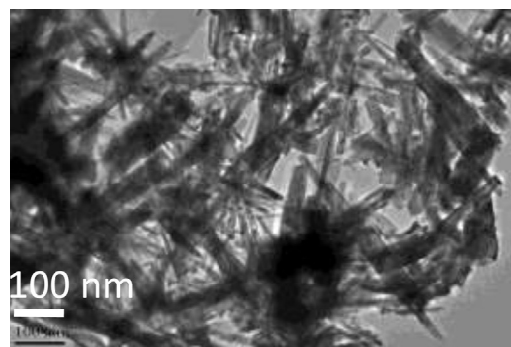
Fig. 4.1.10. TEM image of IrO_2 nanorods obtained through the molten salt method (from ref.[58]).

Another method exploited to produce IrO_2 nanorods is the MOCVD technique, which unfortunately requires a complex reactor in which ultra-pure gases are injected in order to transport and react with the organometallic precursor. Via MOCVD, IrO_2 nanorods were grown on Si substrates using a low-melting Iridium source [(Methylcyclopentadienyl) (1,5-cyclooctadiene) Iridium(I)] [(MeCp)Ir(COD)], a high oxygen pressure (10-60 Torr) and a temperature of *ca*. 350°C.[8] However, IrO_2 nanorods fabricated in this way present a polycrystalline nature with many defects and dislocations (Fig.4.1.11).
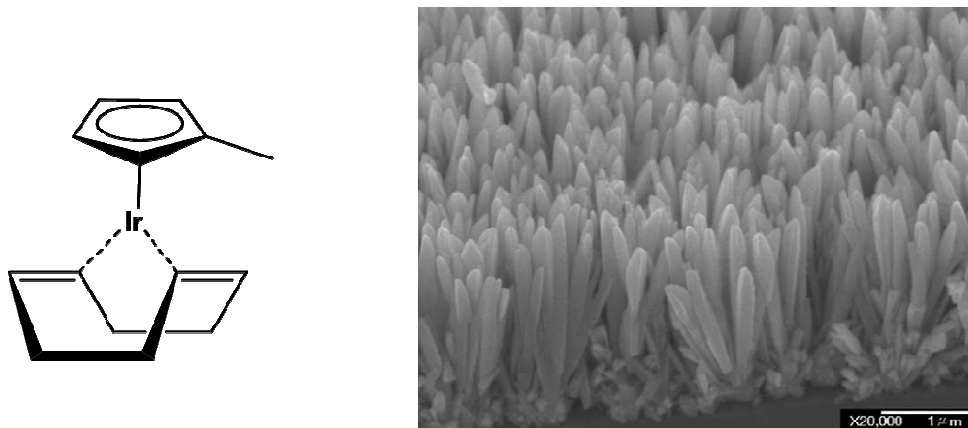
Fig. 4.1.11. Chemical structure of the Ir precursor generally employed in the fabrication of IrO_2 nanostructures through MOCVD, and FESEM images of the IrO_2 nanorods fabricated with this method (from Ref.[8])

Finely by tuning the experimental parameters in a MOCVD experiment, another type of 1D structures, *i.e.* IrO_2 nanowires, is obtainable.[10] For this purpose, [(MeCp)Ir(COD)] as Iridium source, Oxygen as both carrier and reactant gas, high temperature (350-400°C) and high pressure (33 Torr) were needed. Zhang *et al.* prepared in these conditions single crystal IrO_2 nanowires with dimension ranging from 10 to 50 nm in diameter and 1–2 mm in length (Fig.4.1.12).[10]
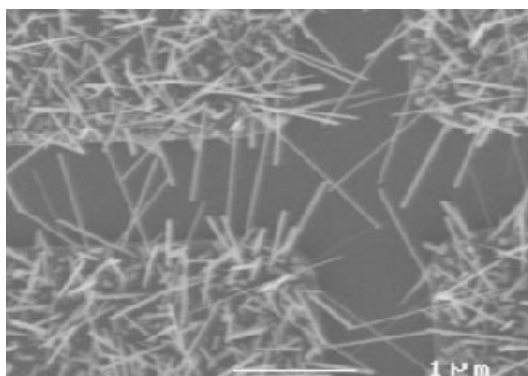
Fig. 4.1.12. SEM image of IrO_2 nanowires obtained through MOCVD (from ref.[10]).

IrO$_2$ nanowires were also grown on Au and Si/SiO$_2$ substrates *via* Vapor Phase Transport (VPT).[9] IrO$_2$ powder was used as source material and placed in a quartz tube furnace under He and O$_2$ flow. The reaching of very high temperature (*ca*. 1000°C) allows the precursor to sublimate and to be transported by the gas flow to the substrates, where recrystallization occurs in the form of nanowires. Kim *et al*. reported the preparation of IrO$_2$ nanowires displaying lateral dimensions ranging from 20 to 100 nm near the nanowire tip, with the length extending up to tens of micrometers.[9]   However, unfortunately, the obtained nanowires presented random orientations with no uniform lateral dimensions along the growth direction as can be observed in the SEM images reported in Fig.4.1.13.
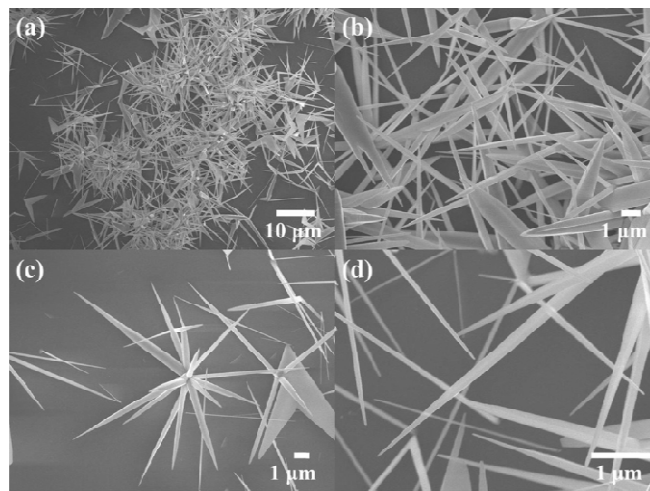
Fig. 4.1.13. SEM images of IrO$_2$ nanowires grown with the Vapor Phase Transport (from Ref.[9]).

4.1.3.3 Nanostructured IrO$_2$ films

IrO$_2$ thin films can be prepared through several techniques, ranging from spray pyrolysis[60] to reactive radio-frequency magnetron sputtering.[36] Anyway, the easiest way to introduce a nanostructuration in a metal oxide film, therefore also in an IrO$_2$ film, is the Evaporation Induced Self-Assembly method (EISA) (Fig.4.1.14).
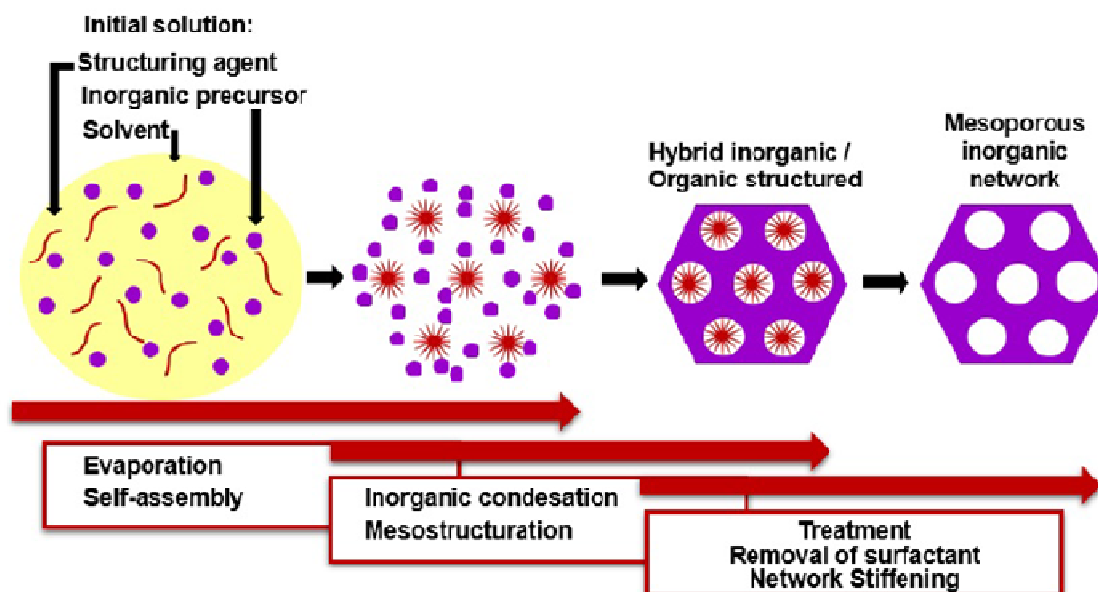
Fig. 4.1.14. Schematic representation of Evaporation Induced Self-Assembly (from Ref.[61])

The EISA route involves the use of a soft-template, usually an ionic organic surfactant or non-ionic polymeric surfactant which self-assembles into a diversity of supramolecular structures, including spherical micelles, hexagonal rods, lamellar liquid crystals and other assemblies in solution, through non-covalent weak interactions such as hydrogen bonding, Van der Waals forces and electrostatic interactions, driven by evaporation of the solvent. These assemblies are the structural directing agents (SDA) for the formation of inorganic mesostructures, indeed the sol–gel precursor hydrolyzes and condenses around the mesostructured polymeric phase. Subsequent thermal treatment induces the removal of the surfactant, the stiffening of the inorganic network and its crystallization. By varying the type of surfactant, its concentration in the starting solution and the deposition conditions, it is possible to tune the pore structure and size of the porous materials. EISA is generally coupled with dip-coating or spin-coating deposition techniques, which allow the formation of a thin layer of precursor on different substrates. By this procedure, Ortel *et al.* synthesized IrO_2 on Silicon wafers through dip-coating and employing PEO_y-PB_x-PEO_y [(poly(ethylene oxide)-poly(butadiene)-poly(ethylene oxide)] as templating agent.[12] These films presented nanocrystalline walls and some areas with locally ordered pores (Fig.4.1.15). Moreover, their electrocatalytic performance toward Oxygen Evolution Reaction was tested and compared to untemplated IrO_2 films obtained with the same experimental procedure. The current response on templated IrO_2 films is about 2.1 times higher with respect to the untemplated IrO_2 films, demonstrating the nanostructuration advantages.
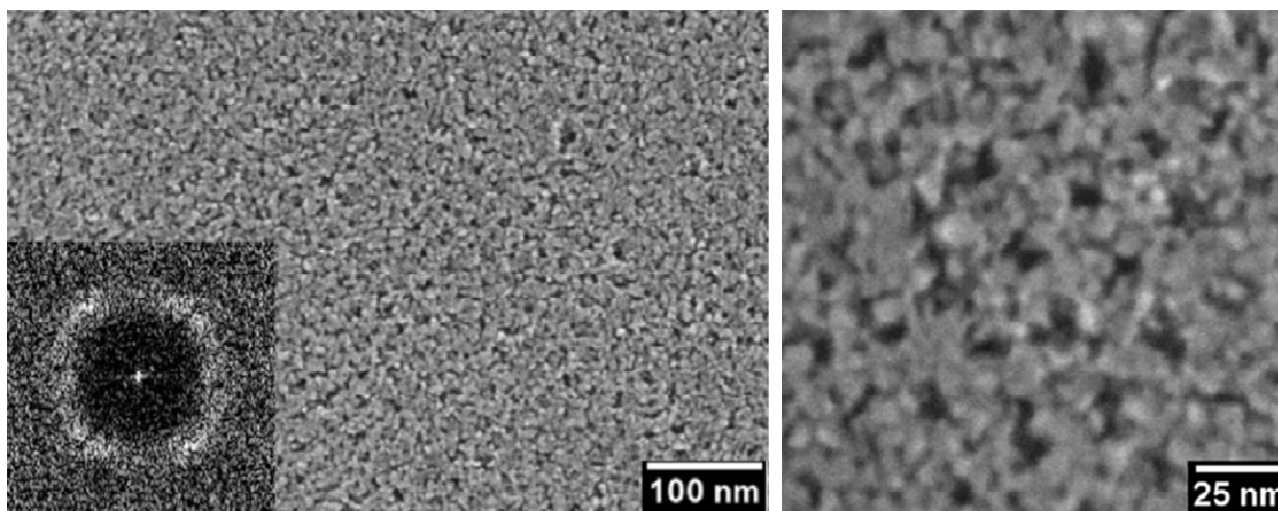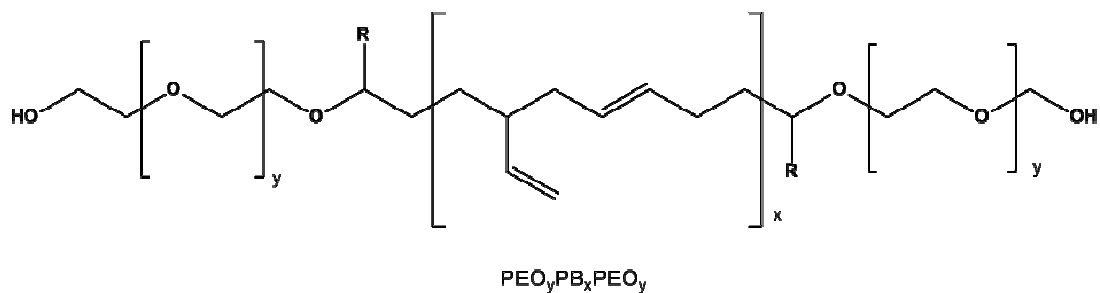
Fig. 4.1.15. Chemical structure of PEO_y-PB_x-PEO_y and SEM images of a IrO_2 mesoporous thin film templated by this copolymer and calcinated at 500°C (from Ref.[12]).

Similarly, Chandra *et al.* developed mesoporous IrO_2 thin films choosing the triblock copolymer "Pluronic F127" ($EO_{106}PO_{70}EO_{106}$) as structural directing agent and spin-coating as deposition technique.[62] They reported that samples calcinated at 400°C present 2D hexagonal mesostructure (*p6mm* symmetry, Fig.4.1.16), but an increase in treatment temperature entails the transformation into disordered mesostructure. The electrocatalytic performance of the mesoporous structure toward OER was found *ca.* 2 times higher than the untemplated IrO_2 electrode, and this performance improvement was ascribed to the larger accessible surface-to-volume ratio.
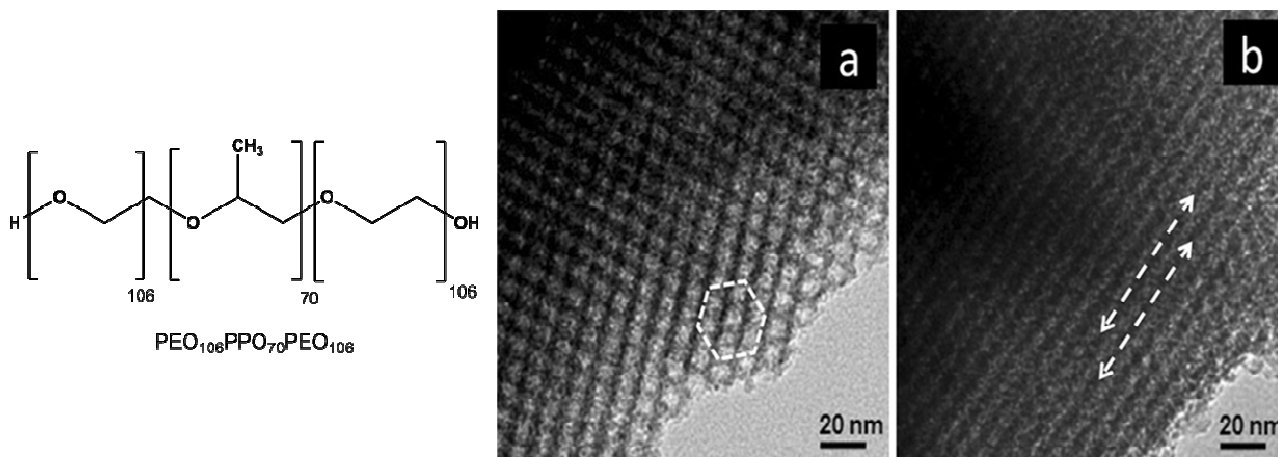
Fig. 4.1.16. Chemical structure of $PEO_{106}PPO_{70}PEO_{106}$ and TEM images of mesoporous IrO_2 films, templated with this copolymer, recorded along the a) [100] and b) [110] axes of the 2D hexagonal structure (from Ref.[62]).

In conclusion, EISA is a very versatile route to induce a nanostructuration into an inorganic material, therefore into IrO_2 films. This method allows the modulation of size and shape of the nanostructures and does not require a complex instrumental equipment.[63] However, an important drawback of this technique is its high dependence on experimental parameters, as temperature, humidity and time: every little variation of these conditions may drastically affect the final nanostructures.[64]

4.2 Preparation of nanostructured IrO$_2$

In this chapter, a new method for the preparation of nanostructured IrO$_2$ is described. The methodology here presented consists in employing the ordered supramolecular gel phases, reported in the previous chapter, as templating agent for the synthesis of nanostructured IrO$_2$. Indeed, as described in paragraph 3.1.5, physical gels have been often used as templates for nanostructured inorganic materials, by virtue of the particular shapes (fibers, ribbons, cylinders, etc.) of their aggregates that can be transferred to the inorganic nanostructures. Many metal oxide (SiO$_2$, TiO$_2$, ZrO$_2$, ZnO and WO$_3$) nanostructures, such as nanotubes, nanoparticles, nanowires, have been efficiently prepared taking advantage of a supramolecular gel as structural directing agent (SDA).[65] The general method requires the in situ formation of a physical gel in the presence of a metal precursor which allows the growth of the inorganic nanostructures around the just formed supramolecular gel assemblies, followed by the template removal.[65] However, up to now, the use of a supramolecular gel for the synthesis of nanostructured IrO$_2$ has not yet been reported. Moreover, the procedure here described employs a supramolecular gel both as templating agent and metal source, representing an innovation in the field of the synthesis of inorganic structures.

Among the synthetized complexes, the compound **[(ppy)$_2$Ir(bpy)]EtOCH$_2$CO$_2$ (15)** is able to generate the most organized supramolecular phase in water, composed by a 2D tetragonal columnar system further organized in a 2D oblique columnar assembly. Therefore **15** was chosen as the more promising example of template to prepare nanostructured IrO$_2$ and to demonstrate the possible use of metallogels to promote nanostructuration in metal oxide. Through the use of complex **15**, IrO$_2$ nanopowder e IrO$_2$ nanostructured thin films have been obtained.

4.2.1 IrO$_2$ nanopowder

IrO$_2$ nanostructured powder has been synthetized employing **[(ppy)$_2$Ir(bpy)]EtOCH$_2$CO$_2$ (15)** both as SDA and Iridium precursor. Its most concentrated gel phase (6% w/w) in water was deposited through the drop-casting method onto glass substrates that were left to dry for several days at room temperature. The corresponding xerogels were calcinated at 600°C for 4h, obtaining non-uniform IrO$_2$ deposits. The metal oxide films were then scraped from the glass substrates, collecting a fine black powder. In order to investigate

the morphology of the obtained IrO_2 powder, a SEM-EDX analysis was carried out. SEM images revealed that the sample actually consists of IrO_2 nanosheets (Fig.4.2.1), that, at the first sight, appear to be smooth and externally non-nanostructured.
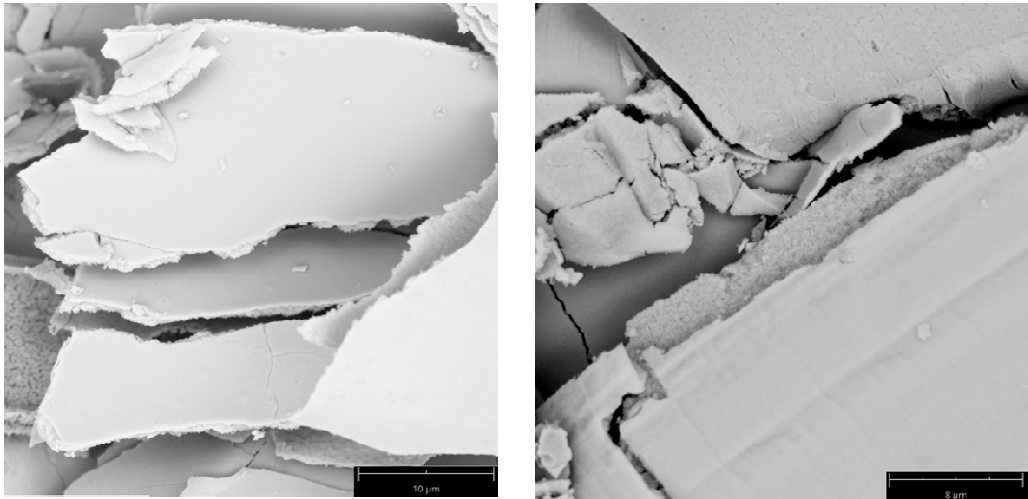
Fig. 4.2.1. SEM images of IrO_2 nanosheets with smooth surface.

However, a closer inspection of the sample revealed the presence of a nanostructuration that becomes evident right beneath the surface (Fig.4.2.2). In particular, fibrous structures of IrO_2, which resemble the fibrous architecture of the gel-xerogel precursor, appear to be entrapped within the nanosheet layers in "wool balls"-like nanostructures (Fig.4.2.2_a and 4.2.2_b). Furthermore, some sample regions show the clear presence of macropores, whose walls are still composed by rather empty fibrous material (Fig.4.2.2_c).
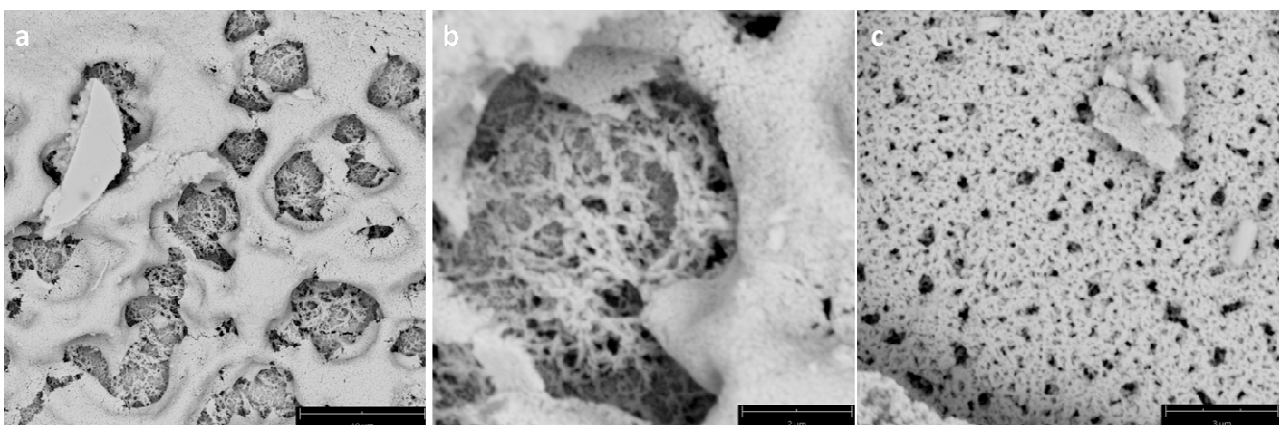
Fig. 4.2.2. SEM images of: (a) IrO_2 nanostructuration present beneath the smooth surface of nanosheets, (b) magnification of a, (c) macropores on the nanosheets.

Furthermore, EDX analysis performed on this sample (Fig.4.2.3) ruled out the presence of organic residues, displaying the exclusive presence of Iridium and Oxygen atoms.

Element Symbol	Atomic Concentration
O	25.0
Ir	75.0
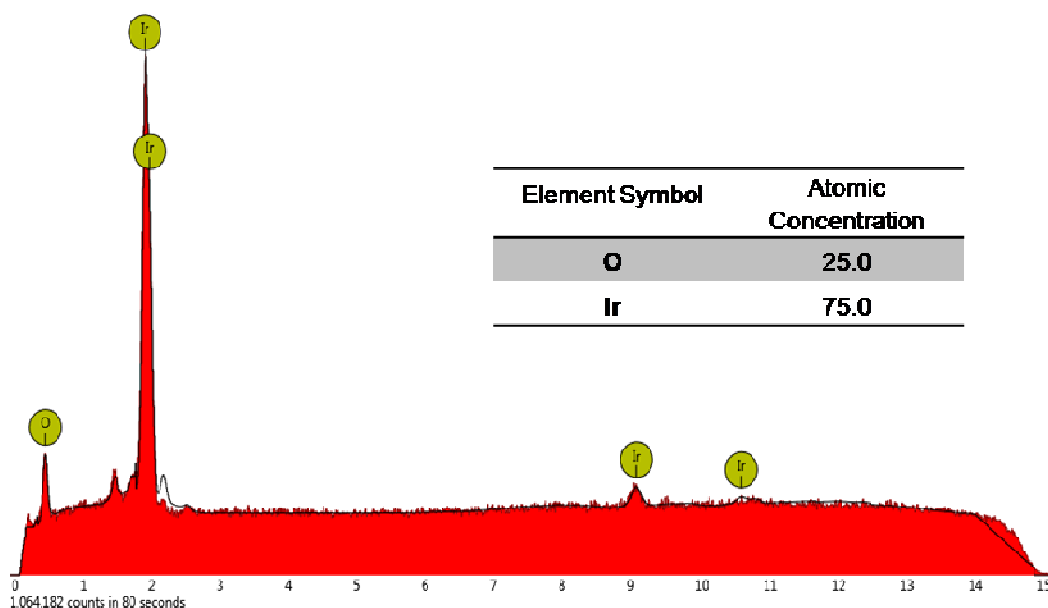
Fig.4.2.3. EDX graph of IrO$_2$ nanopowder.

Unfortunately, the acquisition of SEM micrograph with a larger magnification has not been possible for the IrO$_2$ nanopowder, however, the presence of further smaller pores has been pointed out through TEM analysis (Fig.4.2.4). A magnification of the nanosheets surface, that appears smooth in the SEM images, actually reveals the presence of nanopores with an average dimension of 10 nm.
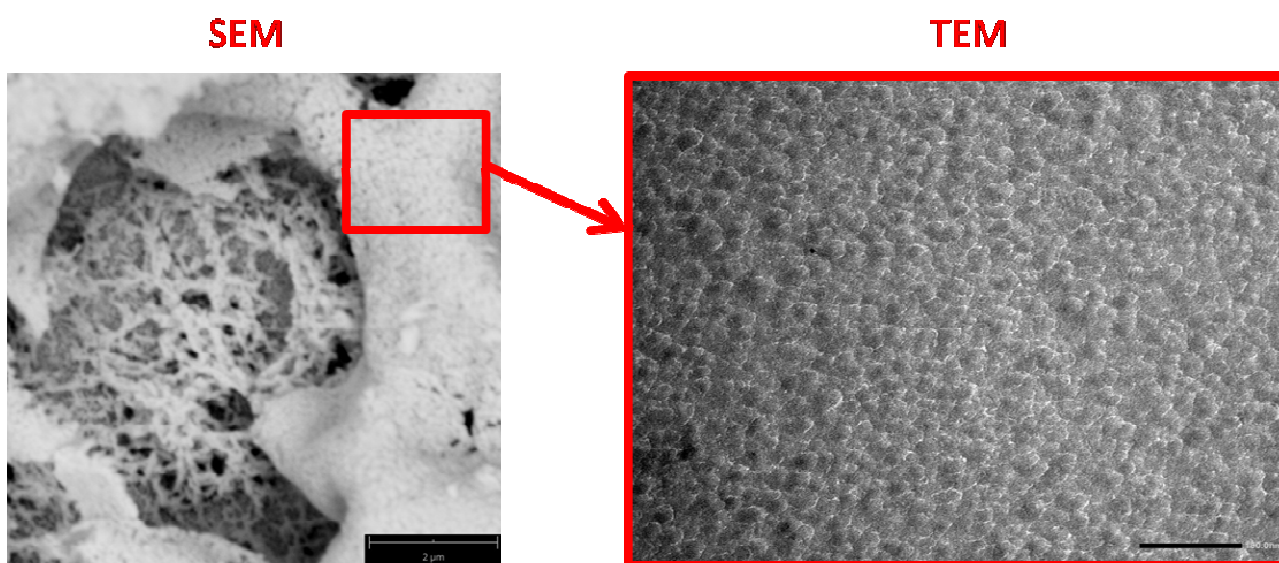
Fig. 4.2.4. SEM (on the left) and TEM micrograph (on the right) of a mesoporous region of IrO$_2$ nanopowder.

It is clear from TEM image that the pores are not through pores, meaning genuine open channels, but they might be closed or blind pores (Fig.4.2.5), since the opening outwards is not visible.

Fig. 4.2.5. Schematic representation of through, closed and blind pores (from ref. [66])

In order to evaluate the nature of these pores (closed or blind), a porosimetric study was performed on an ASAP 2460 instrument using N_2 as gas at the liquid nitrogen temperature. The sample, maintained at 77K in a thermal bath, undergoes to a gradually increasing pressure of N_2, in order to estimate the amount of gas absorbed. This measurement is carried out until the saturation pressure of N_2 has been reached, then the inverse process, which consists in desorbing the gas, is performed. The absorption and desorption isotherms were analyzed employing the BET (Brunauer, Emmett, Teller), BJH (Barrett, Joyner, Halenda) and DA (Dubinin-Astakhov) models, obtaining information about the porosity and the specific area of the analyzed sample.

The adsorption isotherm (Fig.4.2.7) shows the achievement of a plateau state at *ca.* 0.1 relative pressure p/p_0 value. This result is consistent with the micropores filling and with the formation of gaseous mono-layer absorbed on the material surface. Moreover, the desorption isotherm presents an hysteresis, which indicates the capillary condensation of gas into mesopores (2-8 nm).
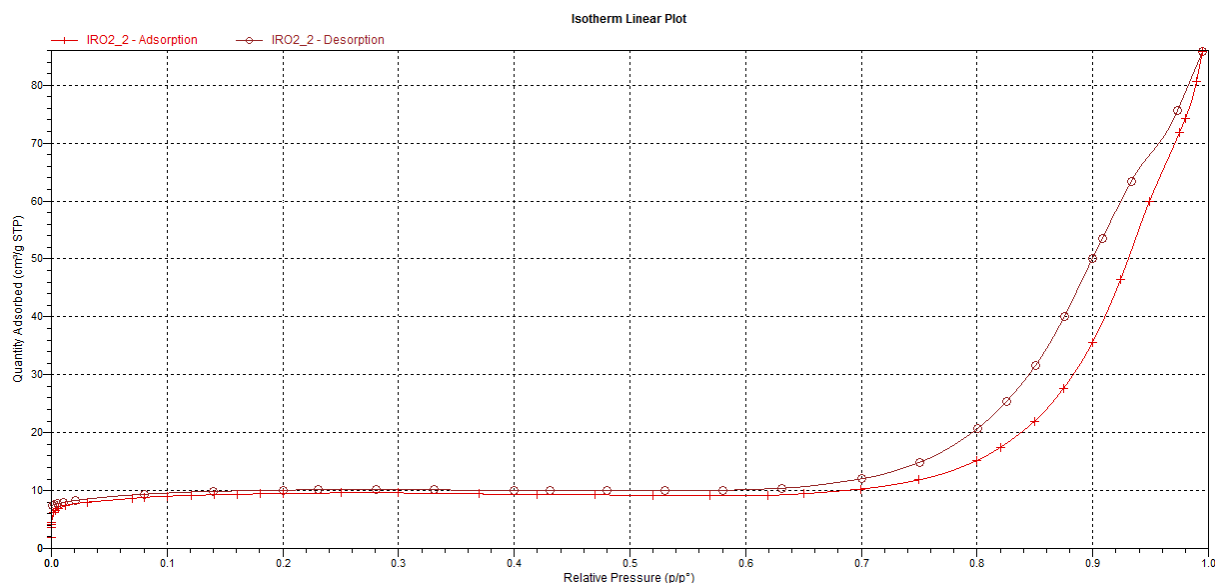
Fig. 4.2.7. Absorption (red) and desorption (deep red) isotherms of IrO_2 nanopowder (IIb type, IUPAC classification).

The data, analysed through BET model, revealed a specific surface area of 35 m^2/g, whereas the cumulative volume of pores, calculated employing BJH model, corresponds to 0.128 cm^3/g.

The sample presents a pore distribution both in the micropores (< 2nm) and the mesopores classes (2-50 nm). Through BJH model it was found that the micropores occupy 35% of the specific surface area and 10% of the total volume, corresponding to 0.014 cm^3/g. Contrary, the mesopores, analyzed employing the DA model occupy 65% of the specific surface area, corresponding to 23m^2/g. The pores dimension distribution, calculated using BJH model, present a peak centered at *ca*. 10 nm characterized by a width (FWHM) of *ca*. 10 nm (Fig.4.2.8).
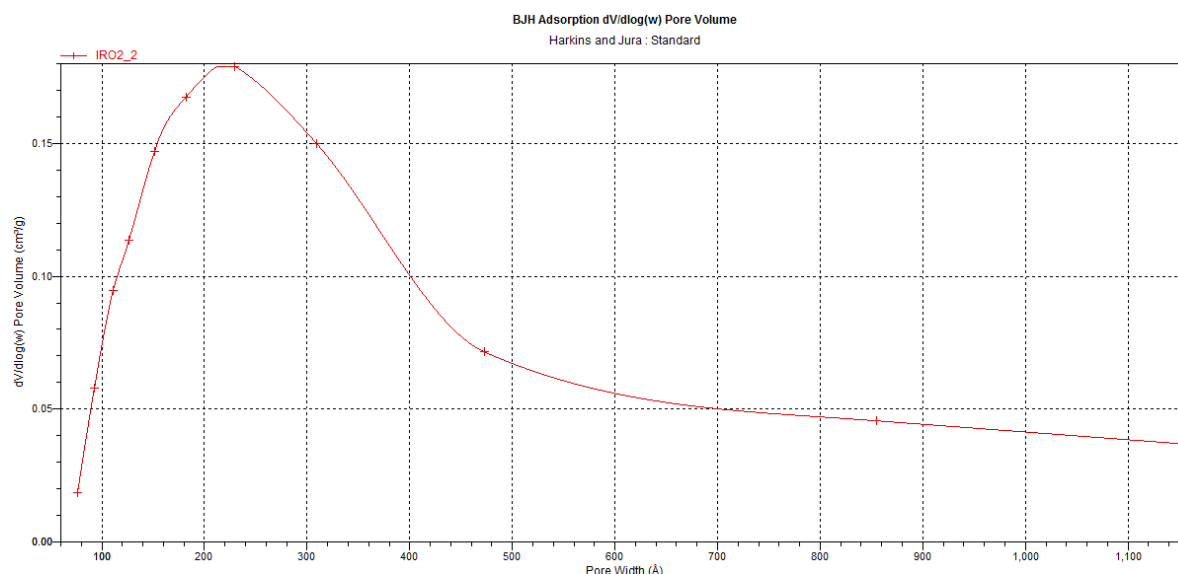
Fig. 4.2.8. Pores distribution (BJH model).

In conclusion, the presence of mesopores was effectively demonstrated by porosity measurements, and, considering the specific surface area value of 35 m^2/g, hence the accessibility of the pores, they can be regarded as blind pores, rather than closed pores. Finally, both mesopores and macropores are present, but most of the pores have a dimension of 10 nm (mesopores), in agreement with the TEM observation.

4.2.2 IrO$_2$ nanostructured thin films

The highly ordered gel phases of **[(ppy)$_2$Ir(bpy)]EtOCH$_2$CO$_2$ (15)** were also employed as organometallic precursors for the formation of nanostructured IrO$_2$ thin films. Contrary to the preparation of IrO$_2$ nanopowder, for whom drop-casting technique was employed, the formation of IrO$_2$ thin films was achieved using spin-coating deposition method. In particular, the gel phases of **15** at different concentrations (3%, 4%, 5% and 6% w/w) were deposited onto quartz substrates through spin-coating and were left to dry at room temperature for several days, obtaining the corresponding xerogels. As described in chapter 3, the anisotropic gel architecture is retained also after its complete dehydration, i.e. in the xerogel, as revealed by the persistence of a well-defined birefringent texture under POM and by the PXRD pattern. These xerogel films, presenting ordered architecture of the constituent molecular motifs, were used both as Iridium source and templating agent for the generation of IrO$_2$ thin films. For this purpose, xerogels films were directly treated at high temperature (600°C) for 4h, obtaining uniform IrO$_2$ thin films (Fig.4.2.9).

Calcination

Xerogel thin film   **IrO₂ thin film**
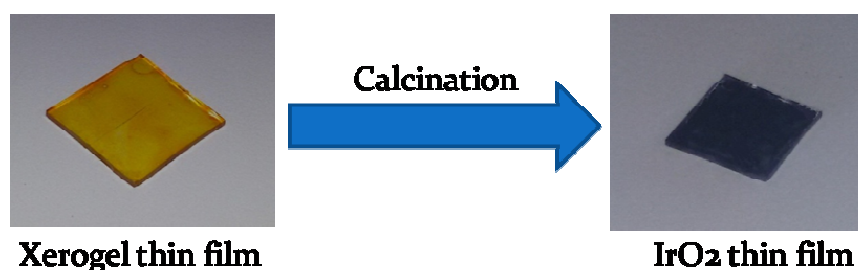
Fig. 4.2.9. Images of the xerogel and the IrO$_2$ thin films deposited onto quartz substrate.

Also in this case, the effective formation of IrO$_2$ and the total degradation of the organic ligands were assured by EDX analysis, which revealed only the presence of Iridium and Oxygen atoms.

The morphology of the IrO_2 films obtained starting from the gel phases at 3, 4, 5 and 6% w/w were analyzed through SEM. Only for samples obtained from 5% and 6% w/w gel phases was observed an inner nanostructuration. For lower gel concentrations (3 and 4% w/w) films resulted too thin for allowing useful observations. In particular, the film obtained starting from the 5% w/w gel phase is composed of a *ca.* 80 nm thick layer highly organised (Figure 4.2.10_a). The micrograph highlights the presence of a dense film composed of ordered vertical IrO_2 arrays that outlines the nanostructure. The metal-oxide film attained using the 6% w/w gel phase shows a self-assembled well-ordered multilayer thin film of an overall $1\mu m$ thickness (Figure 4.2.10_b). However, the sample displays a less homogeneous surface coverage respect to the IrO_2 derived from the 5% w/w gel phase, probably due to the higher viscosity of the 6% w/w gel phase solution, that during spin-coating prevents the efficient and homogeneous coverage of the substrate. Nonetheless, the SEM micrograph reveals the well-ordered nanostructure of each layer, probably resulting for different orientation of the nanostructured arrays of IrO_2 present within each layer. Noteworthy, the top surface layer present identical features of the film obtained for the 5% w/w gel phase with vertical alignment of the IrO_2 arrays. In both cases, the specific arrangement of the IrO_2 structure can reasonably be attributed to be deriving from the ordered self-assembled columnar features of the starting xerogels.
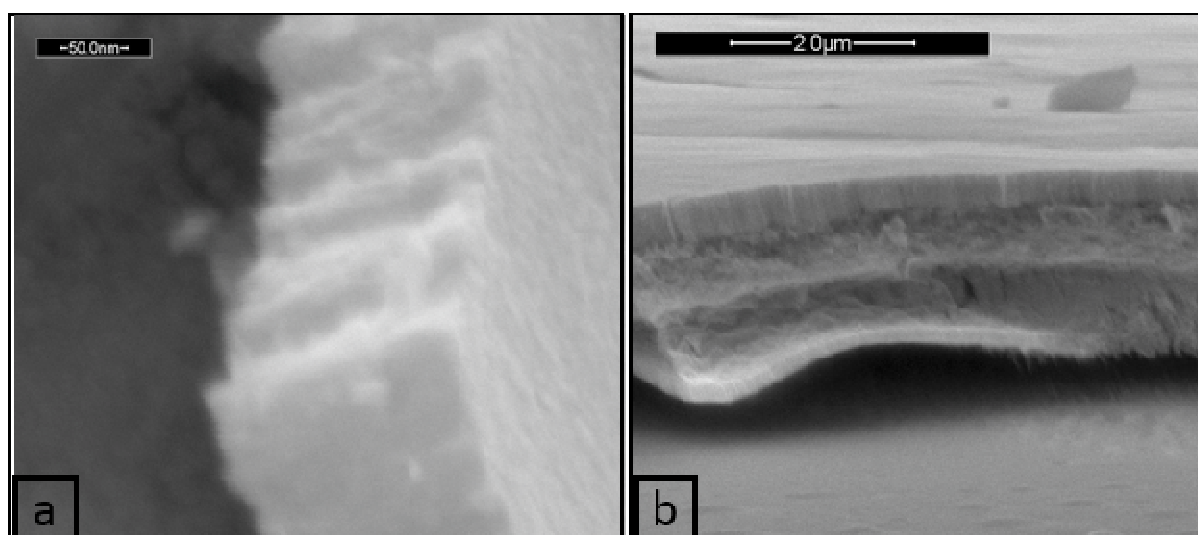
Figure 4.2.10. SEM micrographs of the IrO_2 thin film obtained from the gel phases: 5% w/w (a) and 6% w/w (b).

Furthermore, these inorganic films were investigated through PXRD analysis in order to get information about their eventual crystalline nature. The PXRD patterns of the IrO_2 obtained from all the starting gel concentrations, are identical and are consistent with the rutile phase of IrO_2 (Figure 4.2.11). PXRD data are reported in Table 4.2.1 with the relative observed peak intensity, together with the expected referenced data for the rutile IrO_2 powder[67] for direct comparison.
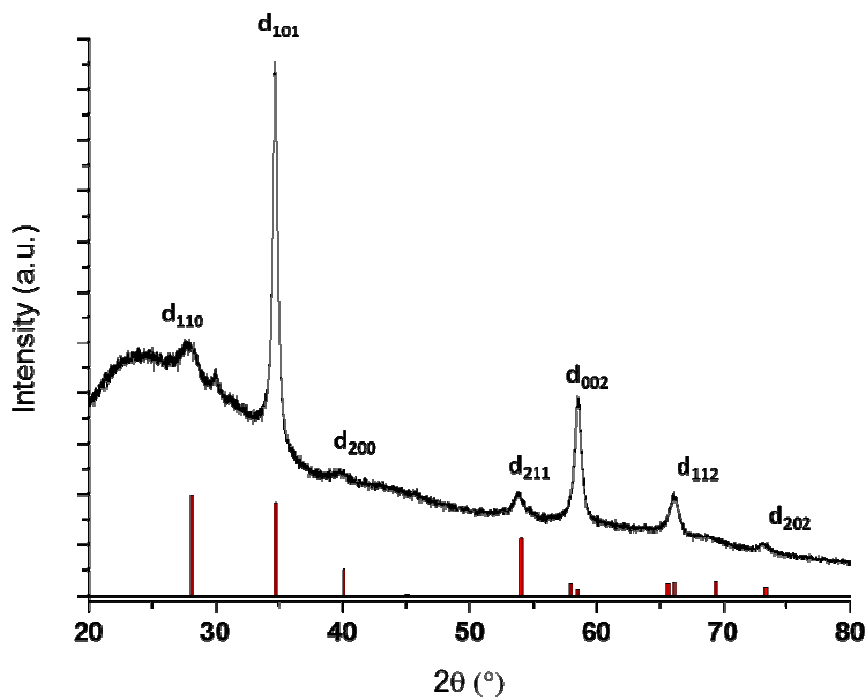
Figure 4.2.11. XRD pattern of IrO_2 thin films.

d_{hkl}	2θ (°)	I_{exp}	I_{theo}[a]
d_{110}	28.07	10	100
d_{101}	34.74	100	92
d_{200}	40.10	5	26
d_{210}	*Not seen*		<1
d_{211}	54.08	8	56
d_{220}	*Not seen*		12
d_{002}	58.50	35	6
d_{310}	*Not seen*		12
d_{112}	66.11	13	13
d_{301}	*Not seen*		14
d_{202}	73.31	3	8

Table 4.2.1. Indexation of the IrO_2 thin film PXRD spectrum and relative intensity of the observed peaks. [a] data extracted from ref. [67].

Noteworthy, the PXRD pattern for the prepared IrO_2 thin films displays relative intensity values for the main reflection peaks different from the reference IrO_2 powder. In particular, in the PXRD pattern of the IrO_2 reference, the (110) is the most intense reflection peak observed, whereas the PXRD pattern of the thin film shows much more intense (101) reflection peak and slightly more intense (002) and (112) reflections. Such variation in intensity can be attributed to a specific crystal growth orientation of the rutile unite cell, predominantly grown into the (101), (002) and (112) directions. This preferential orientation growth can be correlated to the high order self-assembled columnar architecture of the gel phase and is reflected in the nanostructured arrays previously observed by SEM.

4.3 Conclusions

A new method for the preparation of nanostructured IrO_2, in the form of powder and thin films, has been proposed. The procedure here described is based on the use of an ordered starting organometallic material which acts both as metal source and templating agent. The so prepared inorganic materials resemble the ordered architecture of the supramolecular phases used as precursor. In particular, the IrO_2 thin film originated from the 5% w/w gel phase of compound **15** displayed an ordered nanostructure composed of ordered vertical IrO_2 arrays. As described in the present chapter, the nanostructuration of IrO_2, as well as for other transition metal oxides, could enhance its intrinsic properties compared with the bulk material. Specifically, the presence of a highly porous structure, with pores accessible from the surface, results in an increased number of active sites on the material, which induces an enhancement of electrocatalytic and sensing activities of IrO_2. This effect can be efficiently exploited into electrocatalytic applications. Even the application of IrO_2 in electrochromic devices can benefit from the increased surface-to-volume ratio, determining faster colour change in the device.

The procedure described could be the starting point for the development of a new method to prepare ordered IrO_2 thin films and, in a more general perspective, other inorganic nanostructures taking advantage of a well-organized organometallic gel precursor.

4.4 References

1. D. B. Rogers, R. D. Shannon, A. W. Sleight, J. L. Gillson, *Inorg. Chem.,***1969**, 8, 841-849.
2. https://crystallography365.wordpress.com/2014/07/10/rutile-like-but-very-rare/.
3. S. Trasatti, G. Lodi, *Electrodes of Conductive Metallic Oxides*, Part B, Elsevier, Amsterdam, 1981, p. 521.
4. D. B. Rogers, R. D. Shannon, A. W. Sleight, J. L. Gillson, *Inorg. Chem.*, **1969**, 8, 841-849.
5. J. Riga, C. Tenret-Noël, J. J. Pireaux,l R. Caudano, J. J. Verbist, *Phys. Scripta*, **1977**, 16, 351-354.
6. D. Takimoto, K. Fukuda, S. Miyasaka, T. Ishida, Y. Ayato, D. Mochizuki, W. Shimizu, W. Sugimoto, *Electrocatalysis,* **2017**, 8, 144-150.
7. C. M. Nguyen, I. Gurung, H. Cao, S. Rao, J.-C. Chiao, *Sensors,* **2013**, IEEE.
8. R.S. Chen, Y.S. Huang, Y.M. Liang, D.S. Tsai, K.K. Tiong, *J. Alloys Compd.,***2004**, 383, 273-276.
9. Y. Lee, M. Kang, J. H. Shim, N.-S. Lee, J. M. Baik, Y. Lee, C. Lee, M. H. Kim, *J. Phys. Chem. C*, **2012**, 116, 18550 –18556.
10. F. Zhang, R. Barrowcliff, G. Stecker, W. Pan, D. Wang, S.-T. Hsu, *Jpn. J. Appl. Phys*., **2005**, 44, L398-L401.
11. Y. Zhao, E. A. Hernandez-Pagan, N. M. Vargas-Barbosa, J. L. Dysart, T. E. Mallouk**,** *J. Phys. Chem. Lett.*, **2011**, *2* , 402–406.
12. E. Ortel, T. Reier, P. Strasser, R. Kraehnert, *Chem. Mater.*, **2011**, 23, 3201–3209.
13. J. Hu, M. Abdelsalam, P. Bartlett, R. Cole, Y. Sugawara, J. Baumberg, S. Mahajanb, G. Denuault, J. *Mater. Chem*., **2009**, 19, 3855–3858.
14. Y. Cui, Q. Wei, H. Park, C. M. Lieber, *Science,* **2001**, 293, 1289–1292.
15. E. Stern, J. F. Klemic, D. A. Routenberg, P. N. Wyrembak, D. B. Turner-Evans, A. D. Hamilton, D. A. LaVan, T. M. Fahmy, M. A. Reed, *Nature*, **2007**, 445, 519–522.
16. M. Zukalová, A. Zukal, L. Kavan, M. K. Nazeeruddin, P. Liska, M. Grätzel, *Nano Lett.*, **2005**, 5, 1789–1792.
17. Y.Shi, B. Guo, S. A. Corr, Q. Shi, Y.-S. Hu, K. R. Heier, L. Chen, R. Seshadri, G. D. Stucky, *Nano Lett.*, **2009**, 9*,* 4215–4220.
18. F. Jiao, P. G. Bruce, *Adv. Mater*., **2007**, 19, 657–660.
19. https://www.nebb.com/combined-hydrogen-and-power-production
20. W. Hu, Y. Wang, X. Hu, Y. Zhou, S. Chen, *J. Mater. Chem.* **2012**, *22*, 6010–6016.
21. R. D. L. Smith, B. Sporinova, R. D. Fagan, S. Trudel, C. P. Berlinguette,*Chem. Mater.* **2014**, *26*, 1654–1659.
22. S. Siracusano, N. Van Dijk, E. Payne-Johnson, V. Baglio, A. S. Aricò, *Appl.Catal. B-Environ.* **2015**, *164*, 488-495.
23. M. Carmo, D. L. Fritz, J. Mergel, D. Stolten, *Int. J. Hydrogen Energy*, **2013**, 38, 4901–4934.
24. S. Kaya, D. Friebel, H. Ogasawara, A. Nilsson, *Angew. Chem. Int. Ed*., **2014**, 53, 7169-7172.
25. G.S. Nahor, P. Hapiot, P. Neta, A. Harriman, *J. Phys. Chem*., **1991**, 95, 616-621.
26. F. Andolfatto, R. Durand, A. Michas, P. Millet, P. Stevens, *Int. J. Hydrogen Energy*, **1994**, 19, 421–427.
27. S. Siracusano, V. Baglio, A. Stassi, R. Ornelas, V. Antonucci, A.S. Aricò, *Int. J. Hydrogen Energy*, **2011**, 36, 7822-7831.
28. M. Bernicke, E. Ortel, T. Reier, A. Bergmann, J. Ferreira de Araujo, P. Strasser, R. Kraehnert, *ChemSusChem*., **2015**, 8, 1908 – 1915.

29. E. L. Runnerstrom, A. Llorde´s, S. D. Lounis, D. J. Milliron, *Chem. Commun.,* **2014**, 50, 10555-10572.

30. S. Gottesfeld, J. D. E. Mclntyre, G. Beni, J. L. Shay, *Appl. Phys. Letters*, **1978**, 33, 208-210.

31. S. Gottesfeld, J. D. E. Mclntyre, *J. Electrochem. Soc.*, **1979**, 126, 742-750.

32. W. C. Dautremont-Smith, L. M. Schiavone, G. Beni, J. L. Shay, *SID 80 Digest,* **1980**, p.122.

33. W. C. Dautremont-Smith, *Displays,* **1982**, 3, 67-80.

34. J. L. Shay, G. Beni, L. M. Schiavone, *Appl. Phys. Letters,* **1978**, 33, 942-944.

35. K. Yamanaka, *Jpn. J. Appl. Phys.* **1989**, *28*, 632-637.

36. S. Ito, Y. Abe, M. Kawamura, K. H. Kim, *J. Vac. Sci. Technol. B* **2015**, *33*, 041204 , doi:0.1116/1.4923227.

37. I. A. Ges, B. L. Ivanov, A. A. Werdich, F. J. Baudenbacher, *Biosens. Bioelectron*., **2007**, 22, 1303–1310.

38. L.-M. Kuo, Y.-C. Chou, K.-N. Chen, C.-C. Lu, S. Chao, *Sens. Actuators B*, **2014**, 193, 687– 691.

39. M. L. Hitchman, S. Ramanathan, *Anal. Chim. Acta*, **1992**, 263, 53–61.

40. D. O'Hare, K. H. Parker, C. P. Winlove, *Med. Eng. Phys.,* **2006***,* 28, 982-988.

41. S. Głab, A. Hulanicki, G. Edwall, F. Ingman, *Crit. Rev. Anal. Chem*., **1989**, 21, 29–47.

42. A. N. Bezbaruah, T. C. Zhang, *Anal. Chem*., **2002**, 74, 5726-5733.

43. F. Zhang, B. Ulrich, R. K. Reddy, V. L. Venkatraman, S. Prasad, T. Q. Vu, S.-T. Hsu, *Jpn. J. Appl. Phys.*, **2008**, 47, 1147–1151.

44. R. A. Buchanan, I.-S. Lee, and J. M. Williams, *J. Biomed. Mater. Res*., **1990**, 24, 309-318.

45. L. S. Robblee, M. J. Mangaudis, E. D. Lasensky, A. G. Kimball, S. Barry Brummer, *Biomedical Materials, J. M. Williams, M. F. Nichols, and W. Zingg, (eds.), Mat. Res. Soc. Symp. Proc.*, *Materials Research Society, Pittsburgh,* **1986**, 55, 303-310.

46. B.R. Chalamala, Y. Wei, R.H. Reuss, S. Aggarwal, B.E. Gnade, R. Ramesh, J.M. Bernhand, E.D. Sosa, D.E. Golden, *Appl. Phys. Lett*., **1999**, 74, 1394-1396.

47. B.R. Chalamala, Y. Wei, R.H. Reuss, S. Aggarwal, S.R. Perusse, B.E. Gnade, R. Ramesh, *J. Vac. Sci. Technol. B*, **2000**, 18, 1919-1922.

48. B. R. Chalamala, R. H. Reuss, K. A. Dean, E. Sosa, David E. Golden, *J. Appl. Phys*., **2002**, 91, 6141-6146.

49. R.S. Chen, Y.S. Huang, Y.M. Liang, C.S. Hsieh, D.S. Tsai, K.K. Tiong, *Appl. Phys. Lett*., **2004**, 84, 1552-1554.

50. O. Kubaschewski, B. E. Hopkins, *Oxidation of Metals and Alloys,* Butterworths, London, 1962.

51. V. Baglio, D. Sebastian, C. D'Urso, A. Stassi, R. S. Amin, K. M. El-Khatib, A.S. Aricò, *Electrochim. Acta*, **2014**, 128, 304–310.

52. Y.-M. Chen, J.-H. Cai, Y.-S. Huang, K.-Y. Lee, D.-S. Tsai, K.-K. Tiong, *Nanotechnology*, **2011**, 22, 355708.

53. E. Slavcheva, R. Vitushinsky, W. Mokwa, U. Schnakenberg, J. *Electrochem. Soc*., **2004**, 151, E226-E237.

54. A. Marshall, B. Børresen, G. Hagenm, M. Tsypkin, R. Tunold, *Mater. Chem. Phys.,* **2005**, 94, 226–232.

55. F. Bonet, V. Delmas, S. Grugeon, R. Herrera-Urbina, P. Silvert, K. Tekaia-Elhsissen, *NanoStruct. Mater.*, **1999**, 11, 1277-1284.

56. R. Adams, R. Shriner, *J. Am. Chem. Soc*., **1923**, 45, 2171-2179.

57. J. C. Cruz, V. Baglio, S. Siracusano, R. Ornelas, L. Ortiz-Frade, L. G. Arriaga, V. Antonucci, A. S. Aricò, *J Nanopart Res*, **2011**, 13, 1639–1646.

58. J. Ahmed, Y. Mao, *Electrochim. Acta*, **2016**, 212, 686-693.

59. Cuong M. Nguyen, Smitha Rao, and J.-C. Chiao, Hung Cao, Ailing Li, Yuan Bo Peng, SENSORS, 2014 IEEE, **DOI:** 10.1109/ICSENS.2014.6985393.

60. P.S. Patil, R.K. Kawar, S.B. Sadale, *Electrochim. Acta,* **2005**, 50, 2527–2532.

61. "Solar Radiation Applications"*, book edited by Segun Raphael Bello, ISBN 978-953-51-2124-4, Published: May 6, 2015,* Chapter 5, Applications of Mesoporous Ordered Semiconductor Materials — Case Study of TiO2, Antonio E. H. Machado, Karen A. Borges, Tatiana A. Silva, Lidiaine M. Santos, Mariana F. Borges, Werick A. Machado, Bruno P. Caixeta, Marcela Dias França, Samuel M. Oliveira, Alam G. Trovó and Antonio O.T. Patrocínio.

62. D. Chandra, N. Abe, D. Takama, K. Saito, T. Yui, M. Yagi, *ChemSusChem*, **2015**, 8, 795 – 799.

63. C. J. Brinker, Y. Lu, A. Sellinger, H. Fan, *Adv. Mater.*, **1999**, 11, 579-585.

64. D. Grosso, F. Cagnol, G. J. de A. A. Soler-Illia, E. L. Crepaldi, H. Amenitsch, A. Brunet-Bruneau, A. Bourgeois, C. Sanchez, Adv. Funct. Mater., 2004, 4, 309-322.

65. M. Llusar, C. Sanchez, *Chem. Mater.* **2008**, *20*, 782–820 and references reported therein.

66. http://slideplayer.com/slide/4142327/

67. Standard X-ray Diffraction Powder Patterns. U.S. Dept. Of Commerce, National Bureau of Standards: Washington, DC, 1965; Vol.25, Sec.4, page 19.

Chapter 5

Conclusions

In this thesis, the synthesis and the characterization of several water-soluble Ir(III) complexes, **[(ppy)$_2$Ir(biq)]CH$_3$CO$_2$ (2), [(ppy)$_2$Ir(dip)]CH$_3$CO$_2$ (4), [(ppy)$_2$Ir(dpa)]CH$_3$CO$_2$ (6), [(ppy)$_2$Ir(dpc)]CH$_3$CO$_2$ (8), [(ppy)$_2$Ir(dpq)]CH$_3$CO$_2$ (10), [(ppy)$_2$Ir(dppz)]CH$_3$CO$_2$ (12), [(ppy)$_2$Ir(bpy)]EtO (13), [(ppy)$_2$Ir(bpy)]OH (14), [(ppy)$_2$Ir(bpy)]EtOCH$_2$CO$_2$ (15)** and **[(ppy)$_2$Ir(bpy)]MeOCH$_2$CO$_2$ (16)**, have been presented. The solubility in water is a desirable feature that an Ir(III) complex should exhibit in order to be effectively used in biologically-related applications. In the Ir(III) cationic complexes presented herein, the solubility in water has been achieved simply by choosing the appropriate counterion. The hydrophilic nature of the selected counter-anions, **CH$_3$CO$_2^-$, EtO$^-$, OH$^-$, EtOCH$_2$CO$_2^-$** and **MeOCH$_2$CO$_2^-$**, has issued water-solubility to these complexes through easy chemical methodologies, thus avoiding the long, thorny and expensive synthetic procedures commonly used in order to achieve this appealing feature. The synthetized compounds, with the exception of **10** and **12**, are luminescent in high diluted water solution, and, in this context, the complex **[(ppy)$_2$Ir(dpa)]CH$_3$CO$_2$ (6)** has displayed the most interesting photophysical properties, since its luminescence quantum yield (ϕ) is strongly dependent on the presence of molecular oxygen. For this reason, compound **6** may be a valuable candidate as O$_2$ sensor and as photosensitizer in Photodynamic Therapy.

In addition, the compound family of the **[(ppy)$_2$Ir(bpy)]X** type, *i.e.* complexes **13**, **14**, **15** and **16**, was obtained through a newly synthetic pathway, which takes advantage of the versatility of the hydroxy-bridged dimer **[(ppy)$_2$Ir(μ-OH)]$_2$ (II)** used as a precursor. Indeed, depending on the solvent employed in the bridge splitting reaction of **[(ppy)$_2$Ir(μ-OH)]$_2$ (II)**

and in the presence of the ancillary ligand **bpy**, different counterions, derived from solvent molecules, can be introduced in the final complex **[(ppy)$_2$Ir(bpy)]X.**

Moreover, similarly to the parent compounds **[(ppy)$_2$Ir(bpy)]CH$_3$CO$_2$**[1] and **[(ppy)$_2$Ir(phen)]CH$_3$CO$_2$**,[2] some of the presented complexes, *i.e* **[(ppy)$_2$Ir(dpq)]CH$_3$CO$_2$ (10)**, **[(ppy)$_2$Ir(dppz)]CH$_3$CO$_2$ (12)**, **[(ppy)$_2$Ir(bpy)]EtO (13)**, **[(ppy)$_2$Ir(bpy)]OH (14)**, **[(ppy)$_2$Ir(bpy)]EtOCH$_2$CO$_2$ (15)** and **[(ppy)$_2$Ir(bpy)]MeOCH$_2$CO$_2$ (16)**, are able to self-assemble in water in a determined range of concentrations, generating supramolecular phases. In particular, the complexes bearing **bpy** as ancillary ligand, *i.e.* compounds **13**, **14**, **15** and **16**, were found to form highly organized supramolecular metallo-hydrogel phases, presenting characteristic birefringent textures under POM, which are retained also after evaporation of the solvent, thus in the corresponding xerogel films, together with the initial supramolecular structure. These phases have been examined through PXRD technique, pointing out the supramolecular architecture of these samples, consisting in tetragonal columnar strands of the cationic moieties surrounded by the counterions, further arranged in a larger oblique columnar system. Also complexes **10** and **12**, incorporating **dpq** and **dppz** respectively as ancillary ligands, were found to self-aggregate in water, though generating supramolecular phases different from those derived from the compound family **[(ppy)$_2$Ir(bpy)]X**. Indeed, complex **[(ppy)$_2$Ir(dpq)]CH$_3$CO$_2$ (10)**, in concentrated water solution (3-14% w/w), exhibits a behaviour more similar to a lyotropic liquid crystal than to a physical gel. This similarity derived from the observation of the well-known focal conic fan textures and from the role played by the solvent in these phase, whose removal determines the loss of the rectangular columnar organization displayed in the hydrated-phases. On the contrary, compound **[(ppy)$_2$Ir(dppz)]CH$_3$CO$_2$ (12)**, which incorporates a more extended aromatic ancillary ligand, **dppz,** with respect to complexes bearing **bpy** and **dpq**, loses the ability to generate genuine gel-phases, which do not flow in the steady state, but, at the same time, is still capable to form birefringent viscous solutions, whose dehydration evidenced the presence of an hexagonal columnar structure through PXRD analysis and the presence of fibrous aggregates through TEM observation.

[1] Y. J. Yadav, B. Heinrich, G. De Luca, A. M. Talarico, T. F. Mastropietro, M. Ghedini, B. Donnio, E. I. Szerb, *Adv. Opt. Mater.*, **2013**, 1, 844–854.
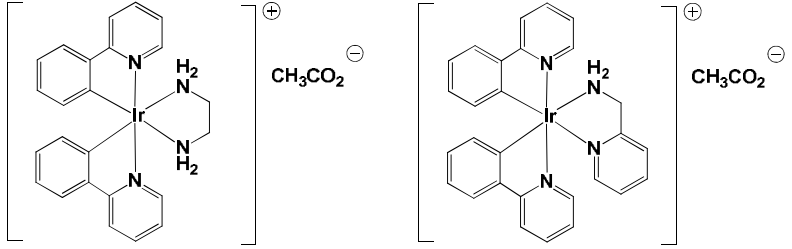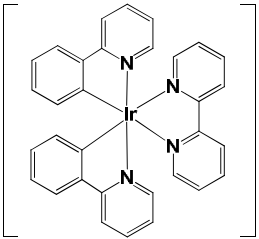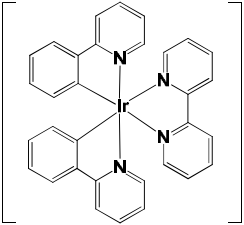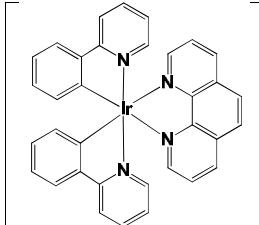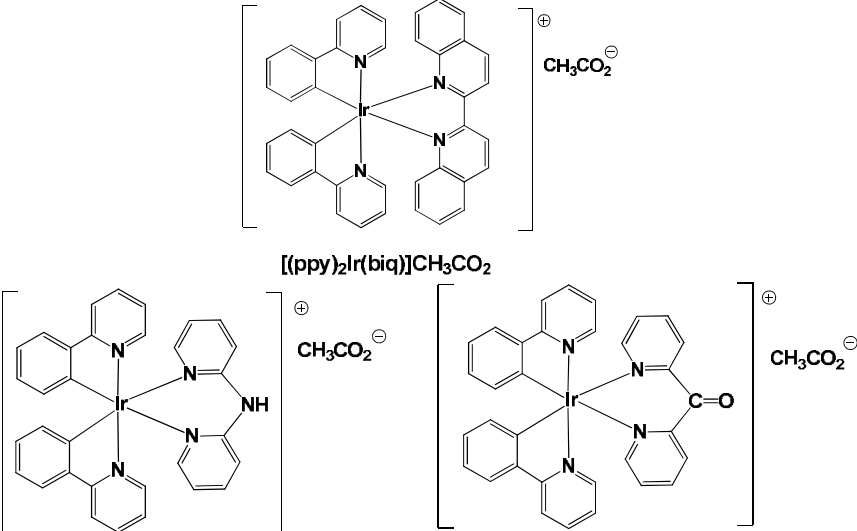[2] C. Oliviero Rossi, C. Cretu, L. Ricciardi, A. Candreva, M. La Deda, I. Aiello, M. Ghedini, E. Ildyko Szerb, *Liquid Crystals*, **2017**, 44, 880-888.

Since the complexes able to self-organize in water, incorporate **bpy**, **phen**, **dpq** and **dppz** as ancillary ligands, the presence of an aromatic rigid and planar N^N ligand seems to be a necessary condition for the generation of physical columnar aggregates. This hypothesis was further confirmed by the absence of supramolecular phases formation for the complexes **[(ppy)₂Ir(en)]CH₃CO₂** and **[(ppy)₂Ir(pam)]CH₃CO₂**.[3]

A deeper insight into this issue has been given by the study of the geometry optimization performed through DFT calculation (Chapter 2). This analysis allowed to determine that, in the synthetized cationic moieties **[(ppy)₂Ir(N^N)]⁺** the HOMO is evenly distributed onto the two **ppy** cyclometalated ligands, whereas the LUMO is mainly localized onto the N^N ancillary ligand. It is therefore reasonable to propose a π-π stacking between **ppy** ligands and the N^N ligand of an adjacent Ir(III) molecule as an origin of the formation of columnar organization of molecules, which further aggregation results in the formation of the fibrous network observed through TEM. In this light, it is not surprising that, **[(ppy)₂Ir(biq)]CH₃CO₂ (2)**, **[(ppy)₂Ir(dip)]CH₃CO₂ (4)**, **[(ppy)₂Ir(dpa)]CH₃CO₂ (6)** and **[(ppy)₂Ir(dpc)]CH₃CO₂ (8)**, although soluble in water, do not form any "gel" phase. Indeed, in the case of complex **4**, which does not form any supramolecular organization, the presence of the **dip** ancillary ligand prevents efficiently stacking of molecules in columnar structures, due to the two phenyl rings free rotation. Moreover, DFT calculations allowed to observe the distortion of **biq**, **dpa** and **dpc** ancillary ligands of complexes **2**, **6** and **8** respectively. The absence of planarity in these ancillary ligands, probably rules out the efficient stacking of adjacent Ir(III) complexes. In addition, in the case of **[(ppy)₂Ir(dpa)]CH₃CO₂ (6)** and **[(ppy)₂Ir(dpc)]CH₃CO₂ (8)**, the presence of the chemical groups –NH and –C=O into the N^N ligands **dpa** and **dpc** respectively, could also be involved in the further formation of hydrogen bonding with water molecules, improving the solubility of these complexes in water, thus disrupting the delicate balance between solubilisation and aggregation required in order to achieve gelation.

The main features of the complexes of type **[(ppy)₂Ir(N^N)]X** (**X= CH₃CO₂⁻, EtO⁻, OH⁻, EtOCH₂CO₂⁻** and **MeOCH₂CO₂⁻**), together with their chemical structures, are summarized in Table 5.1.

[3] L. Ricciardi, T. F. Mastropietro, M. Ghedini, M. La Deda, E. Ildyko Szerb, *J Organomet Chem.*, **2014**, 772–773, 307–313.

Complex	Main features
 [(ppy)$_2$Ir(en)]CH$_3$CO$_2$[3] [(ppy)$_2$Ir(pam)]CH$_3$CO$_2$[3]	Highly water-soluble complexes. The presence of –NH$_2$ groups promotes solubility by hydrogen bonding with H$_2$O molecules, probably preventing gelification.
 [(ppy)$_2$Ir(bpy)]CH$_3$CO$_2$[1]	Water-soluble complex, able to generate birefringent gel-phases. Molecular architecture composed by columnar strands of cations.
 X$_1$ = EtO X$_2$ = OH X$_3$ = EtOCH$_2$CO$_2$ X$_4$ = MeOCH$_2$CO$_2$ [(ppy)$_2$Ir(bpy)]X	Water soluble complexes, able to form highly organized supramolecular structures, composed by tetragonal columnar strands, in turn organized in an oblique columnar structure.
 [(ppy)$_2$Ir(phen)]CH$_3$CO$_2$ [2]	Water-soluble complex, able to generate birefringent gel-phases. Molecular architecture composed by columnar strands of cations.
 [(ppy)$_2$Ir(biq)]CH$_3$CO$_2$ [(ppy)$_2$Ir(dpa)]CH$_3$CO$_2$ [(ppy)$_2$Ir(dpc)]CH$_3$CO$_2$	Water-soluble complexes. No supramolecular phases formation was observed, probably due to the distortion of the **biq, dpa** and **dpc** ligands, which could prevent the formation of the columnar system.
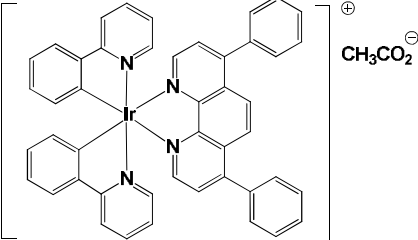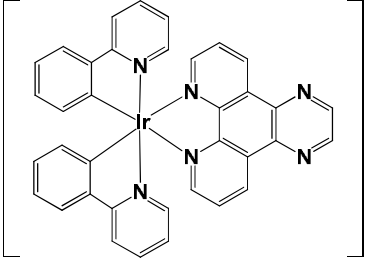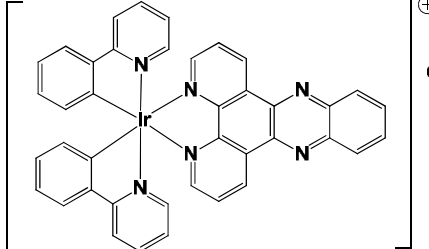
[(ppy)₂Ir(dip)]CH₃CO₂ 	Water-soluble complex. No supramolecular phases formation was observed, probably due to the free rotation of the two phenyl ring in the **dip** ligand, which could disrupt the columnar stacking of the complex molecules.
[(ppy)₂Ir(dpq)]CH₃CO₂ 	Highly water soluble complex. Formation of a columnar lyotropic-like phase, characterized by big strands.
[(ppy)₂Ir(dppz)]CH₃CO₂ 	Water soluble complex. Formation of birefringent viscous phase.

Table 5.1. Chemical structures and main features of the Ir(III) cationic complexes of type **[(ppy)₂Ir(N^N)]X** (**X= CH₃CO₂⁻, EtO⁻, OH⁻, EtOCH₂CO₂⁻ and MeOCH₂CO₂⁻**).

Finally, in this thesis, the highly organized phases of the metallo-hydrogelator **15,** have been employed as template for the synthesis of nanostructured IrO₂. Actually, for the first time, the starting metallogel has acted both as structural directing agent (SDA) for the formation of the inorganic nanostructures and as direct metal source. In this context, the IrO₂ thin film originated from the 5% w/w gel phase of compound **15** displayed an ordered nanostructure composed of ordered vertical IrO₂ arrays, which could be valued for catalytic and electrochromic applications. The procedure described herein could lay the foundations for the development of a new methodology to prepare ordered IrO₂ thin films and, in a more general perspective, other inorganic nanostructures taking advantage of a well-organized organometallic gel precursor.

Chapter 6

Experimental details

6.1 General equipments and procedures

All commercially available starting materials were used as received without further purification. $IrCl_3 \cdot nH_2O$, 2-phenylpyridine, 2,2'-bipyridine, 1,10-phenanthroline, benzene-1,2-diamine, 2,2'-biquinoline, 4,7-diphenyl-1,10-phenanthroline, 2,2'-dipyridyl ketone, 2,2'-dipyridylamine, dipyridinoquinoxaline (pyrazino[2,3-*f*][1,10]phenanthroline), acetic acid, 6-Bromohexanoic acid, 2-ethoxyethanol and 2-methoxyethanol were purchased from Sigma-Aldrich.

Microwave reactions were performed using a CEM Discover Synthesis Unit (CEM Corp., Matthews, NC). This instrument consists of a continuous focused microwave power delivery system with an operator-selectable power output (0–300 W). The reactions were performed in glass vessels (capacity 50 mL) equipped with a condenser under atmospheric pressure. The temperature of the contents of the vessel was monitored using an optical fibre inserted through a specially designed glass-tube directly into the centre of the reaction vessel. The contents of the vessel were stirred by means of a rotating magnetic plate located below the floor of the microwave cavity and a Tefloncoated magnetic stir bar in the vessel.

^{1}H NMR spectra were acquired on a Bruker Avance 300 MHz spectrometer in $CDCl_3$ and CD_3OD solution (with TMS as the internal standard), depending on the solubility of the complexes and on the overlap between the solvent peaks and the aliphatic peaks.

^{13}C NMR spectra were acquired on a Bruker Avance 500 MHz spectrometer in DMSO-d6.

Infrared spectra (KBr) in the range 4000–400 cm^{-1} were recorded with a Spectrum One FT-IR Perkin-Elmer spectrometer.

Elemental analyses were performed with a Perkin-Elmer 2400 microanalyzer.

Mass spectra were obtained using an AB Sciex API 2000 mass spectrometer equipped with a turboion spray ionization source in the positive or negative mode [ion spray voltage (IS) 4500 V; curtain gas 10 psi, temperature 25 °C, ion source gas (1) 20 psi, declustering and focusing potentials 50 and 400 V, respectively] through direct infusion (5 μL min^{-1}) of a solution containing the appropriate compound dissolved in MeOH–H_2O (20 μg mL^{-1}).

Powder X-ray diffraction patterns were acquired on a Bruker D2-Phaser equipped with Cu K$_\alpha$ radiation (λ = 1.5418 Å) and a Lynxeye detector, at 30 kV and 10 mA, with a step size of 0.01° (2θ).

Acquisition of gel PXRD patterns: the gel samples were directly deposited on the instrument sample-holder. Since during measurement water quickly evaporates due to local warming generated by X-ray irradiation, the gels patterns were rapidly acquired with at most 3 scans in order to reduce the effective concentration change of the gel phase. On the contrary, xerogels patterns were registered after slow and complete evaporation of water from gel phases on the sample-holder.

A Leica DMLP polarising microscope equipped with a Leica DFC280 camera and a CalCTec (Italy) heating stage was used to examine the textures of the hydrogels.

Energy dispersive X-ray spectroscopy (EDX) was carried out by the use of a Phenom ProX scanning electron microscope.

SEM morphologic images were acquired on a QUANTA FEG 400 F7 (FEI), equipped with a secondary electrons detector and a back-scattered electrons detector.

TEM images were acquired using a Zeiss EM 10 TEM (Carl Zeiss AG, Oberkochem, Germany). The gel phase, 6% w/w in water, was diluted with distilled water (dil. 1/1000). The samples were prepared by depositing a drop of the diluted solution on 200 mesh formvar/carboncoated copper grids. After evaporation of the solvent in air at room temperature, the xerogel was observed at an operating voltage of 80 kV.

Photophysical characterization: Spectrofluorimetric grade water was used for the photophysical investigations in solution without further purification. A Perkin Elmer Lambda 900 spectrophotometer was employed to obtain the UV/Vis absorption spectra. Steady-state emission spectra were recorded on a Horiba Jobin Yvon Fluorolog 3 spectrofluorimeter, equipped with a Hamamatsu R-928 photomultiplier tube. The

172

luminescence quantum yields were determined through the optical dilution method[1] using Ru(bpy)$_3$Cl$_2$ in air-equilibrated water solution as a reference standard (Φ = 0.028).[2] Solutions were degassed by bubbling argon into quartz cells prior to measurements. Time-resolved measurements were performed using the time-correlated single-photon counting (TCSPC) on the Fluorolog-3 apparatus. A NanoLED pulse centered at 379 nm (FWHM 750 ps with 1 MHz repetition rate) was used as an excitation source and fixed directly on the sample chamber at 90° to a single-grating emission monochromator (2.1 nm mm^{-1} dispersion; 1200 grooves per mm). Data analysis was performed using the commercially available DAS6 software (HORIBA Jobin Yvon IBH). The quality of the fit was assessed by minimizing the reduced χ^2 function. The experimental uncertainties were 1 nm on the band maximum for the absorption and luminescence spectra, 10% on the molar extinction coefficient, 20% on the emission quantum yields and 5% on the lifetime values.

DSC analysis were performed on a DSC Q2000 TA instrument. 10-15 mg of gel samples were placed in aluminium pans and covered with hermetic lids, in order to avoid evaporation of the solvent, hence a change in concentration. The DSC curves were acquired between 10°C and 60°C at a scan rate of 5°C/min.

Porosimetry measurements were performed on ASAP 2460 instrument using N$_2$ as gas at the liquid nitrogen temperature and the data were analyzed through the BET, BJH and DA models.

Confocal microscopy: A 5% w/w gel phase of **[(ppy)$_2$Ir(dpq)]CH$_3$CO$_2$** was drop casted on a pre-cleaned glass slide and covered with a glass coverslip. The cell was sealed in order to avoid evaporation of water. The confocal images were taken on a Leica TCS SP2 confocal laser scanning microscope (LSM).

6.2 Synthesis procedures

Synthesis of [(ppy)₂Ir(μ-Cl)]₂ (I)
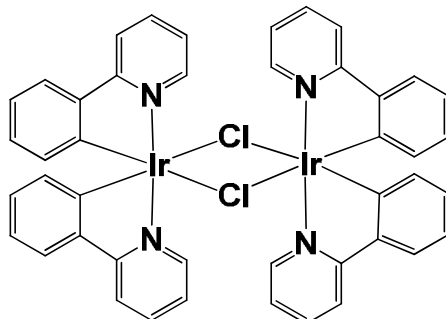
I

To a degassed (N_2) solution of 2-phenylpyridine, **H(ppy)** (0.48 ml, 3.39 mmol) in 2-ethoxyethanol (30 mL) was added a degassed (N_2) aqueous solution of $IrCl_3 \cdot nH_2O$ (400 mg, 1.13 mmol). The resulting mixture was refluxed in a microwave oven at 250 W for 1 h. The resulting precipitate obtained upon addition of water was filtered, washed with water and methanol and dried, to yield the desired product as a bright yellow powder. The crude powder was used in the following step without any further purification. Yield (82%, 492 mg). M.p. >250 °C. Anal. calcd for [$C_{44}H_{32}Cl_2Ir_2N_4$] (MW 1072.09 g mol^{-1}): C: 49.29; H: 3.01; N: 5.23%, found C: 49.32, H: 3.16, N: 5.02%. ^{1}H NMR (300 MHz, CDCl₃, TMS), δ (ppm): 9.23 (d, J = 5.7 Hz, 1H), 7.86 (d, J = 7.9 Hz, 1H), 7.73 (td, J_t = 8.7 Hz, J_d = 1.5 Hz, 1H), 7.48 (d, J = 7.7 Hz, 1H), 6.8–6.7 (m, 2H), 6.55 (td, J_t = 6.7 Hz, J_d = 1.5 Hz, 1H), 5.92 (d, J = 7.7 Hz, 1H). IR (KBr/cm^{-1}): 3036, 1604, 1581, 1475,1421.

Synthesis of [(ppy)₂Ir(μ-OH)]₂ (II)

II
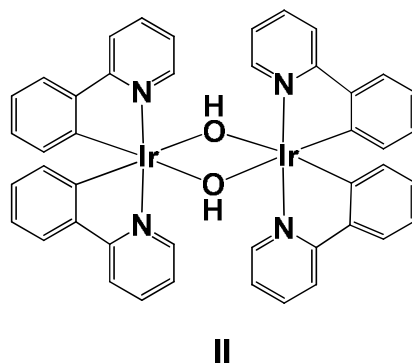
Compound I (400 mg, 0.38 mmol) was suspended in tetrahydrofuran (100 ml) and 2-ethoxyethanol (100 ml). An excess of KOH (900 mg, 16 mmol) was dissolved in H_2O (2–3 ml) and subsequently added to the solution I. Stirring was maintained at room temperature for 48 h. The solution was concentrated and water was added until an orange precipitate was formed. The solid was filtered off and dissolved in tetrahydrofuran (50 ml). The filtered solution was then treated with an aqueous solution of KOH (900 mg in 2–3 ml) and stirred for 3 h. Finally, the solution was concentrated and water was added until precipitation. The orange precipitate was eventually recovered by filtration and dried under vacuum. Yield (74%, 290 mg). M.p. >250 °C. Anal. calcd for [$C_{44}H_{34}Ir_2N_4O_2$] (MW 1035.20 g mol^{-1}): C: 51.05, H: 3.31; N: 5.41%; found C: 51.22, H: 3.12, N: 5.28%. ^{1}H NMR (300 MHz, CDCl₃, TMS), δ (ppm): 8.63 (d, J = 5.7 Hz, 2H), 7.76 (d, J = 7.7 Hz, 2H), 7.50 (t, J = 7.7 Hz, 2H), 7.44 (d, J = 7.8 Hz, 2H), 6.63 (t, J = 7.4 Hz, 2H), 6.53 (t, J = 6.5 Hz, 2H), 6.45 (t, J = 7.4 Hz, 2H), 5.90 (d, J = 7.0 Hz, 2H), −1.62 (s, 1H). IR (KBr/cm^{-1}): 3749, 3610, 3034, 1603, 1580, 1541, 1472, 1413.

Synthesis of CH₃COOAg

To a solution of acetic acid (0.38 ml, 6.6 mmol) in ethanol was added an aqueous solution of NaOH (266 mg, 6.6 mmol). After two hours of stirring at r.t., an equimolecular amount of AgNO₃ (1.12 g, 6,6 mmol) was added and the mixture, protected from light with aluminium foils, was further stirred for 2 hours. The product, formed as a white precipitate in the reaction mixture, was filtered out, washed with water to remove NaNO₃, dried and used without further purification. The product was stored in close vials protected from light. Yield 86%. Anal. Calcd. for [$C_2H_3AgO_2$] (MW 333.82 g/mol): C, 14.39; H, 1.81; found: C, 14.51; H, 1.74. IR(KBr/cm^{-1}): 1569.8, 1408.4.

Synthesis of 1,10-phenanthroline-5,6-dione (a).

a
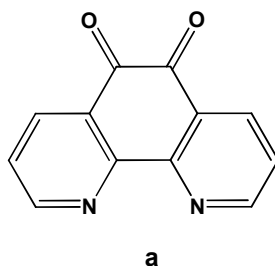
Compound **a** was prepared following the method of Gillard *et al.*[3] An ice-cold mixture of sulphuric acid (20 mL) and nitric acid (10 mL) was slowly added to 1,10-phenanthroline (2 g, 10 mmol) and potassium bromide (2 g, 17 mmol). The red mixture was refluxed (150 °C) for 3 h. The hot yellow solution was then poured over ice and neutralised using a saturated solution of sodium hydroxide. The solution was then filtered, extracted with CH_2Cl_2 and evaporated to dryness. Recrystallisation from hot ethanol, yielded yellow powder. Yield (66%, 1.39 g). Anal. Calcd. for $[C_{12}H_6N_2O_2]$ (MW 210 g/mol): C, 68.57; H, 2.88, N, 13.33; found: C, 68.29; H, 2.93, N, 13.45. ^{1}H NMR (300 MHz, CDCl$_3$, TMS), δ (ppm): 9.13 (dd, J_D = 4.5 Hz, J_d = 1.8, 2H), 8.51 (dd, J_D = 8.7 Hz, J_d = 1.8, 2H), 7.59 (q, J = 6.0 Hz, 2H). IR (KBr/cm^{-1}): 3535, 3425, 3061, 1983, 1703, 1681, 1576, 1560,1459.

Synthesis of dipyridophenazine (dppz) (b).

b
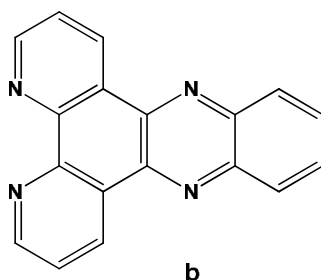
The ligand **b** was prepared following the procedure reported by Wang *et al.*[4] A mixture of of 1,10-phenanthroline-5,6-dione **(a)** (210.2 mg, 1mmol), benzene-1,2-diamine (119 mg, 1.1 mmol), 10 mL of ethanol, and 4-methylbenzenesulfonic acid (1.9 mg, 0.01 mmol) was refluxed for 12h. The crude product was filtered off and then recrystallized from ethanol to give the pure desired product. Yield (64%, 180 mg). Anal. Calcd. for $[C_{18}H_{10}N_4]$ (MW 282 g/mol): C, 76.58; H, 3.57, N, 19.85; found: C, 76.16; H, 3.75, N, 19.22. ^{1}H NMR (300 MHz, CDCl$_3$, TMS), δ (ppm): 9.67 (dd, J_D = 7.5 Hz, J_d = 1.8, 2H), 9.29 (dd, J_D = 4.0 Hz, J_d = 1.8, 2H), 8.40-8.36 (m, 2H), 7.96-7.92 (m, 2H), 7.83-7.79 (m, 2H).

Synthesis of [(ppy)₂Ir(biq)]Cl (1).

1
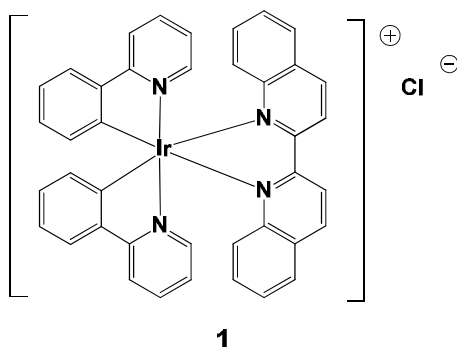
To 20 ml of degassed MeOH, were added compound **I** (200 mg, 0.186 mmol) and the ligand 2,2'-biquinoline (95 mg, 0,372 mmol). The resulting solution was refluxed under inert atmosphere. After 24h the reaction mixture was concentrated and diethyl ether was added. A red precipitate was recovered through filtration. Yield (66%, 194 mg). M.p. (dec.) 184°C. Anal. calcd for $[C_{40}H_{28}IrN_4Cl]$ (MW 792.20 g mol^{-1}): C: 60.63, H: 3.56; N: 7.07 %; found C: 60.22, H: 3.22, N: 7.26%. ^{1}H NMR (300 MHz, CDCl₃, TMS), δ (ppm): 9.58 (d, J = 8.7 Hz, 2H), 8.87 (d, J = 8.7 Hz, 2H), 7.95-7.91 (m, 4H), 7.83 (d, J = 7.8 Hz, 2H), 7.74-7.67 (m, 4H), 7.58 (d, 7.8 Hz, 2H), 7.48 (t, 7.2 Hz, 2H), 7.13 (t, 7.8 Hz, 2H), 7.01-6.85 (m, 6H), 6.22 (d, J = 7.8 Hz, 2H). IR (KBr/cm^{-1}): 3401, 3041, 1605, 1583, 1509, 1478, 1376, 1268.

Synthesis of [(ppy)₂Ir(biq)]CH₃CO₂ (2)

2
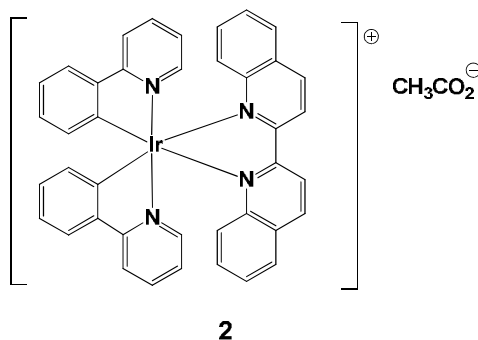
The complex **1** (100 mg, 0.126 mmol) was dissolved in 10 ml of MeOH and AgCH₃COO was added (23 mg, 0.07 mmol). The resulting solution was refluxed protected from light. After 4h the reaction mixture was cooled down and filtrated through celite in order to remove AgCl. The obtained solution was concentrated and diethyl ether was added. A red powder was recovered. Yield (83%, 86 mg). M.p. 170°C. Anal. calcd for $[C_{42}H_{31}IrN_4O_2]$ (MW 816.20 g mol^{-1}): C: 61.82, H: 3.83; N: 6.87 %; found C: 61.34, H: 3.72, N: 6.57%. ^{1}H

NMR (300 MHz, CDCl$_3$, TMS), δ (ppm): 9.50 (d, J = 9 Hz, 2H), 8.85 (d, J = 8.7 Hz, 2H), 7.92 (t, J = 8.7 Hz, 4H), 7.82 (d, J = 8.6 Hz, 2H), 7.70 (t, J = 7.5 Hz, 4H), 7.58 (d, J = 6.9 Hz, 2H), 7.47 (t, J = 7.2 Hz, 2H), 7.11 (t, J = 8.7, 2H), 6.98- 6.85 (m, 6H), 6.23 (d, J = 6.9 Hz, 2H), 2.10 (s, 3H). IR (KBr/cm^{-1}): 3400, 1605, 1581, 1560, 1509, 1477, 1418, 1384.

Synthesis of [(ppy)$_2$Ir(dip)]Cl (3).
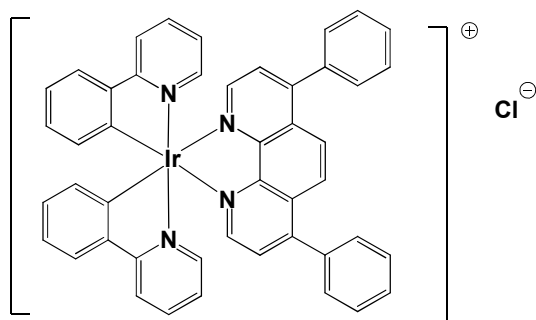
3

To 20 ml of degassed MeOH, were added compound **I** (200 mg, 0.186 mmol) and the ligand 4,7-diphenyl-1,10-phenanthroline (124mg, 0,372 mmol). The resulting solution was refluxed under inert atmosphere. After 24h the reaction mixture was concentrated and diethyl ether was added. An orange powder was recovered through filtration. Yield (88%, 285 mg). M.p.> 250°C. Anal. calcd for [C$_{46}$H$_{32}$IrN$_4$Cl] (MW 868.20 g mol^{-1}): C: 63.62, H: 3.71; N: 6.45 %; found C: 63.27, H: 3.43, N: 6.85%. ^{1}H NMR (300 MHz, CDCl$_3$, TMS), δ (ppm): 8.34 (d, J =5.4 Hz, 2H), 8.17 (s, 2H), 7.96 (d, J = 8.1 Hz, 2H), 7.83 (t, J = 7.2 Hz, 2H), 7.74 (d, J = 5.4 Hz, 4H), 7.59-7.56 (m, 12H), 7.19 (t, J = 6.3 Hz, 2H), 7.10 (t, J = 6.8 Hz, 2H), 7.01 (t, J = 7.2 Hz, 2H), 6.43 (d, J = 7.5 Hz, 2H). IR (KBr/cm^{-1}): 3391, 3042, 1605, 1581, 1515, 1476, 1226, 850, 702.

Synthesis of [(ppy)₂Ir(dip)]CH₃CO₂ (4)

4
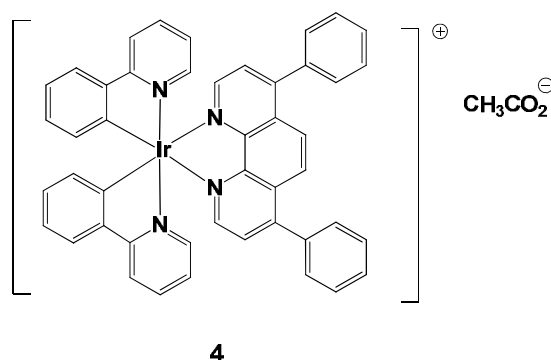
The complex **3** (100 mg, 0.115 mmol) was dissolved in 10 ml of MeOH and AgCH₃COO was added (28 mg, 0.08 mmol). The resulting solution was refluxed protected from light. After 4h the reaction mixture was cooled down and filtrated through celite in order to remove AgCl. The obtained solution was concentrated and diethyl ether was added. A yellow precipitate was recovered. Yield (61%, 71mg). M.p. 237°C. Anal. calcd for [$C_{48}H_{35}IrN_4O_2$] (MW 892.20 g mol⁻¹): C: 64.63, H: 3.95; N: 6.28 %; found C: 64.39, H: 3.77, N: 6.32%. ¹H NMR (300 MHz, CDCl₃, TMS), δ (ppm): 8.34 (d, J = 5.4 Hz, 2H), 8.18 (s, 2H), 7.96 (d, J = 7.8 Hz, 2H), 7.82 (t, J = 8.4 Hz, 2H), 7.74 (d, J = 5.4 Hz, 4H), 7.60-7.52 (m, 12H), 7.09 (t, J = 6.6 Hz, 4H), 6.99 (t, J = 7.2 Hz, 2H), 6.43 (d, J = 7.5 Hz, 2H), 2.33 (s, 3H). IR (KBr/cm⁻¹): 3400, 1605, 1581, 1559, 14767, 1384, 763.

Synthesis of [(ppy)₂Ir(dpa)]Cl (5).

5

To 20 ml of degassed MeOH, were added compound **I** (200 mg, 0.186 mmol) and the ligand 2,2' dipyridylamine (64 mg, 0,372 mmol). The resulting solution was refluxed under inert atmosphere. After 24h the reaction mixture was concentrated and diethyl ether was added. A yellow powder was recovered through filtration. Yield (78%, 205 mg). M.p. 205 °C. Anal. calcd for [$C_{32}H_{25}IrN_5Cl$] (MW 707.14 g mol⁻¹): C: 54.34, H: 3.56; N: 9.90 %; found

C: 54.72, H: 3.44, N: 9.85%. ^{1}H NMR (300 MHz, CDCl$_3$, TMS), δ (ppm): 12.05 (s, 1H), 8.38 (d, J = 8.4 Hz, 2H), 8.16 (d, J = 5.7 Hz, 2H), 7.90 (d, J = 8.1 Hz, 2H), 7.79 (t, J = 7.2 Hz, 2H), 7.61-7.56 (m, 4H), 7.50 (d, J = 6.0 Hz, 2H), 7.11 (t, J = 6.0 Hz, 2H), 6.94 (t, J = 7.5 Hz, 2H), 6.80 (t, J = 7.5 Hz, 2H), 6.52 (t, J = 6.3 Hz, 2H), 6.14 (d, J = 7.8 Hz, 2H). IR (KBr/cm^{-1}): 3400, 3033, 1642, 1606, 1581, 1475, 1417.

Synthesis of [(ppy)$_2$Ir(dpa)]CH$_3$CO$_2$ (6)
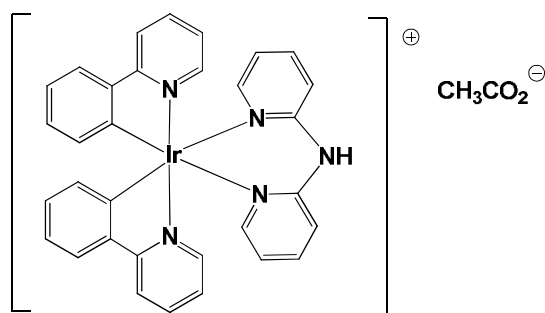
6

The complex **5** (100 mg, 0.141 mmol) was dissolved in 10 ml of MeOH and AgCH$_3$COO was added (25 mg, 0.08 mmol). The resulting solution was refluxed protected from light. After 4h the reaction mixture was cooled down and filtrated through celite in order to remove AgCl. The obtained solution was concentrated and diethyl ether was added. A yellow solid was recovered. Yield (76%, 79mg). M.p.>250 °C. Anal. calcd for [C$_{34}$H$_{28}$IrN$_5$O$_2$] (MW 731.20 g mol^{-1}): C: 55.88, H: 3.86; N: 9.58 %; found C: 55.44, H: 3.76, N: 9.82%. ^{1}H NMR (300 MHz, CDCl$_3$, TMS), δ (ppm): 12.04 (s, 1H), 8.20 (d, J = 5.4 Hz, 2H), 7.97 (d, J = 8.4 Hz, 2H), 7.89 (d, J = 8.4 Hz, 2H), 7.78 (t, J = 8.4 Hz, 2H), 7.60-7.54 (m, 4H), 7.47 (dd, J$_D$ = 5.7 Hz, J$_d$ = 1.5 Hz, 2H), 7.11 (t, J = 7.2 Hz, 2H), 6.93 (t, J = 7.5 Hz, 2H), 6.80 (t, J = 7.5 Hz, 2H), 6.46 (t, J = 7.2 Hz, 2H), 6.15 (d, J = 7.2 Hz, 2H), 2.11 (s, 3H). IR (KBr/cm^{-1}): 3412, 3037, 1640, 1606, 1581, 1476, 1419, 1384.
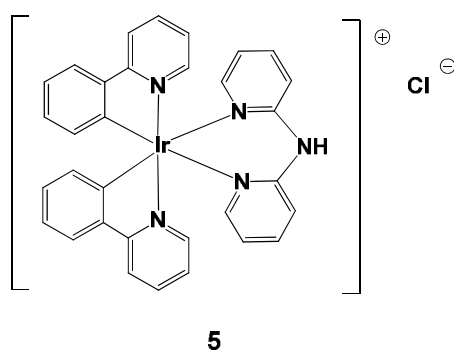
Synthesis of [(ppy)₂Ir(dpc)]Cl (7).

7
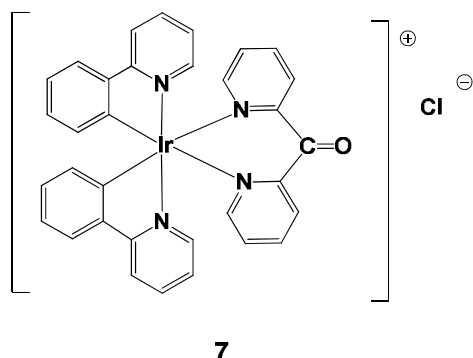
To 20 ml of degassed MeOH, were added compound **I** (200 mg, 0.186 mmol) and the ligand 2,2'-dipyridyl ketone (68 mg, 0,372 mmol). The resulting solution was refluxed under inert atmosphere. After 24h the reaction mixture was concentrated and diethyl ether was added. A red powder was recovered through filtration. Yield (77%, 208 mg). M.p. 140 °C. Anal. calcd for [$C_{33}H_{24}IrN_4ClO$] (MW 720.13 g mol^{-1}): C: 55.03, H: 3.36; N: 7.78 %; found C: 55.12, H: 3.24, N: 7.85%. ^{1}H NMR (300 MHz, CDCl₃, TMS), δ (ppm): 8.29 (d, J = 7.5 Hz, 2H), 8.21-8.15 (m, 4H), 8.07 (d, J = 5.7 Hz, 2H), 7.96-7.86 (m, 4H), 7.62 (d, J = 7.5 Hz, 2H), 7.51 (t, J = 6.0 Hz, 2H), 7.31 (t, J = 5.7 Hz, 2H), 6.98 (t, J = 7.5 Hz, 2H), 6.86 (t, J = 7.8 Hz, 2H), 6.17 (d, J = 7.5 Hz, 2H). IR (KBr/cm^{-1}): 3398, 3041, 1676, 1604, 1582, 1475, 764.

Synthesis of [(ppy)₂Ir(dpc)]CH₃CO₂ (8)

8
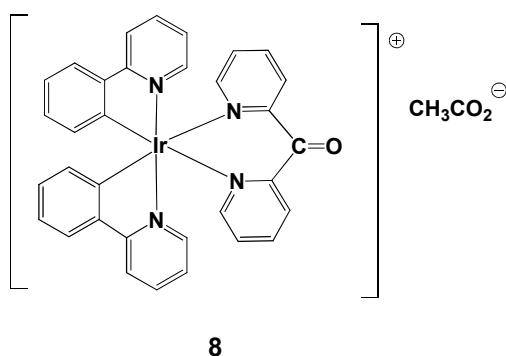
The complex **7** (100 mg, 0.138 mmol) was dissolved in 10 ml of MeOH and AgCH₃COO was added (25 mg, 0.07 mmol). The resulting solution was refluxed protected from light. After 4h the reaction mixture was cooled down and filtrated through celite in order to remove AgCl. The obtained solution was concentrated and diethyl ether was added. A red solid was recovered. Yield (52%, 53 mg). M.p.>250 °C. Anal. calcd for [$C_{35}H_{27}IrN_4O_3$] (MW

744.17 g mol^{-1}): C: 56.51, H: 3.66, N: 7.53%; found C: 56.74, H: 3.62, N: 7.54%. ^{1}H NMR (300 MHz, CDCl$_3$, TMS), δ (ppm): 8.28 (d, J = 7.8 Hz, 2H), 8.15-8.09 (m, 4H), 8.05 (d, J = 5.1 Hz, 2H), 7.94-7.81 (m, 4H), 7.70 (t, J = 7.8 Hz, 2H), 7.61 (d, J = 7.8 Hz, 2H), 7.44 (t, J = 6.0 Hz, 2H), , 6.98 (t, J = 7.2 Hz, 2H), 6.86 (t, J = 7.2 Hz, 2H), 6.17 (d, J = 7.8 Hz, 2H), 1.77 (s, 3H). IR (KBr/cm^{-1}): 3412, 3037, 1640, 1606, 1581, 1476, 1419, 1384.

Synthesis of [(ppy)$_2$Ir(dpq)]Cl (9).

9
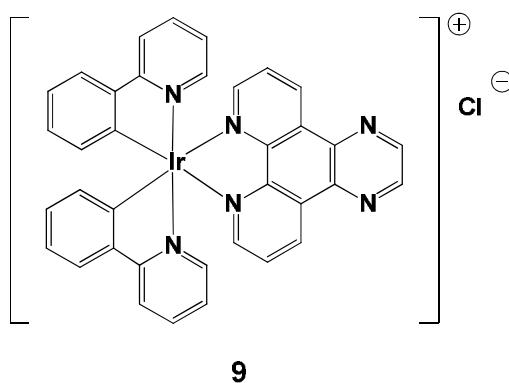
To *ca.* 45 ml of hot and degassed CH$_2$Cl$_2$ was added compound **I** (200mg, 0.186 mmol). At the same time, to *ca.* 15 ml of hot and degassed MeOH was added the ancillary ligand dipyridinoquinoxaline (dpq) (86.6 mg, 0.372 mmol). After mixing up the two solutions, a clear orange solution was obtained. This solution was refluxed under inert atmosphere. After 24h the reaction mixture was evaporated through rotavapor and a yellow precipitate was recovered by addition of petroleum ether, followed by filtration. Yield (96%, 285 mg).M.p.> 250°C. Anal. calcd for [C$_{36}$H$_{24}$ClIrN$_6$] (MW 768.3 g mol^{-1}): C: 56.28, H: 3.15, N: 10.94%; found C: 56.13, H: 3.34, N: 5.01%. ^{1}H-NMR (300 MHz, CDCl$_3$, TMS), δ (ppm): 9.76 (dd, J$_D$ = 8.4 Hz, J$_d$ = 1.8, 2H), 9.20 (s, 2H), 8.41 (dd, J$_D$ = 6.6 Hz, J$_d$ = 1.5, 2H), 8.14 (q, J = 5.1 Hz, 2H), 7.95 (d, J =7.8, 2H), 7.79-7.73 (m, 4H), 7.51 (d, J = 5.7 Hz, 2H), 7.13-6.96 (m, 6H), 6.40 (d, J = 6.9 Hz, 2H). IR (KBr/cm^{-1}): 3367, 3035, 2956, 2917, 1728, 1605, 1581, 1476, 1437.

Synthesis of [(ppy)₂Ir(dpq)]CH₃CO₂ (10).

10
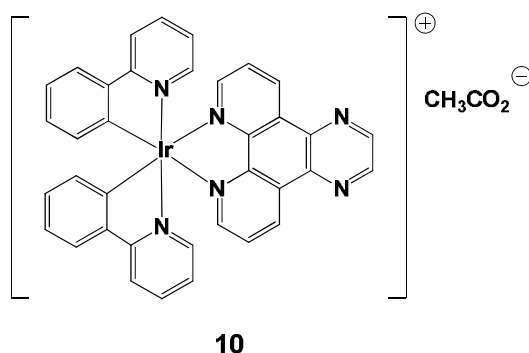
Compound **9** (150 mg, 0.195 mmol) and CH_3COOAg (35.6 mg, 0.215 mmol) were refluxed in *ca*. 40 ml of MeOH, repaired from light. After 4h the suspension was filtered through celite in order to remove AgCl. The solution was evaporated and hexane was added. An orange powder was recovered through filtration. Yield (75%, 115 mg). M.p. (dec.) 185°C. Anal. calcd for $[C_{38}H_{27}IrN_6O_2]$ (MW 792.2 g mol⁻¹): C: 57.64, H: 3.44, N: 10.61%; found C: 57.18, H: 3.54, N: 10.01%. ^{1}H-NMR (300 MHz, CDCl₃, TMS), δ (ppm): 9.75 (d, J = 7.8, 2H), 9.20 (s, 2H), 8.40 (d, J = 4.2 Hz, 2H), 8.10 (q, J = 5.4 Hz, 2H), 7.95 (d, J =8.1, 2H), 7.80-7.73 (m, 4H), 7.46 (d, J = 5.7 Hz, 2H), 7.13-6.96 (m, 6H), 6.40 (d, J = 7.2 Hz, 2H), 1.86 (s, 3H). IR (KBr/cm⁻¹): 3411, 3040, 2961, 2857, 1605, 1581, 1477, 1437, 1404.

Synthesis of [(ppy)₂Ir(dppz)]Cl (11).

11
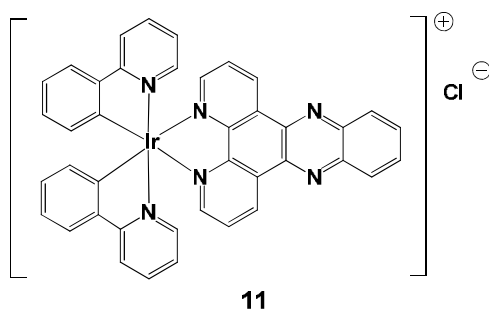
To *ca.* 40 ml of hot and degassed CH_2Cl_2 was added compound **I** (170mg, 0.16 mmol). At the same time, to *ca*. 12 ml of hot and degassed MeOH was added the ancillary ligand dppz **(b)** (89.6 mg, 0.32 mmol). After mixing up the two solutions, a clear orange solution was obtained. This solution was refluxed under inert atmosphere. After 24h the reaction mixture was evaporated through rotavapor and a yellow precipitate was recovered by addition of petroleum ether, followed by filtration. Yield (95%, 248 mg).M.p.> 250°C. Anal.

calcd for [C$_{40}$H$_{26}$ClIrN$_6$] (MW 818.2 g mol^{-1}): C: 58.71, H: 3.20, N: 10.27%; found C: 58.13, H: 3.444, N: 10.81%. ^{1}H-NMR (300 MHz, CDCl$_3$, TMS), δ (ppm): 9.91 (d, J = 7.0 Hz, 2H), 8.47-8.38 (m, 4H), 8.18-8.14 (m, 2H), 8.07-8.04 (m, 2H), 7.96 (d, J =7.8, 2H), 7.80-7.74 (m, 4H), 7.58 (d, J = 5.7 Hz, 2H), 7.13-6.97 (m, 6H), 6.41 (d, J = 6.9 Hz, 2H). IR (KBr/cm^{-1}): 3401, 3042, 2912, 2329, 1605, 1583, 1558, 1477.

Synthesis of [(ppy)$_2$Ir(dppz)]CH$_3$CO$_2$ (12).

12
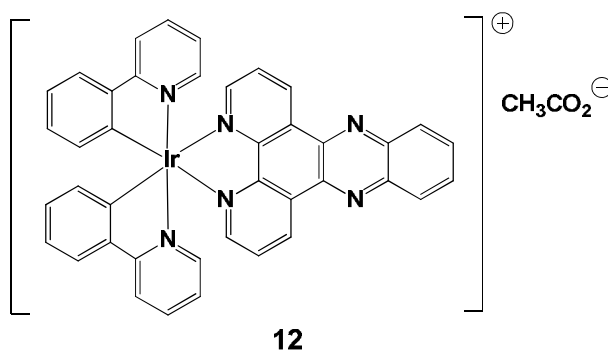
Compound **11** (100 mg, 0.12 mmol) and CH$_3$COOAg (22.3 mg, 0.13 mmol) were refluxed in *ca*. 20 ml of MeOH, repaired from light. After 4h the suspension was filtered through celite in order to remove AgCl. The solution was concentrated through rotavapor and diethyl ether was added. A yellow powder was recovered through filtration. Yield (74%, 75 mg). M.p.> 250°C. Anal. calcd for [C$_{42}$H$_{29}$IrN$_6$O$_2$] (MW 842.2 g mol^{-1}): C: 59.92, H: 3.47, N: 9.98%; found C: 59.33, H: 3.52, N: 10.02%. ^{1}H-NMR (300 MHz, CDCl$_3$, TMS), δ (ppm): 9.90 (dd, J$_D$ = 9.0 Hz, J$_d$ =1.5 Hz, 2H), 8.48-8.38 (m, 4H), 8.14-8.04 (m, 4H), 7.96 (d, J = 8.1 Hz, 2H), 7.81-7.74 (m, 4H), 7.54 (d, J = 5.1 Hz, 2H), 7.13-6.97 (m, 6H), 6.41 (d, J = 6.9 Hz, 2H), 1.84 (s, 3H). IR (KBr/cm^{-1}): 3399, 3041, 2923, 2329, 1606, 1582, 1561, 1419.

Synthesis of [(ppy)₂Ir(bpy)](EtO) (13).

13
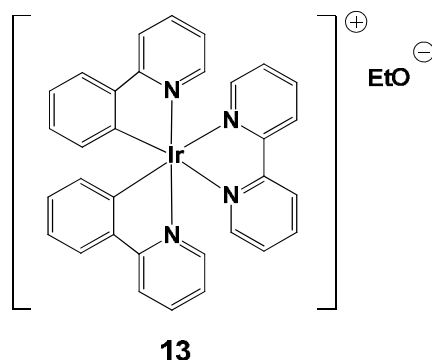
To 70 ml of degassed (N₂) and anhydrous ethanol were added compound **II** (250 mg, 0.24 mmol) and 2,2'-bipyridine **bpy** (75 mg, 0.48 mmol). The resulting solution was refluxed under an inert atmosphere (N₂). After 72 h the solution was concentrated and petroleum ether (50 ml) was added. The obtained yellow precipitate was eventually filtered to yield complex 13 as a yellow powder. Yield (89%, 300 mg). Note that 13 must be kept in a sealed tube under a N₂ atmosphere to avoid slow hydrolysis leading to the formation of **14**. M.p. 155–156 °C. Anal. calcd for [$C_{34}H_{29}IrN_4O$] (MW 701.84 g mol^{-1}): C: 58.18, H: 4.16%; N: 7.98%; found C: 58.02, H: 4.38, N: 8.03%. ^{13}C-NMR (125 MHz, DMSO-d6), δ (ppm): 166.9, 157.5, 155.5, 150.5, 149.9, 148.9, 143.9, 139.8, 138.9, 131.2, 130.4, 128.7, 125.2, 124.0, 122.5, 120.1, 79.2 (–CH₂–OH), 25.5 (CH₃–CH₂–). ^{1}H-NMR (300 MHz, CD₃OD, TMS), δ (ppm): 8.70 (d, J = 7.8 Hz, 2H), 8.2–8.1 (m, 4H), 8.03 (d, J = 5.3 Hz, 2H), 7.9–7.8 (m, 4H), 7.62 (d, J = 5.7 Hz, 2H), 7.56 (t, J = 7.3 Hz, 2H), 7.1–7.0 (m, 4H), 6.89 (t, J = 7.5 Hz, 2H),6.29 (d, J = 7.3 Hz, 2H), 3.48 (q, J = 7.0 Hz, 2H), 1.15 (t, J = 7.0 Hz, 3H). IR (KBr/cm^{-1}): 3399, 3034, 2608, 1645, 1631, 1605, 1582, 1472, 1418.

Synthesis of [(ppy)₂Ir(bpy)](OH) (14).
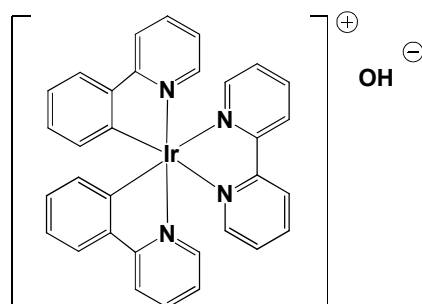
14

Complex (**13**) (100 mg, 0.14 mmol) was dissolved in a small volume of water and THF was added. The solution was slowly added to a large volume of diethyl ether and a yellow precipitate was obtained. (**14**) was recovered by filtration and dried under vacuum. Yield (97%, 93 mg). M.p. (dec.) 165 °C. Anal. calcd for [$C_{32}H_{25}IrN_4O$] (MW 673.7 g mol^{-1}): C: 57.04, H: 3.74; N: 8.32%; found C: 57.33, H: 3.92, N: 8.01%. ^{1}H-NMR (300 MHz, CD$_3$OD, TMS), δ (ppm): 8.71 (d, J = 8.1 Hz, 2H), 8.2–8.1 (m, 4H), 8.04 (d, J = 5.1 Hz, 2H), 7.9–7.8 (m, 4H), 7.63 (d, J = 5.0 Hz, 2H) 7.56 (t, J = 6.3 Hz, 2H), 7.05–7.00 (m, 4H), 6.90 (t, J = 6.6 Hz, 2H), 6.30 (d, J = 7.9 Hz, 2H), 1.88 (s, 1H). IR (KBr/cm^{-1}): 3401, 3036, 1650, 1633, 1605, 1581, 1477, 1438, 1417.

The synthesis of complex **14** was also carried out through a solid state reaction. Compound (**II**) (45 mg, 0.043 mmol) and bpy (13.6 mg, 0.087 mmol) were ground in a ball miller for 4 h in the presence of a small amount of water (20 µl). The reaction evolution was monitored by powder X-ray diffraction (PXRD). The resulting powder was left to air-dry and complex (**14**) was recovered in almost quantitative yield.

Synthesis of [(ppy)₂Ir(bpy)](EtOCH₂CO₂) (15).

15
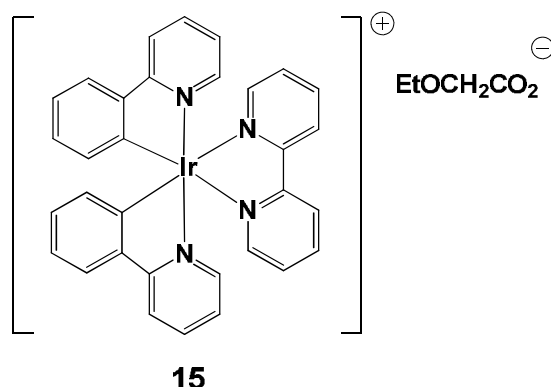
A procedure identical to that reported above for (**13**), but using 2-ethoxyethanol, instead of ethanol, was followed for the synthesis of complex **15**. A yellow precipitate was obtained. Yield (68%, 250 mg). M.p. 157–158 °C. Anal. calcd for [$C_{36}H_{31}IrN_4O_3$] (MW 759.87 g mol^{-1}): C: 56.90, H: 4.11; N: 7.37%; found C: 57.03, H: 3.96, N: 7.11%. ^{13}C-NMR (125 MHz, DMSO-d6), δ (ppm): 171.3 (–CH₂–CO₂), 166.8, 155.3, 150.4, 149.8, 148.8, 143.8, 139.7, 138.8, 131.0, 130.2, 128.7, 125.1, 124.9, 123.9, 122.3, 120.0, 71.1 (–O–CH₂–CO₂), 64.3 (CH₃–CH₂–O–), 15.3 (CH₃–CH₂–). ^{1}H-NMR (300 MHz, CDCl₃, TMS), δ (ppm): 9.76 (d, J = 8.1 Hz, 2H), 8.30 (t, J = 7.2 Hz, 2H), 7.93 (d, J = 5.4 Hz, 2H), 7.85 (d, J = 5.1 Hz, 2H), 7.75 (t, J = 8.2 Hz, 2H), 7.68 (d, J = 7.2 Hz, 2H), 7.47 (d, J = 5.6 Hz, 2H), 7.35 (t, J = 6.7 Hz, 2H), 7.1–6.9 (m, 6H), 6.30 (d, J = 7.7 Hz, 2H), 4.04 (s, 2H), 3.65 (q, J = 7.0 Hz, 2H), 1.23 (t, J = 7.0 Hz, 3H). IR (KBr/cm^{-1}): 3368, 3032, 2971, 2920, 2862, 1607, 1577, 1478, 1439, 1419, 1120. MS (ESI+, direct infusion) m/z = 657 (100% [(ppy)₂Ir(bpy)]$^+$). MS (ESI−, direct infusion) m/z = 103 (100% [EtOCH₂CO₂]$^-$).

Synthesis of [(ppy)₂Ir(bpy)](MeOCH₂CO₂) (16).

16
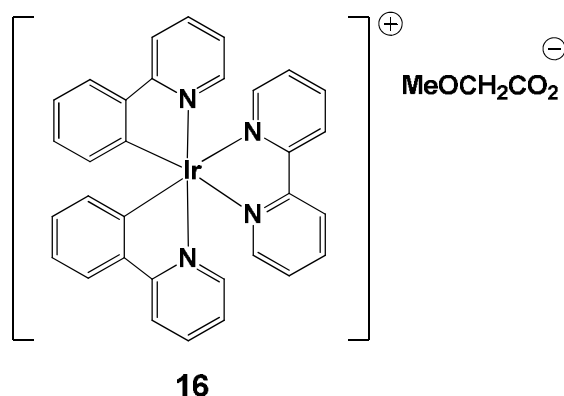
A procedure identical to that reported for (**15**), but using 2-methoxyethanol instead of 2-ethoxyethanol was followed for the synthesis of complex **16**. The obtained precipitate was dissolved in methanol and the resulting solution was filtered off in order to remove undissolved impurities. Finally, re-precipitation in diethyl ether allows recovering (16) as a yellow solid. Yield (93%, 332 mg). M.p. 178 °C. Anal. calcd for [$C_{35}H_{29}IrN_4O_3$] (MW 745.85 g mol^{-1}): C: 56.36, H: 3.92, N: 7.51%; found C: 56.07, H: 4.03, N: 7.79%. ^{13}C-NMR (125 MHz, DMSO-d6): δ (ppm) 172.5($-CH_2-CO_2$), 166.8, 155.4, 150.5, 149.9, 148.9, 143.8, 139.7, 138.8, 131.1, 130.3, 128.7, 125.1, 125.0, 123.9, 122.3, 120.0, 72.8 ($-O-CH_2-CO_2$), 57.2 (CH_3-O-). ^{1}H-NMR (300 MHz, CDCl3, TMS), δ (ppm): 9.41 (d, J = 8.6 Hz, 2H), 8.20 (t, J = 7.8 Hz, 2H), 7.84 (d, J = 7.9 Hz, 2H), 7.80 (d, J = 5.5 Hz, 2H), 7.68 (td, Jt = 7.6 Hz, Jd = 1.4 Hz, 2H), 7.61 (d, J = 7.8 Hz, 2H), 7.41 (d, J = 5.5 Hz, 2H), 7.29 (t, J = 6.5 Hz, 2H), 7.0–6.9 (m, 4H), 6.84 (td, Jt = 7.4 Hz, Jd = 1.2 Hz, 2H), 6.23 (d, J = 7,5 Hz, 2H), 3.89 (s, 2H), 3.40 (s, 3H). IR (KBr/cm^{-1}): 3411, 3035, 2918, 2359, 1605, 1583, 1477, 1438, 1417, 1313, 1161, 1110. MS (ESI+, direct infusion) m/z = 657 (100% [(ppy)₂Ir(bpy)]$^+$). MS (ESI−, direct infusion) m/z = 89 (100% [MeOCH₂CO₂]$^-$).

Synthesis of [(ppy)₂Ir(bpy)](CH₃CO₂) (17).
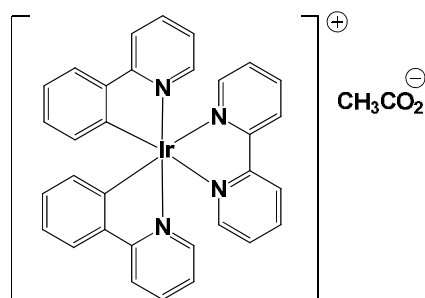
17

Complex (**14**) (100 mg, 0.15 mmol) was dissolved in a small volume of dichloromethane and an excess of acetic acid was added. The solution was stirred under inert atmosphere at room temperature. After 30 min an orange precipitate was recovered through the addition of hexane. Yield (95%, 102 mg). Anal. calcd for [$C_{34}H_{27}IrN_4O_2$] (FW 716.20 g/mol): C, 54.31; H, 4.16; N, 7.45, found: C, 54.12; H, 4.04; N, 7.74. ^{13}C-NMR (75 MHz, CDCl₃): 177.2, 167.9, 156.2, 150.5 , 149.7, 148.5, 143.4, 140.5, 137.9, 131.7, 130.8, 127.8, 127.3, 124.8, 123.2, 122.6, 119.6, 24.7. ^{1}H NMR (300 MHz, CDCl₃), δ (ppm): 9.48 (d, J = 8.4 Hz, 2H), 8.29 (t, J = 7.5 Hz, 2H), 7.90 (m, 4H), 7.75 (t, J = 7.2 Hz, 2H), 7.68 (d, J = 7.7 Hz, 2H), 7.47 (d, J = 5.5 Hz, 2H), 7.37 (t, J = 6.4 Hz, 2H), 7.0 (m, 4H), 6.91 (t, J = 7.5 Hz, 2H), 6.29 (d, J = 7.7 Hz, 2H), 2.03 (s, 3H). IR(KBr/ cm^{-1}): 3392.2, 3062.8, 3038.17, 2924.3, 1562.6, 1403.0.

Synthesis of [(ppy)₂Ir(bpy)](BrCH₂(CH₂)₄CO₂) (18).
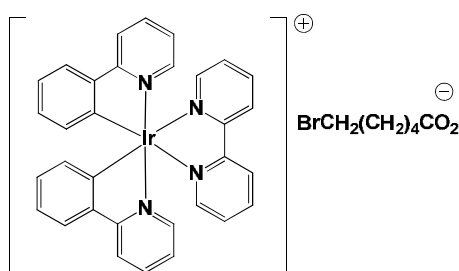
18

Complex (**14**) (100 mg, 0.15 mmol) was dissolved in a small volume of dichloromethane and an excess of 6-Bromohexanoic acid (BrCH₂(CH₂)₄COOH) was added. The solution was stirred under inert atmosphere at room temperature. After 30 min an orange precipitate was recovered through the addition of hexane. Yield (90%, 114 mg). Anal.

calcd for [$C_{38}H_{34}BrIrN_4O_2$] (FW 850.15 g/mol): C, 53.64; H, 4.03; N, 6.59, found: C, 53.32; H, 4.72; N, 6.12. ^{1}H-NMR (CDCl$_3$, 300 MHz, TMS), δ (ppm): 9.61 (d, J= 6.6 Hz, 2H), 8.28 (t, J= 6.1 Hz, 2H), 7.91 (t , J= 9.0 Hz, 4H), 7.71 (t , J= 7.3 Hz, 2H), 7,69 (d , J= 7.9 Hz, 4H), 7.49 (d , J= 5.2 Hz, 2H), 7.40 (t, J= 7.3 Hz, 2H), 7.03 (m, 4H), 6.93 (t , J= 7.5 Hz, 2H), 6.31 (d, J= 7.7 Hz, 2H), 4.07 (t, J= 6.4 Hz, 2H), 3.42 (t, J= 6.6 Hz, 2H), 2.37 (m, 2H), 1.50 (m, 2H).

6.3 Preparation of gel phases

The opportune quantity of metallogelator was dissolved in warm distilled water. The mixture was then heated and shaken in a closed tube until clear solutions were obtained. Subsequently, the solution was slowly cooled down to room temperature. The formation of gel phases was determined through a typical inversion test tube experiment: tubes of increasing concentration were turned upside down until no flow was observed.[5] The gels were stored at room temperature.

6.4 IrO$_2$ thin films preparation

The gel phases of compound **15** at various concentrations (3 %, 4%, 5% and 6% w/w) were deposited onto quartz substrates, previously cleansed with isopropanol, through spin-coating technique, at 1000 rpm for 30 sec. Thin films were deposited onto Suprasil 300 Quartz slides (Starna) using a P6700 Spin-coater (Speedline Technologies). The obtained films were kept at room temperature for several days, allowing the solvent to slowly evaporate and were then calcinated at 600°C for 4hours to produce shining black IrO$_2$ thin films coated onto the quartz substrates.

6.5 References

1. J. N. Demas and G. A. Crosby, *J. Phys. Chem*., **1971**, 75, 991–1024.
2. K. Nakamaru, *Bull. Soc. Chem. Jpn*., **1982**, 55, 2697–2705
3. R. D. Gillard, R. E. E. Hill, R. Maskill, *J. Chem. Soc. A*, **1970**, 1447.
4. C. Zhou, Q. Wang, *Transition Met. Chem.*, **2010**, 35, 605–611.
5. Gels Handbook, The Fundamentals. Edited by: Yoshihito Osada, Kanji Kajiwara, Takao Fushimi, Okihiko Irasa, Yoshitsugu Hirokawa, Tsutomu Matsunaga, Tadao Shimomura, Lin Wang and Hatsuo Ishida. 2001, ISBN: 978-0-12-394690-4. Vol. 1, chapter 2, section 2.

Appendix

DFT calculations

Compounds 13, 14, 15 and 16. Ground state geometry of the cation [(ppy)$_2$Ir(bpy)]$^+$

at B3LYP/6-31G(d)/LanL2DZ level of theory

Charge = 1 Multiplicity = 1

Atom	X	Y	Z
C	-1,7232950	1,6691950	-2,0267750
C	-4,1146940	1,7460840	-2,1146470
H	-0,7371130	1,9760920	-2,3580230
C	-4,1417320	0,8116730	-1,0826460
H	-5,0427150	2,1269350	-2,5294700
C	-2,9396060	0,3281330	-0,5526840
C	-2,8814670	-0,6663840	0,5479600
C	-4,0195300	-1,2820720	1,0822430
C	-1,5179670	-1,8517630	2,0265010
C	-3,8846040	-2,2018070	2,1189860
C	-2,6103760	-2,4924710	2,6035030
H	-0,5030510	-2,0406800	2,3592660
H	-4,7624650	-2,6838890	2,5376650
H	-2,4568340	-3,2022040	3,4092100
N	-1,6449270	-0,9617580	1,0270640
C	-2,8829980	2,1836720	-2,5988410
H	-2,8135210	2,9112780	-3,4002200
C	-0,4136090	-2,0397770	-2,2273090
C	0,7441750	-4,1155220	-2,4879690
H	-1,1422350	-1,3009070	-2,5377220
C	1,4733360	-3,8104220	-1,3476170
H	0,9261950	-5,0438460	-3,0209400
C	1,2437510	-2,6093230	-0,6584530
H	2,2299400	-4,4962410	-0,9853100
C	1,9442760	-2,1627570	0,5437770
C	2,9363560	-2,9229060	1,1873910
C	2,2069410	-0,4188550	2,1902020
C	3,5603230	-2,4319390	2,3282010
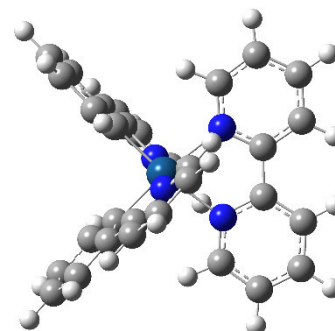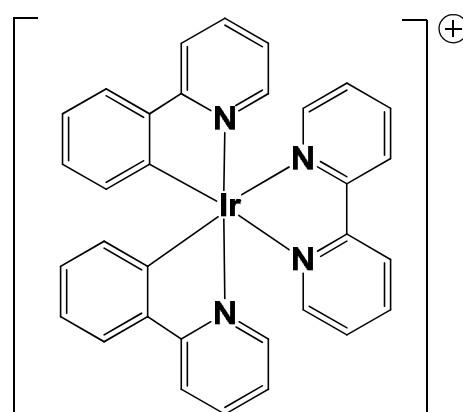
H	3,2260220	-3,8967350	0,8024720
C	3,1925590	-1,1776520	2,8267580
C	1,9524780	0,5538610	2,6006540
H	4,3287960	-3,0171820	2,8239160
H	3,6820240	-0,7864810	3,7151530
C	-0,2216530	-3,2118560	-2,9420420
H	-0,8116640	-3,4059860	-3,8308480
C	2,1525440	0,6647350	-2,1837960
C	3,2607980	2,8220100	-2,3263470
C	1,4477860	1,0585220	-1,0364310
H	2,0153110	-0,3326040	-2,5908880
C	2,5821890	3,2394240	-1,1875300
H	3,9557590	3,4920180	-2,8232480
C	1,6846700	2,3701630	-0,5430320
H	2,7555330	4,2416070	-0,8054410
C	0,9359020	2,7347230	0,6578870
C	1,0297100	3,9532260	1,3483400
C	-0,6502570	1,9835190	2,2236430
C	0,2701200	4,1743970	2,4881890
H	1,7066690	4,7187170	0,9880960
C	-0,5906720	3,1690360	2,9396560
H	-1,2931150	1,1685290	2,5329400
H	0,3483810	5,1163040	3,0226650
H	-1,1997500	3,2956350	3,8277680
N	0,0858290	1,7642920	1,1155200
C	3,0436560	1,5316570	-2,8212880
H	3,5768750	1,1978190	-3,7079050
Ir	0,0677300	0,0034070	-0,0008970
N	-1,7460160	0,7649270	-1,0325650
C	1,5561340	-0,8884980	1,0396410
N	0,2914160	-1,7400580	-1,1176730
H	-5,0041570	-1,0556930	0,6917240
H	-5,0932550	0,4725410	-0,6916790

Compound 2. Ground state geometry of the cation [(ppy)₂Ir(biq)]⁺

at B3LYP/6-31G(d)/LanL2DZ level of theory

Charge = 1 Multiplicity = 1

Atom	X	Y	Z
Ir	-0,0001000	-0,2817310	0,0000380
N	-1,3354420	1,5862810	0,4309490
C	0,7365090	2,7323380	-0,0905870
C	2,1183430	-2,1242510	0,7785740
C	-1,4298660	-2,5786560	1,4913130
H	-0,8033360	-2,3804150	2,3557270
C	2,6875620	1,6087710	-0,7150170
C	0,6229710	0,4224050	2,9047310
H	-0,1734960	1,1369150	2,7358950
C	2,3745100	-3,6063350	-1,5644800
H	2,4638190	-4,1889310	-2,4779630
C	1,2894100	-1,8050570	-0,3293130
N	1,3354300	1,5859850	-0,4316320
C	1,9083960	-1,3165200	1,9781740
C	2,2887140	-0,6232740	4,2660930
H	2,8239640	-0,7257610	5,2052590
C	-2,3745020	-3,6056080	1,5664040
H	-2,4638360	-4,1876220	2,4802550
N	0,9253490	-0,3723420	1,8584620
C	-1,2894640	-1,8049930	0,3302160
C	1,4297730	-2,5794540	-1,4899420
H	0,8031230	-2,3818350	-2,3544120
C	2,6009890	-1,4445390	3,1914240
H	3,3797050	-2,1922400	3,2851550
C	-2,6876300	1,6093790	0,7140580
C	3,2000300	-3,8957290	-0,4726630
H	3,9316130	-4,6957260	-0,5328910
C	-0,7361890	2,7325150	0,0900610
C	1,2768470	0,3311610	4,1241650
H	0,9956770	0,9894770	4,9386440
C	3,0671710	-3,1576530	0,6979130
H	3,7023960	-3,3928240	1,5473740
C	-3,4720970	2,7960490	0,5187810
N	-0,9254620	-0,3734800	-1,8583070
C	3,4723470	2,7952390	-0,5198120
C	-3,1998650	-3,8957870	0,4746910
C	-2,1182640	-2,1249740	-0,7775610
H	-3,9313770	-4,6958180	0,5353430

195
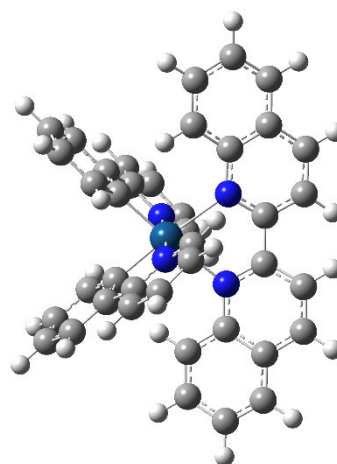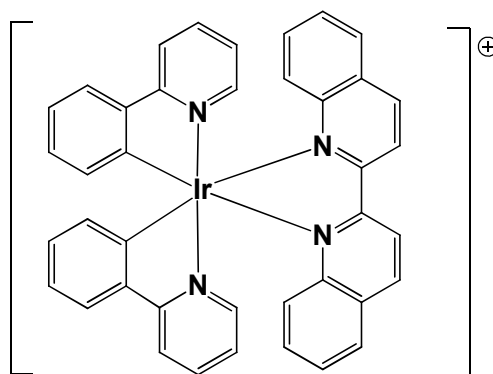
C	-3,0669750	-3,1584260	-0,6963440
H	-3,7021020	-3,3941990	-1,5457120
C	-1,9083330	-1,3179130	-1,9776050
C	-2,6007690	-1,4467110	-3,1908530
C	-0,6231590	0,4207880	-2,9049540
H	0,1731230	1,1355740	-2,7364100
C	-1,2769030	0,3287710	-4,1244070
H	-0,9957970	0,9867300	-4,9391960
C	-2,2885470	-0,6259500	-4,2659320
H	-2,8236940	-0,7290450	-5,2050890
H	-3,3793370	-2,1946060	-3,2842700
C	-1,4553250	3,9384110	-0,1201310
C	1,4559810	3,9380320	0,1196290
C	2,8146960	3,9583820	-0,0627720
C	-2,8140670	3,9590860	0,0620260
H	3,3873830	4,8627370	0,1243100
H	-3,3864850	4,8636100	-0,1250570
H	-0,9363340	4,8232090	-0,4659480
H	0,9372670	4,8229240	0,4656260
C	-4,8618040	2,7792080	0,8018610
C	-3,3294410	0,4658390	1,2501510
C	-5,4589830	1,6433720	1,2979400
H	-6,5212060	1,6351530	1,5221590
C	-4,6782270	0,4877310	1,5351470
C	4,8619800	2,7781190	-0,8032440
C	3,3289810	0,4651310	-1,2513610
C	4,6776990	0,4867600	-1,5367130
H	5,1450240	-0,3998670	-1,9547380
C	5,4587750	1,6422050	-1,2996070
H	-5,1458610	-0,3988300	1,9529680
H	-2,7440230	-0,4197830	1,4448900
H	-5,4381030	3,6850020	0,6345060
H	5,4385210	3,6837640	-0,6359180
H	2,7433590	-0,4203860	-1,4459690
H	6,5209320	1,6337740	-1,5241310

Compound 4. Ground state geometry of the cation [(ppy)₂Ir(dip)]⁺

at B3LYP/6-31G(d)/LanL2DZ level of theory

Charge = 1 Multiplicity = 1

Atom	X	Y	Z
Ir	1,5004090	-0,0000520	-0,0000030
N	-0,2584640	1,3418870	-0,1296050
C	-1,4720920	-0,7179910	0,0775790
C	3,2335800	-1,9965270	-1,2344690
C	3,6158040	1,9386690	-1,1470150
H	3,4276310	1,5270540	-2,1342770
C	-0,2308950	-2,6699830	0,2361520
H	0,7538550	-3,1249620	0,2648560
C	0,8986230	0,1708480	-2,9959800
H	0,2232220	0,9477190	-2,6592090
C	4,5495700	-2,9696180	1,0155200
H	5,0661900	-3,3426940	1,8964170
C	2,9312740	-1,4289930	0,0330470
N	-0,2585250	-1,3418920	0,1298950
C	2,5066280	-1,4259110	-2,3665780
C	1,9152490	-1,1631610	-4,7003940
H	2,0371440	-1,4475590	-5,7412330
C	4,5496000	2,9693020	-1,0160490
H	5,0660910	3,3423450	-1,8970360
N	1,6164820	-0,4409140	-2,0330020
C	2,9313620	1,4287940	-0,0332980
C	3,6158780	-1,9389110	1,1466440
H	3,4279160	-1,5272720	2,1339370
C	2,6576000	-1,7943250	-3,7125980
H	3,3646810	-2,5721250	-3,9754960
C	-0,2307770	2,6699840	-0,2358250
H	0,7539930	3,1249140	-0,2646060
C	4,8307600	-3,5218520	-0,2389930
H	5,5588170	-4,3213670	-0,3373030
C	-1,4720650	0,7180720	-0,0771530
C	1,0151270	-0,1562480	-4,3381560
H	0,4183480	0,3681610	-5,0761680
C	4,1737140	-3,0340940	-1,3623980
H	4,3977290	-3,4636160	-2,3350190
C	-1,3925600	3,4443350	-0,3349370
H	-1,3007050	4,5184850	-0,4550910
N	1,6168650	0,4407990	2,0329750
C	-1,3927210	-3,4442850	0,3353200
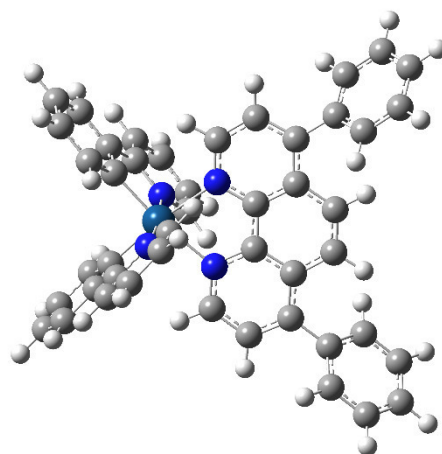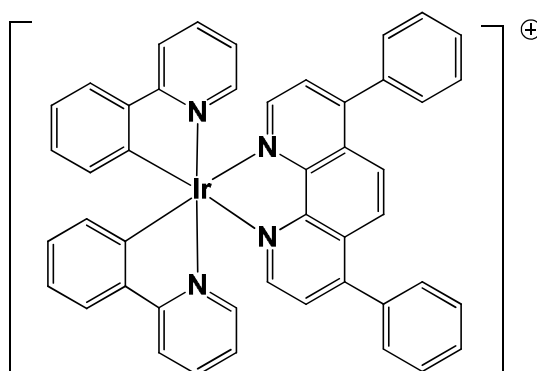
C	4,8310600	3,5215020	0,2384180
C	3,2339370	1,9962960	1,2341680
H	5,5592000	4,3209580	0,3366040
C	4,1741760	3,0337880	1,3619370
H	4,3984010	3,4632850	2,3345210
C	2,5071380	1,4257310	2,3664010
C	2,6583620	1,7941330	3,7123960
C	0,8991200	-0,1709100	2,9960710
H	0,2236040	-0,9477280	2,6594090
C	1,0158740	0,1561750	4,3382280
H	0,4191790	-0,3681890	5,0763400
C	1,9161300	1,1630220	4,7003160
H	2,0382190	1,4474110	5,7411340
H	3,3655410	2,5718830	3,9751760
H	-1,3009560	-4,5184600	0,4553350
C	-2,6984210	1,4260070	-0,1709290
C	-2,6984640	-1,4258610	0,1715150
C	-3,9187180	-0,6774950	0,0783880
C	-3,9186900	0,6777140	-0,0773430
C	-3,8621600	-3,6894870	0,4889530
C	-4,8179990	-3,4181980	1,4839280
C	-4,0378380	-4,8174870	-0,3304510
C	-5,9226460	-4,2530400	1,6488330
H	-4,6793380	-2,5708810	2,1495650
C	-5,1496400	-5,6432560	-0,1704150
H	-3,3110880	-5,0332630	-1,1088790
C	-6,0940370	-5,3637540	0,8196580
H	-6,6459030	-4,0391220	2,4303640
H	-5,2781540	-6,5044610	-0,8194900
H	-6,9573500	-6,0101510	0,9471570
C	-3,8619370	3,6897160	-0,4887230
C	-4,8185480	3,4175100	-1,4827220
C	-4,0367440	4,8188260	0,3293660
C	-5,9230460	4,2524830	-1,6479280
H	-4,6805740	2,5693980	-2,1474810
C	-5,1483920	5,6447350	0,1690500
H	-3,3094690	5,0353300	1,1070990
C	-6,0935490	5,3642860	-0,8200330
H	-6,6468810	4,0378120	-2,4287170
H	-5,2762050	6,5067810	0,8171450
H	-6,9567540	6,0107830	-0,9477550
C	-2,6495870	-2,8471220	0,3317450
C	-2,6494900	2,8472650	-0,3313090
H	-4,8598660	-1,2112830	0,1297030
H	-4,8598230	1,2115600	-0,1282510

Compound 6. Ground state geometry of the cation [(ppy)₂Ir(dpa)]⁺

at B3LYP/6-31G(d)/LanL2DZ level of theory

Charge = 1 Multiplicity = 1

Atom	X	Y	Z
Ir	0,0648750	-0,0315950	0,0014830
N	0,3055700	2,0854120	-0,7494570
C	-1,3116350	-2,6014690	-0,0605550
C	1,6035390	-1,3336690	-2,3400850
H	0,6678230	-1,4145560	-2,8849270
C	-1,8206630	0,1274750	-2,4144820
H	-1,3537370	1,0976220	-2,5266340
C	-0,0427450	-3,8949620	2,0520790
H	0,4622980	-4,3993740	2,8720850
C	-0,2832520	-1,9180490	0,6402160
N	-1,6077090	0,8065950	1,2802050
C	-1,9023850	-1,8706200	-1,1805200
C	-3,3403290	-1,5843030	-3,1074020
H	-4,1025520	-1,9662030	-3,7798500
C	2,7722730	-1,8094670	-2,9392460
H	2,7273500	-2,2450120	-3,9342810
N	-1,3910930	-0,6158850	-1,3751540
C	1,6217670	-0,7675440	-1,0573040
C	0,3444260	-2,6005650	1,6929610
H	1,1488100	-2,1254650	2,2471880
C	-2,8920720	-2,3590070	-2,0471000
H	-3,2962920	-3,3516410	-1,8884000
C	-1,0687290	-4,5480200	1,3620850
H	-1,3673000	-5,5534810	1,6425710
C	-2,7895260	-0,3143630	-3,3025040
H	-3,0975240	0,3204100	-4,1259700
C	-1,6994190	-3,9018460	0,3046520
H	-2,4904940	-4,4168480	-0,2332560
N	1,6149800	0,3453690	1,3420810
C	3,9986140	-1,7359120	-2,2695190
C	2,8747600	-0,7019090	-0,3889090
H	4,9041260	-2,1097250	-2,7375940
C	4,0490170	-1,1820380	-0,9960200
H	5,0031340	-1,1285260	-0,4790880
C	2,8500360	-0,0864950	0,9374360
C	3,9571080	0,0942770	1,7810040
C	1,4750290	0,9530750	2,5372740
H	0,4712480	1,2717650	2,7894400
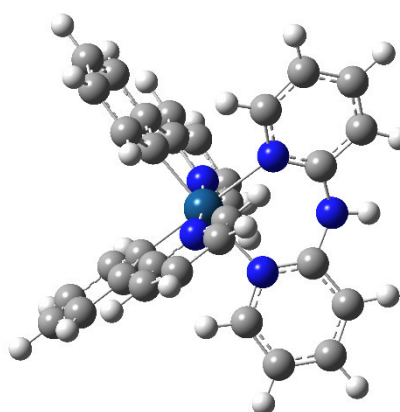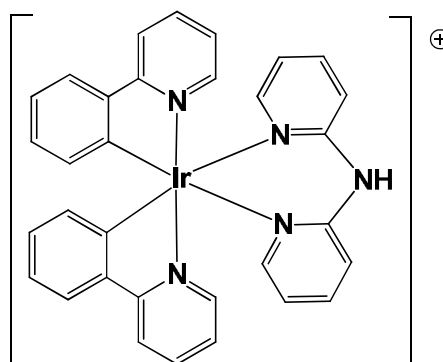
C	2,5386150	1,1569550	3,4029750
H	2,3737110	1,6483400	4,3554210
C	3,8060590	0,7124390	3,0142880
H	4,6638080	0,8487800	3,6659390
H	4,9323260	-0,2544500	1,4625560
C	-0,4888510	4,3107500	-1,2141420
C	-3,4461680	2,3108880	1,6727630
C	-3,8890570	1,5403050	2,7327240
C	0,7055000	4,6397470	-1,8312800
H	-4,7771250	1,8315690	3,2851250
H	0,8481310	5,6308920	-2,2506720
H	-1,2894560	5,0399440	-1,1304660
H	-3,9719390	3,2176880	1,3883490
C	-0,6588880	3,0212950	-0,6719260
C	-2,2900200	1,9218100	0,9660460
C	-3,1638850	0,3965770	3,0836450
H	-3,4623730	-0,2373480	3,9108200
C	-2,0448470	0,0750760	2,3365600
H	-1,4633510	-0,8123130	2,5547300
C	1,4778480	2,4342020	-1,3349690
H	2,2256040	1,6523910	-1,3688850
C	1,7209100	3,6797810	-1,8868860
H	2,6778800	3,8875150	-2,3519160
N	-1,9007410	2,7381600	-0,0977610
H	-2,5546890	3,4967750	-0,2390300

Compound 8. Ground state geometry of the cation [(ppy)₂Ir(dpc)]⁺

at B3LYP/6-31G(d)/LanL2DZ level of theory

Charge = 1 Multiplicity = 1

Atom	X	Y	Z
Ir	-0,1482140	0,0301010	0,0020080
N	0,3890070	-2,0676390	-0,6067660
C	0,2803910	2,9126970	-0,1296770
C	-1,8747550	0,6087210	-2,4941330
H	-0,9844870	0,9616580	-3,0056020
C	1,8139310	0,4476300	-2,3269010
H	1,7007960	-0,6242750	-2,4272590
C	-1,4884240	3,7691310	1,8415570
H	-2,1879560	4,0995350	2,6052660
C	-0,5032390	1,9456310	0,5521020
N	1,6235670	-0,1081360	1,4058280
C	1,1524050	2,3895530	-1,1807830
C	2,7226260	2,5481740	-3,0179260
H	3,3572040	3,1446540	-3,6662790
C	-3,0942170	0,6381020	-3,1748200
H	-3,1298030	1,0045830	-4,1975990
N	1,1015620	1,0309180	-1,3412230
C	-1,7898750	0,1441780	-1,1741060
C	-1,3931650	2,4088150	1,5323100
H	-2,0282720	1,7086960	2,0677240
C	1,9752960	3,1565080	-2,0188390
H	2,0159060	4,2311290	-1,8869110
C	-0,6974580	4,7074090	1,1720990
H	-0,7735700	5,7632870	1,4129940
C	2,6363620	1,1634330	-3,1837760
H	3,1895250	0,6446920	-3,9586090
C	0,1832920	4,2786450	0,1848840
H	0,7885200	5,0133830	-0,3385650
N	-1,5672410	-0,7959090	1,2875260
C	-4,2702210	0,2060560	-2,5518540
C	-2,9926350	-0,2917730	-0,5546890
H	-5,2163490	0,2337910	-3,0835770
C	-4,2185790	-0,2592450	-1,2435830
H	-5,1338250	-0,5951080	-0,7641570
C	-2,8509960	-0,7985050	0,8094110
C	-3,8900780	-1,2849800	1,6182000
C	-1,3084280	-1,2889250	2,5156130
H	-0,2699170	-1,2723210	2,8215670
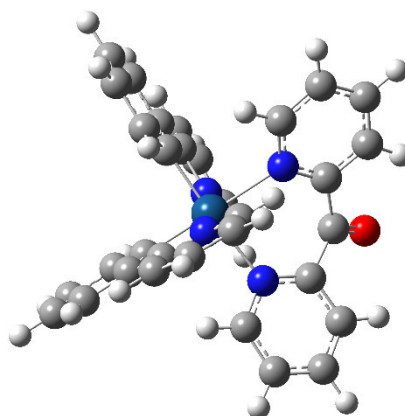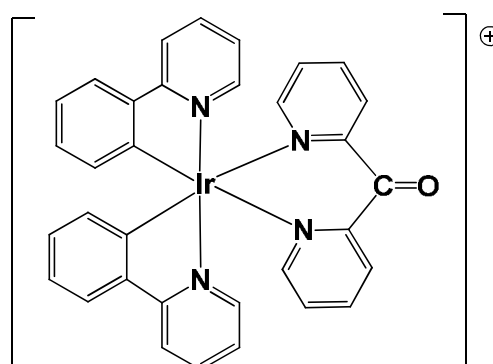
C	-2,2995040	-1,7857000	3,3478650
H	-2,0401220	-2,1680580	4,3288220
C	-3,6202070	-1,7744730	2,8882910
H	-4,4261750	-2,1473620	3,5130190
H	-4,9065380	-1,2744740	1,2430290
C	1,9441940	-3,8675280	-0,9876730
C	3,9064830	-0,7020510	1,8908010
C	3,9137500	0,1218870	3,0117360
C	0,9254280	-4,6864160	-1,4642500
H	4,8036680	0,2099790	3,6272050
H	1,1383620	-5,6982710	-1,7947420
H	2,9726860	-4,2042510	-0,9433230
H	4,7789900	-1,2711810	1,5942790
C	1,6444810	-2,5705210	-0,5521380
C	2,7436870	-0,8094620	1,1173560
C	2,7532090	0,8275360	3,3196670
H	2,6986400	1,4854340	4,1806510
C	1,6436990	0,6944380	2,4888080
H	0,7393270	1,2620000	2,6721290
C	-0,5879810	-2,8637400	-1,0853900
H	-1,5741700	-2,4205310	-1,1421950
C	-0,3674300	-4,1709030	-1,5105080
H	-1,2014480	-4,7595450	-1,8778610
C	2,8211060	-1,7731170	-0,0402350
O	3,9242950	-2,0383840	-0,4935830

Compound 10. Ground state geometry of the cation [(ppy)₂Ir(dpq)]⁺

at B3LYP/6-31G(d)/LanL2DZ level of theory

Charge = 1 Multiplicity = 1

Atom	X	Y	Z
Ir	-0,7930460	0,0000000	-0,0000010
N	0,9706820	0,9167270	1,0036300
C	2,1765290	-0,4965220	-0,5306590
C	-2,5212340	-2,3050280	-0,4532680
C	-2,9047480	0,6435300	2,1601270
H	-2,7201820	-0,3302700	2,6039340
C	0,9417020	-1,8381000	-1,9714250
H	-0,0445140	-2,1391760	-2,3090120
C	-0,1955120	-1,9091530	2,3192100
H	0,4769260	-1,1091860	2,6036430
C	-3,8362640	-1,4904760	-2,7658260
H	-4,3531170	-1,1654040	-3,6653070
C	-2,2202860	-1,0268790	-0,9970240
N	0,9706810	-0,9167360	-1,0036240
C	-1,7970870	-2,6550350	0,7668810
C	-1,2083020	-4,0482510	2,6584460
H	-1,3299630	-4,9648360	3,2276990
C	-3,8362900	1,4904820	2,7657940
H	-4,3531550	1,1654090	3,6652680
N	-0,9099830	-1,7043510	1,1944990
C	-2,2202910	1,0268840	0,9970110
C	-2,9047270	-0,6435260	-2,1601500
H	-2,7201500	0,3302730	-2,6039570
C	-1,9479270	-3,8406250	1,5029380
H	-2,6527530	-4,5912000	1,1654270
C	0,9417040	1,8380910	1,9714310
H	-0,0445110	2,1391700	2,3090160
C	-4,1151430	-2,7491900	-2,2225370
H	-4,8413500	-3,4035200	-2,6950700
C	2,1765290	0,4965090	0,5306670
C	3,3409750	1,9592790	2,0638930
H	4,2703130	2,3486740	2,4645270
C	-0,3114120	-3,0618700	3,0805060
H	0,2830560	-3,1780920	3,9798620
C	-3,4586530	-3,1545340	-1,0665260
H	-3,6813140	-4,1311530	-0,6457910
C	2,1071410	2,3847790	2,5260100
H	2,0267640	3,1300550	3,3101060
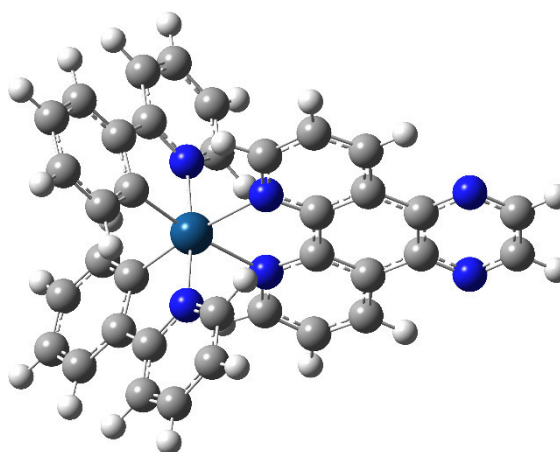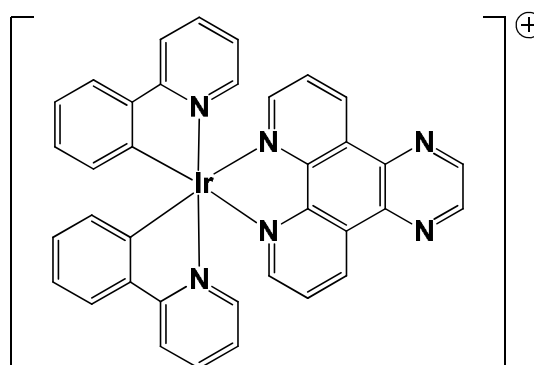
N	-0,9099600	1,7043590	-1,1944950
C	2,1071380	-2,3847910	-2,5260020
C	-4,1151570	2,7491990	2,2225060
C	3,3409720	-1,9592940	-2,0638830
C	-2,5212270	2,3050360	0,4532560
H	-4,8413670	3,4035300	2,6950320
C	-3,4586510	3,1545440	1,0665050
H	-3,6813030	4,1311650	0,6457700
C	-1,7970620	2,6550460	-0,7668820
C	-1,9478830	3,8406430	-1,5029320
C	-0,1954730	1,9091640	-2,3191960
H	0,4769630	1,1091940	-2,6036250
C	-0,3113530	3,0618880	-3,0804840
H	0,2831270	3,1781120	-3,9798310
C	-1,2082430	4,0482720	-2,6584280
H	-1,3298890	4,9648620	-3,2276760
H	-2,6527090	4,5912210	-1,1654240
H	2,0267600	-3,1300660	-3,3100990
H	4,2703100	-2,3486920	-2,4645170
C	3,3927510	0,9917260	1,0435480
C	3,3927500	-0,9917420	-1,0435380
C	4,6526460	-0,4885750	-0,5100710
C	4,6526470	0,4885560	0,5100820
C	6,9313830	0,4887310	0,5090530
C	6,9313820	-0,4887520	-0,5090430
N	5,8067950	0,9727420	1,0143540
N	5,8067930	-0,9727620	-1,0143430
H	7,8658110	0,8743820	0,9100290
H	7,8658100	-0,8744080	-0,9100140

Compound 12. Ground state geometry of the cation [(ppy)₂Ir(dppz)]⁺

at B3LYP/6-31G(d)/LanL2DZ level of theory

Charge = 1 Multiplicity = 1

Atom	X	Y	Z
Ir	-1,3932320	-0,0000020	-0,0000500
N	0,3679510	0,9580210	0,9623920
C	1,5742990	-0,5192170	-0,5113100
C	-3,1245290	-2,3222890	-0,3412950
C	-3,5088960	0,7435790	2,1245450
H	-3,3241900	-0,2080130	2,6142690
C	0,3341040	-1,9176160	-1,8940870
H	-0,6534260	-2,2312230	-2,2156650
C	-0,7947590	-1,7972690	2,4062110
H	-0,1215320	-0,9851830	2,6521130
C	-4,4433790	-1,6167090	-2,6870570
H	-4,9617810	-1,3338950	-3,5998670
C	-2,8222080	-1,0720410	-0,9459200
N	0,3679280	-0,9579140	-0,9624360
C	-2,3985180	-2,6149960	0,8928550
C	-1,8075080	-3,9179550	2,8470040
H	-1,9284430	-4,8068450	3,4587660
C	-4,4435280	1,6164910	2,6869620
H	-4,9619770	1,3335990	3,5997210
N	-1,5104730	-1,6457080	1,2738710
C	-2,8222760	1,0719460	0,9458560
C	-3,5087640	-0,7437600	-2,1246720
H	-3,3240170	0,2077930	-2,6144550
C	-2,5484650	-3,7647670	1,6838790
H	-3,2536120	-4,5301500	1,3823180
C	0,3341340	1,9177100	1,8940500
H	-0,6533940	2,2313790	2,2155770
C	-4,7236190	-2,8473710	-2,0834790
H	-5,4523390	-3,5219950	-2,5224690
C	1,5743080	0,5192710	0,5112960
C	2,7321980	2,0397830	1,9867910
H	3,6611010	2,4438620	2,3735860
C	-0,9101930	-2,9128150	3,2211360
H	-0,3146980	-2,9866130	4,1243020
C	-4,0651560	-3,1982190	-0,9109150
H	-4,2890460	-4,1530610	-0,4433000
C	1,4968620	2,4843950	2,4296880
H	1,4154550	3,2600250	3,1837210
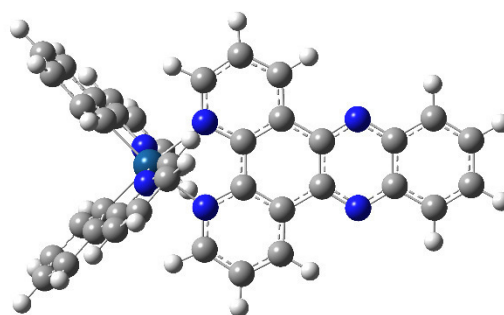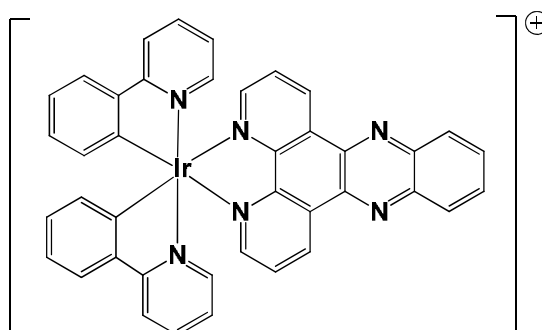
N	-1,5104860	1,6457740	-1,2738710
C	1,4968220	-2,4843810	-2,4296570
C	-4,7237410	2,8471980	2,0834680
C	2,7321660	-2,0398220	-1,9867280
C	-3,1245700	2,3222470	0,3413180
H	-5,4524800	3,5217910	2,5224760
C	-4,0652140	3,1981390	0,9109660
H	-4,2890840	4,1530180	0,4434170
C	-2,3985260	2,6150420	-0,8927920
C	-2,5484140	3,7649000	-1,6837030
C	-0,7947400	1,7974300	-2,4061800
H	-0,1215270	0,9853520	-2,6521470
C	-0,9101290	2,9130540	-3,2210030
H	-0,3146130	2,9869190	-4,1241510
C	-1,8074240	3,9181840	-2,8467950
H	-1,9283190	4,8071370	-3,4584710
H	-3,2535430	4,5302740	-1,3820800
H	1,4154000	-3,2600320	-3,1836650
H	3,6610630	-2,4439640	-2,3734700
C	2,7882750	1,0341160	1,0063570
C	2,7882560	-1,0341250	-1,0063250
C	4,0587930	-0,5148500	-0,4984750
C	4,0588030	0,5148150	0,4985130
C	6,3492140	0,5178400	0,5015310
C	6,3492050	-0,5178980	-0,5015070
C	7,5884170	1,0186870	0,9866930
C	8,7672810	0,5116240	0,4956170
H	9,7156290	0,8915500	0,8635720
C	8,7672730	-0,5117080	-0,4956050
H	9,7156140	-0,8916380	-0,8635720
C	7,5884000	-1,0187630	-0,9866700
H	7,5656620	-1,7981440	-1,7413540
H	7,5656920	1,7980680	1,7413770
N	5,1893890	1,0145200	0,9825350
N	5,1893720	-1,0145640	-0,9825040

Acknowledgements

List of publications

- F. Scarpelli, A. Ionescu, L. Ricciardi, P. Plastina, I. Aiello, M. La Deda, A. Crispini, M. Ghedini, N. Godbert, "A Novel Route Towards Water-Soluble Luminescent Iridium(III) Complexes via a Hydroxy-bridged Dinuclear Precursor", Dalton Trans., 2016, 45, 17264-17273.

- F. Scarpelli, A. Ionescu, I. Aiello, M. La Deda, A. Crispini, M. Ghedini, E. Brunelli, S. Sesti, N. Godbert. "High Order in a Self-Assembled Iridium(III) Complex Gelator Towards Nanostructured IrO_2 Thin Films", Chem. Asian J., 2017, 12, 2703-2710.

Side projects:

- T. F. Mastropietro, C. Meringolo, T. Poerio, F.Scarpelli, N.Godbert, G. Di Profio and E. Fontananova, "Multistimuli Activation of TiO_2/α-Alumina Membranes for Degradation of Methylene Blue", Ind. Eng. Chem. Res., 2017, 56, 11049–11057.

- H. K. Koduru, L. Marino, F. Scarpelli, Y. G. Marinov, G. B. Hadjichristov, M. T. Iliev and N. Scaramuzza, "Structural and dielectric properties of $NaIO_4$ – Complexed PEO/PVP blended solid polymer electrolytes", Curr. Appl. Phys., 2017, 1518-1531.